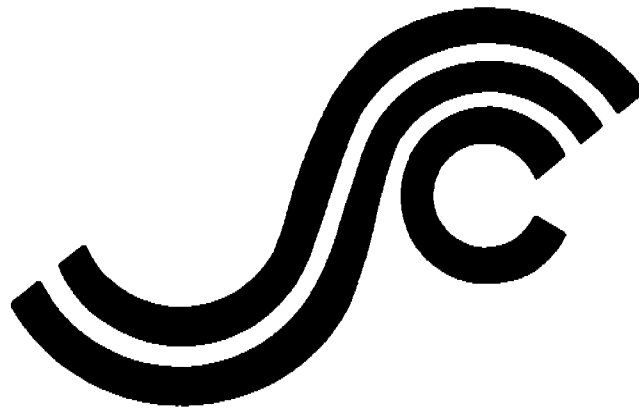


SSC-345

(PART 1)

**ELASTIC - PLASTIC
FRACTURE MECHANICS**

A CRITICAL REVIEW



This document has been approved
for public release and sale; its
distribution is unlimited

SHIP STRUCTURE COMMITTEE

1990

SHIP STRUCTURE COMMITTEE

The SHIP STRUCTURE COMMITTEE is constituted to prosecute a research program to improve the hull structures of ships and other marine structures by an extension of knowledge pertaining to design, materials, and methods of construction.

RADM J. D. Sipes, USCG, (Chairman)
Chief, Office of Marine Safety, Security
and Environmental Protection
U. S. Coast Guard

Mr. Alexander Malakhoff
Director, Structural Integrity
Subgroup (SEA 55Y)
Naval Sea Systems Command

Dr. Donald Liu
Senior Vice President
American Bureau of Shipping

Mr. H. T. Haller
Associate Administrator for Ship-
building and Ship Operations
Maritime Administration

Mr. Thomas W. Allen
Engineering Officer (N7)
Military Sealift Command

CDR Michael K. Parmelee, USCG,
Secretary, Ship Structure Committee
U. S. Coast Guard

CONTRACTING OFFICER TECHNICAL REPRESENTATIVES

Mr. William J. Siekierka
SEA 55Y3
Naval Sea Systems Command

Mr. Greg D. Woods
SEA 55Y3
Naval Sea Systems Command

SHIP STRUCTURE SUBCOMMITTEE

The SHIP STRUCTURE SUBCOMMITTEE acts for the Ship Structure Committee on technical matters by providing technical coordination for determining the goals and objectives of the program and by evaluating and interpreting the results in terms of structural design, construction, and operation.

AMERICAN BUREAU OF SHIPPING

Mr. Stephen G. Arntson (Chairman)
Mr. John F. Conlon
Mr. William Hanzalek
Mr. Philip G. Rynn

MILITARY SEALIFT COMMAND

Mr. Albert J. Attermeyer
Mr. Michael W. Touma
Mr. Jeffery E. Beach

MARITIME ADMINISTRATION

Mr. Frederick Seibold
Mr. Norman O. Hammer
Mr. Chao H. Lin
Dr. Walter M. Maclean

NAVAL SEA SYSTEMS COMMAND

Mr. Robert A. Sielski
Mr. Charles L. Null
Mr. W. Thomas Packard
Mr. Allen H. Engle

U. S. COAST GUARD

CAPT T. E. Thompson
CAPT Donald S. Jensen
CDR Mark E. Noll

SHIP STRUCTURE SUBCOMMITTEE LIAISON MEMBERS

U. S. COAST GUARD ACADEMY

LT Bruce Mustain

U. S. MERCHANT MARINE ACADEMY

Dr. C. B. Kim

U. S. NAVAL ACADEMY

Dr. Ramswar Bhattacharyya

STATE UNIVERSITY OF NEW YORK MARITIME COLLEGE

Dr. W. R. Porter

WELDING RESEARCH COUNCIL

Dr. Martin Prager

NATIONAL ACADEMY OF SCIENCES - MARINE BOARD

Mr. Alexander B. Stavovy

NATIONAL ACADEMY OF SCIENCES - COMMITTEE ON MARINE STRUCTURES

Mr. Stanley G. Stiansen

SOCIETY OF NAVAL ARCHITECTS AND MARINE ENGINEERS - HYDRODYNAMICS COMMITTEE

Dr. William Sandberg

AMERICAN IRON AND STEEL INSTITUTE

Mr. Alexander D. Wilson

Member Agencies:

*United States Coast Guard
Naval Sea Systems Command
Maritime Administration
American Bureau of Shipping
Military Sealift Command*



**Ship
Structure
Committee**

**An Interagency Advisory Committee
Dedicated to the Improvement of Marine Structures**

Address Correspondence to:

**Secretary, Ship Structure Committee
U.S. Coast Guard (G-MTH)
2100 Second Street S.W.
Washington, D.C. 20593-0001
PH: (202) 267-0003
FAX: (202) 267-0025**

December 17, 1990

**SSC-345
SR-1321**

**ELASTIC-PLASTIC FRACTURE MECHANICS
A CRITICAL REVIEW**

The use of fracture mechanics as a tool for structural design and analysis has increased significantly in recent years. Fracture theories provide relationships among fracture toughness, stress, and flaw size and are used, for example, to establish acceptance standards for material defects in structures. This first part of a two part report provides a critical review of the history and state-of-the-art of elastic-plastic fracture mechanics. Part 2 presents the results of an analytical and experimental study of fracture in the ductile-brittle transition zone of hull steels.

A handwritten signature in black ink, appearing to read 'J. D. Sipes', with a long horizontal stroke extending to the right.

J. D. SIPES

**Rear Admiral, U.S. Coast Guard
Chairman, Ship Structure Committee**

1. Report No. SSC-345 - Part 1		2. Government Accession No.		3. Recipient's Catalog No.	
4. Title and Subtitle Elastic-Plastic Fracture Mechanics - A Critical Review				5. Report Date April 1990	
				6. Performing Organization Code	
7. Author(s) T. L. Anderson				8. Performing Organization Report No. SR-1321	
9. Performing Organization Name and Address Texas A & M Research Foundation P. O. Box 3578 College Station, TX 77843				10. Work Unit No. (TRAILS)	
				11. Contract or Grant No. DTCG23-88-C-20037	
12. Sponsoring Agency Name and Address Commandant U.S. Coast Guard 2100 Second Street, SW Washington, DC 20593				13. Type of Report and Period Covered Final Report	
				14. Sponsoring Agency Code G-M	
15. Supplementary Notes Sponsored by the Ship Structure Committee and its member agencies.					
16. Abstract This document reviews the history and current state-of-the-art in elastic-plastic fracture mechanics as applied to welded steel structures. Fundamental concepts and underlying assumptions are described. Standardized test methods and recent developments are reviewed. The results of a parametric study comparing several elastic-plastic design analyses are presented.					
17. Key Words Fracture Mechanics Elastic-Plastic Deformation Fracture Toughness Transition Region			18. Distribution Statement Available from: Nat'l Technical Information Service Springfield, VA 22161 or Marine Tech. Information Facility National Maritime Research Center Kings Point, NY 10024-1699		
19. Security Classif. (of this report) Unclassified		20. Security Classif. (of this page) Unclassified		21. No. of Pages 160	22. Price

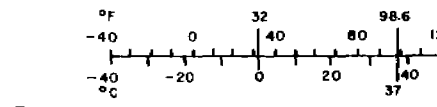
METRIC CONVERSION FACTORS

Approximate Conversions to Metric Measures

Approximate Conversions from Metric

Symbol	When You Know	Multiply by	To Find	Symbol
LENGTH				
in	inches	*2.5	centimeters	cm
ft	feet	30	centimeters	cm
yd	yards	0.9	meters	m
mi	miles	1.6	kilometers	km
AREA				
in ²	square inches	6.5	square centimeters	cm ²
ft ²	square feet	0.09	square meters	m ²
yd ²	square yards	0.8	square meters	m ²
mi ²	square miles	2.6	square kilometers	km ²
	acres	0.4	hectares	ha
MASS (weight)				
oz	ounces	28	grams	g
lb	pounds	0.45	kilograms	kg
	short tons (2000 lb)	0.9	tonnes	t
VOLUME				
tsp	teaspoons	5	milliliters	ml
Tbsp	tablespoons	15	milliliters	ml
fl oz	fluid ounces	30	milliliters	ml
c	cups	0.24	liters	l
pt	pints	0.47	liters	l
qt	quarts	0.95	liters	l
gal	gallons	3.8	liters	l
ft ³	cubic feet	0.03	cubic meters	m ³
yd ³	cubic yards	0.76	cubic meters	m ³
TEMPERATURE (exact)				
°F	Fahrenheit temperature	5/9 (after subtracting 32)	Celsius temperature	°C

Symbol	When You Know	Multiply by
LENGTH		
mm	millimeters	0.04
cm	centimeters	0.4
m	meters	3.3
km	kilometers	1.1
		0.6
AREA		
cm ²	square centimeters	0.16
m ²	square meters	1.2
km ²	square kilometers	0.4
ha	hectares (10,000 m ²)	2.5
MASS (weight)		
g	grams	0.035
kg	kilograms	2.2
t	tonnes (1000 kg)	1.1
VOLUME		
ml	milliliters	0.03
l	liters	2.1
l	liters	1.06
l	liters	0.26
m ³	cubic meters	35
m ³	cubic meters	1.3
TEMPERATURE (exact)		
°C	Celsius temperature	9/5 (then add 32)



*1 in = 2.54 exactly. For other exact conversions and more detailed tables, see NBS Monograph 286, Units of Weights and Measures, Page 52-25, SD Catalog No. C11.10.286.

EXECUTIVE SUMMARY

This document reviews the history and current state of the art in elastic-plastic fracture mechanics, as applied to welded steel structures. First, the fundamental concepts and underlying assumptions of fracture mechanics are described. A review of fracture mechanics test methods follows, including standardized test methods as well as recent developments that are not yet standard practice. Next, the various procedures for applying fracture mechanics concepts to structures are outlined. The results of a parametric study which compares several elastic-plastic design analyses are presented. This review has led to a number of conclusions and recommendations.

The ductile-brittle transition region is the critical area of concern for welded steel structures. If the material is on the lower shelf of toughness, it is usually too brittle for structural application; if it is on the upper shelf, fracture will not be a significant problem in most structural steels. One difficulty with applying fracture mechanics to welded structures in the transition region is the lack of standardized fracture toughness test procedure for weldments. An additional problem is that the size dependence of fracture toughness in the transition region has not been quantified. Scatter of toughness data in the lower transition region is reasonably well understood, but the upper transition region introduces complexities that require further study.

The comparison of elastic-plastic fracture analyses revealed that predicted failure stress and critical crack size are insensitive to the analysis equation. Under linear elastic conditions, all analyses were identical. In the other extreme of fully plastic conditions, the analyses approached similar collapse limits. Since most elastic-plastic fracture analysis equations predict similar results, the simplest equation seems to be most appropriate.

Current elastic-plastic fracture analyses tend to be conservative when applied to complex welded structures. In order to improve their accuracy, a number of issues need to be addressed: the driving force in weldments, residual stress measurements, three-dimensional effects, gross-section yielding and crack tip constraint.

TABLE OF CONTENTS

	<u>PAGE</u>
1. INTRODUCTION.....	1
2. FUNDAMENTAL CONCEPTS.....	4
2.1 ENERGY APPROACH TO FRACTURE MECHANICS.....	4
2.2 STRESS INTENSITY APPROACH TO FRACTURE MECHANICS.....	6
2.3 ELASTIC-PLASTIC FRACTURE MECHANICS.....	10
2.3.1 Irwin Plastic Zone Correction.....	10
2.3.2 Strip Yield Plastic Zone Correction.....	13
2.3.3 Plastic Zone Shape.....	14
2.3.4 Crack Tip Opening Displacement.....	16
2.3.5 The J Contour Integral.....	17
2.3.6 Relationship Between J and CTOD.....	20
2.3.7 The Effect of Yielding on Crack Tip Stress Fields.....	21
2.3.8 Effect of Thickness on Crack Tip Stress Fields.....	25
2.4 MICROMECHANISMS OF FRACTURE IN FERRITIC STEEL.....	27
2.4.1 Cleavage.....	29
2.4.2 Microvoid Coalescence.....	35
2.4.3 The Ductile-Brittle Transition.....	37
3. FRACTURE TOUGHNESS TESTING.....	39
3.1 K_{Ic} TESTING.....	41
3.2 J_{Ic} AND J-R CURVE TESTING.....	44
3.3 CTOD TESTING.....	47
3.4 WELDMENT TESTING.....	52
3.4.1 Specimen Design and Fabrication.....	53
3.4.2 Notch Location and Orientation.....	55
3.4.3 Fatigue Precracking.....	57
3.4.4 Post-Test Analysis.....	59
3.5 SCATTER AND SIZE EFFECTS IN THE TRANSITION REGION.....	62
3.5.1 Scatter in the Lower Transition Region.....	63
3.5.2 Large Scale Yielding.....	72

3.6	DYNAMIC FRACTURE TOUGHNESS AND CRACK ARREST	78
3.7	COMPARISONS BETWEEN J AND CTOD AS TOUGHNESS.....	82
3.8	CHARPY-FRACTURE TOUGHNESS RELATIONSHIPS.....	84
3.8.1	Empirical Correlations.....	85
3.8.2	Theoretical CVN-Fracture Toughness Relationships	87
4.	APPLICATION TO STRUCTURES.....	90
4.1	HISTORICAL BACKGROUND.....	90
4.1.1	Linear Elastic Fracture Mechanics (LEFM)	90
4.1.2	The CTOD Design Curve.....	91
4.1.3	The R-6 Failure Assessment Diagram.....	94
4.1.4	The EPRI J Estimation Procedure.....	97
4.1.5	Recent Advances in Elastic-Plastic Analysis.....	100
4.2	THE REFERENCE STRESS APPROACH.....	100
4.3	THE THREE TIER APPROACH (REVISED PD6493)	102
4.3.1	Level 1	102
4.3.2	Level 2	104
4.3.3	Level 3	106
4.4	COMPARISON OF DRIVING FORCE EQUATIONS: A PARAMETRIC STUDY	107
4.5	PROBABILISTIC FRACTURE MECHANICS	118
4.6	TEARING INSTABILITY ANALYSIS.....	119
4.7	SIMPLIFIED ELASTIC-PLASTIC ANALYSES	123
4.7.1	The Yield-Before-Break Criterion	123
4.7.2	Critical Tearing Modulus	124
4.8	UNRESOLVED ISSUES IN ELASTIC-PLASTIC FRACTURE ANALYSIS	125
4.8.1	Driving Force in Weldments.....	126
4.8.2	Residual Stresses.....	126
4.8.3	Three-Dimensional Effects	127
4.8.4	Crack Tip Constraint	127
4.8.5	Gross-Section Yielding.....	128
5.	DISCUSSION	129
5.1	FRACTURE TOUGHNESS TESTING.....	129

5.2 APPLICATION TO STRUCTURES.....	131
6. CONCLUSIONS.....	133
6.1 FRACTURE TOUGHNESS TESTING.....	133
6.2 APPLICATION TO STRUCTURES.....	133
7. REFERENCES.....	135

1. INTRODUCTION

Fracture mechanics is an extremely powerful tool for structural analysis. It quantifies the critical relationship between stress, flaw size and fracture toughness, as illustrated in Fig. 1.1. The stress is usually fixed by the design, while the fracture toughness is a property of the material. All materials contain flaws on some scale; nondestructive evaluation techniques determine the size and location of such flaws. Fracture mechanics provides the mathematical relationship between these three variables at the moment of failure. A critical value of any one of these quantities can be determined if the other two are known. For example, if the design stress in the structure and the fracture toughness of the material are specified, one can determine the critical flaw size by means of a fracture mechanics analysis. This is a departure from the traditional mode of design that relates applied stresses to the yield strength of the material.

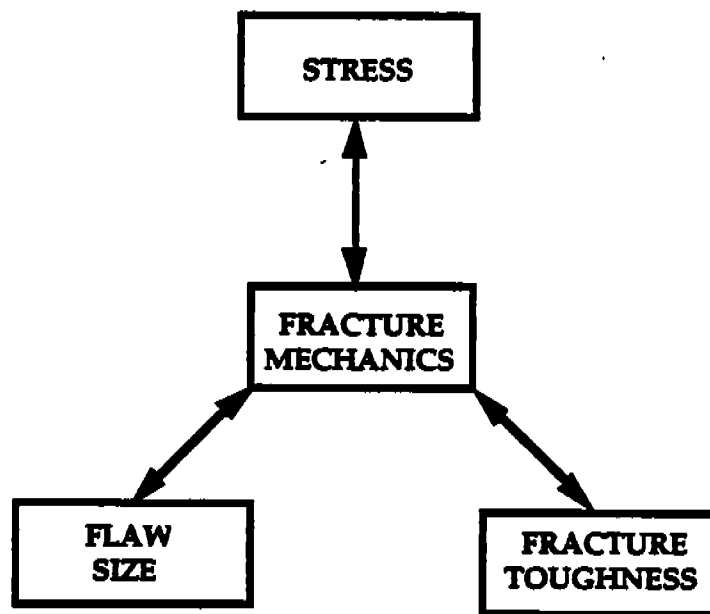


FIG. 1.1 Fracture mechanics provides a mathematical relationship between critical combinations of stress, flaw size and fracture toughness.

The field of fracture mechanics has developed rapidly since World War II, with many important advances made by American researchers, such as Professors G. R. Irwin, J. R. Rice, and P.C. Paris. Ironically, most U.S. industries have been slow to

adopt the concepts of fracture mechanics, while their counterparts in Europe and Japan have embraced this technology with open arms. Where it has been applied, fracture mechanics has resulted not only in increased safety, but also in enormous economic benefits. For example, hundreds of millions of dollars have been saved in North Sea platform construction by basing weld flaw acceptance standards on fracture mechanics analyses (1).

U.S. industrial attempts to incorporate fracture mechanics technology have often applied linear elastic fracture mechanics (LEFM), which is appropriate in some applications but unsuitable for many others. With local or global plastic deformation in the structure, LEFM can be extremely nonconservative.

Elastic-plastic fracture mechanics should be applied in situations where LEFM is invalid. Unfortunately, this technology is not well known to most U.S. industries. One exception is the nuclear power industry in the United States. Because of their concern for safety, electric utilities and government regulating bodies have funded extensive research in elastic-plastic fracture mechanics over the past 20 years. This work has produced well established procedures in the form of design handbooks, testing standards, and regulatory guides. In addition, numerous articles have been published in technical journals and conference proceedings.

Although the elastic-plastic fracture technology in the U.S. is fairly well advanced, much of it cannot be translated directly to industries other than nuclear power. Since nuclear reactors operate at several hundred degrees above room temperature, the steel in these structures is on the upper shelf of toughness. More conventional welded steel structures, such as ships, bridges, and pipelines, operate at much lower temperatures, where the material may be in the ductile-brittle transition region. In this region, failure occurs by rapid, unstable cleavage fracture, but this so-called brittle fracture is often preceded by significant plastic deformation and ductile crack growth. Thus, fracture in the transition region is elastic-plastic in nature, but the procedures developed by the nuclear power industry are intended to analyze ductile fracture on the upper shelf.

Considerable research in elastic-plastic fracture in the ductile-brittle transition region in the United Kingdom, driven largely by the development of oil reserves in the North Sea, has helped oil companies to build platforms both safely and economically. The design codes and regulatory guides for North Sea construction contain requirements for fracture mechanics testing and analysis. Consequently, a number of American oil companies with platforms in the North Sea are becoming familiar with elastic-plastic fracture technology.

In recent years significant technology transfer among fracture mechanics researchers in the U.S., Europe, and Japan has benefited all countries involved. For example, the analyses developed in Britain for the transition region have incorporated some of the advances that been made by the nuclear industry in the U.S. In addition,

researchers in the U.S. have begun to turn their attention to the transition region, primarily as a result of interactions with researchers on the other side of the Atlantic.

Thus much of the fracture mechanics technology needed by U.S. industries that construct and use welded steel structures is in place. The problem is the availability of relevant information to engineers in these industries. The details of fracture mechanics testing, analysis, and application are scattered throughout the published literature.

This review attempts to define the state of the art in elastic-plastic fracture mechanics, as applied to welded steel structures. The advantages and shortcomings of existing approaches are outlined, and possible future directions are discussed. Information from a wide variety of resources is included. The author hopes that this review will help to codify elastic-plastic fracture mechanics so that it will gain more widespread acceptance in industry.

Chapter 2 summarizes some of the fundamental concepts and basic assumptions of fracture mechanics. This chapter serves as a framework for subsequent topics; later chapters refer back to the concepts in Chapter 2. Chapter 3 covers fracture toughness testing, including standardized tests methods and newer test methods, such as fracture testing of welds. Recent research on data scatter and crack tip constraint is also reviewed. Chapter 4 describes the application of fracture toughness data to design, and critiques the available methods, identifying the shortcomings of existing approaches and making recommendations for future work. Chapter 5 summarizes the major points in the two previous chapters and gives the author's perspective on the state of the art in elastic-plastic fracture mechanics.

2. FUNDAMENTAL CONCEPTS

Modern fracture mechanics traces its beginnings back Griffith (2), who in 1920 used a simple energy balance to predict the onset of fracture in brittle materials. The Griffith model, with some modifications, is still applied today. An alternative but equivalent view of fracture considers the stresses and strains near the tip of the crack. Both of these approaches are outlined below for the case of linear elastic material behavior. This is followed by an introduction to elastic-plastic fracture mechanics and a brief review of the micromechanisms of fracture in steels and weldments.

2.1 ENERGY APPROACH TO FRACTURE MECHANICS

Consider a plate with a crack that is subjected to an external force, as illustrated in Fig. 2.1. The crack will grow when the energy available for crack extension is greater than or equal to the work required for crack growth. Stated another way, crack extension occurs when

driving force for fracture \geq material resistance.

This is essentially a restatement of the first law of thermodynamics. If the plate in Fig. 2.1 is held at a fixed displacement, the conditions for crack advance are given by

$$-\left(\frac{\partial U}{\partial a}\right)_{\Delta} \geq \frac{dW}{da} \quad [2.1]$$

where U is the elastic energy (per unit thickness) stored in the plate and W is the work required to grow the crack. Irwin (3) defined the term on the left of side of this inequality as the energy release rate, G , and the term on the right as the material resistance, R . Figure 2.1 illustrates the energy release rate concept. If the crack extends an increment da under fixed grip conditions, the stored energy decreases by dU . For this incremental crack extension to occur, dU must be at least as large as dW , the work required to fracture the material and create new surface.

If the driving force, G , is greater than the material resistance, R , the crack extension is unstable. If $G = R$, the crack growth may be stable or unstable, depending on the material and configuration. When G and R are equal, stability depends on the second derivative of work, as discussed below.

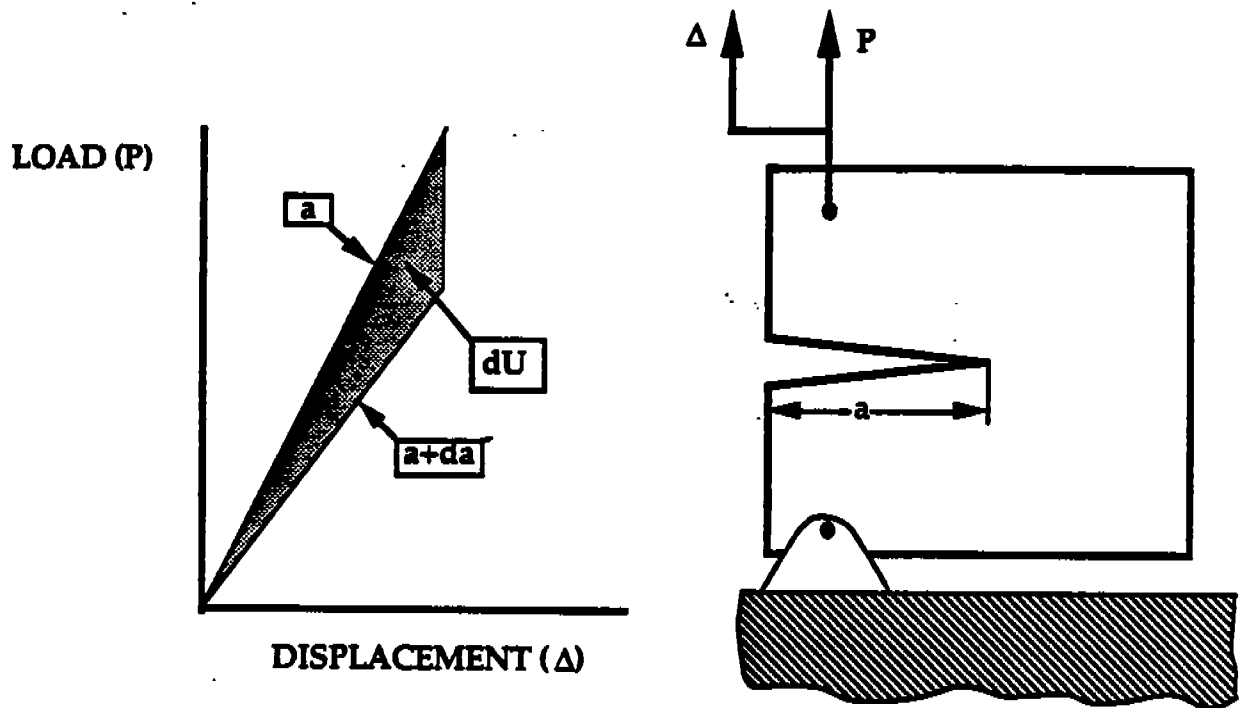


Fig. 2.1 Definition of energy release rate for fixed grip conditions.

Figure 2.2 illustrates stable and unstable behavior for a structure with an initial crack of length a_0 . The driving force is represented by a series of G versus crack length curves for various load levels. Figure 2.2(a) corresponds to a material in which R remains constant with crack growth. When the load = P_1 , the crack does not grow from its initial value because $G < R$. When the load is increased to P_2 , $G = R$, and the structure is unstable because any crack growth will cause G to be greater than R . The critical value of energy release rate, G_c , is a measure of the fracture toughness of the material. Some materials have a rising R curve, as illustrated in Fig. 2.2(b). In this case, when the load reaches P_2 , the crack grows a small amount, but further crack growth at this load is impossible, the driving force would be less than the material resistance. The crack grows an additional increment when the load increases to P_3 . When the load reaches P_4 , the structure is unstable because the rate of increase in G with crack extension exceeds the material's resistance. The instability occurs at the point of tangency between the driving force and the R curve. Thus the conditions for *stable* crack growth are as follows:

$$G = R \quad [2.2 a]$$

and

$$\frac{dG}{da} \leq \frac{dR}{da} \quad [2.2 b]$$

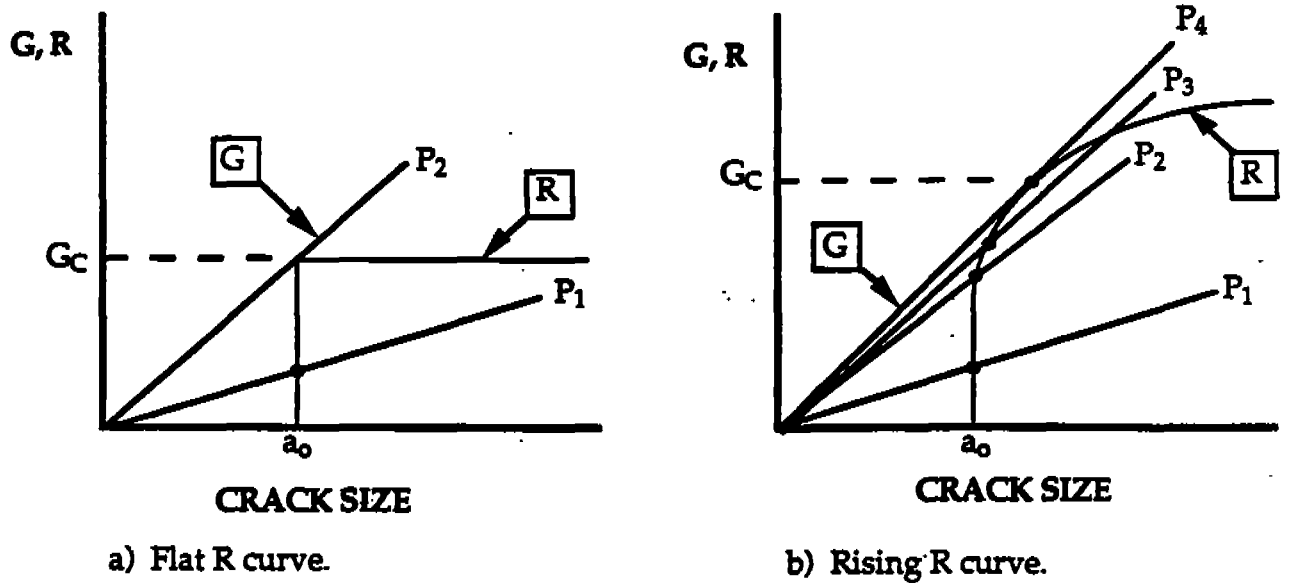


FIG. 2.2 Schematic driving force and resistance curves that illustrate stable and unstable behavior.

2.2 STRESS INTENSITY APPROACH TO FRACTURE MECHANICS

In 1939, Westergaard (4) performed an elastic stress analysis of a continuum with a sharp crack. Irwin (5) and Williams (6) later applied this analysis to engineering problems. The Westergaard-Irwin-Williams solution for the stresses near the crack can be written as

$$\sigma_{ij} = \frac{K}{\sqrt{2\pi r}} f_{ij}(\theta) + \text{other terms} \quad [23]$$

where σ_{ij} is the stress tensor, K is the stress intensity factor, r is the radial distance from the crack tip, and f_{ij} is a dimensionless function of θ , the angle from the crack plane. Both r and θ are defined in Fig. 2.3. The higher order terms, which depend on the configuration of the cracked body, are negligible near the crack tip.

Figure 2.4 shows the variation of stress ahead of the crack tip. The Westergaard solution implies that stresses approach infinity as r approaches zero. Real materials, however, deform plastically at finite stress levels (see Section 2.3). The stress intensity factor, K , is a proportionality constant that measures the severity of the stresses at the crack tip. If K doubles, for example, the stresses at a given r and θ also double.

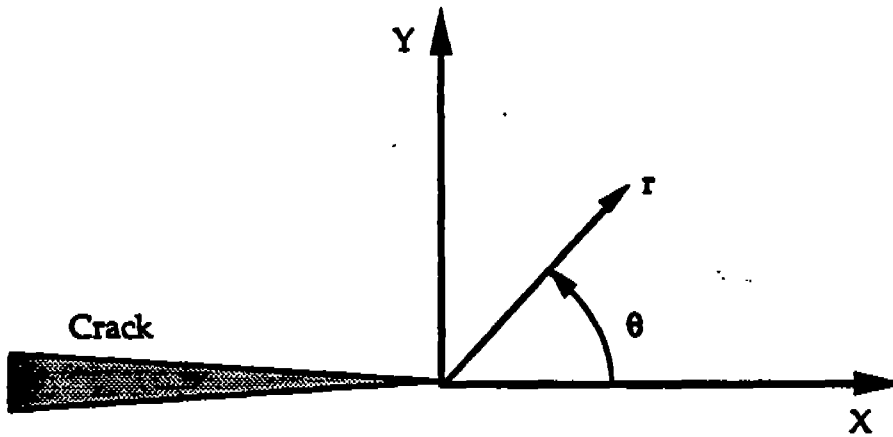


FIG. 2.3 Definition of x,y and polar coordinates at the tip of a crack.

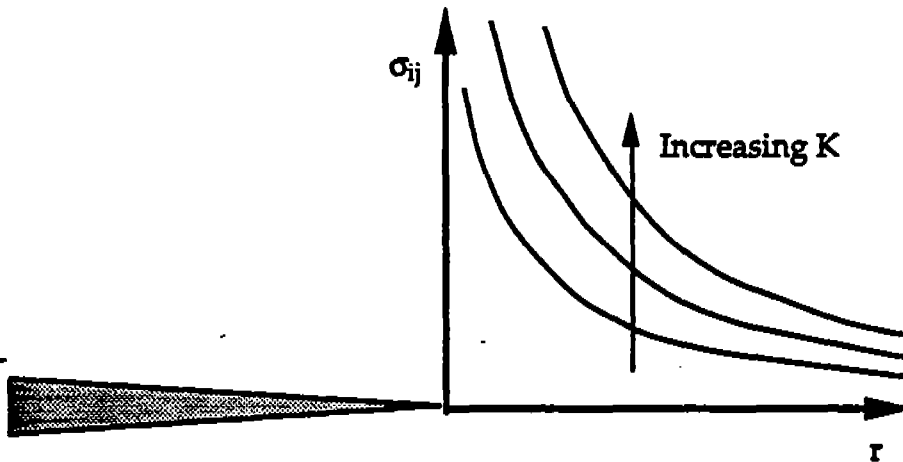


FIG. 2.4 Schematic stress distributions ahead of a crack in an elastic material.

Irwin and Williams identified three ways in which a cracked body could be loaded: opening (Mode I), sliding (Mode II) and out-of-plane shear (Mode III). In each case, the resulting stresses ahead of the crack tip can be described by Eq. [2.3]. The stress intensity factor typically has a subscript to identify the mode of loading: K_I , K_{II} or K_{III} . In most metals, the Mode I component of loading is the most important because it controls fracture. This document will consider only Mode I loading. (See Fig. 2.1 for an example of Mode I opening of a cracked body.)

The most important ramification of the Westergaard analysis is that all nine components of the stress tensor, as well as all components of the strain tensor, are completely defined by a single constant, K . That is, if K is known for a given situation, all stresses and strains near the crack tip can be computed from Eq. [2.3].

Consider a small element of material at the crack tip. It is reasonable to assume that this material element fails when it experiences a critical combination of stress and strain. Thus, this material element must fail at a critical K value. This philosophy led to the definition of a critical stress intensity, K_{IC} , at the onset of crack extension (7).

Although the stress intensity factor contains much information about the crack tip environment, it would be of little practical value if it were not possible to relate K to remote loads and displacements. Fortunately, K is related to global behavior. For example, if an infinitely wide plate with a crack of length $2a$ is loaded to a remote stress σ (Fig 2.5), the stress intensity factor is given by

$$K_I = \sigma \sqrt{\pi a} \quad [24]$$

The subscript is on K in this case because the configuration in Fig. 2.5 produces pure Mode I loading. Note that K_I , and thus the crack tip stresses, can be increased either by increasing the remote stress or by increasing the crack length. In addition,

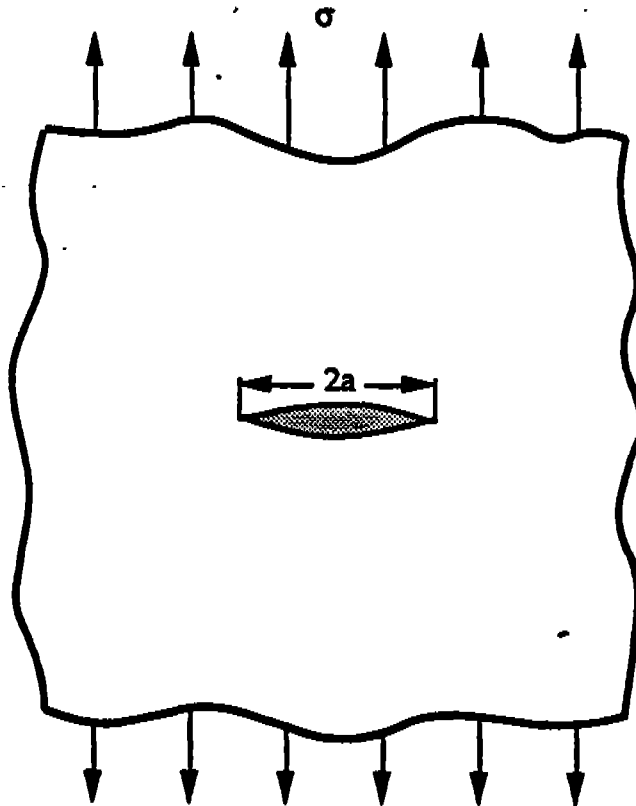


FIG. 2.5 Through thickness crack in a infinitely wide plate subjected to a remote stress.

by setting K_I to the critical value for the material, it is possible to relate stress, fracture toughness (K_{IC}), and critical crack size:

$$K_{IC} = \sigma \sqrt{\pi a_c} \quad [25]$$

Equation [2.4] applies only to a through-thickness crack in an infinite plate; i.e., a plate whose width is $\gg 2a$. For other configurations, K_I can be written in the following form.

$$K_I = Y\sigma \sqrt{\pi a} \quad [26]$$

where Y is a dimensionless geometry correction factor. In this case, σ is a characteristic stress and a is a characteristic crack dimension. Stress intensity equations can be expressed in a wide variety of ways but can always be reduced to the form of Eq. [2.6]. A number of handbooks of stress intensity factors for a wide range of configurations have been published over the last 20 years (8-10).

Given the stress intensity solution of a particular structure, it is possible to predict the fracture behavior of this structure from a small-scale laboratory specimen, as long as both the structure and the specimen behave in a linear elastic manner. Although the specimen and structure may be of vastly different size and shape, the crack tip conditions are identical as long as both configurations are loaded to the same K_I value. This situation is analogous to design against yielding. That is, a simple tensile test can predict the onset of yielding in a complex structure, given an appropriate stress analysis of the structure.

The previous section describes the energy approach to fracture mechanics, where the energy release rate, G , is compared to the material resistance, R . This section outlines the stress intensity approach, where the applied mode I stress intensity factor, K_I , is compared to the critical value for fracture initiation, K_{IC} . Irwin showed that the energy and stress intensity approaches are equivalent by demonstrating a unique relationship between K and G for linear elastic materials:

$$G = \frac{K^2}{E'} \quad [27]$$

where $E' = E$ (Young's modulus) for plane strain and $E' = E/(1 - \nu^2)$; ν is Poisson's ratio. The stress intensity approach to linear elastic fracture mechanics is more common than the energy approach. Fracture toughness data are seldom reported in terms of critical G values. The energy approach, however, does have merit in some situations. For example, stability analyses, such as that presented in the previous section, are more straightforward with an energy parameter such as G . In addition, G

is more convenient than K in mixed mode problems because G components are additive:

$$G_{\text{total}} = G_I + G_{II} + G_{III}$$

but

$$K_{\text{total}} \neq K_I + K_{II} + K_{III}$$

All of the above analyses are strictly valid only for isotropic materials that behave in a perfectly linear elastic manner. When there is a small amount of plastic deformation at the tip of the crack, linear elastic fracture mechanics (LEFM) gives a good approximation of actual material behavior. Eventually, however, the theory breaks down. The following section describes the limitations of LEFM and the existing methods to account for crack tip plasticity.

2.3 ELASTIC-PLASTIC FRACTURE MECHANICS

Fracture mechanics approaches to crack tip plasticity fall into two main categories: 1) simple corrections to LEFM theory, and 2) fracture parameters which allow for nonlinear material behavior. Irwin (11) proposed a simple plastic zone correction to the stress intensity factor. An alternative plastic zone correction was developed by Dugdale (12) and Barenblatt (13). The first truly elastic-plastic fracture parameter, the crack tip opening displacement (CTOD), was proposed by Wells (14) in 1961. Several years later, Rice (15) developed the J contour integral, a parameter that approximates elastic-plastic deformation with a nonlinear elastic material assumption. The J integral can be viewed as both an energy parameter and a stress intensity-like quantity. In addition, J is uniquely related to CTOD under certain conditions.

2.3.1 Irwin Plastic Zone Correction

Equation [2.3] predicts infinite stresses at the crack tip, but no material is capable of withstanding infinite stress. In metals, a plastic zone forms at the tip of the crack, thereby limiting the maximum stress in the material.

Consider the stresses normal to the crack plane ($\theta=0$) in mode I loading. Equation [2.3] reduces to

$$\sigma_{yy} = \frac{K_I}{\sqrt{2\pi r}} \quad [2.8]$$

For plane stress conditions ($\sigma_{zz}=0$), the material yields when $\sigma_{yy} = \sigma_{ys}$, the uniaxial yield strength of the material. Assuming a nonhardening material, the

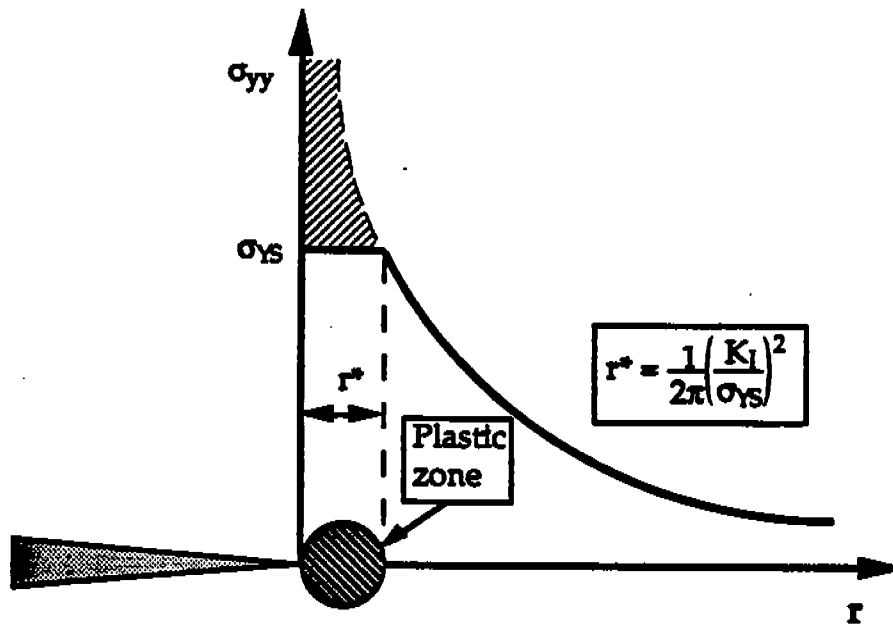


FIG. 2.6 First order estimate of plastic zone size for plane stress conditions.

stress field is truncated as indicated in Fig. 2.6. Substituting σ_{YS} into Eq. [2.8] gives a first order estimate of the plastic zone size:

$$r^* = \frac{1}{2\pi} \left(\frac{K_I}{\sigma_{YS}} \right)^2 \quad [29]$$

However, the schematic in Fig. 2.6 is not totally correct. The shaded area represents load that would be carried by a purely elastic material, but cannot be carried by an elastic-plastic material. In order for the structure to remain at equilibrium, the load represented by the shaded area must be redistributed, as shown in Fig. 2.7. Note that this increases the plastic zone size. Irwin (11) estimated the overall plastic zone to be $2r^*$.

An important effect of the redistribution in crack tip stresses is that the effective stress intensity increases. Outside of the plastic zone, Eq. [2.8] holds only if K_I is larger than the pure LFM value. Irwin (11) modeled this increase in the effective K_I by treating the crack as if it were slightly longer than its true physical length:

$$K_{eff} = Y\sigma \sqrt{\pi a_{eff}} \quad [210]$$

The effective crack length is obtained by adding a plastic zone correction to the physical crack length:

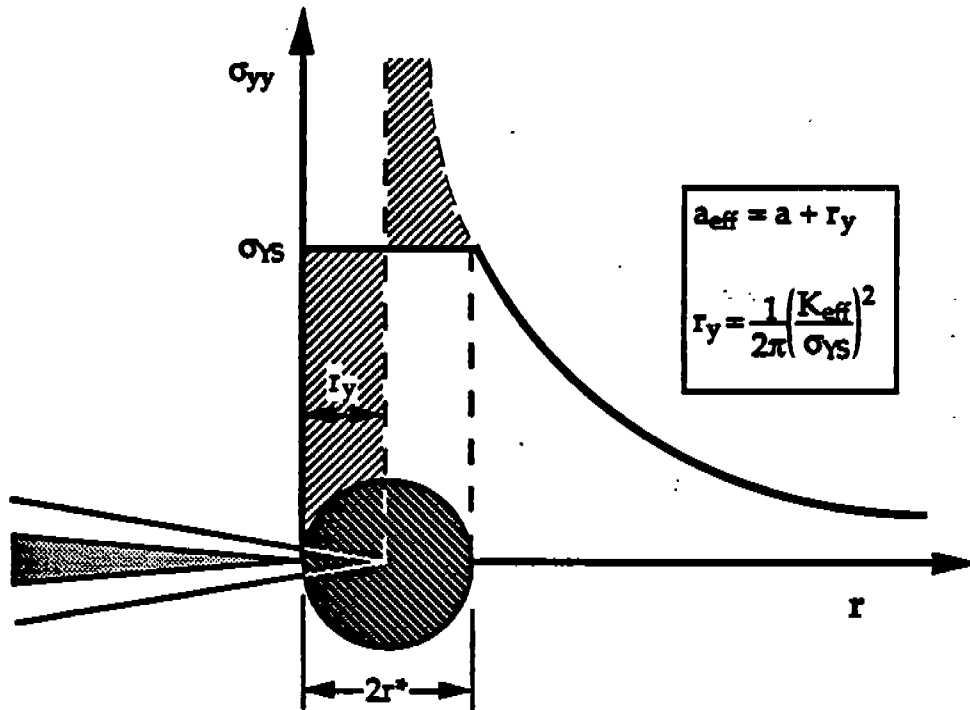


FIG. 2.7 Irwin plastic zone correction for plane stress conditions.

$$a_{\text{eff}} = a + r_y \quad [2.11]$$

The geometry correction factor, Y , in Eq. [2.10] must take account of the longer effective crack. For plane stress conditions, $r_y = r^*$; thus the plastic zone correction is given by

$$r_y = \frac{1}{2\pi} \left(\frac{K_{\text{eff}}}{\sigma_{\text{YS}}} \right)^2 \quad [2.12a]$$

For plane strain conditions, yielding is restrained and the plastic zone correction is smaller:

$$r_y = \frac{1}{6\pi} \left(\frac{K_{\text{eff}}}{\sigma_{\text{YS}}} \right)^2 \quad [2.12b]$$

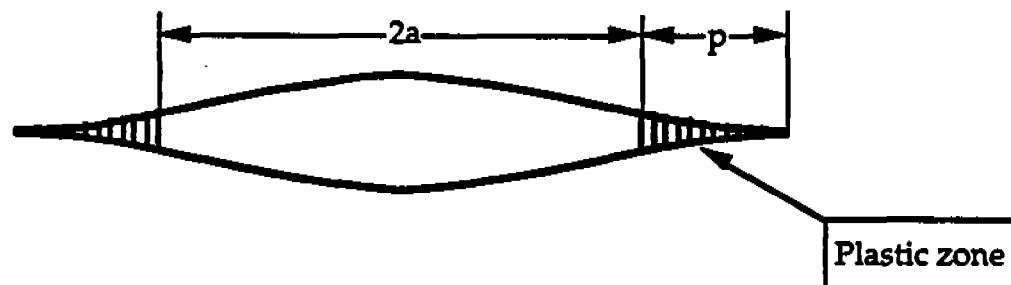
Calculation of K_{eff} is an iterative process: r_y is computed from K_{eff} , a new K_{eff} is computed from the r_y , a new r_y is then computed from this K_{eff} , and so on. The process usually requires only two or three iterations to converge on an accurate estimate of K_{eff} . Some simple configurations have a closed form solutions. For example, K_{eff} for a through crack in an infinite plate (Fig. 2.5) is given by

$$K_{\text{eff}} = \frac{\sigma\sqrt{\pi a}}{\left[1 - \frac{1}{2}\left(\frac{\sigma}{\sigma_{YS}}\right)^2\right]^{1/2}} \quad [2.13]$$

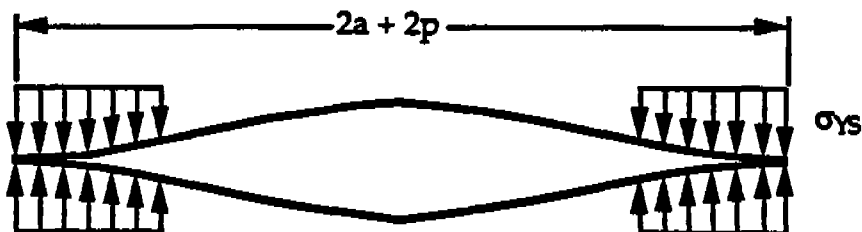
2.3.2 Strip Yield Plastic Zone Correction

In 1960, Dugdale (12) modeled plasticity ahead of a notch in a thin plate as a thin strip of yielded material. Barenblatt (13) independently developed a similar model. The strip yield model is illustrated in Fig. 2.8. The assumptions of this model include plane stress deformation and a nonhardening material. The initial analyses considered only a through crack in an infinite plate.

As indicated in Fig. 2.8, a plastic zone of length p is produced at each crack tip according to the model. Since the material cannot support stresses higher than yield, the model treats the problem as a crack of length $2a + 2p$, with closure stresses equal to yield at each end (Fig. 2.8b). The plastic zone size, relative to the physical crack size, is given by



a) Strip yield plastic zones.



b) Assumed closure stresses in the strip yield zone.

FIG. 2.8 The strip yield model for a through crack of length $2a$.

$$\frac{a}{a+p} = \cos\left(\frac{\pi}{2} \frac{\sigma}{\sigma_{YS}}\right) \quad [2.14]$$

If a_{eff} is taken as $(a+p)$, the effective K_I is given by

$$K_{\text{eff}} = \sigma \sqrt{\pi a \sec\left(\frac{\pi}{2} \frac{\sigma}{\sigma_{YS}}\right)} \quad [2.15]$$

However, this equation leads to overestimates of K_{eff} because closure stresses cause the true effective crack length to be somewhat less than $(a+p)$. Burdenkin and Stone analyzed the strip yield model further and derived a more appropriate relationship for K_{eff} :

$$K_{\text{eff}} = 0.9 \sigma_{YS} \sqrt{\pi a \left[\ln \sec\left(\frac{\pi}{2} \frac{\sigma}{\sigma_{YS}}\right) \right]^{1/2}} \quad [2.16]$$

Figure 2.9 shows a comparison between a pure LEFM analysis, the Irwin plastic zone correction for plane stress (Eq [2.13]), and the Burdenkin and Stone strip yield equation. The effective stress intensity, nondimensionalized by $\sigma_{YS} \sqrt{\pi a}$, is plotted against the normalized stress. The LEFM analysis predicts a linear relationship between K and stress. Both the Irwin and strip yield corrections deviate significantly from LEFM theory at stresses greater than $0.5 \sigma_{YS}$. The two plasticity corrections agree with each other up to approximately $0.85 \sigma_{YS}$. According to the strip yield model, K_{eff} approaches infinity as stress approaches the yield strength. Since this model assumes a nonhardening material, it is not surprising that it predicts that the plate cannot withstand stresses greater than yield. Obviously, the strip yield model is conservative for materials that strain harden. More sophisticated analyses that account for strain hardening are described in Chapter 4.

2.3.3 Plastic Zone Shape

Figures 2.6 and 2.7 idealize the plastic zone ahead at the tip of a crack tip as circular. The previous section modeled the plastic zone as a narrow-strip ahead of the crack. Neither of these viewpoints is correct in the case of metals. (Some plastics, however, exhibit crack tip damage zones which closely resemble Fig. 2.8a (16).) Figure 2.10 shows the computed plastic zone shape at several stress levels (17). For metals the plastic zone typically has a "butterfly" shape.

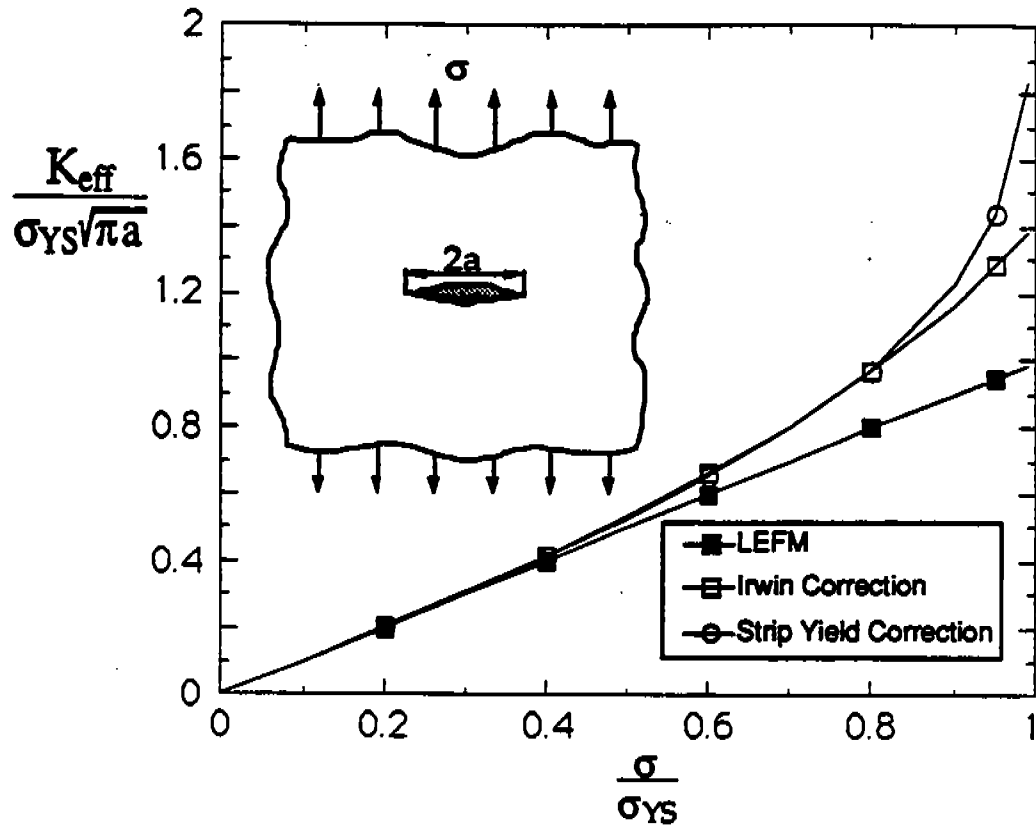


FIG. 2.9 Nondimensional plot of K_{eff} versus stress for a through crack in an infinite plate.

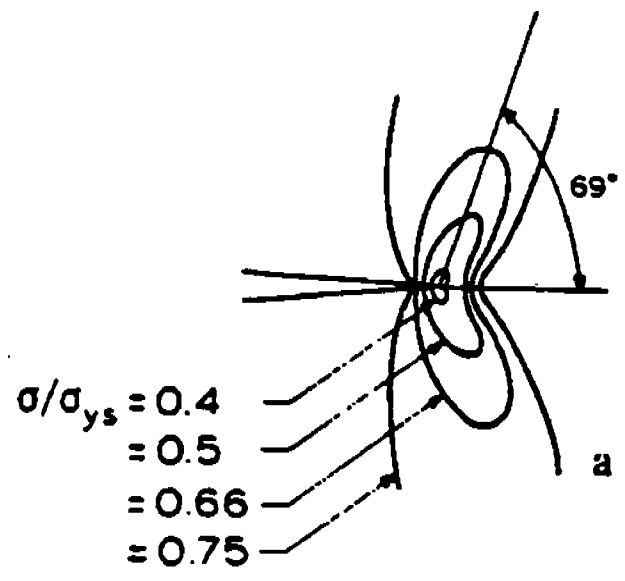


FIG. 2.10 Plastic zone shapes computed by Tuba (17).

2.3.4 Crack Tip Opening Displacement

In the late 1950s, Wells attempted to apply Irwin's stress intensity concept to measure the fracture toughness of a series of medium strength structural steels. He found that these materials exhibited a high degree of plastic deformation prior to fracture. This was good news from a design engineer's standpoint because it indicated high toughness in these steels. However, significant plasticity was bad news for theoreticians because it meant that linear elastic fracture mechanics was not applicable to typical structural steels.

Wells noticed that the crack faces moved apart prior to fracture in test specimens which exhibited a high degree of plasticity. In 1961, he proposed using the displacement of the crack faces as a measure of fracture toughness (14). The crack opening displacement (COD) was defined at the original crack tip, as illustrated in Fig. 2.11. Today Wells' COD is called the crack *tip* opening displacement (CTOD) to distinguish it from other displacement measurements along the crack flanks.

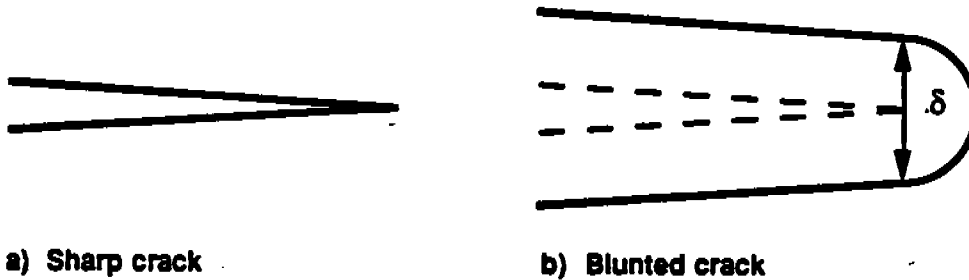


FIG. 2.11 Crack tip opening displacement (CTOD), defined at the original crack tip.

Wells (14) added credibility to CTOD as a fracture mechanics parameter by demonstrating a relationship between K_I and CTOD for plane stress small scale yielding conditions:

$$\delta = \frac{K_I^2}{\sigma_{YS} E} \quad [2.17]$$

where δ is the CTOD. Of course the intent was to apply CTOD beyond the limits of LEFM, but it was encouraging to learn that CTOD was consistent with the stress intensity approach in the limit of linear elastic behavior.

Burdenkin and Stone (18) used the strip yield model to estimate CTOD in an infinite plate with a through crack:

$$\delta = \frac{8 \sigma_{YS} a}{\pi E} \ln \sec \left(\frac{\pi \sigma}{2 \sigma_{YS}} \right) \quad [2.18]$$

Series expansion of the ln sec term yields

$$\delta = \frac{8 \sigma_{YS} a}{\pi E} \left[\frac{1}{2} \left(\frac{\pi \sigma}{2 \sigma_{YS}} \right)^2 + \frac{1}{12} \left(\frac{\pi \sigma}{2 \sigma_{YS}} \right)^4 + \dots \right] \quad [2.19a]$$

$$= \frac{K_I^2}{\sigma_{YS} E} \left[1 + \frac{1}{6} \left(\frac{\pi \sigma}{2 \sigma_{YS}} \right)^2 + \dots \right] \quad [2.19b]$$

Thus when σ/σ_{YS} is small, the Burdekin and Stone equation reduces to the Wells relationship for small scale yielding (Eq. [2.17]).

2.3.5 The J Contour Integral

Plasticity theory is more complex than the theory of elasticity. When a material deforms elastically, it is possible to deduce the current stresses from the current strains, and vice versa. However, material response to plastic deformation is history dependent. Since a set of plastic strains does not uniquely define the stresses in the material, a closed-form solution to the crack tip stress field, similar to the Westergaard solution for linear elastic materials, is not possible for an elastic-plastic material.

In certain cases, however, approximate stress analyses of elastic-plastic materials are possible by assuming a nonlinear elastic material response, as illustrated in Fig. 2.12. On loading, the stress-strain behavior of the nonlinear elastic material is identical to that of an elastic-plastic material. Only on unloading do the stress-strain curves differ. The similarity between stress-strain curves of elastic-plastic and nonlinear elastic materials does not necessarily carry over to three-dimensional loading situations, but there are many situations where the nonlinear elastic model gives a good approximation of real material behavior.

Rice (15) utilized a nonlinear elastic material assumption to derive the J contour integral, a parameter that describes the conditions near the tip of a crack. Prior to publishing his results, Rice discovered that Eshelby (19) had earlier published a series of conservation integrals, one of which was identical to Rice's J, but Eshelby did not apply his results to crack problems.

The J integral is obtained by integrating the following expression along an arbitrary path around the tip of a crack (Fig. 2.13):

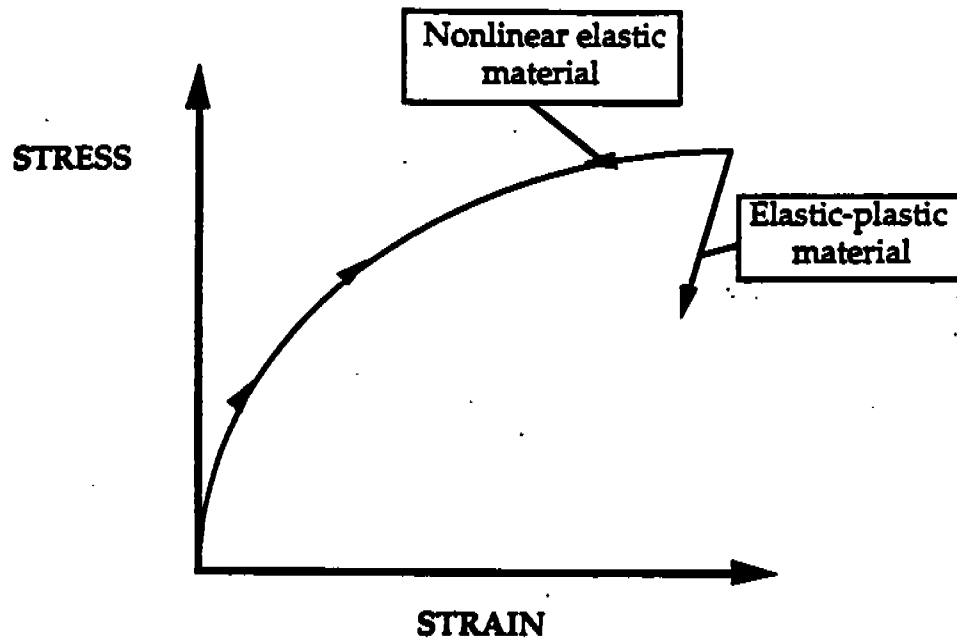


FIG. 2.12 Comparison of nonlinear elastic and elastic plastic material behavior. A nonlinear elastic material will unload along the same path as it was loaded.

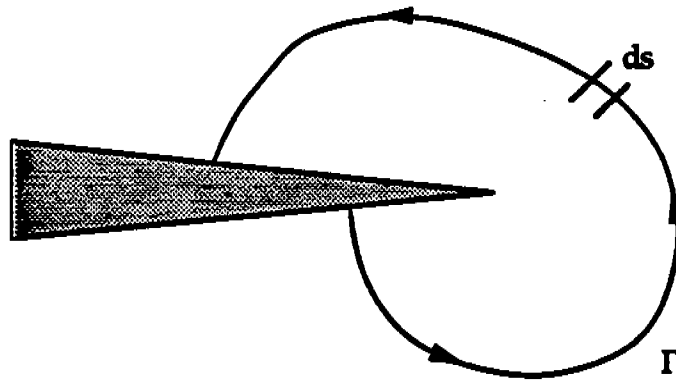


FIG. 2.13 Arbitrary contour around a crack tip.

$$J = \int_{\Gamma} \left(W dy - T \cdot \frac{\partial \mathbf{u}}{\partial x} ds \right) \quad [2.20]$$

where Γ is the path of integration, W is the strain energy density, T is the traction vector, \mathbf{u} is the displacement vector, and ds is an increment along Γ . The coordinates x and y are as defined in Fig. 2.3. For nonlinear elastic materials, Rice showed that the value of J is independent of the integration path as long as the contour encloses the crack tip, as illustrated in Fig. 2.13.

The J integral can also be defined as a nonlinear elastic energy release rate:

$$J = - \left(\frac{\partial U}{\partial a} \right)_{\Delta} \quad [2.21]$$

where U is the strain energy per unit thickness, as in Eq. [2.1], and Δ is the displacement in the loading direction. Figure 2.14 illustrates the energy release rate definition of J . For a *linear* elastic material, it is obvious that $J = G$. Thus the J integral reduces to the LFM energy release rate under small scale yielding conditions.

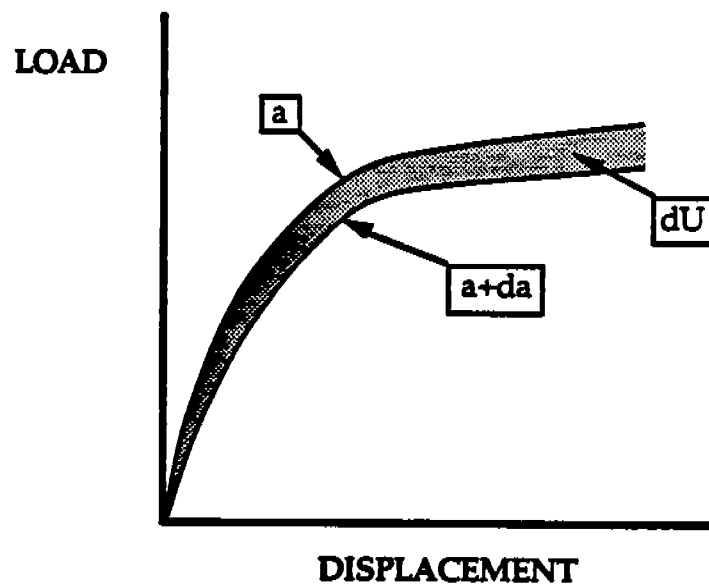


FIG. 2.14 Energy release rate definition of the J Integral.

In addition to being an energy release rate, J can be viewed as a stress intensity parameter. Hutchinson (20) and Rice and Rosencren(21) independently derived a crack tip stress and strain solution for nonlinear elastic materials, which became known as the HRR singularity. The HRR solution was derived for materials with a power law stress-strain relationship:

$$\frac{\varepsilon}{\varepsilon_0} = \alpha \left(\frac{\sigma}{\sigma_0} \right)^n \quad [2.22]$$

where σ_0 is a reference value of stress (usually σ_{YS}), $\varepsilon_0 = \sigma_0/E$, and α and n are material constants. The HRR stress and strain fields near the tip of the crack are given by

$$\sigma_{ij} = \sigma_0 \left(\frac{EJ}{\alpha \sigma_0^2 I_n r} \right)^{1/(n+1)} g_{ij}(n, \theta) \quad [2.23]$$

and

$$\varepsilon_{ij} = \frac{\alpha \sigma_0}{E} \left(\frac{EJ}{\alpha \sigma_0^2 I_n r} \right)^{n/(n+1)} h_{ij}(n, \theta) \quad [2.24]$$

where I_n is a dimensionless constant that depends on n , and g_{ij} and h_{ij} are dimensionless functions of n and θ . These parameters also depend on stress state (plane stress v. plane strain). For a linear elastic material, $n = 1$ and stress varies as $J/r (=G/r \text{ or } K/\sqrt{r})$, which is consistent with the Westergaard solution (Eq. [2.3]). As with the stress intensity factor in linear elastic materials, J completely characterizes the crack tip stresses and strains in nonlinear elastic materials. Thus J is an excellent fracture mechanics parameter for elastic-plastic materials, as long as the nonlinear elastic assumption gives a reasonable approximation of real material behavior. The limitations of the J integral approach are discussed in Section 2.3.7

2.3.6 Relationship Between J and CTOD

Under small scale yielding conditions, $J = G$, and CTOD and K_I are related (for plane stress) by Eq. [2.17]. Thus, for linear elastic, plane stress conditions, J and CTOD are related as follows:

$$J = \sigma_{YS} \delta \quad [2.25]$$

Shih (22) used the HRR singularity to derive a relationship between J and CTOD for elastic-plastic conditions:

$$J = \frac{\sigma_0 \delta}{d_n} \quad [2.26]$$

where d_n is a dimensionless constant that depends on material flow properties (ϵ_0 , n , α) and stress state (plane stress versus plane strain). Shih defined CTOD at the intersection of 90° vertices drawn from the crack tip, as illustrated in Fig 2.15. Typical structural steels blunt in a roughly semicircular shape (23). Thus the 90° intercept definition is approximately equal to the CTOD defined at the original crack tip.

Medium strength structural steels typically have an n value in the range of 8 to 12. The d_n value for such materials in plane strain is approximately 0.5. In the limit of no strain hardening, where n becomes large, d_n approaches 1.0 for plane stress. This agrees with Eq. [2.25], based on the Wells (14) and Burdekin and Stone (18) analyses. Both of these analyses assumed a nonhardening material.

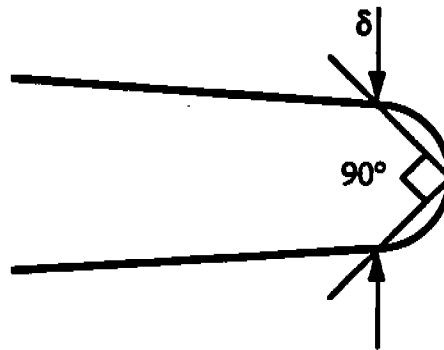


FIG. 2.15 The 90° Intercept definition of crack tip opening displacement.

2.3.7 The Effect of Yielding on Crack Tip Stress Fields

Figure 2.16 is a series of schematics showing the effect of plastic deformation on crack tip conditions. Part (a) illustrates small scale yielding behavior. The region moderately close to the crack tip where the crack tip stress and strain fields are described by Eq. [2.3] is called the K controlled region because the stress intensity factor completely defines the stresses and strains. Somewhat closer to the crack tip, in the plastic zone, is the J controlled region where Eqs. [2.23] and [2.24] apply. The small area very close to the crack tip is the large strain region where the HRR solution is no longer valid. A log-log plot of stress versus r has a slope of $-1/(n+1)$

in the J controlled region and a slope of -1/2 in the K controlled region. Outside the K controlled region, the stress field is influenced by the higher order terms in the Westergaard solution. In the case of small scale yielding, one can characterize the severity of the crack tip conditions with either K or J. Since $J=G$ in this case, K and J are directly related:

$$J = \frac{K^2}{E'} \quad [2.27]$$

As the plastic zone grows with additional loading, the K controlled region disappears, as illustrated in Fig. 2.16(b), but there is still a region in which the HRR solution is valid. Thus the crack tip conditions can be characterized with J, but K is no longer defined. It is possible to define an effective K based on the J value and Eq. [2.27]:

$$K_{\text{eff}} = \sqrt{J E'} \quad [2.28]$$

This effective K does not describe the actual stress field, but the stress field that would be present under small scale yielding, as indicated by the dashed line in Fig. 2.16(b).

Note that the large strain region is much bigger in Fig. 2.16(b). The size of this region is approximately 2δ (24). The HRR solution is not valid in the large strain region because of crack blunting. Equation [2.23] predicts that stresses approach infinity as r approaches zero. However, the tip of the blunted crack is a free surface which cannot support a triaxial stress state. Material in the large strain region has partially unloaded; thus the nonlinear elastic material assumption leads to erroneous predictions. The stresses in the large strain region are lower than predicted by the HRR singularity.

Under large scale yielding conditions (Fig. 2.16(c)), the large strain region engulfs the J controlled region, and neither J nor K characterize crack tip conditions. Because of a loss in triaxiality, the stresses are lower than predicted by both J theory and K theory.

The sizes of the J and K controlled regions depend on the size and geometry of the cracked structure. Because J and K controlled conditions exist longer in larger structures, fracture mechanics test standards usually contain specimen size requirements. For example, the American Society for Testing and Materials (ASTM) standard for K_{IC} testing (25) includes the following requirement:

$$B, b \geq 2.5 \left(\frac{K_{IC}}{\sigma_{YS}} \right)^2 \quad [2.29]$$

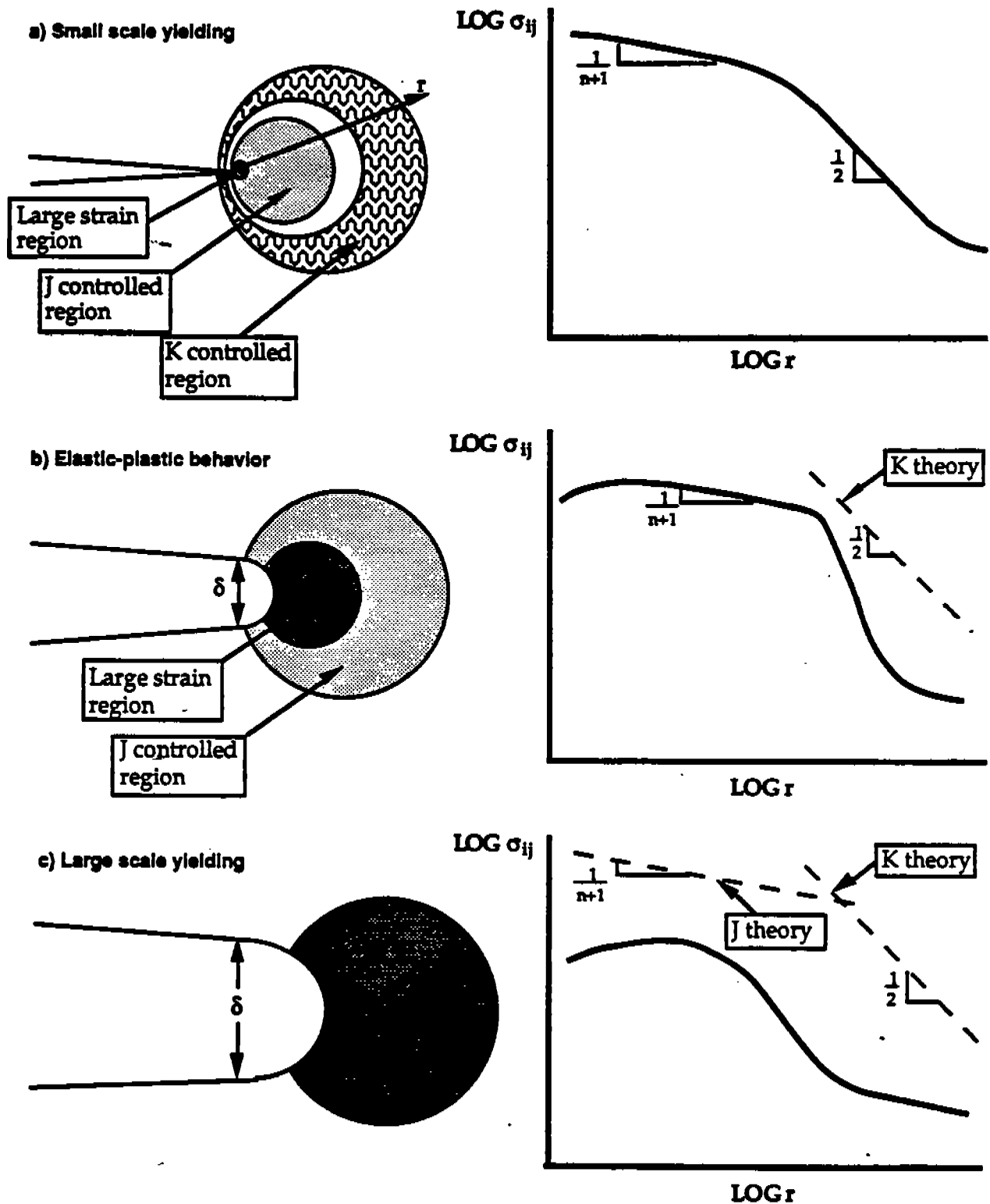


FIG. 2.16 Schematic showing the effect of plastic deformation on the crack tip stress field.

where B is the specimen thickness and b is the uncracked ligament length, as defined in Fig. 2.17. By comparing this requirement with Irwin's estimate of the plane strain plastic zone size (Eq. [2.12b]) one concludes that the plastic zone size must be no more than $\sim 1/50$ of characteristic specimen dimensions. The ASTM J_{IC} testing standard (26) also has a size requirement:

$$B, b \geq \frac{25 J}{\sigma_Y} \quad [2.30]$$

where σ_Y is the flow stress, defined as the average between the yield and tensile strengths. For a material with $d_n = 0.5$ and $\sigma_Y = 1.1\sigma_{YS}$, this requirement implies that the relevant specimen dimensions should be at least 45 times larger than the CTOD. Equation [2.30] is much less stringent than Eq. [2.29] because J controlled conditions exist much longer than K controlled conditions, as illustrated in Fig 2.16.

In many practical situations, it is impossible to satisfy Eq. [2.29] with laboratory specimens, but a large structure made from the same material may behave in a linear elastic manner at the design stress. This is illustrated schematically in Fig. 2.18, where a large structure and a small laboratory specimen are loaded to the same applied J . The plastic zone is too large for there to be a K controlled region in the small specimen, but the plastic zone is small compared to structural dimensions.

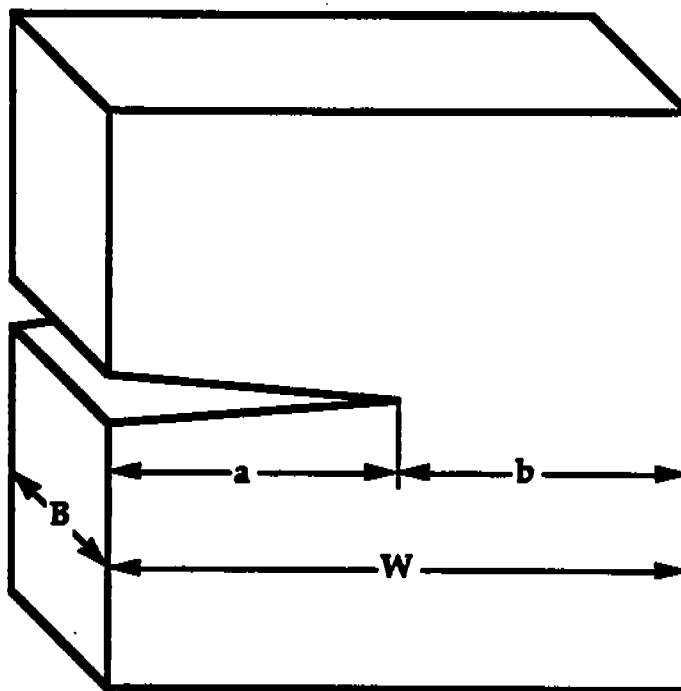


FIG. 2.17 Critical dimensions of a fracture mechanics specimen.

Thus the structure has both K and J controlled regions, but the specimen has only a J controlled region. Near the crack tip, the stress fields of the two configurations are identical. Further from the crack tip, however, the stress fields are different because the stresses in the small specimen are influenced by its finite size. In situations such as this, it is possible to measure a J_{IC} value on the small specimen, convert this value to an equivalent K_{IC} using Eq. [2.28], and apply this K_{IC} to the structure. Linear elastic fracture mechanics design analyses are much simpler than elastic-plastic analyses.

The issues raised in this section are discussed further in Chapters 3 and 4.

2.3.8 Effect of Thickness on Crack Tip Stress Fields

The discussion so far has focused on the x-y plane of a cracked structure because existing fracture mechanics analyses are two-dimensional. Equations [2.3], [2.23], and [2.24] apply only to purely plane stress or plane strain conditions. Real structures and specimens, however, contain regions that are neither plane stress nor plane strain.

Plane strain conditions at the tip of a crack produce a triaxial stress state, while plane stress conditions are biaxial by definition. Because of the different stress states, the plastic zone at a given K value is larger in plane stress, as indicated by Eqs. [2.12a] and [2.12b]. Both the stress normal to the crack plane, σ_{YY} , and the stress parallel to the crack propagation, σ_{XX} , are lower in plane stress than in plane strain. Since the local stress plays a key role in the failure of most materials, the measured fracture toughness is usually higher in plane stress.

The ASTM standards for K_{IC} and J_{IC} testing (25,26) have requirements on thickness as well as ligament length (Eqs. [2.29] and [2.30]). The thickness requirements are needed for the following reasons:

- Both J and K analyses assume two-dimensional deformation: either plane stress or plane strain. Thus fracture mechanics tests should approximate one of these two situations.
- Since plane strain is the more severe of the two cases, test specimens should be sufficiently thick to ensure predominantly plane strain conditions.

Wellman et al. (27) demonstrated the effect of thickness with three-dimensional finite element analysis of a fracture mechanics specimen of A36 steel. Figure 2.19 is a plot of σ_{YY} along the crack front for two thicknesses and three CTOD values, corresponding to $\theta = 0$ and a constant r value near the crack tip. The normalized thickness refers to the relative position along the crack front; $Z/T = 0$ corresponds to

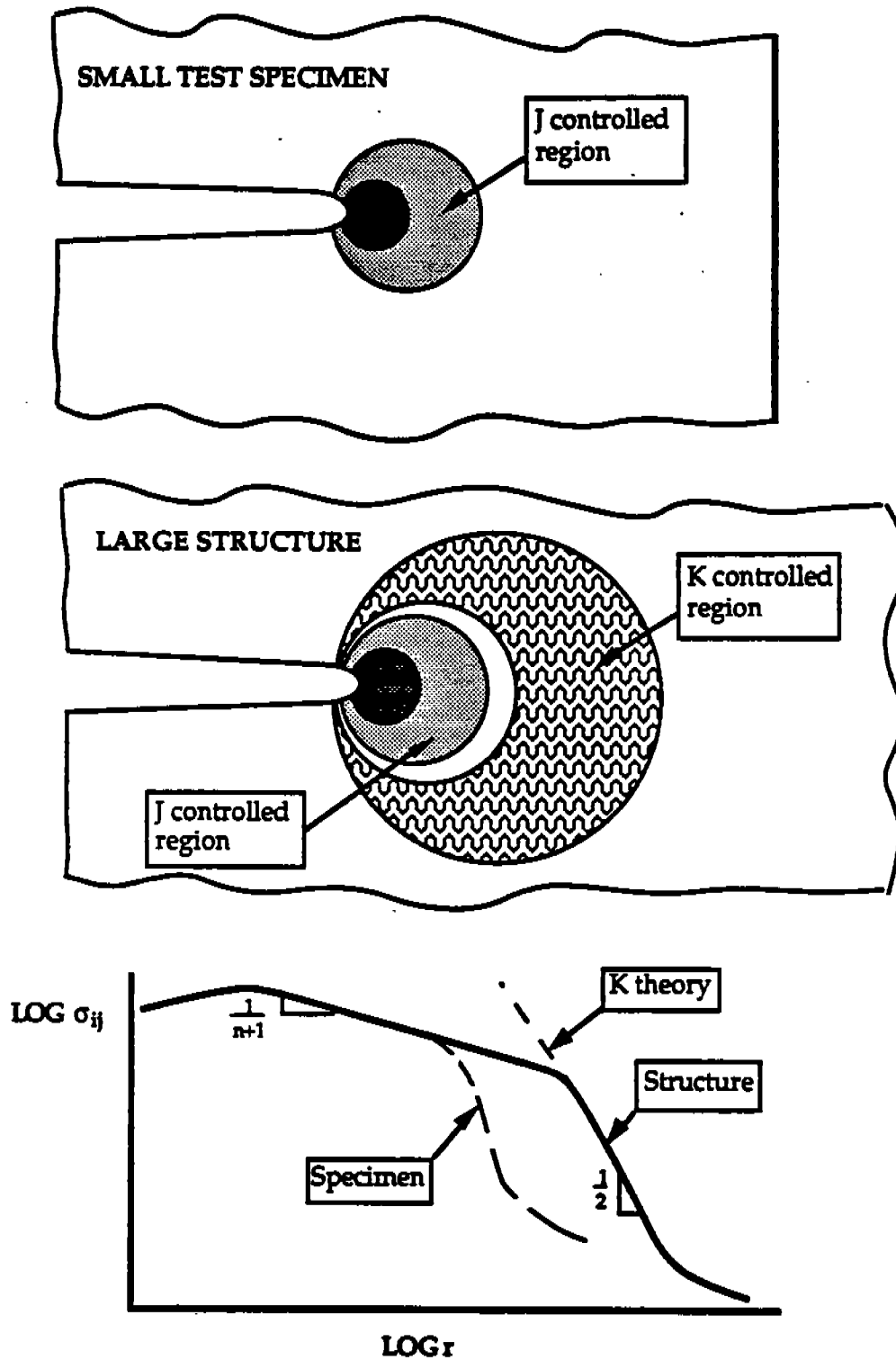


FIG. 2.18 Schematic stress fields in a small test specimen and a large structure loaded to the same applied J.

the center of the specimen and $Z/T = 1.0$ corresponds to an outer edge. Note that near the center of the specimen the curves are flat, indicating plane strain conditions. Near the edge of the specimen, stress decreases rapidly as the plane stress limit is approached. The size of the plane strain region decreases with increasing CTOD. The thicker specimen has a larger relative plane strain region at a constant CTOD, an effect is seen more clearly in Fig. 2.20, which is a plot of the relative size of the plane strain region versus CTOD/thickness. For this plot, the boundary of the plane strain region was defined arbitrarily as the point where the stress fell to 90 percent of the center plane value. The K_{IC} thickness requirement for this material is superimposed for comparison. According to Fig. 2.20, approximately 85 percent of the crack front is in plane strain when Eq. [2.29] is satisfied. The thickness requirement of Eq. [2.30] for this material corresponds to $CTOD/B = 0.022$, which is well off the scale of Fig. 2.20. Thus the crack front of a specimen that just satisfies the J_{IC} standard has less than 50 percent plane strain along the crack front. Whether or not this is sufficient to measure a fracture toughness value indicative of pure plane strain conditions depends on the micromechanism of fracture.

2.4 MICROMECHANISMS OF FRACTURE IN FERRITIC STEEL

Fracture in steel parent material and welds usually occurs by one of three mechanisms:

1. Transgranular cleavage
2. Microvoid coalescence
3. Intergranular fracture

Cleavage is rapid, unstable fracture usually associated with brittle materials, while microvoid coalescence (or ductile tearing) can occur in a slow, stable manner. Intergranular cracking can be either ductile or brittle. It is usually associated with a corrosive environment, grain boundary segregation, or both. In the absence of adverse environmental conditions and detrimental heat treatments such as temper embrittlement, fracture in ferritic materials nearly always occurs by mechanisms (1) and (2). Consequently, this section focuses on cleavage and microvoid coalescence.

Cleavage occurs when the local stress is sufficient to propagate a crack nucleus that forms from a microstructural feature such as a carbide or inclusion. For ductile tearing, a critical strain must be reached for the coalescence of voids that form around second phase particles. The fracture toughness will necessarily differ for the different fracture mechanisms (28).

Figures 2.21 and 2.22 are scanning electron microscope (SEM) fractographs that compare the appearance of the two fracture mechanisms (23,29). Cleavage produces a relatively flat, faceted surface because the fracture propagates along specific

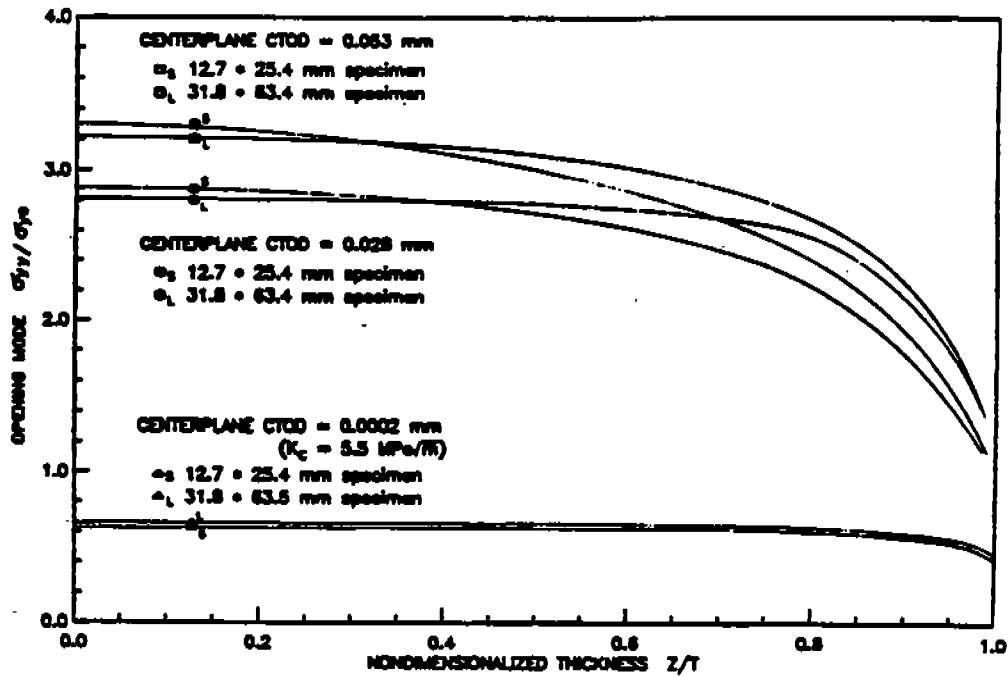


FIG. 2.19 Crack tip stress along the crack front for two specimen thicknesses and three CTOD values. After Wellman, et. al.(27)

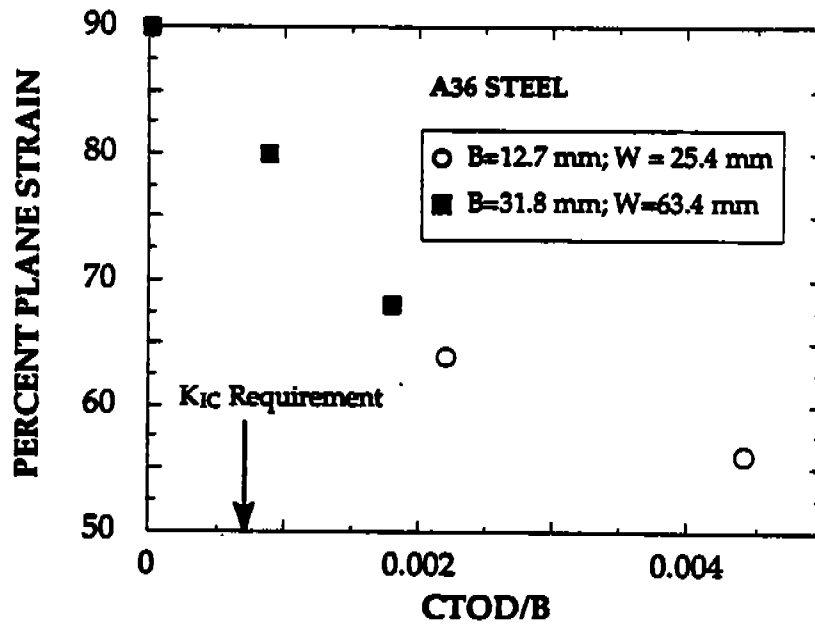


FIG. 2.20 Percent of the crack front where nonminally plane strain condition exist as a function of thickness and CTOD. Based on Wellman, et. al. results (27).

crystallographic planes ($\{100\}$ planes in the case of BCC iron). The microvoid coalescence fracture surface has a fibrous appearance because of the growth and coalescence of voids formed at inclusions. Some of the inclusions that nucleated voids are visible in Fig. 2.22. These two fracture mechanisms are described in more detail below.

2.4.1 Cleavage

Cleavage on the atomic level involves breaking bonds along the cleavage plane. Thus, the cohesive strength of the material must be exceeded locally. However, a macroscopic crack is only capable of producing stresses 3 to 5 times the uniaxial yield strength (24), well below the stress required to break bonds. Ferritic materials contain microstructural features capable of nucleating sharp microcracks that provide sufficient local stress elevation to cause failure.

This mechanism of cleavage nucleation is illustrated in Fig. 2.23. The macroscopic crack provides a local stress and strain concentration. A second phase particle, such as a carbide or inclusion, cracks because of the plastic strain in the surrounding matrix. At this point the microcrack can be treated as a Griffith (2) crack. If the stress ahead of the macroscopic crack is sufficient, the microcrack propagates into the ferrite matrix, causing failure by cleavage. For example, if the particle is spherical and it produces a penny-shaped crack, the fracture stress is given by

$$\sigma_f = \left(\frac{\pi E' \gamma_p}{C_o} \right)^{1/2} \quad [2.31]$$

where γ_p is the plastic work required to create a unit area of fracture surface in the ferrite and C_o is the particle diameter.

The nature of the microstructural feature that nucleates cleavage depends on the alloy and heat treatment. In mild steels, cleavage usually initiates at grain boundary carbides (28,30,31). In quenched and tempered alloy steels, the critical feature is usually either a spherical carbide or an inclusion (28). Various models (28,30-33) have been developed to explain the relationship between cleavage fracture stress and microstructure. Most of these models resulted in expressions similar to Eq. [2.31]; some models differ from Eq. [2.31] because they account for dislocation interactions with the particles (31,32).

Susceptibility to cleavage fracture is enhanced by almost any factor that increases the yield strength, such as low temperature, a triaxial stress state, radiation damage, high strain rate, and strain aging. Grain size refinement increases the yield strength but also increases σ_f . There are a number of reasons for the grain size effect. In mild



FIG. 2.21 SEM fractograph of cleavage fracture in pure iron (23).

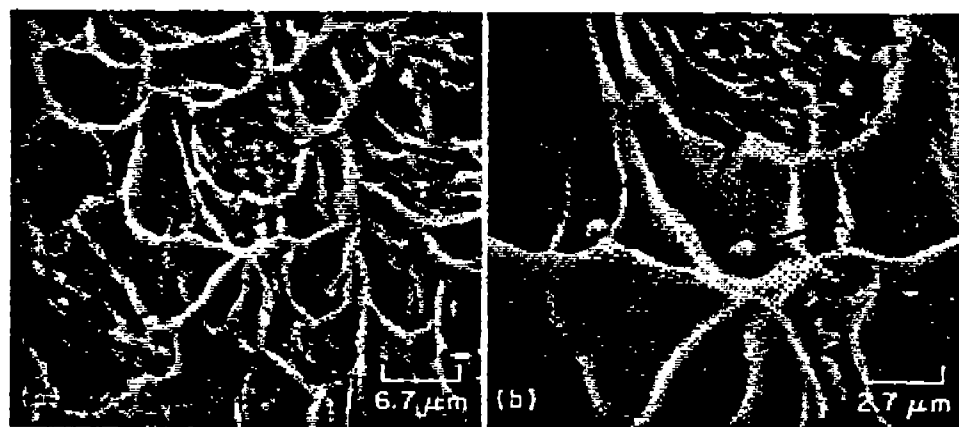


FIG. 2.22 SEM fractographs of microvoid coalescence in hot rolled 1040 steel (29).

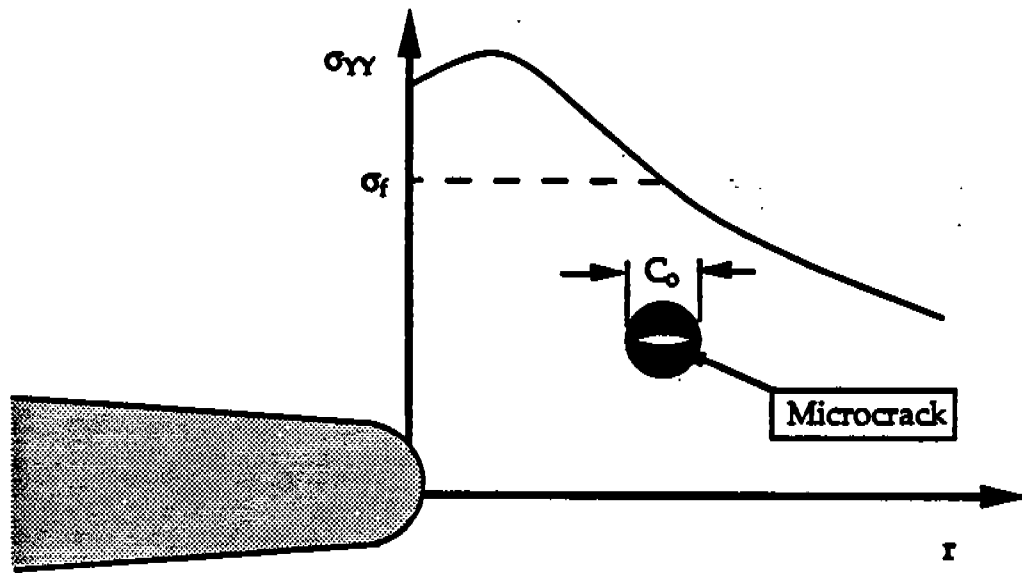


FIG. 2.23 Nucleation of a sharp microcrack ahead of a macroscopic crack.

steels, a decrease in grain size implies an increase in grain boundary area, which leads to smaller grain boundary carbides and an increase in σ_f . In fine grained steels, the critical event may be propagation of the microcrack across the first grain boundary it encounters. In such cases the Griffith model implies the following expression for fracture stress:

$$\sigma_f = \left(\frac{\pi E' \gamma_{gb}}{d} \right)^{1/2} \quad [2.32]$$

where γ_{gb} is the plastic work per unit area required to propagate into the adjoining grain, and d is the grain diameter. Since there tends to be a high degree of mismatch between grains in a polycrystalline material, $\gamma_{gb} > \gamma_p$. Equation [2.32] assumes an equiaxed grain structure. For martensitic and bainitic microstructures, Dolby and Knott (33) derived a modified expression for σ_f based on the packet diameter.

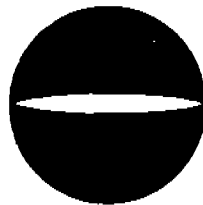
Figure 2.24 summarizes the the cleavage fracture process. Although this schematic shows a spherical particle in the center of a ferrite grain, the concepts represented apply to all types of cleavage nucleation. Part (a) illustrates crack nucleation in the particle. The particle cracks because it is unable to strain plastically with the matrix. If the stress is high enough to satisfy Eq. [2.31], the microcrack propagates into the surrounding matrix, as illustrated in Fig. 2.24(b). When the propagating crack

reaches the grain boundary, it must change orientation to align itself with the nearest cleavage plane of the next grain (Fig. 2.24c), requiring additional work, as discussed above.

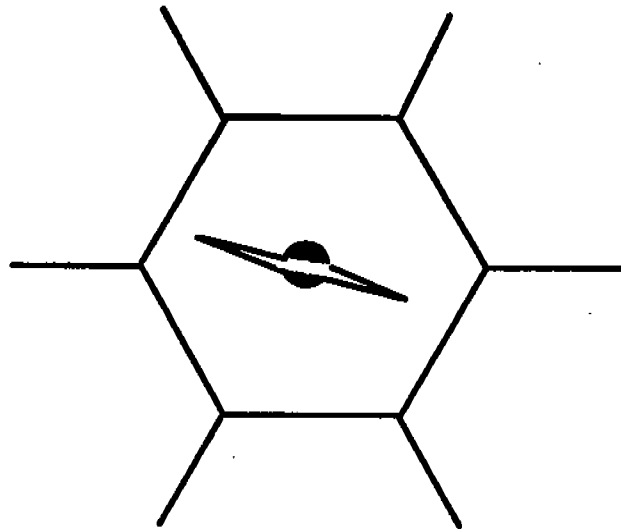
In some cases cleavage nucleates, but total fracture of the specimen or structure will not occur. Figure 2.25 illustrates three examples of unsuccessful cleavage events. Part (a) shows a microcrack that has arrested at the particle/matrix interface. The particle cracks due to strain in the matrix, but the crack is unable to propagate because the applied stress is less than the required fracture stress. This microcrack does not re-initiate because subsequent deformation and dislocation motion in the matrix causes the crack to blunt. Microcracks must remain sharp in order for the stress on the atomic level to exceed the cohesive strength of the material. If a microcrack in a particle propagates into the ferrite matrix, it may arrest at the grain boundary, as illustrated in Fig. 2.25(b). This corresponds to a case where Eq. [2.32] governs cleavage. Even if a crack successfully propagates into the surrounding grains, it may still arrest if there is a steep stress gradient ahead of the macroscopic crack (Fig. 2.25c). This tends to occur at low applied K_I values. Locally, the stress is sufficient to satisfy Eqs. [2.31] and [2.32] but the stress decays rapidly away from the macroscopic crack and eventually can no longer satisfy the Griffith energy criterion.

The phenomena illustrated in Fig. 2.25 have been observed experimentally. Gerberich (34) monitored fracture toughness tests with acoustic emission and observed many micro-cleavage events before final fracture. Lin et al. (35) provided metallographic evidence of cracked carbides and crack arrest at grain boundaries in a 1008 spheroidized steel. Irwin (36) observed numerous cleavage initiation sites on the fracture surfaces of notched round bars which were tested at very high strain rates. The dynamic loading caused cleavage nucleation at very low K_I values. These early cleavage events arrested, apparently because of the steep stress gradient. Final failure of each specimen occurred when the applied K_I was sufficient for a crack to propagate through the specimen.

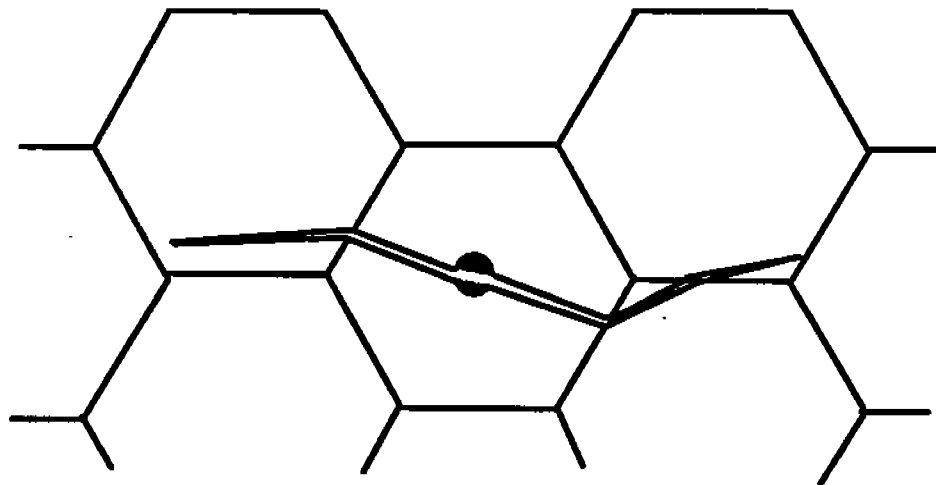
Cleavage fracture is a weakest link phenomenon. A specimen or structure needs only one critical microstructural feature for catastrophic failure to occur. The local fracture stress depends on the largest or most favorably oriented particle that occurs in the material near the tip of a macroscopic crack. A finite amount of material must be sampled in order to find a critical particle. Ritchie et al. (37) were among the first to recognize this when they proposed a simple model for cleavage. Their model states that cleavage will occur when the critical fracture stress, σ_f , is exceeded over a critical distance, x_c , ahead of the crack tip. They assumed that σ_f and x_c were single valued material constants. Curry and Knott (38) used a statistical argument to develop a model in which a critical sample volume was required in order to cause failure. Later, Curry (39) demonstrated that their statistical interpretation of cleavage was essentially equivalent to the Ritchie et al. model. Recently, a number of more sophisticated statistical models for cleavage fracture have been developed (35,40-44). These models predict the effect of microstructure on fracture toughness. In addition,



a) Particle cracks.

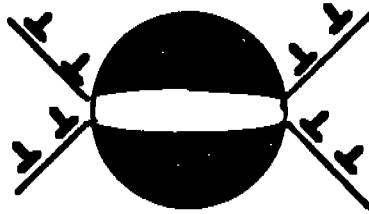


b) Microcrack propagates into the ferrite matrix.

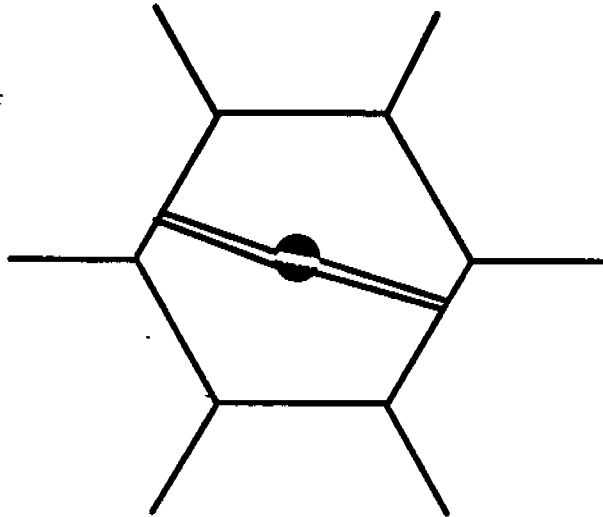


c) Cleavage crack propagates into adjoining grains.

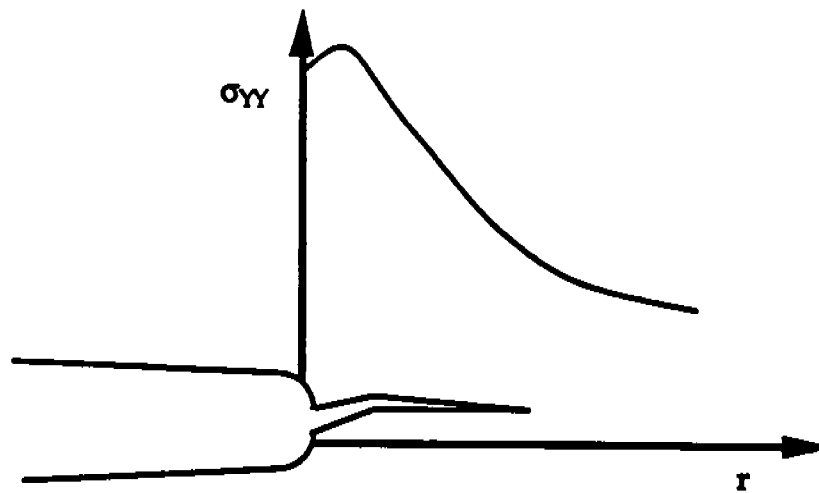
FIG. 2.24 Schematic drawings of the cleavage fracture process in ferritic steels.



a) Arrest at the particle/matrix interface, followed by crack blunting.



b) Arrest at a ferrite grain boundary.



c) Arrest due to a steep stress gradient

FIG. 2.25 Examples of unsuccessful cleavage events.

the statistical models quantify the scatter in fracture toughness data, which is a direct result of the weakest link nature of cleavage. This scatter is particularly severe in the ductile-brittle transition of steels. Some of the methods for analyzing scatter are described in Section 3.5.

2.4.2 Microvoid Coalescence

In ferritic steels, as the temperature increases and the flow stress decreases it becomes more difficult to produce high enough stresses to initiate cleavage. When conditions for cleavage are unfavorable a ductile fracture mechanism, microvoid coalescence, operates. This is the dominant fracture mechanism of FCC alloys, even at very low temperatures. The typical microstructural changes which occur during initiation and growth of a fibrous crack are (28):

1. Formation of a free surface at a second phase particle or inclusion by either interface decohesion or particle cracking
2. Growth of a void around the particle, with the aid of hydrostatic stress
3. Coalescence of the growing void with the crack tip

Crack growth by microvoid coalescence is illustrated schematically in Fig. 2.26. The above events occur continuously as the crack advances. That is, as voids at the crack tip coalesce, additional voids nucleate and grow further away from the crack tip. A number of models have been developed to describe this fracture process (45-47). Rice and Tracey (45) proposed the following equation to describe the growth of a void.

$$\ln\left(\frac{R}{R_0}\right) = 0.283 \int_0^{\epsilon_{eq}} \exp\left(\frac{1.5 \sigma_m}{\sigma_{YS}}\right) d\epsilon_{eq} \quad [2.33]$$

where R is the void radius, R_0 is the initial radius, ϵ_{eq} is the equivalent plastic strain, and σ_m is the mean (or hydrostatic) stress, defined as

$$\sigma_m = \frac{\sigma_{xx} + \sigma_{yy} + \sigma_{zz}}{3} \quad [2.34]$$

Rice and Tracey assumed a nonhardening material in their analysis. More recent models (46,47) have modified the above expression to take account of strain hardening.

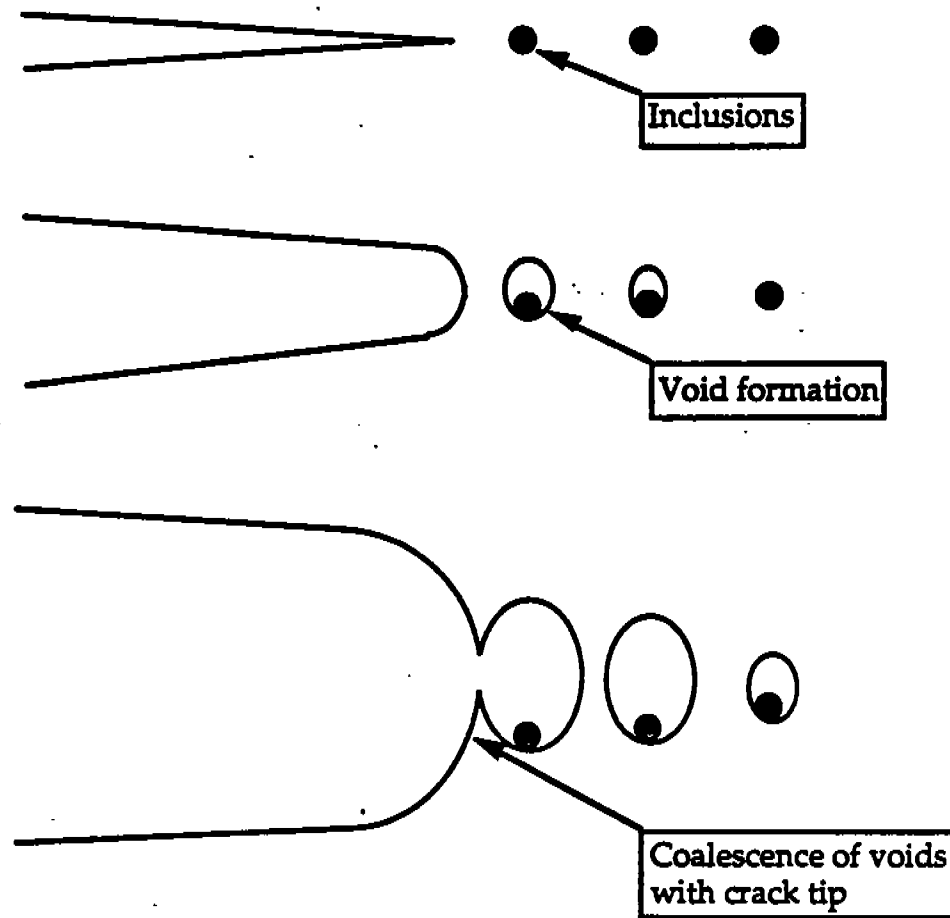


FIG. 2.26 Crack growth by microvoid coalescence.

The Rice and Tracey model, as well as the more recent versions, indicate that microvoid coalescence is essentially strain controlled fracture, but that the hydrostatic stresses play an important role.

2.4.3 The Ductile-Brittle Transition

The fracture toughness of ferritic steels can change drastically over a small temperature range, as illustrated in Fig 2.27. At low temperatures, the steel is brittle and fails by cleavage. At high temperatures, the material is ductile and fails by microvoid coalescence. Ductile fracture initiates at a particular toughness value, as indicated by the dashed line in Fig. 2.27. The crack grows as load is increased. Eventually, the specimen fails by plastic collapse or tearing instability. In the transition region between ductile and brittle behavior, both micromechanisms of fracture can occur in the same specimen. In the lower transition region, the fracture mechanism is pure cleavage, but the toughness increases rapidly with temperature because cleavage is becoming more difficult. In the upper transition region, a crack initiates by microvoid coalescence but ultimate failure occurs by cleavage. On initial

loading in the upper transition region, cleavage does not occur because there are no critical particles near the crack tip. As the crack grows by ductile tearing, however, more material is sampled. Eventually, the growing crack samples a critical particle and cleavage occurs. Because fracture toughness in the transition region is governed by these statistical sampling effects, the data tend to be highly scattered.

Recent work by Heerens and Read (48) demonstrates of the weakest-link sampling nature of cleavage fracture. They performed a large number of fracture toughness tests on a quenched and tempered alloy steel at several temperatures in the transition region. As expected, the data at a given temperature were highly scattered. Some specimens failed without significant stable crack growth while other specimens sustained high levels of ductile tearing prior to cleavage. Heerens and Read examined the fracture surface of each specimen to determine the site of cleavage initiation. The measured distance from the initiation site to the original crack tip correlated very well with the measured fracture toughness. In specimens that exhibited low toughness, this distance was small; a critical nucleus was available near the crack tip. In the specimens that exhibited high toughness, there were no critical particles near the crack tip. The crack had to grow and sample additional material before a critical cleavage nucleus was found. Figure 2.28 is a plot of fracture fracture toughness versus the critical distance, r_c , which Heerens and Read measured. In every case, cleavage initiated near the location of the maximum tensile stress. A similar fractographic study by Wantanabe et al. (49) also revealed a correlation between J_c and r_c .

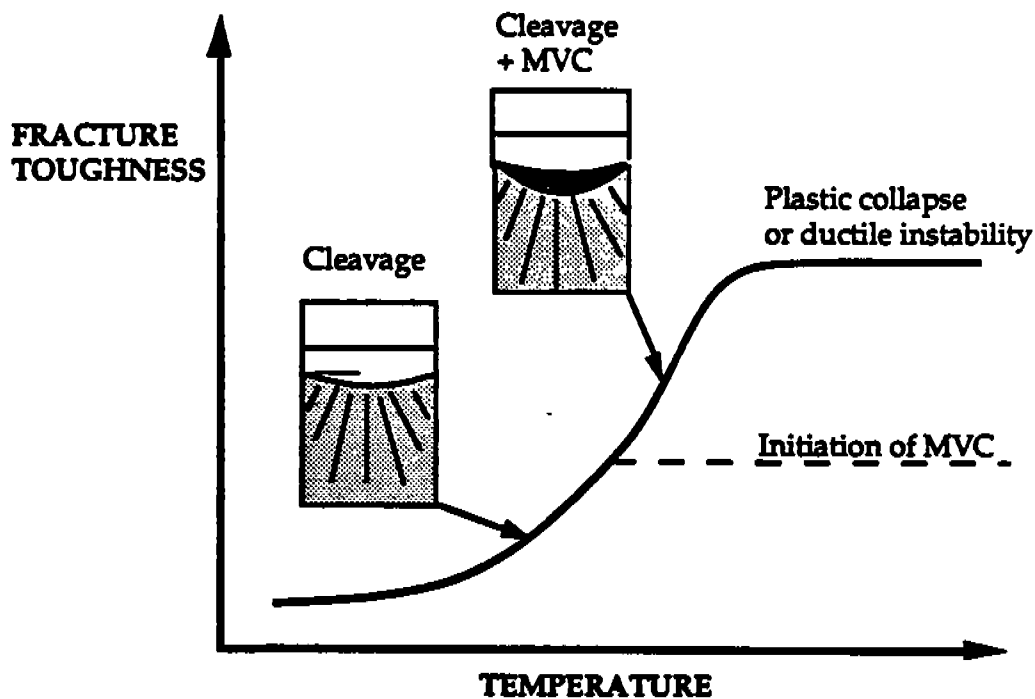


FIG. 2.27 The ductile-brittle transition of ferritic steels.

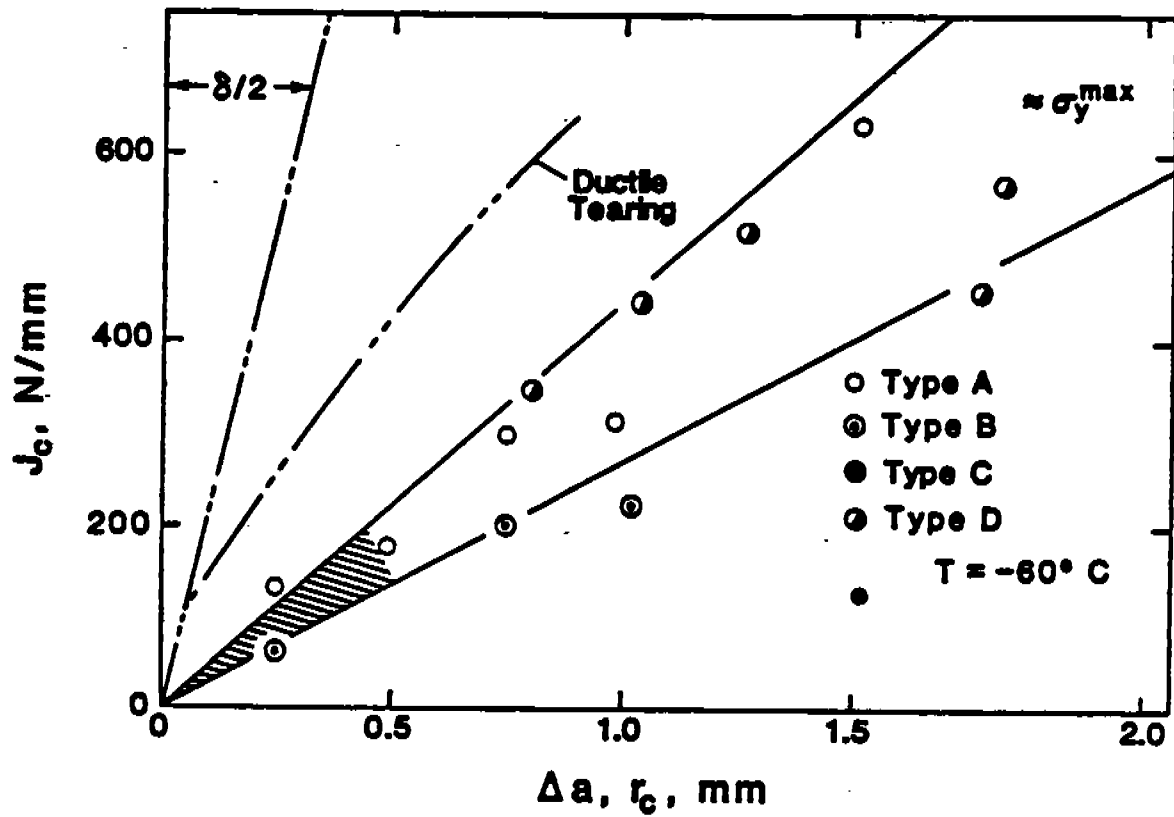


FIG 2.28 Correlation between fracture toughness and the distance from the crack tip to the site of cleavage initiation (48).

3. FRACTURE TOUGHNESS TESTING

A fracture toughness test measures the resistance of a material to crack extension. Such a test may yield either a single value of fracture toughness or a resistance curve, where a toughness parameter such as K_{IC} , J , or CTOD is plotted against crack extension. A single toughness value is usually sufficient to describe a test that fails by cleavage, because this fracture mechanism is typically unstable. The situation is similar to the schematic in Fig 2.2(a), which illustrates a material with a flat R curve. For reasons discussed in Section 3.6, cleavage actually has a falling R curve after initiation. Crack growth by microvoid coalescence, however, usually yields a rising R curve, such as that shown in Fig. 2.2(b). Thus ductile crack growth can be stable, at least initially. When ductile crack growth initiates in a test specimen, that specimen seldom fails immediately. Therefore one can quantify upper shelf fracture toughness either by the initiation value or by the entire resistance curve.

There are several ASTM standards for fracture toughness testing. The K_{IC} standard, ASTM E399-83 (25), is intended for relatively brittle materials or thick sections. The J_{IC} standard, ASTM E813-87 (26), measures a J value near initiation of ductile tearing. Another standard, E1152-87 (50), gives guidelines for measuring a J resistance curve. A CTOD testing standard has been published recently: ASTM E1290-89 (51).

Most standard fracture toughness tests are conducted on one of two specimen types: the compact specimen and the single edge notched bend (SENB) specimen. The K_{IC} standard permits two additional specimen configurations but the other standards mentioned allow only the compact and SENB geometries. Figures 3.1 and 3.2 illustrate the SENB and compact specimens, respectively. The compact specimen is pin loaded; the SENB specimen is loaded in three point bending at a span of $4W$. Both specimen types contain sharp machined notches from which fatigue cracks are grown.

Fracture properties of a material typically depend on orientation. For example, a typical steel plate appears to be much tougher if the crack propagates through the thickness rather than along the rolling direction, parallel to the plate surface. Thus it is important to specify the orientation of the fracture specimen. Fig. 3.3 illustrates the standard nomenclature for specimens extracted from rolled plate.

The field of fracture toughness testing is relatively mature, as evidenced by the numerous standard test methods that have gained world-wide acceptance, but these standards fail to address a number of important issues. For example, none of these standards gives guidelines on weldment testing. In addition, the ductile-brittle transition region presents unique problems for which current standards are inadequate.

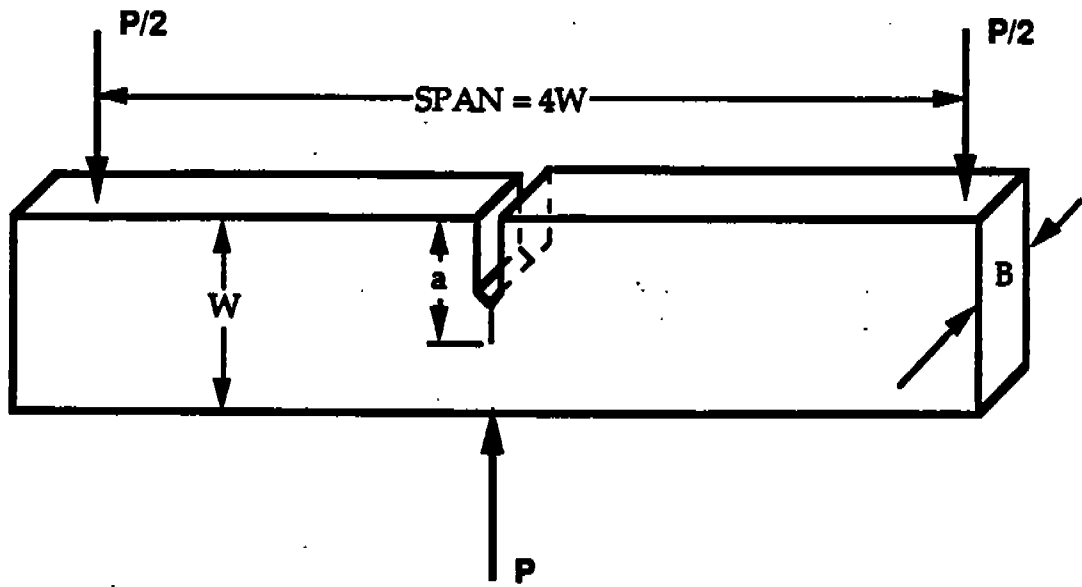


FIG. 3.1 Single edge notched bend (SENB) specimen.

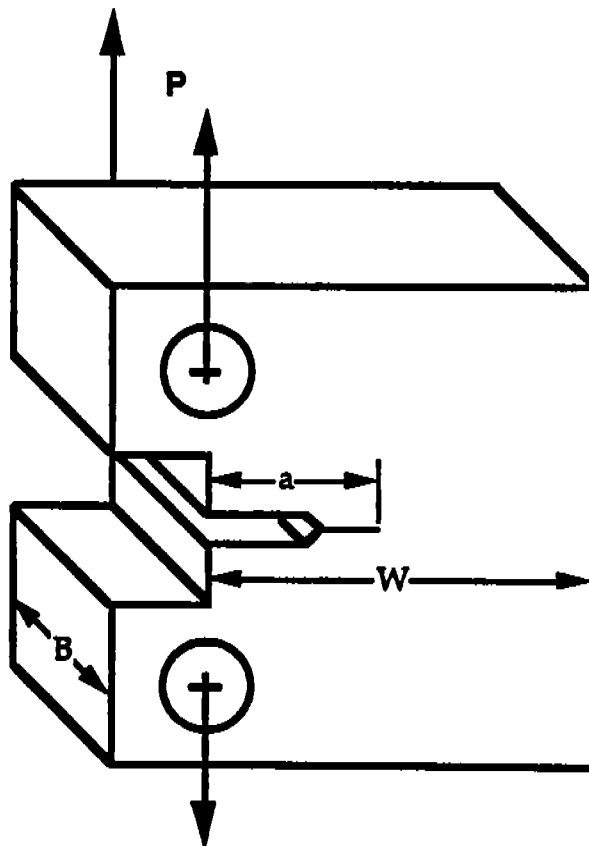


FIG 3.2 Compact specimen.

The following sections summarize the standardized test methods and describe recent progress and current research in such areas as weldment testing, scatter, size effects, loading rate effects, and the relationship between fracture tests.

3.1 K_{IC} TESTING

The ASTM Standard E399 was first published in 1970; the most recent revision was made in 1983. The title, "*Standard Test Method for Plane Strain Fracture Toughness of Metallic Materials*," is somewhat misleading. Although plane strain is a necessary condition for a valid K_{IC} test, it is not sufficient; a specimen must also behave in a linear elastic manner. The validity requirements in this standard are very stringent because even a relatively small amount of plastic deformation invalidates the assumptions of K theory.

Specimens for K_{IC} tests are usually fabricated with the width, W , equal to twice the thickness, B . They are fatigue precracked so that the crack length/width ratio (a/W) lies between 0.45 and 0.55. Thus the specimen design is such that all the critical dimensions, a , B , and $b (= W-a)$, are approximately equal. This design results in efficient use of material, since each of these dimensions must be large compared to the plastic zone.

When a test specimen is loaded to failure, load and displacement are monitored. Three types of load-displacement curves are shown in Fig. 3.4. The critical load, P_Q , is defined in one of several ways, depending on the type of curve. One must construct a 5% secant line (i.e. a line from the origin with a slope equal to 95% of the initial elastic loading slope) to determine P_5 . In the case of Type I behavior, the load-displacement curve is smooth and it deviates slightly from linearity before ultimate failure at P_{max} . This nonlinearity can be caused by plasticity, subcritical crack growth, or both. For a Type I curve, $P_Q = P_5$. With a Type II curve, a small amount of unstable crack growth (i.e. a pop-in) occurs before the curve deviates from linearity by 5%. In this case P_Q is defined at the pop-in. A specimen that exhibits Type III behavior fails completely before achieving 5% nonlinearity. In such cases, $P_Q = P_{max}$.

Once P_Q is determined, a provisional fracture toughness, K_Q , is computed from the following relationship:

$$K_Q = \frac{P_Q}{B\sqrt{W}} f(a/W) \quad [3.1]$$

where $f(a/W)$ is a dimensionless function of a/W . This function is given in polynomial form in the E399 standard for both the compact and SENB specimens. Individual values of $f(a/W)$ are also tabulated in the standard.

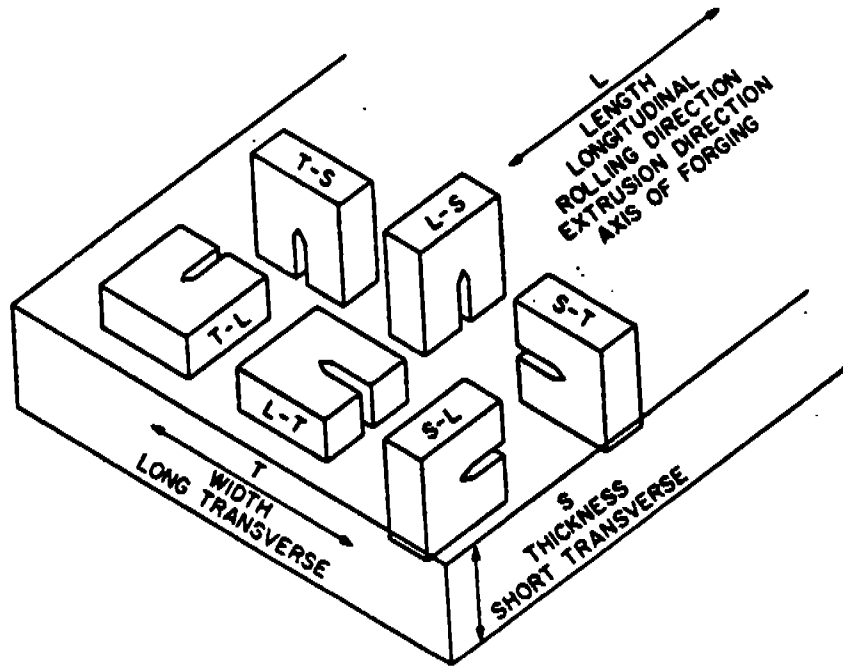


FIG. 3.3 Definition of specimen orientations in a rolled plate (25).

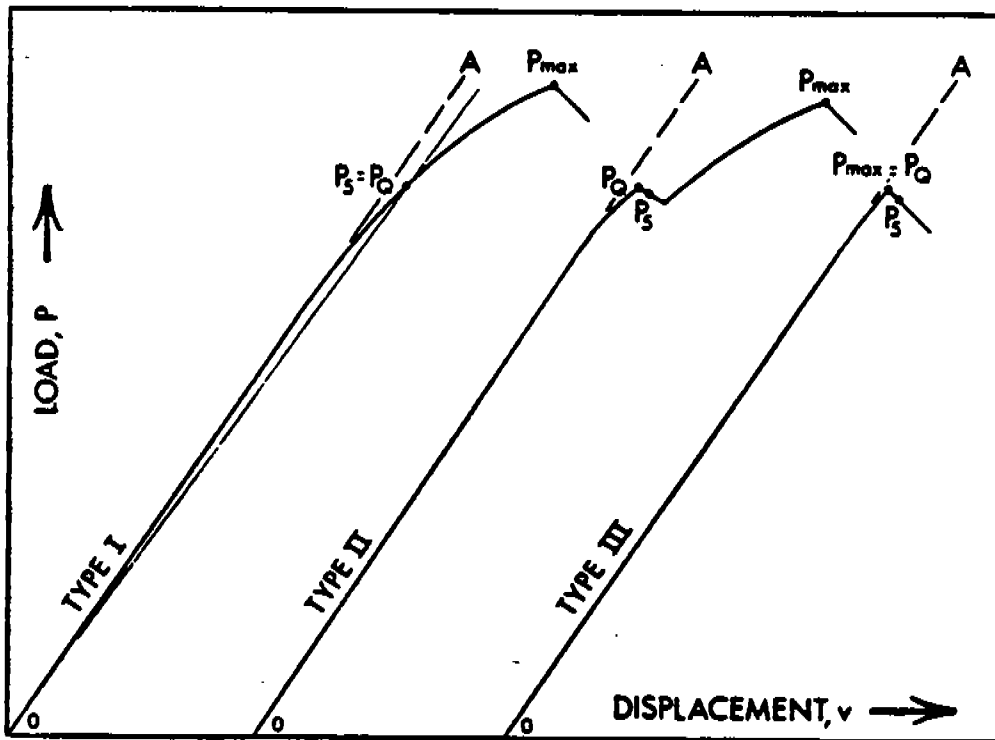


FIG. 3.4 Typical load-displacement curves in a K_{Ic} test (25).

Recall from Section 2.2 that expressions for K can always be reduced to the form of Eq. [2.6]. Equation [3.1] is no exception. If we define a characteristic stress as $P/(BW)$, the geometry correction factor for the compact and SENB specimens is given by

$$Y = f(a/W) \left(\frac{W}{\pi a} \right)^{1/2} \quad [3.2]$$

The characteristic stress, $P/(BW)$, has no physical meaning for these test specimens since they are loaded predominantly in bending. Thus Eq. [3.1] is a more convenient form in this case than Eq. [2.1].

The K_Q value computed from Eq. [3.1] is a valid K_{IC} result only if all validity requirements in the standard are met. The main validity requirements are as follows.

$$0.45 \leq a/W \leq 0.55 \quad [3.3a]$$

$$P_{\max} \leq 1.10 P_Q \quad [3.3b]$$

$$B, W-a \geq 2.5 \left(\frac{K_Q}{\sigma_{YS}} \right)^2 \quad [3.3c]$$

The last requirement is a restatement of Eq. [2.29]. If the test meets all of the above criteria as well as additional requirements of ASTM E399, then $K_Q = K_{IC}$.

Most structural steels cannot meet the validity requirements of E399 except at very low temperatures, as demonstrated by a few sample calculations. Consider a medium strength steel with $\sigma_{YS} = 50$ ksi. On the upper shelf, the fracture toughness corresponding to initiation of ductile crack growth is typically around $200 \text{ ksi} \sqrt{\text{in}}$ for such materials (23). Substituting these values for strength and toughness into Eq. [3.3c], reveals that a fracture toughness specimen must be 40 in thick to obtain a valid K_{IC} ! If the 50 ksi material is produced as 1 in thick plate, the maximum valid K_{IC} that can be measured is $32 \text{ ksi} \sqrt{\text{in}}$. If a structure made from a material with this toughness were loaded to half the yield strength (25 ksi), the critical crack size (estimated from Eq. [2.5]) would be approximately 0.5 in. If this were a welded structure with yield magnitude residual stresses, the critical crack size would only be 0.06 in.

Thus it is virtually impossible to perform a valid K_{IC} test on most structural steels at ambient temperatures. Such a material could meet the validity requirements with a reasonable section thickness only by poor fabrication practice or by cooling the material so that it is on the lower shelf of toughness. In either case, the material would probably be too brittle for structural application. When linear elastic test

methods are invalid, fracture toughness must be quantified by an elastic-plastic parameter such as J or CTOD.

3.2 J_{IC} AND J-R CURVE TESTING

There are two ASTM standards currently for J testing. The J_{IC} standard, E813(26), which was first published in 1981 and revised in 1987, outlines a test method for estimating the critical J near initiation of ductile crack growth. The J-R curve testing standard, E1152(50), was first published in 1987.

Both test methods produce a J-R curve, a plot of J versus crack extension. The E1152 standard applies to the entire J-R curve; E813 is concerned only with J_{IC} , a single point on the R curve. The same test can be reported in terms of both standards. This is analogous to a tensile test, where one can report either the yield strength or the entire stress-strain curve.

In the case of the J_{IC} standard, the R curve can be generated by either multiple specimen or single specimen techniques. With the multiple specimen technique, a series of nominally identical specimens are loaded to various levels and then unloaded. Some stable crack growth occurs in most specimens. This crack growth is marked by heat tinting or fatigue cracking after the test. Each specimen is then broken open and the crack extension is measured. The most common single specimen test technique is the unloading compliance method. The crack length is computed at regular intervals during the test by partially unloading the specimen and measuring the compliance. As the crack grows, the specimen becomes more compliant (less stiff). Both E813 and E1152 provide polynomial expressions that relate a/W to compliance. An alternative single specimen test method is the potential drop procedure, yet to be standardized by ASTM, in which crack growth is monitored through the change in electrical resistance which accompanies a loss in cross sectional area. Both single specimen procedures are practical only in conjunction with a computer data acquisition and analysis system.

Regardless of the method for monitoring crack growth, a corresponding J value must be computed for each point on the R curve. For estimation purposes, both standards divide J into elastic and plastic components:

$$J = J_{el} + J_{pl} \quad [3.4]$$

The elastic J is computed from the elastic stress intensity:

$$J_{el} = \frac{K^2(1-\nu)}{E} \quad [3.5]$$

where K is computed from load with Eq. [3.1]. The J_{IC} standard enables the plastic J at each point on the R curve to be estimated from the plastic area under the load-displacement curve:

$$J_{pl} = \frac{\eta A_{pl}}{B b_0} \quad [3.6]$$

where η is a dimensionless constant, A_{pl} is the plastic area under the load-displacement curve (see Fig. 3.5), and b_0 is the initial ligament length. For an SENB specimen,

$$\eta \approx 2.0 \quad [3.7a]$$

For a compact specimen,

$$\eta = 2 + 0.522 b_0/W \quad [3.7b]$$

Equation [3.6] was derived from the energy release rate definition of J (Eq. [2.21]).

The J-R curve testing standard requires a somewhat more detailed calculation of J_{pl} , performed incrementally since the crack length increases and the net cross-sectional area decreases throughout the test. Since E813-87 is concerned with the initiation point rather than the shape of the R curve, the more detailed formula that corrects J for crack growth is optional in J_{IC} tests. In the limit of a stationary crack, both formulas give identical results. Thus the measured initiation toughness is insensitive to the choice of J equation.

The E813-87 procedure for computing J_Q , a provisional J_{IC} , from the R curve is illustrated in Fig. 3.6. Exclusion lines are drawn at crack extension (Δa) values of 0.15 and 1.5 mm. These lines have a slope of $2\sigma_y$, which corresponds approximately to the component of crack extension that is due to crack blunting, as opposed to ductile tearing. A horizontal exclusion line is defined at a maximum value of J :

$$J_{max} = \frac{b_0 \sigma_y}{15} \quad [3.8]$$

All data that fall within the exclusion limits are fit to a power law expression:

$$J = C_1(\Delta a)^{C_2} \quad [3.9]$$

The J_Q is defined as the intersection between Eq. [3.9] and a 0.2 mm offset line. If all other validity criteria are met, $J_Q = J_{IC}$ as long the following size requirements are satisfied:

$$B, b_0 \geq \frac{25 J_Q}{\sigma_y} \quad [3.10]$$

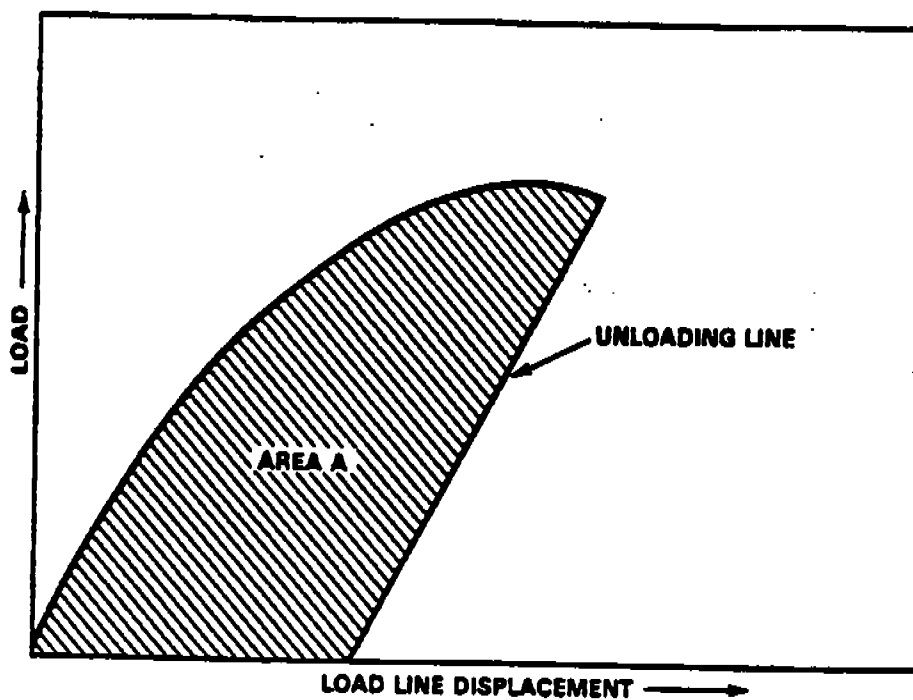


FIG. 3.5 Definition of the plastic area for J_p calculations (26).

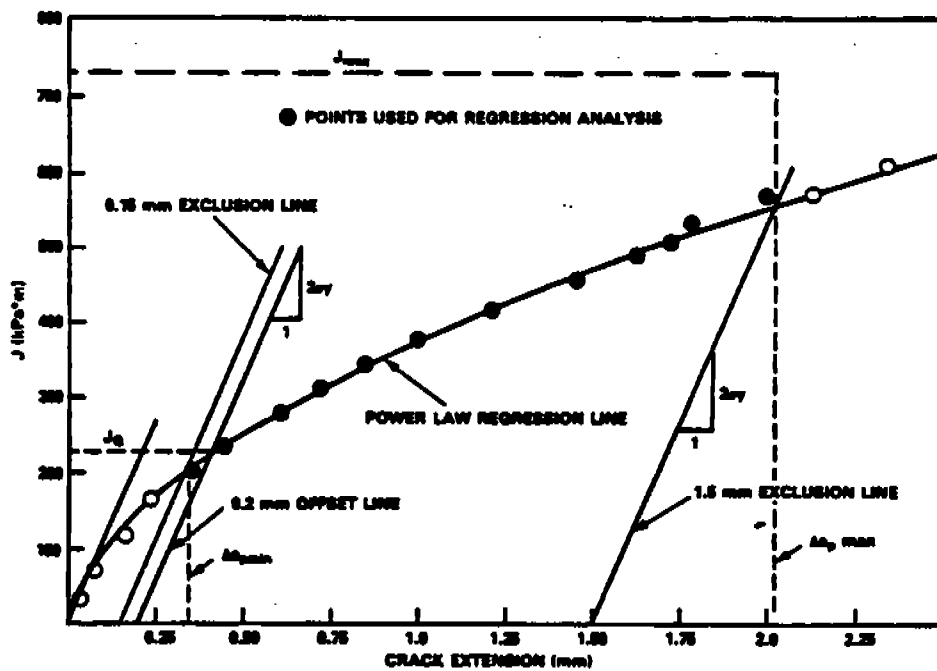


FIG. 3.6 Typical J-R curve which illustrates the calculation of J_0 (26).

The J-R curve standard has limits on J_{\max} and crack extension relative to specimen size:

$$B, b_0 \geq \frac{20 J_{\max}}{\sigma_y} \quad [3.11]$$

and

$$\Delta a_{\max} \leq 0.10 b_0 \quad [3.12]$$

Figure 3.6 (50) shows a typical J-R curve with the E1152-87 validity limits. The portion of the J-R curve that falls outside these limits is considered invalid. Note that the limit on J_{\max} in ASTM E1152-87 is more severe than the J_{\max} limit of ASTM E813-87 (Eq. 3.8)], but this limit is less restrictive than the J_{IC} size criterion (Eq. [3.10]).

3.3 CTOD TESTING

Because of the strict limits on plastic deformation, the K_{IC} test can only be used on the lower shelf of toughness in structural steels and welds. The J_{IC} and J-R curve test methods allow considerably more plastic deformation, but these tests are only valid on the upper shelf. The CTOD test is currently the only standardized method to measure fracture toughness in the ductile-brittle transition region.

The first CTOD test standard was published in Great Britain in 1979(52). ASTM recently published E1290-89, an American version of the CTOD standard. The British CTOD standard allows only the SENB specimen; the ASTM standard provides for CTOD measurements on both the compact and SENB specimens. Both standards allow two configurations of SENB specimens: 1) a rectangular cross section with $W = 2B$, the standard geometry for K_{IC} and J_{IC} tests; and 2) a square cross section with $W = B$. The rectangular specimen is most useful with L-T or T-L orientations (see Fig. 3.3); the square section is generally used in the L-S or T-S orientations.

Experimental CTOD estimates are made by separating the CTOD into elastic and plastic components, similar to the J_{IC} and J-R tests. The elastic CTOD is obtained from the elastic K :

$$\delta_{el} = \frac{K^2(1-\nu^2)}{2\sigma_{ys} E} \quad [3.13]$$

The elastic K is related to applied load through Eq. [2.1]. The above relationship assumes that $d_n = 0.5$ for linear elastic conditions (see Eq. [2.26]). The plastic component of CTOD is obtained by assuming that the test specimen rotates about a plastic hinge. This concept is illustrated in Fig. 3.7 for an SENB specimen. The

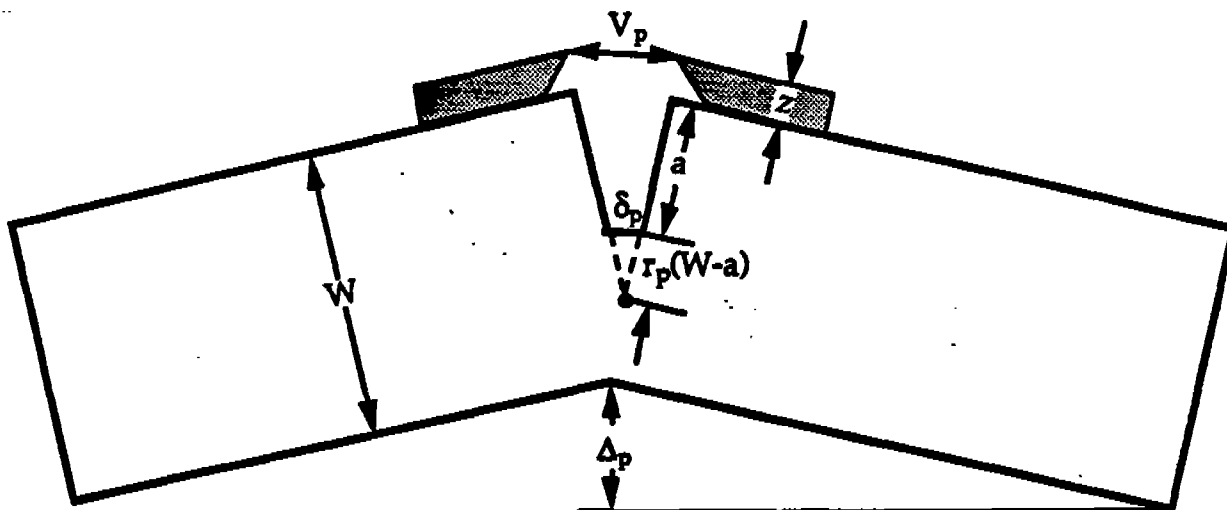


FIG. 3.7 Rotation of an SENB specimen about a plastic hinge.

plastic displacement at the crack mouth, V_p , is related to the plastic CTOD through a similar triangle construction:

$$\delta_{pl} = \frac{r_p (W-a) V_p}{r_p (W-a) + a + z} \quad [3.14]$$

where r_p is the rotational factor, a constant between 0 and 1 that defines the relative position of the apparent hinge point. The mouth opening displacement is measured with a clip gage. In the case of an SENB specimen, knife edges must often be attached in order to hold the clip gage. Thus Eq. [3.14] must correct for the knife edge height, z . The compact specimen can be designed so that $z = 0$. The plastic component of V is obtained from the load-displacement curve by constructing a line parallel to the elastic loading line, as illustrated in Fig. 3.8. The plastic rotational factor is given by

$$r_p = 0.44 \quad [3.15a]$$

for the SENB specimen and

$$r_p = 0.4 \left\{ 1 + 2 \left[\left(\frac{a}{b_0} \right)^2 + \frac{a}{b_0} + 0.5 \right]^{1/2} - 2 \left[\frac{a}{b_0} + 0.5 \right] \right\} \quad [3.15b]$$

for the compact specimen.

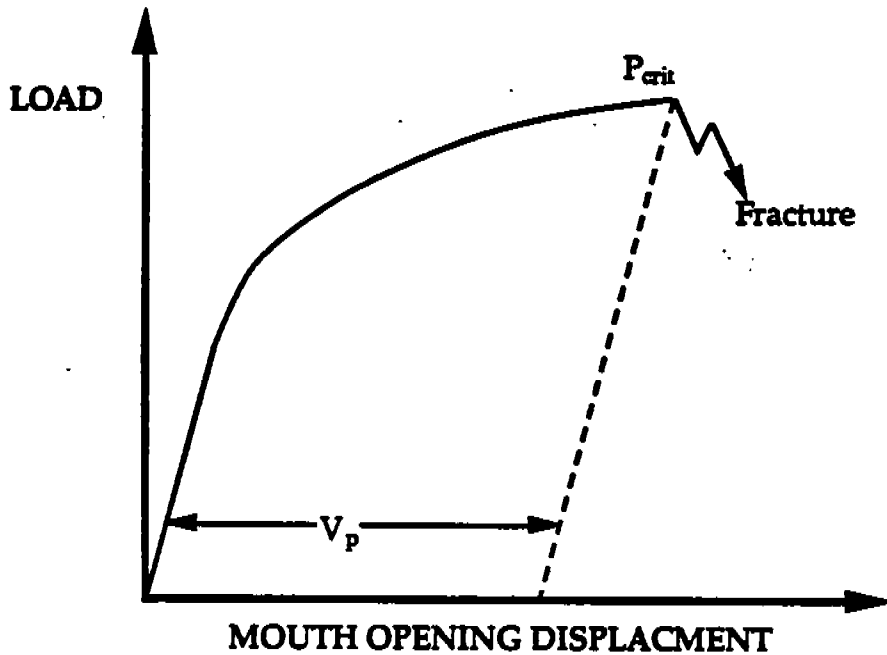


FIG. 3.8 Estimation of V_p from the load-displacement curve.

Figure 3.7 indicates that the crack mouth opening displacement, V , on an SENB specimen is not the same as the load line displacement, Δ . The latter displacement measurement is required for J estimation because A_{pl} in Fig. 3.5 and Eq. [3.6] represents the plastic energy absorbed by the specimen. The CTOD standard utilizes V_p because this displacement is easier to measure in SENB specimens. However, if r_p is known, it is possible to infer J from a P - V curve or CTOD from a P - Δ curve (53,54). The compact specimen simplifies matters somewhat because $V = \Delta$ as long as $z = 0$.

The CTOD standard test method can be applied to ductile and brittle materials, as well as steels in the ductile-brittle transition. This standard includes a notation for critical CTOD values that describes the fracture behavior of the specimen:

- δ_c - Critical CTOD at the onset of unstable fracture without prior stable crack growth. This corresponds to the lower shelf and lower transition region of steels where the fracture mechanism is pure cleavage.
- δ_u - Critical CTOD at the onset of unstable fracture which has been preceded by stable crack growth. In the case of ferritic steels, this corresponds to the "ductile thumbnail" observed in the upper transition region (see Fig. 2.27).

δ_i - CTOD at the initiation of stable crack growth. This measure of toughness is analogous to J_{IC} .

δ_m - CTOD at the maximum load plateau. This occurs on or near the upper shelf of steels.

Figure 3.9 is a series of schematic load-displacement curves that manifest each of the above failure scenarios. Curve (a) illustrates a test that results in a δ_c value; cleavage fracture occurs at P_c . Figure 3.9 (b) corresponds to a δ_u result, where ductile tearing precedes cleavage. The ductile crack growth initiates at P_i . A test on the upper shelf produces a load-displacement curve like Fig. 3.9(c). A maximum load plateau occurs at P_m . The specimen is still stable after maximum load because the material has a rising R curve and the test is performed in displacement control. (See Section 4.6 for further discussion on stable and unstable crack growth.) Three types of CTOD result, δ_c , δ_u and δ_m , are mutually exclusive; i.e, they cannot occur in the same test. It is possible, however, to measure a δ_i value in the same test as either a δ_m or δ_u result.

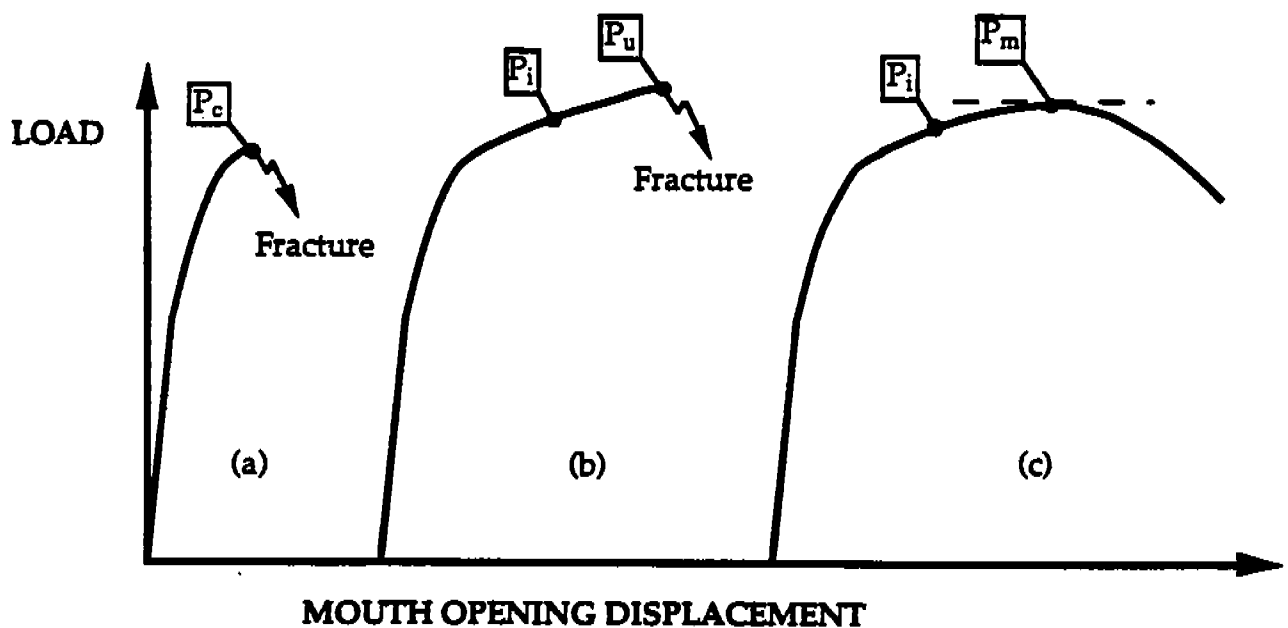


FIG. 3.9 Typical load-displacement curves that illustrate possible behavior in a CTOD test.
 a) δ_c result; b) δ_u result; c) δ_m result.

As illustrated in Fig. 3.9, there is usually no detectable change in the load-displacement curve at P_i . The only deviation in the load-displacement behavior is the reduced rate of increase in load as the crack grows. The maximum load plateau (Fig. 3.9c) occurs when the rate of strain hardening is exactly balanced by the rate of decrease in the cross section. However, the initiation of crack growth can not be detected from the load-displacement curve because the loss of cross section is gradual. Thus δ_i must be determined from an R curve.

As with the J_{IC} standard, the δ -R curve can be generated by either single or multiple specimen procedures, but the way in which the initiation point is defined differs from ASTM E813. Figure 3.10 illustrates the E1290-89 procedure for δ_i determination from a δ -R curve. CTOD values are plotted against the physical crack extension, Δa_p . Vertical exclusion lines are drawn at 0.15 and 1.5 mm of crack extension. The data are then fit to an offset power law expression:

$$\delta = C_1 (C_2 + \Delta a_p)^{C_3} \quad [3.16]$$

The initiation toughness, δ_i , is then defined at the CTOD value corresponding to $\Delta a_p = 0.2$ mm.

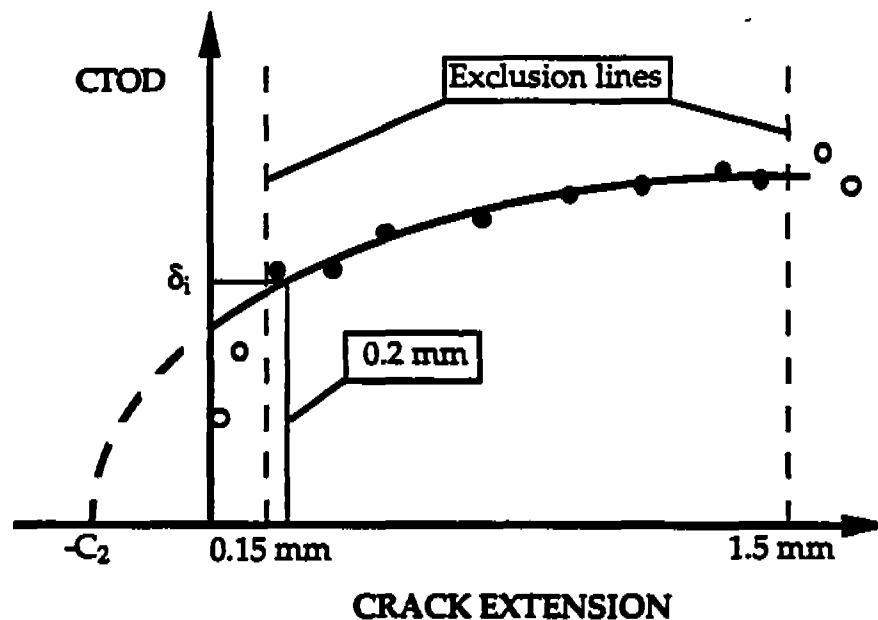


FIG. 3.10 CTOD R curve for the determination of δ_i according to ASTM E1290-89 (51).

The only specimen size requirement of the British and ASTM CTOD standards is a recommendation to test full section thicknesses. For example, if a structure is to be made of 1 in thick plate, then B in the test specimens should be nominally 1 in. If the specimen is notched from the surface (L-S or T-S orientations), a square section specimen is required for B to equal the plate thickness. The British CTOD standard allows a/W ratios ranging from 0.15 to 0.75, while the ASTM standard restricts the permissible a/W values to the range of 0.45 to 0.55. In an earlier draft, the ASTM standard allowed a much wider range of a/W in the square section specimen, but concerns about the possible variation of r_p with a/W led the members of the ASTM CTOD task group to restrict the allowable range until the uncertainties in r_p could be resolved. Future revisions of this standard will probably relax the a/W restriction. Shallow cracked specimens have certain advantages, particularly for weldment tests (see Section 3.4).

The ASTM CTOD standard recognizes that since it does not contain size requirements relative to the degree of plasticity, the measured critical CTOD value may be geometry dependent. The standard correctly assumes that if a test specimen's thickness matches that of the structure being evaluated, the crack tip conditions in the specimen will be at least as severe as in the structure. Experimental data and numerical analysis indicate that a small scale bend specimen is more highly constrained than a large panel loaded in tension.

3.4 WELDMENT TESTING

All the standards discussed are suitable for specimens extracted from uniform sections of homogeneous material, but welded joints have decidedly heterogeneous microstructures and, in many cases, irregular shapes. Weldments also contain complex residual stress distributions. Existing fracture toughness testing standards do not address the special problems associated with weldment testing. The factors that make weldment testing difficult (i.e. heterogeneous microstructures, irregular shapes, and residual stresses) also tend to increase the risk of brittle fracture in welded structures. Thus, one cannot simply evaluate the regions of a structure where ASTM testing standards apply and ignore the fracture properties of weldments.

Although there are currently no fracture toughness testing standards for weldments, a number of laboratories and industries have significant experience in this area. The Welding Institute in Cambridge, England which probably has the most expertise, has recently published detailed recommendations for weldment testing (55). The International Institute of Welding (IIW) has produced a similar document (56), although not as detailed. The American Petroleum Institute (API) has published guidelines for heat affected zone (HAZ) testing as part of a weld procedure qualification approach (57). Committees within ASTM and the British Standards Institute (BSI) are currently drafting weldment test methods, relying heavily on 20 years of practical experience as well as the aforementioned documents.

Some of the general considerations and current recommendations for weldment testing are outlined below, with emphasis on the Welding Institute procedure (55) because it is the most complete document to date. Early drafts of both the ASTM and BSI documents are similar to The Welding Institute approach.

When performing fracture toughness tests on weldments, a number of factors need special consideration. Specimen design and fabrication is more difficult because of the irregular shapes and curved surfaces associated with some welded joints. The heterogeneous microstructure of typical weldments requires special attention to the location of the notch in the test specimen. Residual stresses make fatigue precracking of weldment specimens more difficult. After the test, a weldment must often be sectioned and examined metallographically to determine whether or not the fatigue crack sampled the intended microstructure.

3.4.1 Specimen Design and Fabrication

The underlying philosophy of the Welding Institute (55) guidelines on specimen design and fabrication is that the specimen thickness should be as close to the section thickness as possible. Thicker specimens tend to produce more crack tip constraint, and hence lower toughness (See Chapter 2). Achieving nearly full thickness weldment specimens often requires sacrifices in other areas. For example if a specimen is to be extracted from a curved section such as a pipe, one can either produce a subsize rectangular specimen which meets the tolerances of the existing ASTM standards, or a full thickness specimen that is curved. The Welding Institute recommends the latter.

Figure 3.11 illustrates the recommended tolerances for misalignment, curvature and angular distortion in SENB specimens (55). Distortion and curvature in the long axis of the specimen is limited to 10% of W (Fig. 3.11a,b,c); curvature in the width direction (Fig. 3.11d) is limited to 2.5% W . Note that the top and bottom surfaces in the SENB specimen must still be flat and parallel at the loading points. If a weldment specimen has more than 10% W curvature or distortion in the long axis, the specimen can be straightened by bending on either side of the notch to produce a "gull wing" configuration, which is illustrated in Fig. 3.12. The bending must be performed so that the three loading points are aligned.

Fabrication of either a compact or SENB weldment specimen is possible, but the SENB specimen is preferable in nearly every case. Although the compact specimen consumes less material (for a given B and W) in parent metal tests, it requires more weld metal in a through-thickness orientation (L-T or T-L) than an SENB specimen. It is impractical to use a compact geometry for surface notched specimens (T-S or L-S). Such a specimen would be greatly undersized with the standard $B \times 2B$ geometry.

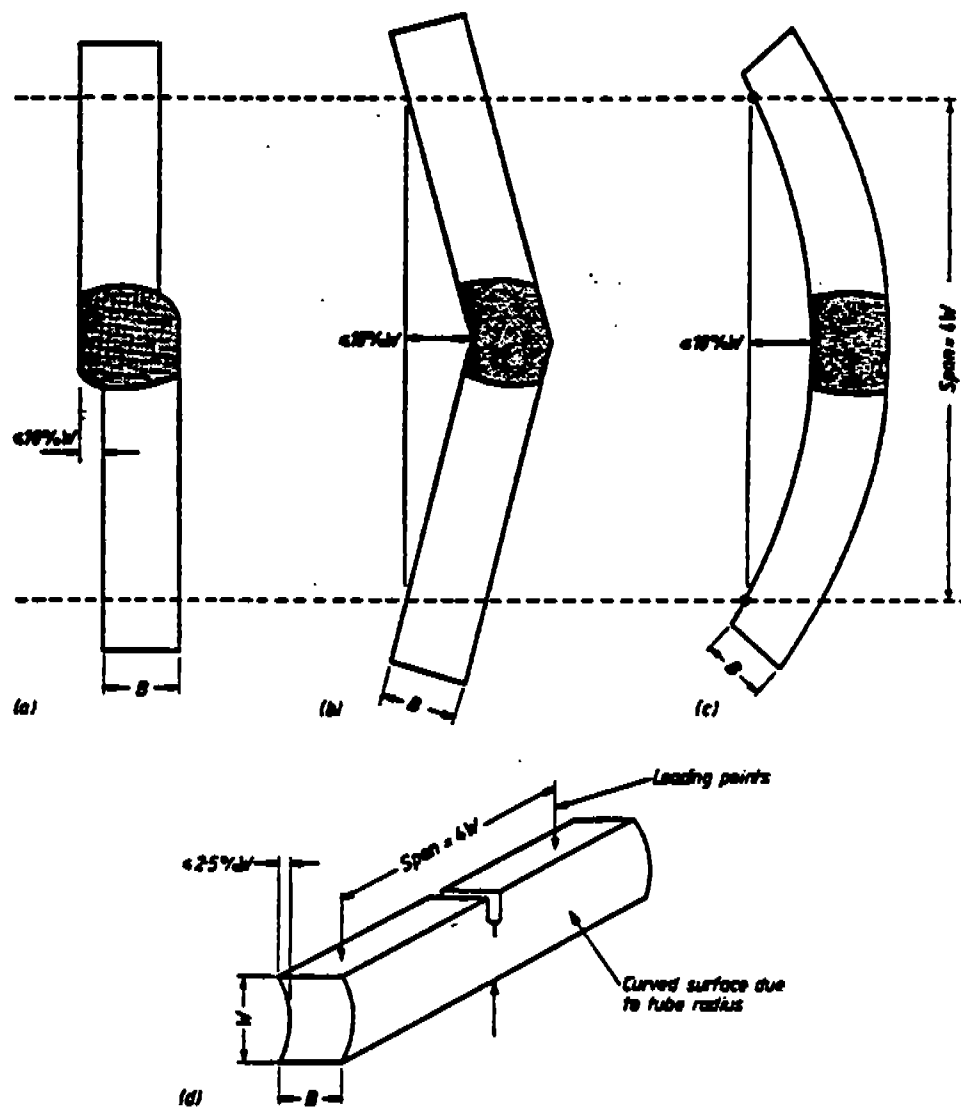


FIG. 3.11 Recommended allowances for misalignment, angular distortion and curvature (55).

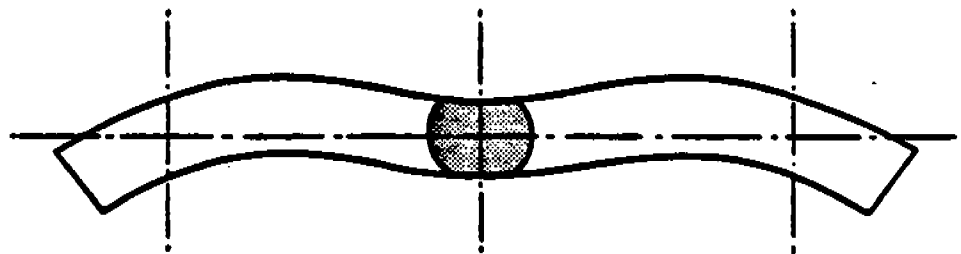


FIG. 3.12 "Gull wing" configuration which corrects for excessive curvature and angular distortion (55).

The Welding Institute recommendations cover both the rectangular and square section SENB specimens. The appropriate choice of specimen type depends on the orientation of the notch.

3.4.2 Notch Location and Orientation

Weldments have a highly heterogeneous microstructure. Fracture toughness can vary considerably over relatively short distances. Thus it is important to take great care in locating the fatigue crack in the correct region. If the fracture toughness test is designed to simulate an actual structural flaw, then the fatigue crack must sample the same microstructure as the structural flaw. For a weld procedure qualification or a general assessment of a weldment's fracture toughness, location of the crack in the most brittle region may be desirable, but it is difficult to know in advance which region of the weld has the lowest toughness. In typical C-Mn structural steels, low toughness is usually associated with the coarse grained HAZ and the intercritically reheated HAZ. A microhardness survey can help identify low toughness regions because high hardness is often coincident with brittle behavior. The safest approach is to perform fracture toughness tests on a variety of regions in a weldment.

Once the microstructure of interest is identified, a notch orientation must be selected. The Welding Institute gives two alternatives: a through-thickness notch and a surface notch, as illustrated in Fig. 3.13. Since full thickness specimens are desired, the surface notched specimen should be square section (BxB), while the through thickness notch will usually be in a rectangular (B X 2B) specimen.

For weld metal testing, the through-thickness orientation is usually preferable because a variety of regions in the weld are sampled. Since brittle fracture is a weakest link phenomenon (Section 2.4), the fracture behavior of the test specimen is controlled by the region with lowest toughness. However, there may be cases where the surface notched specimen is the most suitable for testing the weld metal. For example, a surface notch can sample a particular region of the weld metal, such as the root or cap, or the notch can be located in a particular microstructure, such as unrefined weld metal.

Notch location in the HAZ often depends on the type of weldment. If welds are produced solely for mechanical testing, for example as part of a weld procedure qualification or a research program, the welded joint can be designed to facilitate HAZ testing. The Welding Institute (55) recommends a K or a half-K preparation to simulate double-V and single-V welds, respectively. These geometries are illustrated in Fig. 3.14. The plates should be tilted when these weldments are made, to have the same angle of attack for the electrode as in an actual single- or double-V joint. For fracture toughness testing, a through-thickness notch is placed in the straight side of the K or half-K HAZ.

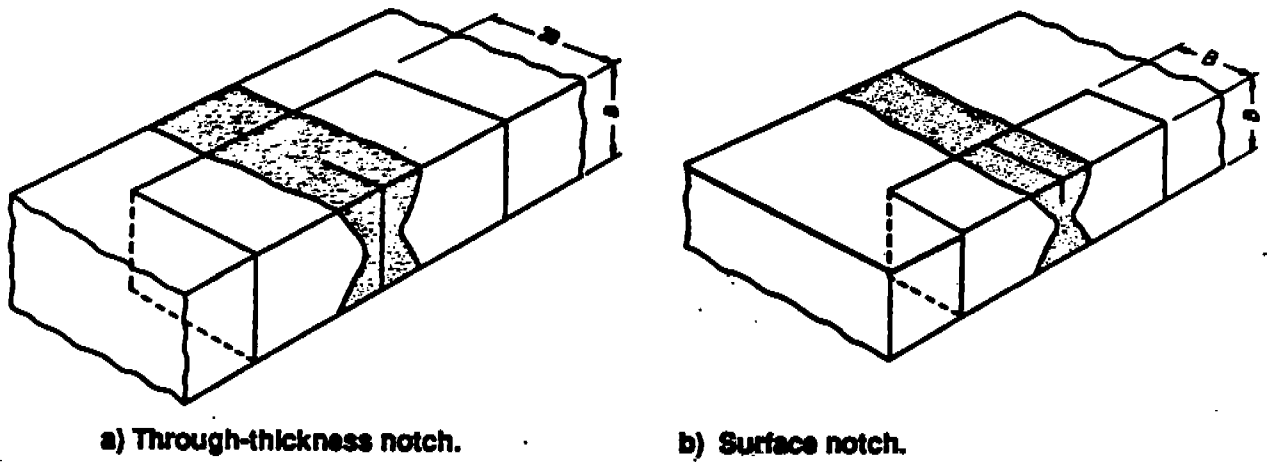


FIG. 3.13 Notch orientation for weldment specimens (55).

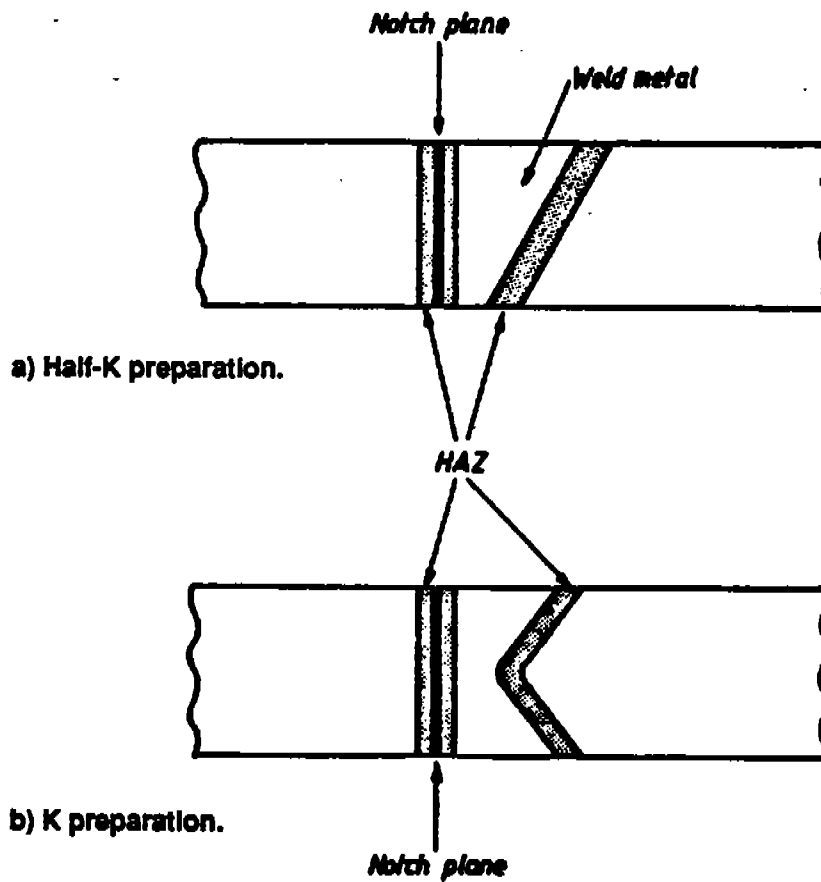


FIG. 3.14 Special welded joints for HAZ fracture toughness testing (55).

In many instances, fracture toughness testing must be performed on an actual production weldment, where the joint geometry is governed by the structural design. In such cases, a surface notch is often necessary for the crack to sample sufficient HAZ material. The measured toughness is sensitive to the volume of HAZ material sampled by the crack tip because of the weakest link nature of cleavage fracture (see Section 3.5). Figure 3.15 illustrates several types of notches in production welds. According to the Welding Institute (55), a through thickness notch is acceptable if the HAZ is sufficiently straight for at least one-third of the crack front to be located in the HAZ (Fig. 3.15a). The disadvantage of the notch orientation in Fig. 3.15(a) is that the notched region of the HAZ is on the edge of the specimen, where the constraint is low.

Another application of the surface notched orientation is the simulation of structural flaws. Figure 3.16 illustrates HAZ flaws in a structural weld (Part a) and a surfaced notched fracture toughness specimen that models one of the flaws.

Figures 3.15 and 3.16 demonstrate the advantages of allowing a range of a/W ratios in surface notched specimens. A shallow notch is often required to locate a crack in the desired region, but existing ASTM standards do not allow a/W ratios less than 0.45. As stated in Section 3.3, more liberal a/W allowances were removed from the CTOD standard because of uncertainty on the effect of crack depth on the rotational factor. An additional problem is the tendency of shallow notched fracture toughness specimens to have lower constraint than deeply cracked specimens. The question of the rotational factor can be resolved fairly easily but the constraint issue is more difficult. Some fracture mechanics specialists argue that shallow notched tests should be permissible because they simulate the constraint in an actual structure which contains a shallow flaw. Others believe that a fracture mechanics test should be performed under conditions where a single parameter characterizes crack tip conditions (see Section 2.3.7). Such a test would yield a geometry-independent fracture toughness value that could be viewed as a material property. A test on a shallow notched specimen, they argue, is invalid because it does not satisfy these criteria. The Welding Institute and the Edison Welding Institute are addressing these issues in a cooperative research program.

3.4.3 Fatigue Precracking

Weldments that have not been stress relieved typically contain complex residual stress distributions that interfere with fatigue precracking of fracture toughness specimens. Figure 3.17, a typical fatigue crack that is produced in an as-welded specimen, was extracted from a double-V weld and was given a through-thickness notch. The fatigue crack did not grow in the center of the specimen because the residual stresses were compressive in this region.

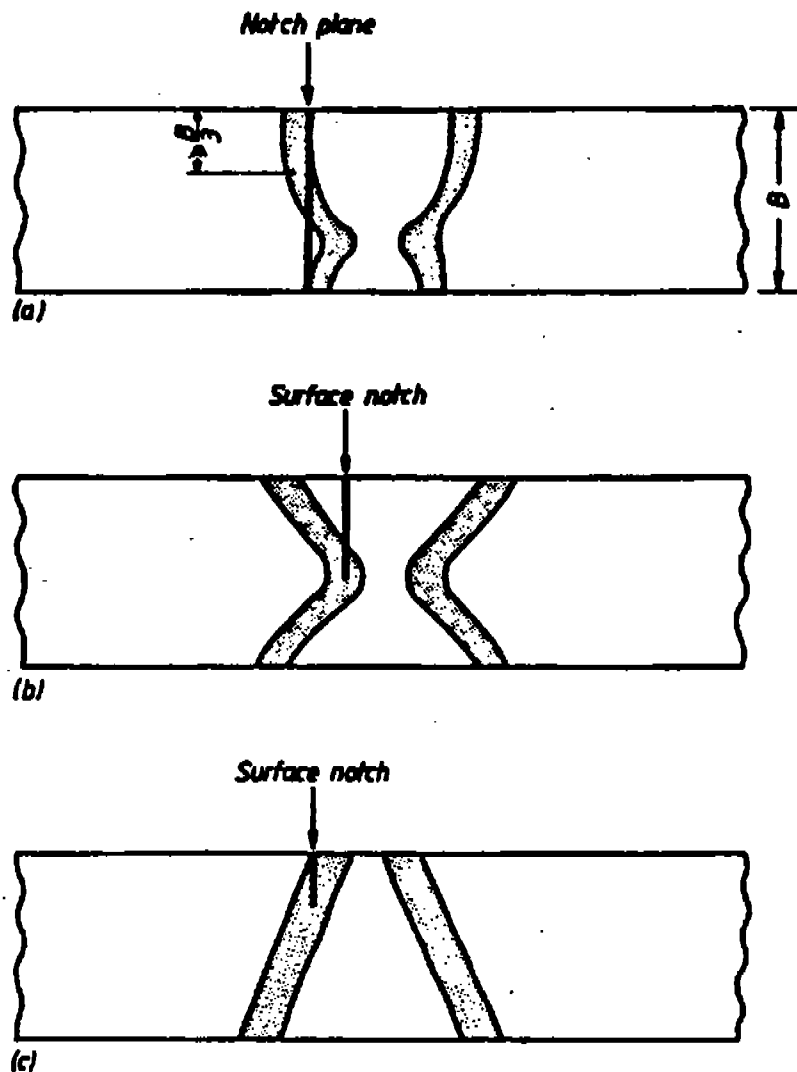


FIG. 3.15 Various notch orientations for HAZ specimens

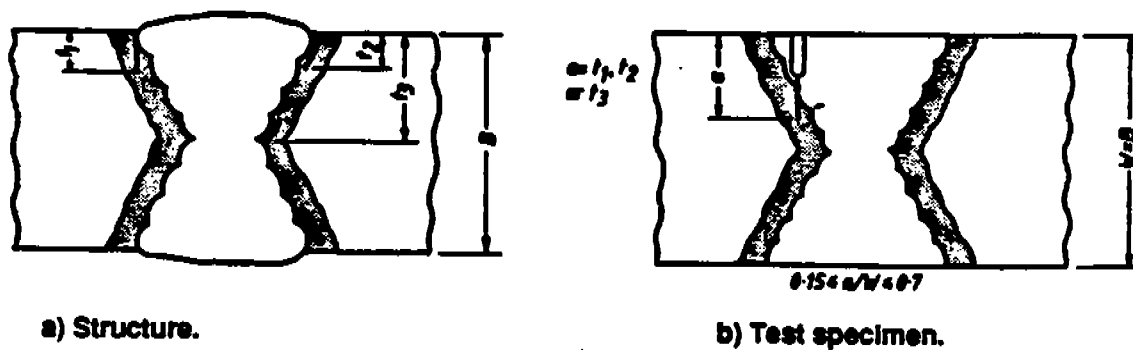


FIG. 3.16 Simulation of structural flaws with a surface notched SENB specimen (55).

Towers and Dawes (58) evaluated the various methods for producing straight fatigue cracks in welded specimens, including reverse bending, high R ratio, and local compression.

The first method bends the specimen in the opposite direction to the normal loading configuration to produce residual tensile stresses along the crack front that counterbalance the compressive stresses. Although this technique gives some improvement, it does not produce acceptable fatigue crack fronts.

The R ratio in fatigue cracking is the ratio of the minimum stress to the maximum. A high R ratio minimizes the effect of residual stresses on fatigue, but also tends to increase the apparent toughness of the specimen (60). In addition, fatigue precracking at a high R ratio takes much longer than precracking at $R = 0.1$, the recommended R ratio of the various ASTM fracture testing standards.

The only method evaluated which produced consistently straight fatigue cracks was local compression, which is illustrated in Fig. 3.18. The ligament is compressed to produce nominally 1% plastic strain through the thickness, mechanically relieving the residual stresses. However, local compression can reduce the toughness slightly. Towers and Dawes concluded that the benefits of local compression outweigh the disadvantages, particularly in the absence of a viable alternative.

3.4.4 Post-Test Analysis

Correct placement of a fatigue crack in weld metal is usually not difficult because this region is relatively homogeneous. The microstructure in the HAZ, however, can change dramatically over very small distances (60). Correct placement of a fatigue crack in the HAZ is often accomplished by trial and error. Because fatigue cracks are usually slightly bowed, the precise location of the crack tip in the center of a specimen cannot be inferred from observations on the surface of the specimen. Thus HAZ fracture toughness specimens must be examined metallographically after the test to determine the microstructure that initiated fracture. In certain cases, post-test examination may be required in weld metal specimens.

Figure 3.19 illustrates the Welding Institute's (55) recommended procedure for sectioning surface notched and through-thickness notched specimens. First, the origin of the fracture must be located by the chevron markings on the fracture surface. After marking the origin with a small spot of paint the specimen is sectioned perpendicular to the fracture surface and examined metallographically. The specimen should be sectioned slightly to one side of the origin and polished down to the initiation site. The spot of paint appears on the polished specimen when the origin is reached.

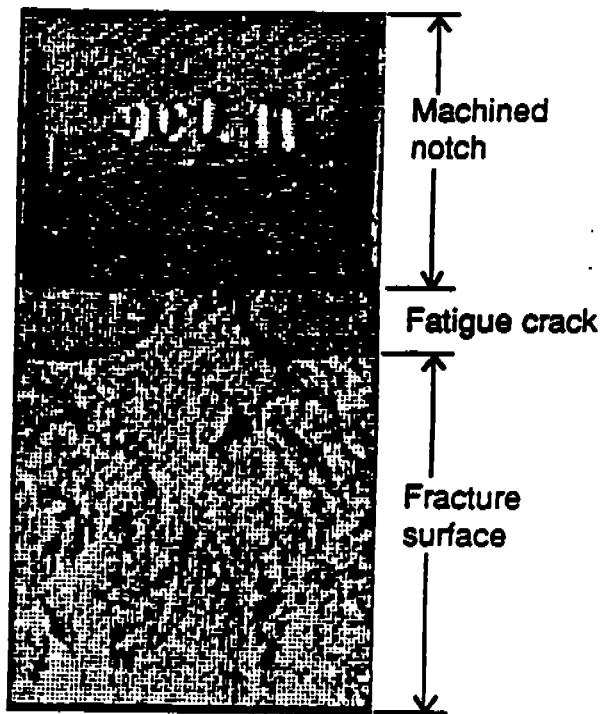


FIG. 3.17 Fracture surface of weldment specimen with invalid fatigue crack (58).

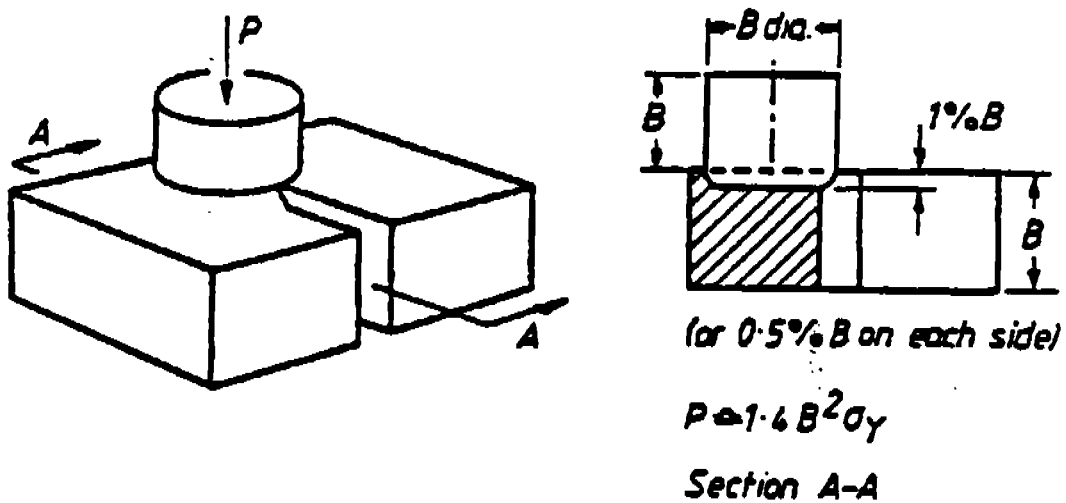


FIG. 3.18 Local compression applied to the ligament of a weldment specimen to relieve residual stresses prior to fatigue cracking (55).

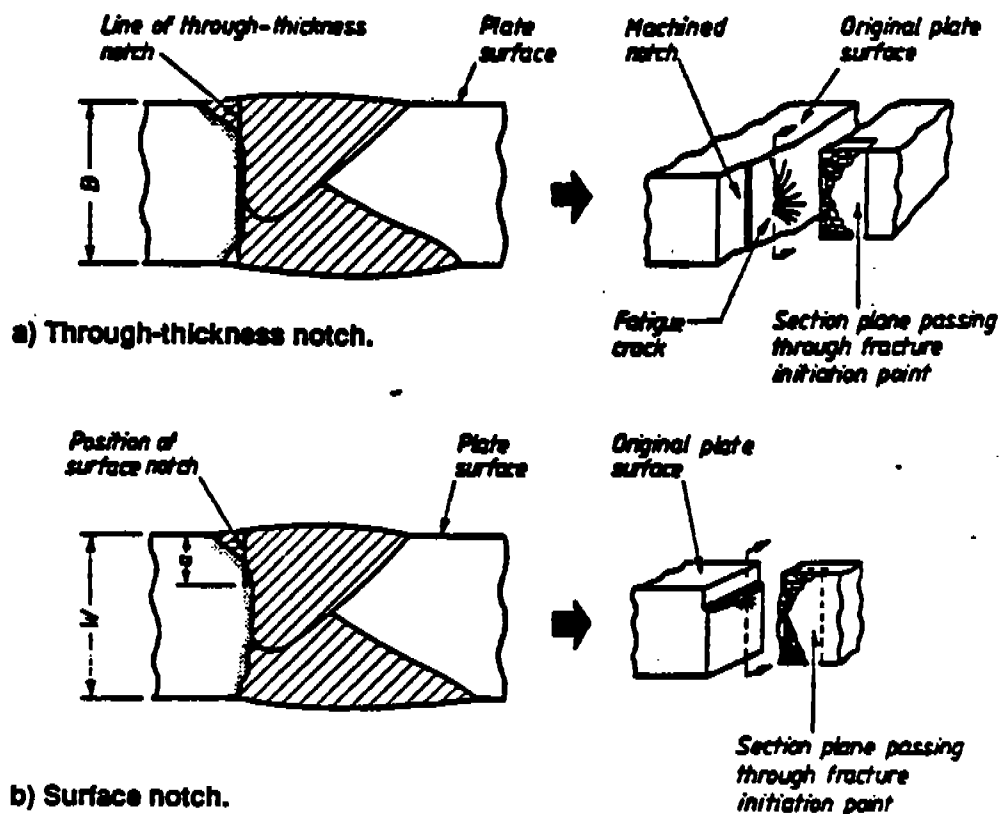


FIG. 3.19 Post-test sectioning techniques for HAZ specimens (55).

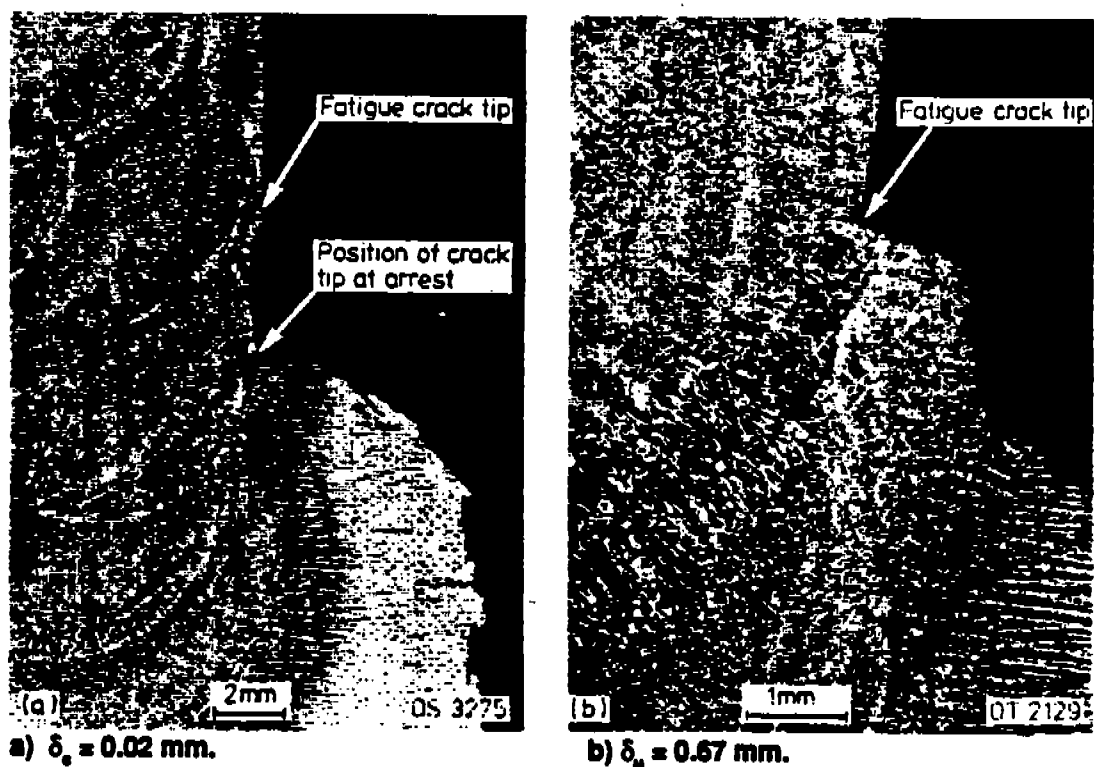


FIG. 3.20 Metallographic sections from two surface notched specimens (69).

Figure 3.20 shows photomicrographs of two typical sections of fracture toughness specimens. Fracture in the specimen on the left initiated at the fusion boundary at a δ_c of 0.02 mm. The crack propagated a short distance and arrested in the weld metal. Further loading was required to cause complete failure. The specimen on the right fractured at a δ_u of 0.67 mm. The initial fatigue crack was in the weld metal, which has a reasonably high toughness. On loading, the crack blunted and grew by ductile tearing. Cleavage fracture occurred when the growing crack reached the HAZ. These two cases illustrate how slightly different notch placement can result in vastly different fracture behavior.

The API document RP2Z (57) outlines a post-test analysis of HAZ specimens which is more detailed and cumbersome than the procedure outlined above. In addition to sectioning the specimen, the amount of coarse-grained material at the crack tip must be quantified. For the test to be valid, at least 15% of the crack front must be in the coarse-grained HAZ. The purpose of this procedure is to prequalify welding procedures and steels with respect to HAZ toughness, identifying those that produce low HAZ toughness so that they can be rejected before fabrication.

3.5 SCATTER AND SIZE EFFECTS IN THE TRANSITION REGION

In the ductile-brittle transition region of steels, ultimate failure occurs by cleavage; but this is often preceded by extensive plastic deformation and/or ductile tearing. There are a number of problems associated with fracture toughness testing in the transition region. Toughness data tend to be highly scattered because of the weakest-link nature of cleavage fracture, and existing measures of fracture toughness in the transition region often depend on specimen size.

The CTOD test is the only standardized method that is valid in the transition region, but it has no specimen size limitations to guarantee a single parameter description of crack tip conditions. As discussed in Chapter 2, a single parameter description is required for a geometry-independent measure of fracture toughness. The J_{IC} standard contains size requirements (Eq. [3.10]) for initiation of ductile tearing. A material's resistance to cleavage fracture can, in principle, be quantified by a critical J value. In fact, the nuclear power industry uses such an approach in the transition region, but it has not been standardized by ASTM. Size requirements for critical J values for cleavage have not been established. Equation [3.10] is probably not stringent enough for the transition region because cleavage fracture toughness is more sensitive to constraint loss than is ductile tearing (61).

Recent research has led to a number of simple, yet accurate analyses of scatter in cleavage fracture toughness data (44), but they are valid only as long as the crack tip is characterized by a single parameter such as J or CTOD. Thus the analyses are restricted to the lower transition region. In the upper transition region, the stresses at the crack tip relax and the crack grows by ductile tearing; fracture toughness becomes geometry dependent and the data scatter worsens.

3.5.1 Scatter in the Lower Transition Region

When an experimental measurement displays a high degree of scatter, it is customary to attempt to reduce this scatter by exercising tighter control over the experiment. Much of the observed scatter in cleavage fracture toughness data is an inherent feature of the material, however, that cannot be eliminated by improving the experimental procedure. Fortunately, fracture toughness scatter obeys certain rules and its magnitude can be predicted.

Statistical Aspects of Fracture

A number of micromechanical models for cleavage fracture have been proposed in the past few years(35,38-44); all based on weakest link statistics. Each model relates a material's microstructure to cleavage fracture toughness.

When fracture occurs by a weakest link mechanism, the failure probability is equal to the probability of sampling at least one critical microstructural feature. The Poisson distribution appropriately describes the failure probability in this case (43):

$$F = 1 - \exp\left(-\int_{V^*} \rho dV\right) \quad [3.17]$$

where F is the failure probability, V^* is the volume in the process zone ahead of the crack tip, and

$$\rho = \frac{\# \text{ particles } \geq \text{ critical size}}{\text{unit volume}}$$

The parameter ρ contains the inherent fracture properties of the microstructure. The macroscopic fracture properties of a structure or test specimen can be obtained by integrating ρ over the appropriate volume. In a uniaxial tensile specimen, ρ is constant throughout the gage section if the stress is constant, but ρ varies with position when a crack is present because ρ depends on stress. The critical particle size is related to stress through Eq. [2.31]. As stress increases, critical size decreases; ρ increases with stress because more particles are capable of initiating cleavage. Anderson (43) modeled the stress dependence of ρ with a modified power law:

$$\rho = \frac{(\sigma_1 - \sigma_u)^m}{\psi} \quad [3.18]$$

where σ_1 is the maximum principal stress at a point, and σ_u , m and ψ are material constants that characterize the fracture properties of the microstructure. The

quantity σ_u is the threshold stress, corresponding to the largest conceivable particle in the material.

If fracture occurs by a weakest link mechanism and the crack tip stresses are completely characterized by J (e.g. Fig. 2.16 a-b), it can be shown (44) that fracture toughness data follows a characteristic distribution function:

$$F = 1 - \exp\left[-\frac{B}{B_0}\left(\frac{J_c}{\theta_J}\right)^2\right] \quad [3.19a]$$

or

$$F = 1 - \exp\left[-\frac{B}{B_0}\left(\frac{\delta_c}{\theta_\delta}\right)^2\right] \quad [3.19b]$$

or

$$F = 1 - \exp\left[-\frac{B}{B_0}\left(\frac{K_{IC}}{\theta_K}\right)^4\right] \quad [3.19c]$$

for critical J , CTOD and K values, respectively; B_0 is a reference thickness. The quantities θ_J , θ_δ , and θ_K are the 63rd percentile values of the corresponding fracture toughness parameters when specimen thickness = B_0 . These three constants are related through Eqs. [2.26] and [2.28]. Equation [3.19] is derived in the Appendix. A number of investigators (44, 62, 63) have derived nearly identical cleavage fracture toughness distributions.

Equations [3.19 a-c] have the form of a Weibull distribution. The Weibull shape parameter (or slope) = 2.0 for critical J and CTOD values, and because of the relationship between J and K , the shape parameter = 4.0 for K_{IC} or effective K values computed from J (see Eq. [2.28]).

Figure 3.21 (64) gives an experimental validation of a theoretical Weibull slope. Experimental values of the Weibull slope from published fracture toughness data are plotted as a function of data set size. All J and CTOD data were converted to equivalent K_{IC} values through Eqs. [2.26] and [2.28]. Although the computed Weibull slopes are widely scattered for small sample sizes, the data approach the theoretical value of 4.0 as sample size increases. The scatter in computed slopes can be attributed to small sample effects. The curves in Fig. 3.21 represent 95% confidence limits which were computed by Monte Carlo simulation. Finite samples were randomly taken from a hypothetical population of fracture toughness data with a true slope of 4.0, and Weibull slopes were computed. This process was repeated numerous times for various sample sizes. Note that the computed confidence limits

describe well the variability of the real experimental data. Thus Fig. 3.21 shows strong experimental evidence for the validity of Eq. [3.19].

The discovery of a characteristic Weibull slope for fracture toughness distributions has important ramifications. If the 63rd percentile fracture toughness of a given material is known, the entire toughness distribution is defined by Eq. [3.19]. Thus scatter in cleavage fracture toughness data can be quantified.

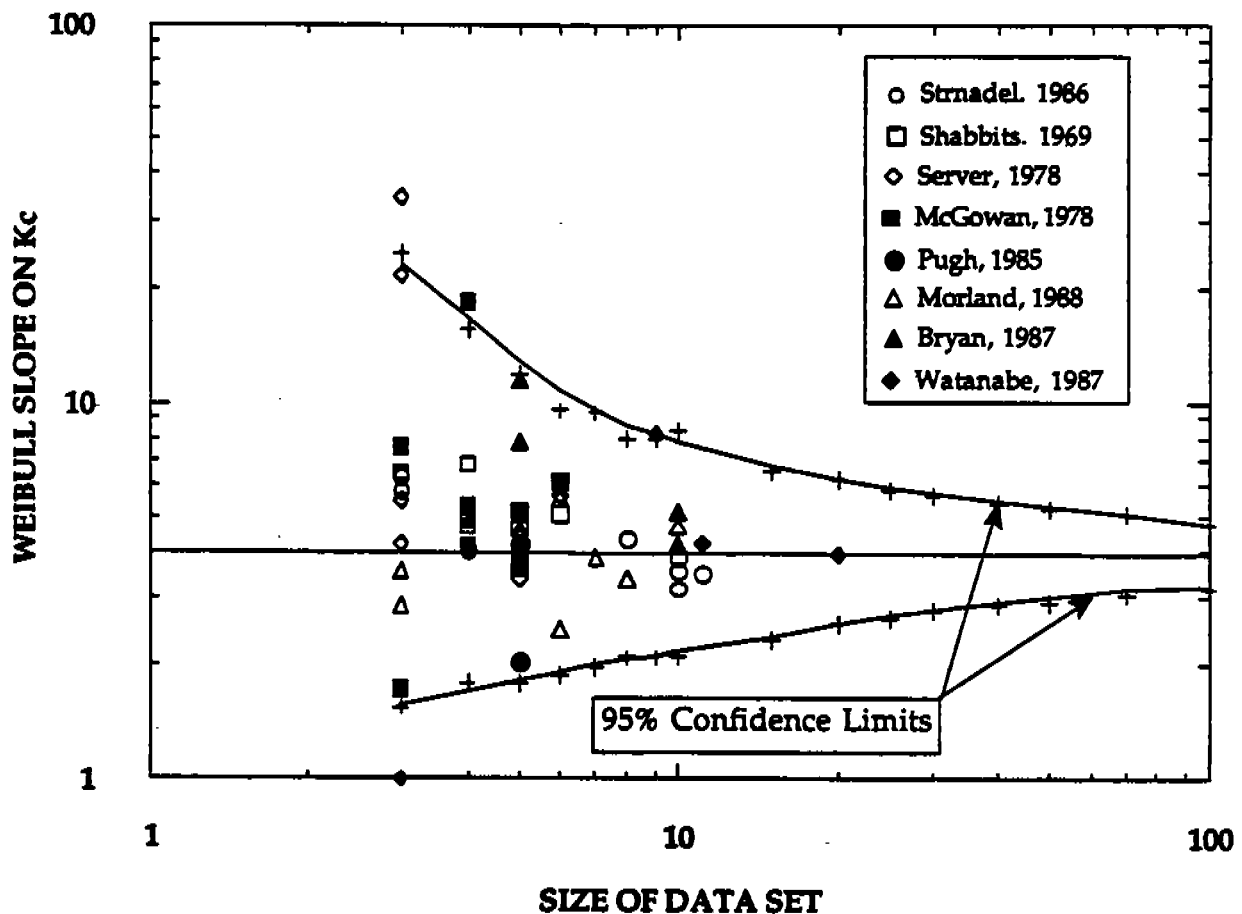


FIG. 3.21 Comparison of experimental Weibull slopes on K_c with the theoretical value of 4.0 (64). The confidence limits were generated by Monte Carlo simulation.

Analysis of Scatter

The value of Eq. [3.19] can be illustrated by introducing two quantities that characterize scatter: the confidence band ratio and the lower bound ratio. The confidence band ratio is obtained by dividing the confidence band width by the median value. For example, the 80% confidence band ratio for CTOD data is given by

$$CBR_{0.8} = \frac{\delta_{0.9} - \delta_{0.1}}{\delta_{0.5}} = \frac{\sqrt{-\ln(0.1)} - \sqrt{-\ln(0.9)}}{\sqrt{-\ln(0.5)}} = 1.43 \quad [3.20]$$

where $\delta_{0.9}$, $\delta_{0.1}$, and $\delta_{0.5}$ are the 90% upper bound, 10% lower bound and median CTOD values, respectively. Note that the confidence band ratio is independent of temperature, specimen thickness, and material properties. Although the scatter in absolute terms increases with median toughness, the relative scatter is constant.

The lower bound ratio is defined as the ratio of the median to a particular lower limit in the distribution. This is probably a more useful quantity than the CBR because the lower tail of a toughness distribution causes the most concern in structural applications. The 10% lower bound ratio is given by

$$LBR_{0.1} = \frac{\delta_{0.5}}{\delta_{0.1}} = \sqrt{\frac{\ln(0.5)}{\ln(0.9)}} = 2.57 \quad [3.21a]$$

Similarly, the 1% lower bound ratio can be computed:

$$LBR_{0.01} = \sqrt{\frac{\ln(0.5)}{\ln(0.99)}} = 8.30 \quad [3.21b]$$

Thus, if the median CTOD is known, the 1 percent lower bound toughness can be estimated by dividing the median by 8.30.

The confidence band and lower bound ratios would be identical for J and CTOD data since both parameters have the same Weibull exponent, but K values have a Weibull exponent of 4.0, causing the data scatter to be somewhat different. For example, the 1 percent lower bound ratio for critical stress intensity data is given by

$$LBR_{0.01} = \frac{K_{0.5}}{K_{0.01}} = \left(\frac{\ln(0.5)}{\ln(0.99)}\right)^{1/4} = 2.88 \quad [3.21c]$$

Critical K data for cleavage appears to be less scattered than J or CTOD data only because both J and CTOD are proportional to K^2 under small-scale yielding

conditions. No benefit would be realized by quantifying toughness with K rather than J or CTOD. The uncertainty in critical crack size calculations that results from toughness scatter is the same regardless of the fracture parameter.

Analysis of Small Data Sets

Equations [3.20] and [3.21] estimate relative scatter, but to determine absolute values in the distribution with these equations, a single value (e.g. the median) must be known. Stated another way, at least one point on the distribution must be known in order to compute θ and thereby define the entire distribution. The degree of confidence to which θ can be estimated depends on the size of the available data set.

In most cases, a relatively small number of fracture toughness tests are used to characterize a given material at a constant temperature, partly because fracture toughness testing tends to be expensive and time consuming. In addition, many still view fracture mechanics analysis as deterministic; i.e., a single value of toughness is typically used to estimate critical crack size. Consequently, large fracture toughness data sets are often unavailable

Stienstra et al. (64) developed an approach for inferring useful information from small fracture toughness data sets by utilizing order statistics to estimate a lower-bound toughness value from the available data. The analysis assumes that Eq. [3.19] describes the toughness distribution. The lower-bound value is related to measured values by a multiplying factor. For example, the 10% lower-bound CTOD is estimated with 90% confidence as follows.

$$\delta_{0.1,0.9} = k_{0.1,0.9(n)} \delta_{\min} \quad [3.22]$$

where $k_{0.1,0.9(n)}$ is a multiplying factor, n is the sample size, and δ_{\min} is the lowest CTOD in a set of n values. Whenever statistical inferences are made from limited data sets, two probability values must be specified. The above equation corresponds to an *estimate* of the 10% lower bound for the toughness distribution. This is a conservative estimate because the *true* 10% lower bound lies above the estimate 90% of the time. Table 3.1 lists multiplying factors for four combinations of confidence levels and lower bounds. This approach to lower bound estimates has a built-in retest rational, as illustrated in the following example.

Consider a set of three CTOD values for a given material, with $\delta_{\min} = 0.10$ mm. According to Table 3.1, the 10% lower bound, estimated with 90% confidence, is 0.037 mm. Imagine a hypothetical application where $\delta_{0.1,0.9}$ must be at least 0.05 mm. Given the existing data, one must conclude that the material's toughness is inadequate for the application. However, additional tests may reveal that the material is acceptable and that the low CTOD value in the first three tests was a rarity.

If a total of seven tests are performed and δ_{min} remains at 0.10 mm, the estimated lower bound increases to 0.057, which is above the minimum acceptable value.

The use of small data sets to estimate lower bound values is not without cost. In order to obtain 90 or 95% confidence that the estimate is below the true value, the estimate must be conservative when the sample size is small. In general, the estimate is less conservative if more data are available (64). *Thus there is a trade-off between the cost of performing a large number of fracture toughness tests and the cost of rejecting a material that may be adequate for the application.*

TABLE 3.1. Multiplying factors for estimating lower bound toughness from small data sets(64).

NUMBER OF VALID TESTS	MULTIPLYING FACTOR (k)			
	10% Lower Bound		5% Lower Bound	
	90%Confidence	95%Confidence	90%Confidence	95%Confidence
3	0.3705	0.3248	0.2585	0.2266
5	0.4783	0.4193	0.3337	0.2926
7	0.5660	0.4962	0.3949	0.3462
10	0.6764	0.5930	0.4720	0.4138
15	0.8285	0.7260	0.5781	0.5068
20	0.9566	0.8387	0.6675	0.5852

Thickness Effects

The weakest link nature of cleavage leads to a size dependence on fracture toughness. This is apparent from Eq. [3.19] because thickness appears in the exponent. For a constant failure probability, critical J and CTOD values are proportional to $1/\sqrt{B}$, and K_{IC} (or K_{eff}) is proportional to $B^{-1/4}$. Early studies (7, 65) on the size dependence of critical K values concluded that a plateau value is reached above a critical thickness, but the statistical model predicts that average K_{IC} decreases by 16% each time thickness is doubled. Early investigators probably lacked sufficient data to detect the continual decrease in toughness. Statistical thickness effects can be masked by the scatter in toughness.

Landes and Schaffer (66) were the first to apply a weakest-link statistical argument to relate fracture toughness data from large and small specimens. They fit Weibull distributions to small specimen data and estimated the average toughness of large specimens with the following relationship:

$$\text{Avg. } K_{IC} (\text{large specimen}) = \text{Avg. } K_{IC} (\text{small specimen}) \times \left(\frac{B_{\text{small}}}{B_{\text{large}}} \right)^{1/\beta} \quad [3.23]$$

where β is the Weibull slope. The Landes and Schaffer analysis of thickness effects is similar to Eq. [3.19], except they left the Weibull slope as a variable. The discovery of a characteristic Weibull slope for cleavage toughness (44, 62, 63) came several years after the Landes and Schaffer study.

Specimen size effects on fracture toughness cannot always be explained completely by weakest link statistics. When fracture is preceded by large scale plasticity or ductile tearing, additional size effects are observed (67), as discussed in Section 3.5.2.

Threshold Toughness

The decrease in toughness with increasing thickness does not continue indefinitely. Fracture toughness data exhibit an absolute minimum that is above zero (62, 64). One reason for this is that the fatigue precracking procedure introduces warm prestress effects at the crack tip. The plastic zone formed during precracking results in compressive residual stresses when the specimen is unloaded. When the specimen is reloaded at the test temperature, these stresses must be overcome for fracture to occur. The compressive residual stresses can be represented by a negative stress intensity that reduces the effective K_I :

$$K_{\text{eff}} = K_I - K_0 \quad [3.24]$$

where K_I is the apparent stress intensity, and K_0 is the stress intensity of the compressive residual stresses. Equation [3.19c] can be modified to account for warm prestress effects:

$$F = 1 - \exp \left[- \frac{B}{B_0} \left(\frac{K_{IC} - K_0}{\theta_K - K_0} \right)^4 \right] \quad [3.25]$$

Thus K_0 represents the threshold toughness for the material, analogous to the threshold ΔK caused by crack closure effects during fatigue.

Experimental and theoretical estimates of K_0 indicate that it is approximately 20 MPa $\sqrt{\text{m}}$ for steels. The temperature dependence of K_0 is unclear. Current research at Texas A&M University is establishing more accurate estimates of K_0 .

The threshold toughness significantly influences the toughness distribution only on the lower shelf, where the average toughness is of the same order as K_0 . In the transition region, K_0 can be neglected for most analyses. Unless otherwise specified, K_0 is assumed to equal zero in this document, and the cleavage fracture toughness distribution is described with Eq. [3.19].

Local Brittle Zones

Some materials contain localized regions of low toughness. Since cleavage fracture is a weakest-link phenomenon, these local brittle zones (LBZs) can dominate the fracture process.

The most common instance of local brittle zones is in the heat-affected zone (HAZ) of a steel weldment (60, 68, 69). A typical weld HAZ contains a wide range of microstructures because of the various thermal treatments encountered. For example, the material at the fusion boundary experiences a very high austenitizing temperature and cooling rate, while material a short distance away is subjected to a much lower temperature and cooling rate. In addition, certain regions are tempered by subsequent welding passes. Some of the microstructures produced are extremely brittle.

The fracture behavior of such materials is complex. The crack tip in a fracture mechanics specimen is likely to sample a number of microstructural regions. The fracture toughness distribution depends on the relative volume of each microstructure that is sampled.

The statistical model described above is capable of characterizing fracture toughness distributions in composite microstructures such as weld HAZs. The contribution of each microstructural region to the failure probability can be summed to obtain an overall probability of failure. For example, if p constituent microstructures are sampled by the crack tip, the CTOD distribution is given by

$$F = 1 - \exp\left(-\frac{B}{B_0} \delta_c^2 \sum_{i=1}^p \frac{\alpha_i}{\theta_i^2}\right) \quad [3.26]$$

where α_i is the fraction of the crack front that samples the microstructural constituent, and θ_i is a characteristic toughness for the constituent. Note that CTOD still follows a Weibull distribution with the slope = 2. Equation [3.26] reduces to Eq. [3.19b] when $p = 1$.

Consider a duplex ($p=2$) microstructure with local brittle zones in a matrix that is three times as tough as the LBZs (i.e., $\theta_1 = 9\theta_2$). Figure 3.22 is a plot of normalized CTOD versus percent LBZ(44). The median CTOD decreases with increasing volume fraction of LBZ. Beyond 40 percent LBZ, however, the rate of decrease in toughness is small. Figure 3.22 includes plots for matrix/LBZ toughness ratios of three, ten, and infinity. The curve for toughness ratio = 10 is essentially identical to the curve corresponding to an infinitely tough matrix. This implies that a constituent ten times as tough as the most brittle constituent does not contribute to the overall

failure probability. Figure 3.23 (44) illustrates the effect of LBZ on scatter when the toughness ratio is 3.0.

The above analysis is a means for estimating the probability of fracture initiation in materials with local brittle zones. Cleavage cracks that initiate in the LBZs may arrest in the surrounding material. The statistical model will be conservative in these cases because it does not consider crack arrest. The crack arrest behavior of complex microstructures such as weld HAZs is not well enough understood for reliable predictions. Thus it is usually advisable to design against cleavage initiation.

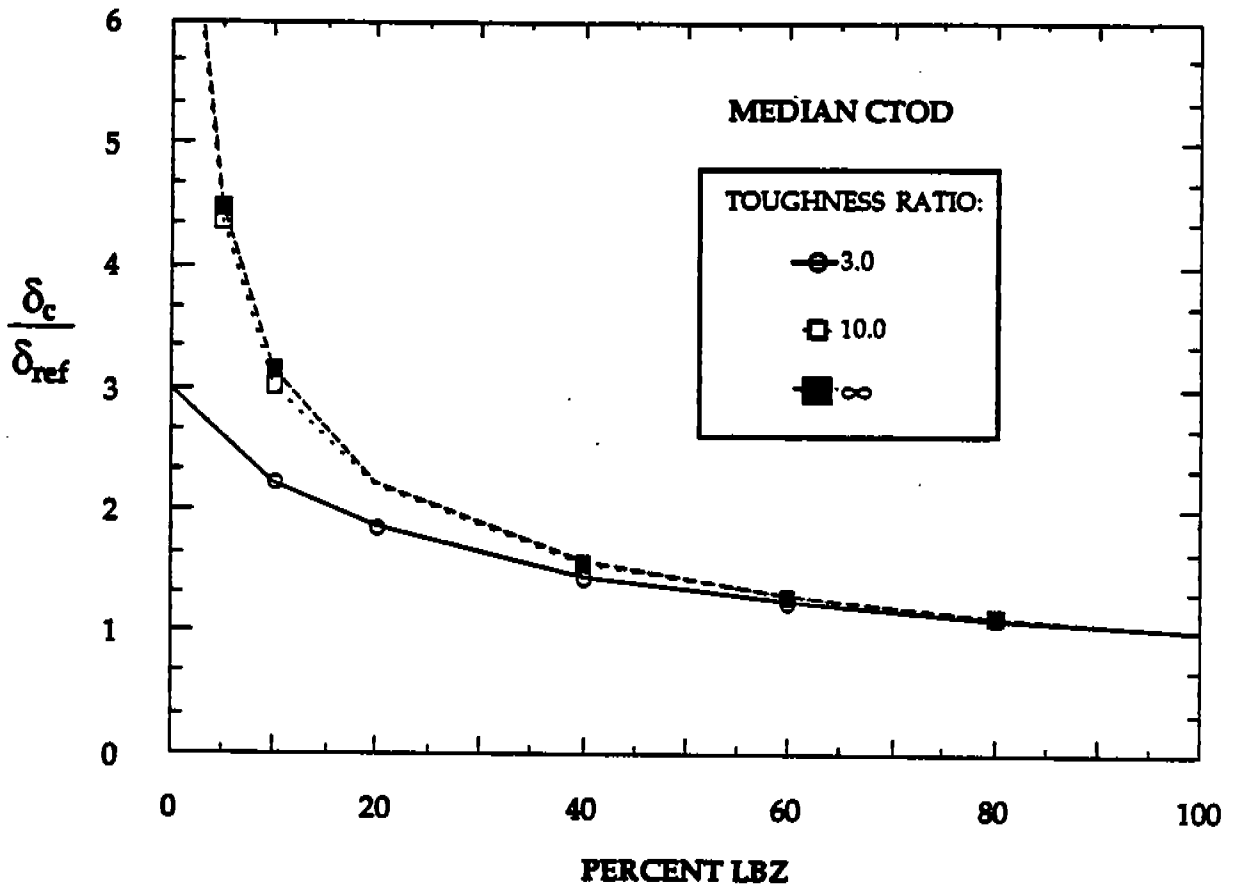


FIG. 3.22 Effect of the percent local brittle zone (LBZ) along the crack front on median fracture toughness in the heat affected zone. The toughness ratio is defined as the matrix toughness/LBZ toughness.

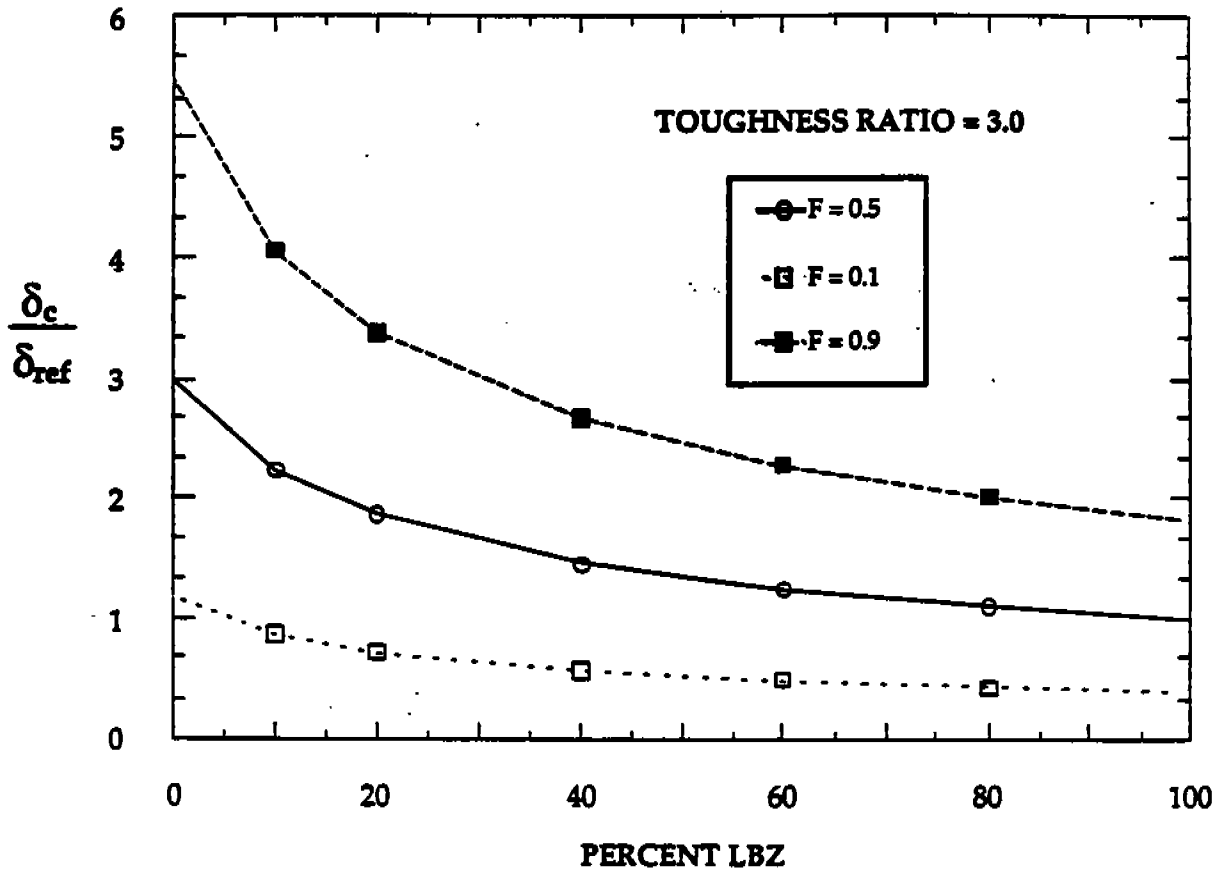


FIG. 3.23 Predicted scatter in CTOD data for weldments with a matrix/LBZ toughness ratio of 3.0 (44).

3.5.2 Large Scale Yielding

The J integral and crack tip opening displacement approaches allow significantly more plasticity than linear elastic fracture parameters such as stress intensity, but elastic-plastic fracture theory eventually breaks down. In such cases, J does not uniquely characterize crack tip conditions (Fig. 2.16c). The apparent fracture toughness depends on the size and geometry of the specimen or structure. This effect is most pronounced in the upper transition region, where cleavage is preceded by large scale yielding and ductile crack growth.

Bending Versus Tension

Figures 3.24 and 3.25 show crack tip stress fields computed from finite element analysis (70) for a center cracked tension panel and an SENB specimen, respectively. The results are plotted so that all data collapse onto a single curve when J integral theory is valid. In the case of the center cracked panel, the computed stresses in large scale yielding lie well below the HRR solution. The stresses in the

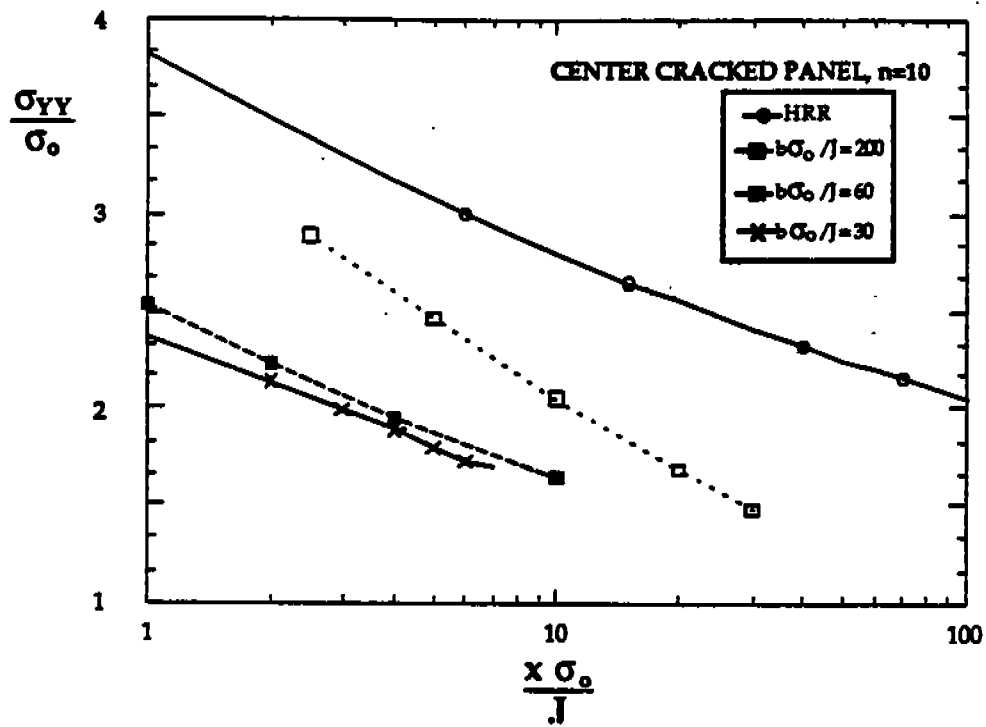


FIG. 3.24 Finite element solution for crack tip stress fields in a center cracked panel loaded in plane strain tension(70).

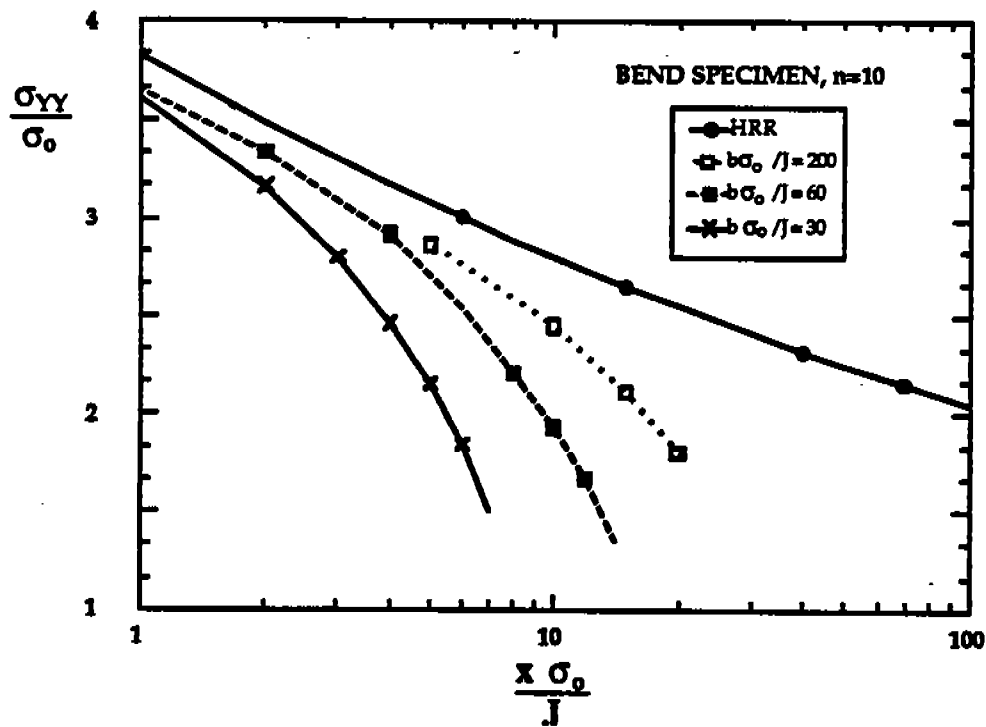


FIG. 3.25 Finite element solution for crack tip stress fields in a plane strain SENB specimen(70).

bend specimen are close to the HRR solution near the crack tip but diverge at greater distances. Since the stresses at the crack tip control fracture, J is a good characterizing parameter in bend specimens up to relatively high levels of plasticity. The highest J value plotted in Figs. 3.24 and 3.25 is slightly less than the value corresponding to the ASTM size limit for J_{IC} (Eq. [3.10]). It is apparent from these two figures why the ASTM size requirements apply only to specimens loaded predominantly in bending.

According to Figs. 3.24 and 3.25, bending produces more constraint than tensile loading. Because of this constraint effect, the apparent cleavage toughness is higher in specimens and structures loaded predominantly in tension. Figure 3.26 shows CTOD data for SENB specimens as well as wide plates with surface cracks and through-thickness notches (71). The material is a BS 4360-50D steel tested at -65°C (72). Although the scatter bands overlap, the critical CTOD in the wide plates tends to be significantly higher than in the bend specimens.

Scatter in Toughness

Loss of crack tip constraint not only increases the average toughness, but also increases the relative scatter (44). This is evident in Fig. 3.26, where the wide plate data are more scattered than the SENB data. Under large scale yielding conditions, scatter in fracture toughness data can no longer be described by Eq. [3.19]. This relationship was derived assuming HRR conditions (see Appendix). When crack tip constraint relaxes, an incremental increase in J (or CTOD) produces a smaller increase in stress than predicted by HRR theory. Large increases in J have relatively little effect on the actual driving force at the crack tip. The failure probability also increases more gradually with increasing J . Thus critical values of J or CTOD are widely scattered.

Prior stable crack growth also tends to increase the level of scatter in cleavage toughness (44). As the crack grows, the crack tip stress field deviates from HRR theory. The effect on failure probability and the fracture toughness distribution is similar to that associated with constraint loss at a stationary crack. In a typical structural steel in the upper transition region, constraint loss and stable crack growth combine to produce a high degree of scatter in fracture toughness. Wallin (73, 74) characterized upper transition behavior with a modified statistical model for cleavage.

Figure 3.27 is a schematic Weibull plot of fracture toughness data in the ductile-brittle transition region, with distributions for two specimen sizes. At the lower end of the distribution, Eq. [3.19] applies and critical J or CTOD data have a slope of 2.0 on a Weibull graph. At higher toughness values, the slope decreases because a combination of large scale plasticity and ductile crack growth. A low Weibull slope indicates a high degree of scatter. Under J controlled conditions when the Weibull slope = 2.0, the distributions for the two thickness can be collapsed onto a single curve by multiplying the data for the smaller specimens by $\sqrt{B_2/B_1}$. This multiplying factor does not correct for thickness at large J values.

Constraint loss and crack growth produce a thickness dependence in addition to that associated with statistical sampling effects.

Size Effects

Size effects on fracture toughness in the transition region can be caused by a combination of constraint and statistical sampling effects. Figure 3.28 is a schematic plot of median fracture toughness versus specimen size. If the specimen is large enough to maintain J-controlled conditions, the size dependence of toughness is due only to statistical effects. The effect of thickness can be inferred from Eq. [3.19]. For smaller sizes, the loss in crack tip constraint produces an additional size dependence, as indicated by the shaded area in Fig. 3.28.

The statistical size dependence on fracture toughness cannot be avoided, but it has been quantified (Eq. [3.19]). Thus it is relatively easy to correct for statistical effects when analyzing a flaw in a structure. Since there are currently no proven corrections for crack tip constraint, J and CTOD tests in the transition region should be performed on sufficiently large specimens to ensure J controlled conditions at the crack tip. The minimum size requirements for cleavage toughness have not been established. The development of such criteria should be the subject of future research.

Corrections for Crack Tip Constraint

In certain instances, it may not be practical to perform a fracture toughness test under J controlled conditions. For example, an engineer may want to test a specimen with a shallow crack in order to simulate a surface flaw in a structure. In such cases, the resulting fracture toughness will be influenced by constraint loss. Although there are no proven methods to correct for constraint loss, a recently developed analysis shows some promise. Anderson(61) derived a J-like parameter to characterize the stress normal to the crack plane (σ_{YY}) under large scale yielding conditions:

$$J_{yy}^* = \frac{\delta \sigma_0}{d_n} \left(\frac{d_n dJ}{\sigma_0 d\delta} \right)^{n+1} \quad [3.27]$$

Recall that d_n is a dimensionless constant that relates J and CTOD under HRR conditions (Eq. [2.26]). Equation [3.27] characterizes the loss in triaxiality through the change in the J-CTOD relationship from the HRR solution. When the HRR solution is valid, $J_{yy}^* = J$. Figure 3.29 shows the finite element results from Fig. 3.24, normalized in terms of J_{yy}^* rather than J. This new parameter appears to correct the stress fields for constraint loss. Since σ_{YY} near the crack tip governs cleavage, J_{yy}^* can be viewed as the effective driving force for cleavage. Further validation of this parameter is needed before it can be applied to practical situations.

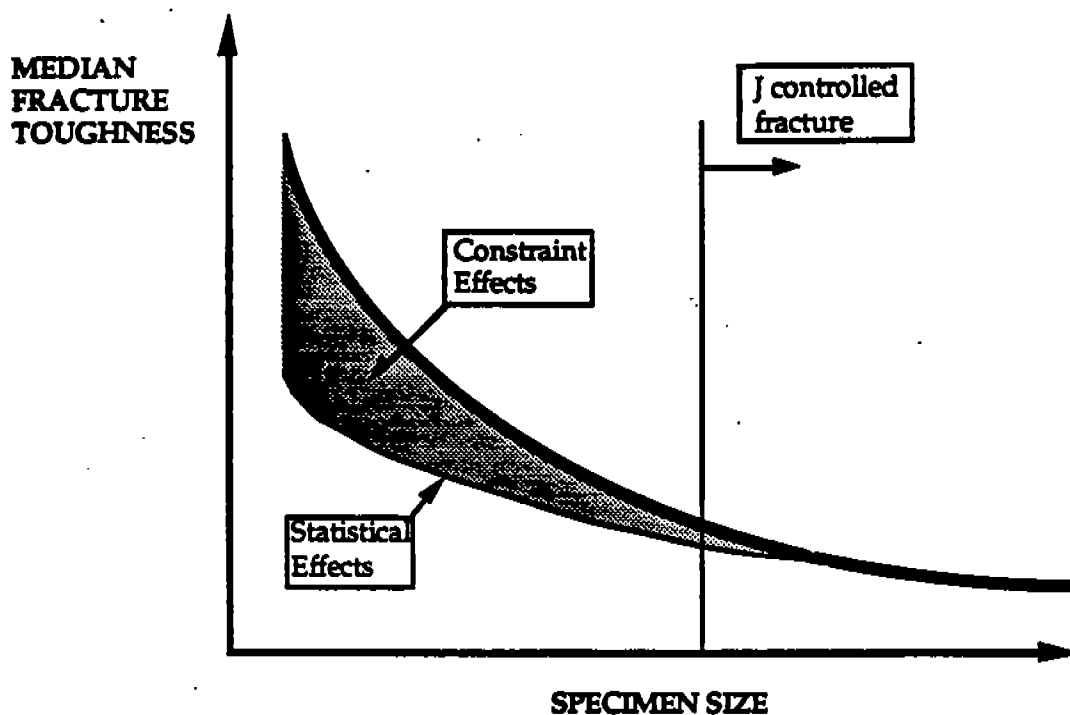


FIG. 3.28 Schematic plot of the effect of specimen size on fracture toughness.

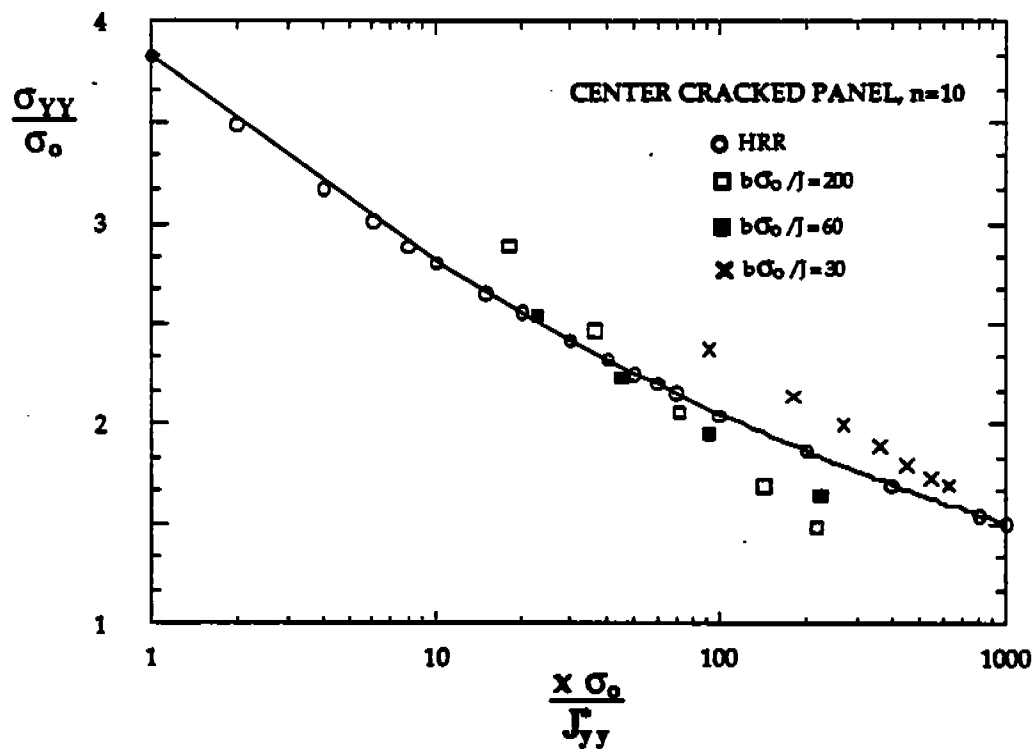


FIG. 3.29 Crack tip stress fields from Fig. 3.24, normalized by $J_{yy}^{*}(61)$.

3.6 DYNAMIC FRACTURE TOUGHNESS AND CRACK ARREST

When fracture is associated with either a high loading rate or a rapidly propagating crack, the problem is complicated by two factors: the inertia of the structure and the strain rate sensitivity of the material. With inertia effects, calculation of crack tip parameters such as J and K is much more difficult (75). When the strain rate varies over several orders of magnitude, metals behave in a viscoplastic manner, even at low temperatures. A material's flow stress increases with strain rate; thus quasistatic tensile properties are not relevant at high strain rates.

The relationship between loading rate and fracture toughness is complex. Inertia effects tend to increase the apparent toughness of the material because the total fracture energy includes a significant kinetic energy component. Viscoplastic material behavior can either increase or decrease the toughness with loading rate, depending on the fracture mechanism. Cleavage fracture toughness tends to decrease with strain rate because cleavage is stress controlled. Increasing the flow stress makes it easier for material at the crack tip to reach the critical cleavage stress. Since microvoid coalescence is predominantly strain controlled, upper shelf toughness usually increases with strain rate. As the flow stress increases, more energy is required to deform the material near the crack tip to a critical strain. During rapid propagation of a crack in a large specimen or structure, the crack speed (and hence the local strain rate) can vary considerably. In such cases it is not unusual for the fracture mechanism to alternate between cleavage and ductile tearing, as one mechanism becomes more favorable than the other (76).

Inertia effects are most pronounced immediately after application of the load (77). The material oscillates as stress waves propagate through the specimen, and the amplitude of these oscillations decreases rapidly. After a short time, the local inertia effects are small and the behavior is dominated by global inertia effects. At long times, the behavior of the specimen is similar to that of the quasistatic case, with the exception of viscoplastic material flow properties. Nakamura et al. (77) developed the concept of a transition time, t_T , to delineate between short time response, where inertia effects are important, and long time behavior, where inertia effects are small relative to the total energy in the specimen. Dynamic finite element analysis performed by Nakamura et al. indicates that inertia effects are small at times greater than $2t_T$. As long as fracture initiation occurs after $2t_T$, the dynamic J_{IC} can be computed from the quasistatic relationships in ASTM E813-87.

Joyce and Hackett (78, 79) have applied the transition time concept to dynamic J testing. They have perfected experimental techniques for high rate fracture toughness tests on SENB specimens. These specimens are typically 25 mm thick and are heavily instrumented. Impact loading is applied by a drop tower. Nakamura et al. estimated the transition time for these specimens to be 300 μ s. Materials that Joyce and Hackett have tested are relatively ductile. Fracture initiation in these materials usually occurs between one and two milliseconds after the tup contacts the specimen. Since the time to fracture is greater than $2t_T$ in this case, J can be

computed with Eqs. [3.5] to [3.7a]. Joyce and Hacket developed a key curve method to infer crack growth during the test. Figure 3.30 (78) compares quasistatic J-R curves for a 3-Ni steel with dynamic curves obtained from their method. The viscoplastic material behavior causes the material resistance to increase with strain rate, as expected.

When inertia effects are minimal, dynamic loading reduces cleavage fracture toughness. Since plastic deformation in steels is a thermally activated process, increasing the strain rate is equivalent to testing at a lower temperature. Thus, when the loading rate increases, the ductile-brittle transition curve shifts upward in temperature. For example, Fig. 3.31 shows fracture toughness data for an A572 Grade 50 steel at three loading rates (80). The transition curves shift approximately 200°F (110°C) between the lowest and highest strain rate.

Once cleavage initiates, whether from quasistatic or dynamic loading, a propagating cleavage crack moves rapidly through the specimen. Material near this propagating crack is subjected to very high strain rates. Thus the situation is analogous to a continuous dynamic fracture toughness test. In order for the crack propagation to continue, the driving force for fracture must be at least as large as the material resistance. Resistance of a steel to cleavage fracture can be represented by a falling R curve, as illustrated in Fig. 3.32. When fracture initiates at K_{IC} , the crack propagates in a rapid and unstable manner. The fracture process then becomes dynamic, and resistance to cleavage decreases. In many loading situations, the driving force increases with crack length or remains constant, and the crack continues to propagate. In some cases, however, the driving force may decrease until it intersects the material resistance curve, and the crack arrests because further propagation is impossible. The arrest toughness, K_{Ia} , is a measure of a material's ability to stop a rapidly propagating crack.

There are a number of practical situations in which crack arrest can occur. A specimen or structure loaded in displacement control can have a falling driving force curve. A falling driving force curve can also result from a transient load, as when a ship collides with another vessel. The transient load may be sufficient to initiate cleavage, but the driving force decreases rapidly as the stress waves are damped by the structure. Another common scenario for crack arrest involves a toughness gradient. For example, a crack may initiate in a cold region of a structure, where the toughness is low, and propagate into material at a higher temperature and toughness level. The crack arrests when the K_{Ia} exceeds the driving force. A toughness gradient could also result from variations in microstructure, such as in welded structures. If a cleavage crack initiates in a brittle region of the weld, it may arrest when it reaches the parent metal, which usually has higher toughness.

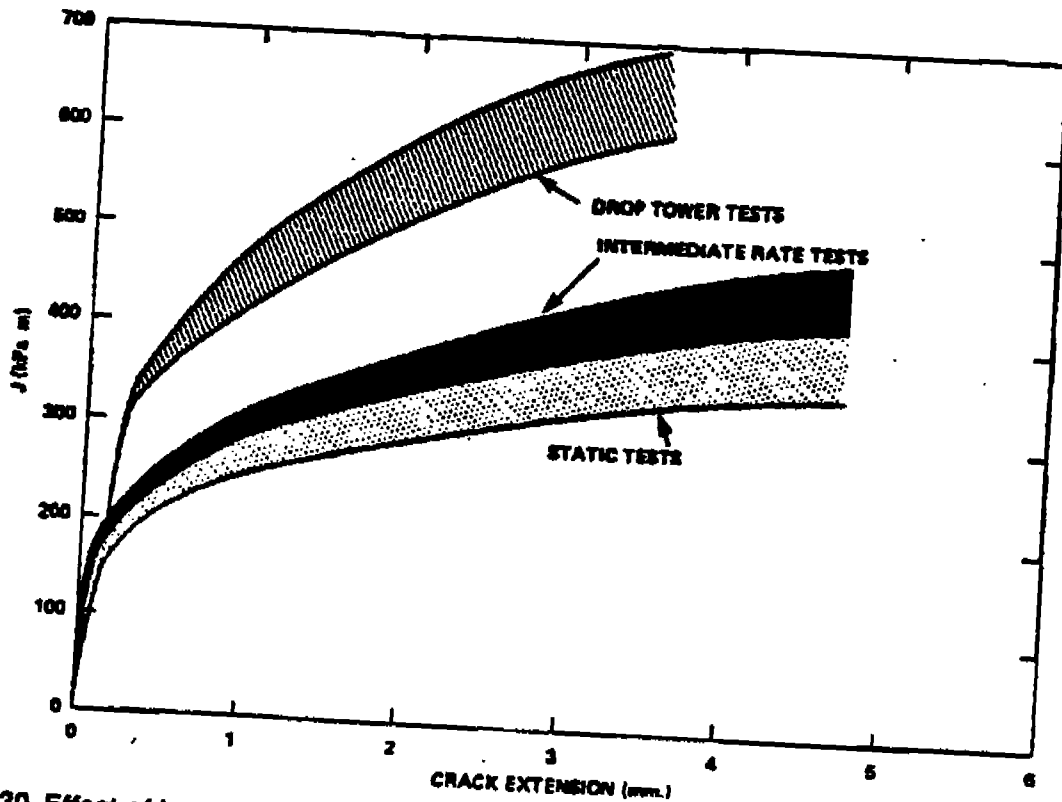


FIG. 3.30 Effect of loading rate on J-R curves for a 3-Ni steel (78).

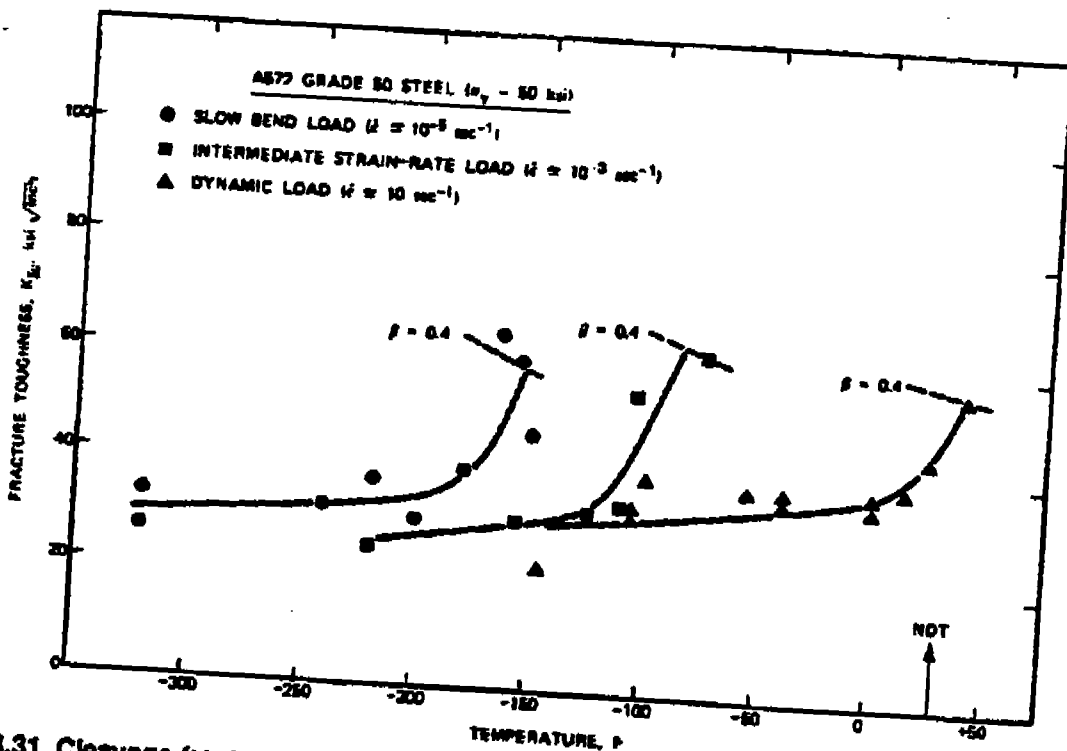


FIG. 3.31 Cleavage fracture toughness at three strain rates for A572 Grade 50 steel (80).

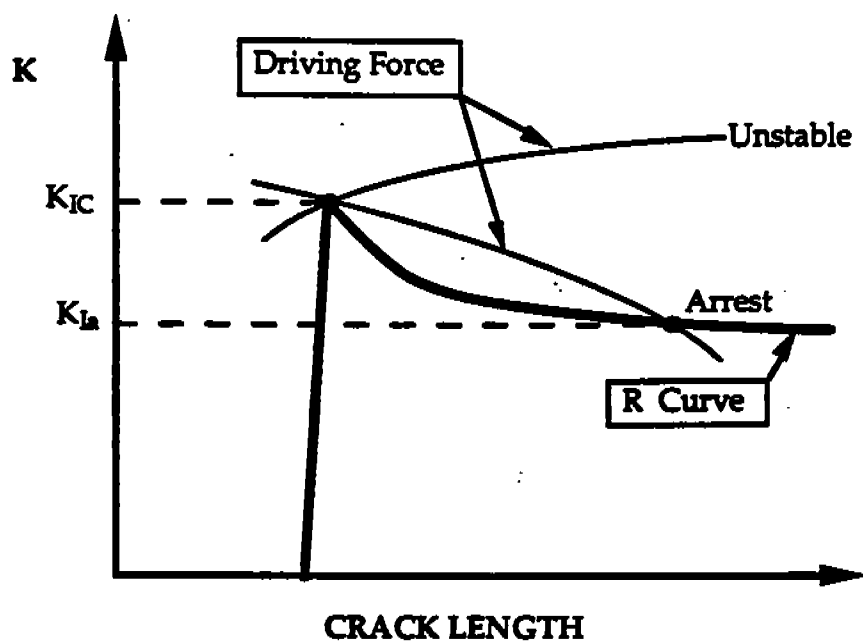


FIG. 3.32 Schematic driving force/resistance curve behavior for cleavage fracture.

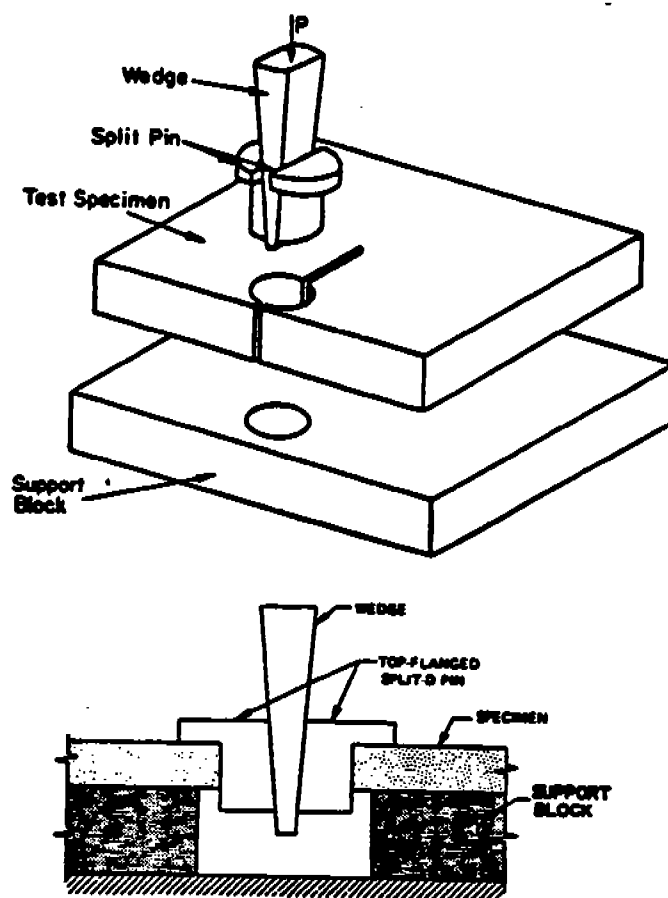


FIG. 3.33 Test specimen and apparatus for K_{Ic} tests according to ASTM E1221-88 (81).

Because several industries, including nuclear power and natural gas, have become increasingly interested in designing structures to arrest rapidly propagating cracks, a standardized method to quantify arrest toughness, K_{Ia} , was needed. In 1988, ASTM published E1221 (81), a standard test method for measuring K_{Ia} . The test method utilizes a compact crack arrest specimen that slightly resembles the ordinary compact fracture toughness specimen. Figure 3.33 illustrates the crack arrest testing procedure. The specimen is laid on its side and a wedge is driven through a hole in the specimen until fracture initiates. This produces nearly pure displacement-controlled loading, which results in a falling driving force curve. The K_{Ia} can be inferred from the final crack length after arrest.

3.7 COMPARISONS BETWEEN J AND CTOD AS TOUGHNESS PARAMETERS

The CTOD approach developed in Great Britain has been applied primarily to welded steel structures in the transition region. One of the major driving forces for CTOD technology was the development of oil reserves in the North Sea. Most of the early work on J integral testing and analysis was funded by the nuclear power industry in the United States. Since typical service temperatures for reactor pressure vessels are well on the upper shelf, where fracture occurs by ductile tearing, most research in J integral technology has focused on upper shelf behavior.

Because of the history of these two toughness parameters, J is normally viewed as a ductile fracture parameter, while CTOD is usually associated with the transition region and weldments. However, there are no sound technical reasons for not using J and CTOD for all types of fracture behavior in steels. Both are equally valid elastic-plastic measures of fracture toughness.

Under small scale yielding conditions, there is a unique relationship between J and CTOD for a given material. Shih (22) derived this relationship (Eq. [2.26]) from the HRR crack tip solution. Thus when the assumptions of the HRR analysis are valid, J and CTOD are equivalent measures of toughness.

When fracture is preceded by large scale yielding, the J-CTOD relationship depends on the geometry of the specimen or structure. Equation [2.26] implies a constant ratio between J and CTOD, but under fully plastic conditions this ratio varies with displacement. Experimental estimates of plastic CTOD are proportional to displacement (Eq. [3.14]); J_{pl} is proportional to the plastic area under the load-displacement curve.

Figures 3.34 and 3.35 show the effect of plastic deformation on the J-CTOD relationship in a center cracked panel and a bend specimen, respectively. Each of these plots compares the small scale yielding solution (d_n) with a fully plastic solution and an elastic plastic finite element solution. The fully plastic J-CTOD relationships (61) were derived from remote loads and displacements, obtained from

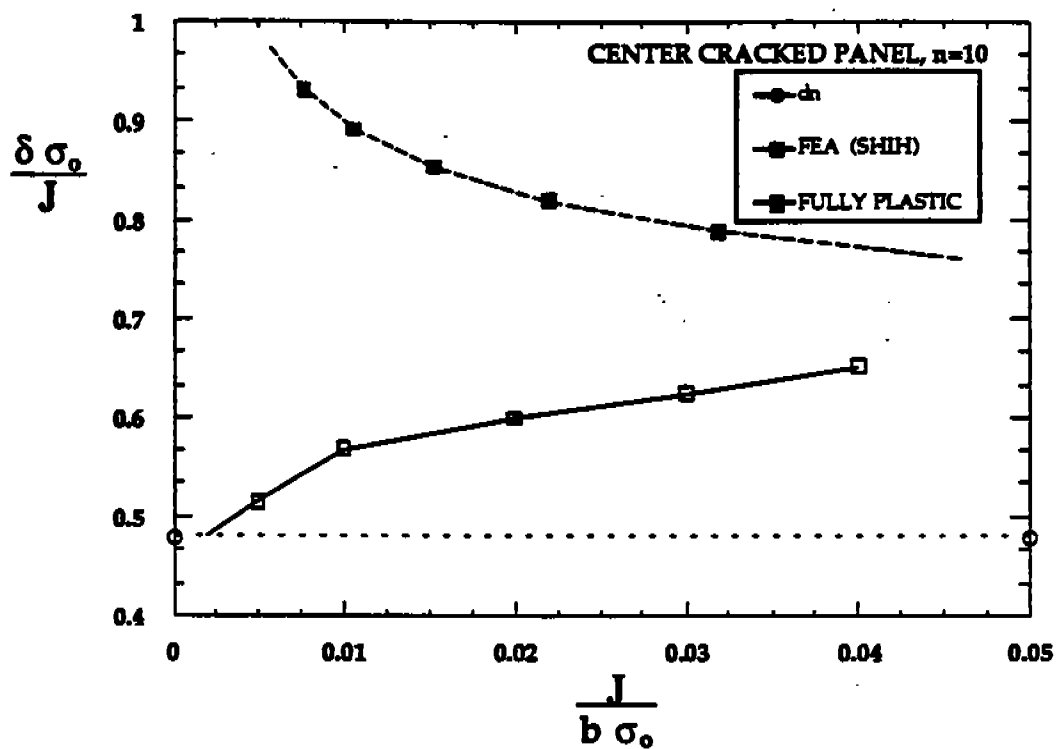


FIG. 3.34 The relationship between J and CTOD for a center cracked panel in plane strain(22,61).

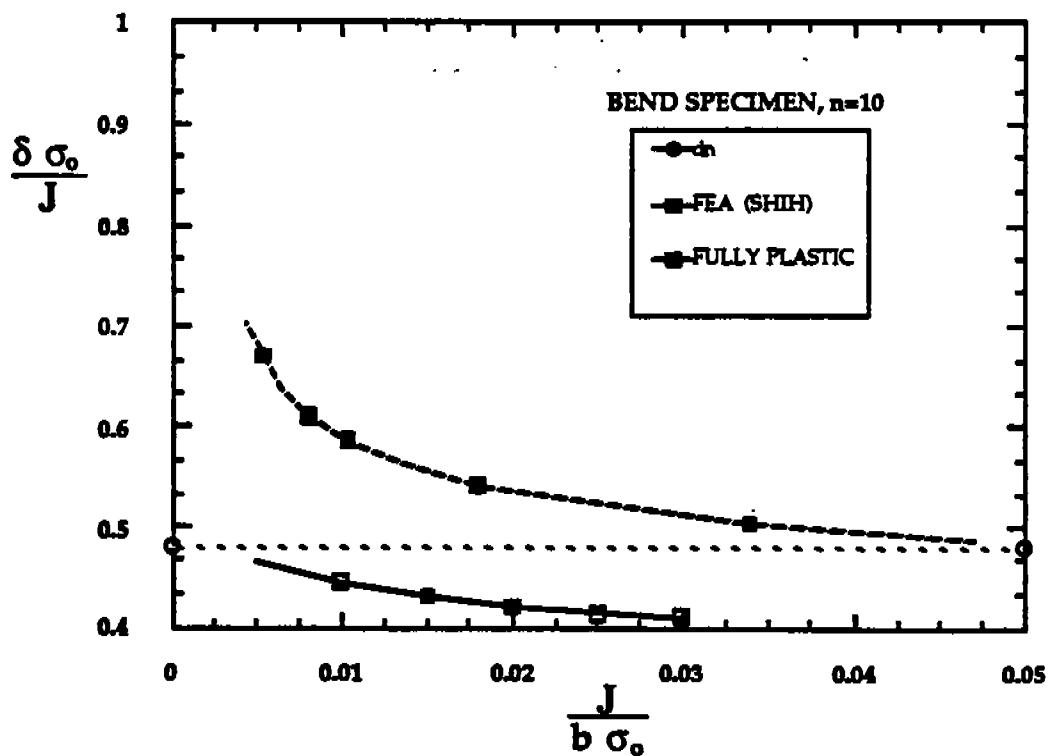


FIG. 3.35 The J -CTOD relationship an SENB specimen in plane strain (22,61).

the Electric Power Research Institute (EPRI) elastic-plastic fracture handbook (82). The elastic-plastic finite element solutions were performed by Shih (22). In the case of the center cracked panel (Fig. 3.34), the elastic-plastic J-CTOD relationship deviates significantly from the small scale yielding value. Note that the finite element solution and the fully plastic estimate tend to converge at high J values. The elastic-plastic J-CTOD relationship for the bend specimen is very close to d_n ; the fully plastic relationship coincides with d_n at moderately high J values. Thus the small scale yielding solution for the J-CTOD relationship is fairly accurate for bend specimens well into the plastic range; the small scale yielding solution does not apply to tensile loading, except at very low J values.

The above observations are consistent with the stress fields for bending and tension (Figs 3.24 and 3.25). The crack tip stresses in bending are close to the HRR solution at high J values, but the center cracked panel cannot maintain sufficient constraint with plastic deformation. A loss of constraint appears to be accompanied by a deviation of the J-CTOD relationship from Eq. [2.26]. Equation [3.27] implies that constraint loss is directly related to the J-CTOD relationship.

Neither J nor CTOD appears to have a clear advantage over the other parameter as a measure of fracture toughness. When the assumptions of the HRR theory are approximately valid, the two parameters are uniquely related, and either can characterize crack tip conditions. When the HRR theory breaks down, neither parameter characterizes crack tip conditions; both critical J and critical CTOD values depend on the configuration of the specimen or structure in such cases. Equation [3.27] and Fig. 3.29 indicate that simultaneous measurement of both parameters may be needed to characterize the critical conditions for fracture in large scale yielding.

3.8 CHARPY-FRACTURE TOUGHNESS RELATIONSHIPS

Fracture toughness testing is a relatively new phenomenon. In many industries, the Charpy V-notch (CVN) test is still the only accepted method for quantifying a material's toughness. Most design codes for welded steel structures do not address fracture mechanics methodology. Typically, these codes specify a minimum CVN energy for the base material and strict flaw tolerances for the welds. Both the CVN and flaw acceptance criteria are usually arbitrary and often very conservative. In some cases, however, fracture control procedures based on CVN toughness can be nonconservative. For example, a large number of steel bridges which were designed with such a procedure have sustained brittle fractures over the last 15 years (83).

Since the Charpy test did not become obsolete with the advent of fracture mechanics, there have been many attempts to correlate CVN toughness measurements with fracture mechanics parameters such as K_{Ic} . The problem with such correlations is that the CVN test is very different from fracture mechanics tests. The Charpy specimen contains a blunt notch, while fracture toughness tests are performed on specimens with sharp fatigue cracks. The Charpy test is performed in impact loading,

but most fracture toughness tests are performed quasistatically. Another difficulty with the Charpy test is that the specimen is small. Recall that fracture mechanics tests must be performed on sufficiently large specimens to guarantee a single parameter description of crack tip conditions. When the specimen is too small, toughness is size dependent; a small specimen may indicate ductile behavior, but a large specimen tested at the same temperature may be brittle.

Most CVN-fracture correlations published to date are empirical. That is, the investigators measured both CVN and K_{IC} , and then curve-fit the results to produce a mathematical relationship between the two parameters. Because of the differences between CVN and fracture mechanics tests, each of these empirical correlations usually works well only for the material originally used to generate the correlation. None of these correlations can be successfully applied to all steels (84).

Recently, some investigators have attempted to develop theoretical relationships between CVN and fracture toughness. These approaches address the differences between the two types of tests.

3.8.1 Empirical Correlations

The various empirical correlations can produce widely differing estimates of K_{IC} when applied to the same CVN data. These approaches differ in three ways:

1. The type of steel from which the correlation was generated
2. The way in which the data were fit; i.e., the form of the equation
3. The fracture behavior analyzed; e.g., transition region or upper shelf.

Some of the more common empirical correlations are summarized below.

Mandaret and Sanz (85) applied a transition temperature approach to data for C-Mn and low alloy steels. They defined the beginning of the transition at 28 J and 100 MPa \sqrt{m} for the CVN and K_{IC} data, respectively. They correlated transition temperature with the following expression.

$$T (K_{IC} 100) = 9 + 1.37 T (CVN_{28}) \quad [3.28]$$

where T is the temperature in °C. Assuming that the K_{IC} and CVN transition curves had a similar shape, they estimated K_{IC} at other temperatures from the following relationship:

$$K_{IC} = 19 \sqrt{CVN} \quad [3.29]$$

where K_{IC} is in MPa \sqrt{m} and CVN is in J. Note that one must apply the temperature shift (Eq. [3.28]) when using the above expression.

Rolfe and Novak (86) developed the following correlations for upper shelf toughness in steels:

$$\left(\frac{K_{IC}}{\sigma_{YS}}\right)^2 = \frac{5}{\sigma_{YS}} \left(CVN - \frac{\sigma_{YS}}{20} \right) \quad [3.30]$$

where K_{IC} is in ksi \sqrt{in} , CVN is in ft-lb, and σ_{YS} is in ksi. The good correlation with Rolfe and Novak's experimental data was attributed to upper shelf fracture not being as sensitive to notch acuity as cleavage. An additional explanation is that upper shelf toughness data are not nearly as scattered as data in the transition region. Pisarski (84) pointed out that much of Rolfe and Novak's data did not meet the K_{IC} size requirements and were therefore not valid.

Rolfe and Barsom (87) developed the following correlation for the transition region.

$$\frac{K_{IC}^2}{E} = 2 (CVN)^{3/2} \quad [3.31]$$

where K_{IC} is in psi \sqrt{in} , CVN is in ft-lb, and E is in psi. The data displayed a considerable degree of scatter about the proposed correlation. The poor correlation is probably due to differences in strain rate and notch acuity. However, even a perfect correlation would not eliminate all data scatter in the transition region because it is an inherent feature of the material.

Barsom (80) attempted to reduce the scatter in CVN-fracture toughness correlations by correcting for dynamic effects. He developed a two step correlation for the transition region. First, he correlated CVN data with dynamic fracture toughness (K_{Id}) tests. He then determined an empirical temperature shift between K_{IC} and K_{Id} data. Figure 3.31 shows some of the data for the latter correlation. Barsom fit K_{Id} and CVN data for a number of steels to the following equation:

$$\frac{K_{Id}^2}{E} = A (CVN) \quad [3.32]$$

where A is a constant. The units on K_{Id} , CVN, and E are the same as in Eq. [3.31]. For standard CVN specimens, A is approximately 5. This constant is approximately 4 if the CVN specimen contains a fatigue precrack. The empirical temperature shift between K_{IC} and K_{Id} data is given by

$$T_{shift} = 215 - \sigma_{YS} \quad (\text{for } \sigma_{YS} \leq 140 \text{ ksi}) \quad [3.33]$$

where temperature is in °F and σ_{ys} is in ksi. Thus one must first estimate a K_{I_d} value at a given temperature from Eq. [3.32], and then apply the temperature shift (Eq. [3.33]) in order to convert this value into a K_{I_C} estimate.

There are several other CVN- K_{I_C} correlations including those by Sailors and Corten (88), Begley and Logsdon (89), and Ito et al. (90). Pisarski (84) reviewed a large number of correlations and applied them to a range of experimental data. He concluded that most correlations work well for high strength steels but tend to be conservative for low and medium strength steels. Wellman and Rolfe (91) also applied several published correlations to data for various steels; the empirical correlations worked well on the lower shelf but were excessively conservative in the transition region. The correlations failed to predict the rapid increase in toughness at the onset of the ductile-brittle transition.

Observations by Pisarski (84) and Wellman and Rolfe (91) imply that the empirical CVN- K_{I_C} correlations apply only to linear elastic behavior, associated with the lower shelf or high strength steels; none work in the elastic-plastic regime.

Dolby (92) attempted to develop an elastic-plastic CVN-fracture toughness correlation for weld metals, relating the 0.1mm CTOD transition temperature to a corresponding CVN transition temperature. He concluded that acceptable correlations could be found only when the materials were sufficiently delineated according to welding process, consumables, etc. No universal CVN-CTOD correlation was found.

3.8.2 Theoretical CVN-Fracture Toughness Relationships

Some investigators have taken a more fundamental approach to CVN-fracture toughness relationships. Norris et al. (93) developed an elastic-plastic, dynamic finite element model of the Charpy test and applied a local ductile failure criterion to both the Charpy specimen and a compact specimen to correlate upper shelf CVN energy with J_{I_C} .

A somewhat similar approach by Anderson and Zapata (94) for the lower shelf and transition region used a statistical model developed by Anderson (43) to quantify the inherent microstructural fracture properties of a given material. This information, in conjunction with Norris' finite element solution for the CVN specimen and sharp crack solutions by Shih and German (70), relates macroscopic fracture properties of CVN and fracture toughness specimens. Since this model is statistical, it predicts not only average toughness, but also any level of lower bound.

Figure 3.36 (94) shows a sample comparison between experimental fracture toughness and toughness predicted from CVN data. The material was a 25 mm thick plate of ABS Grade EH36 steel. Experimental CTOD data are plotted with predicted median and 10% lower bound curves. The agreement between theory and experiment in the transition region is reasonably good, although the predictions are slightly conservative.

Anderson (95) also developed a theoretical relationship for the upper shelf that is different from the Norris approach in attempting to characterize the slope of the R curve rather than J_{IC} . The R curve slope is estimated by considering the tearing resistance of a CVN specimen and relating it to initiation and propagation energy. The resulting expression for the initial R curve slope is as follows:

$$\frac{dJ}{da} = \frac{4 \text{ CVN}}{B b^2} \left(\frac{1}{2f_p} + \frac{1}{(n+1)f_i} \right)^{-1} \quad [3.34]$$

where B and b are the thickness and ligament length in the CVN specimen, respectively; f_p is the fraction of the total energy required for propagation; f_i ($= 1-f_p$) is the initiation fraction; and n is the strain hardening exponent, as defined in Eq. [2.22]. Predictions from Eq. [3.34] are compared in Fig. 3.37 with experimental data from a variety of steels published by Garwood (96). For the predictions in Fig. 3.37, f_p was assumed to be 0.75 and n was assumed to equal 10. The agreement between theory and experiment is very good except for two data points at high CVN energy levels.

The theoretical CVN-fracture toughness relationships for both the upper shelf and the transition region should be investigated further. Although early results are encouraging, additional validation and refinement is needed to make such approaches practical.

One practical use of reliable correlations will be the evaluation of the structural relevance of existing CVN toughness criteria. If more quantitative measures of fracture toughness can be inferred from CVN values, it will be possible to estimate critical flaw sizes and allowable design stresses from the appropriate driving force relationships.

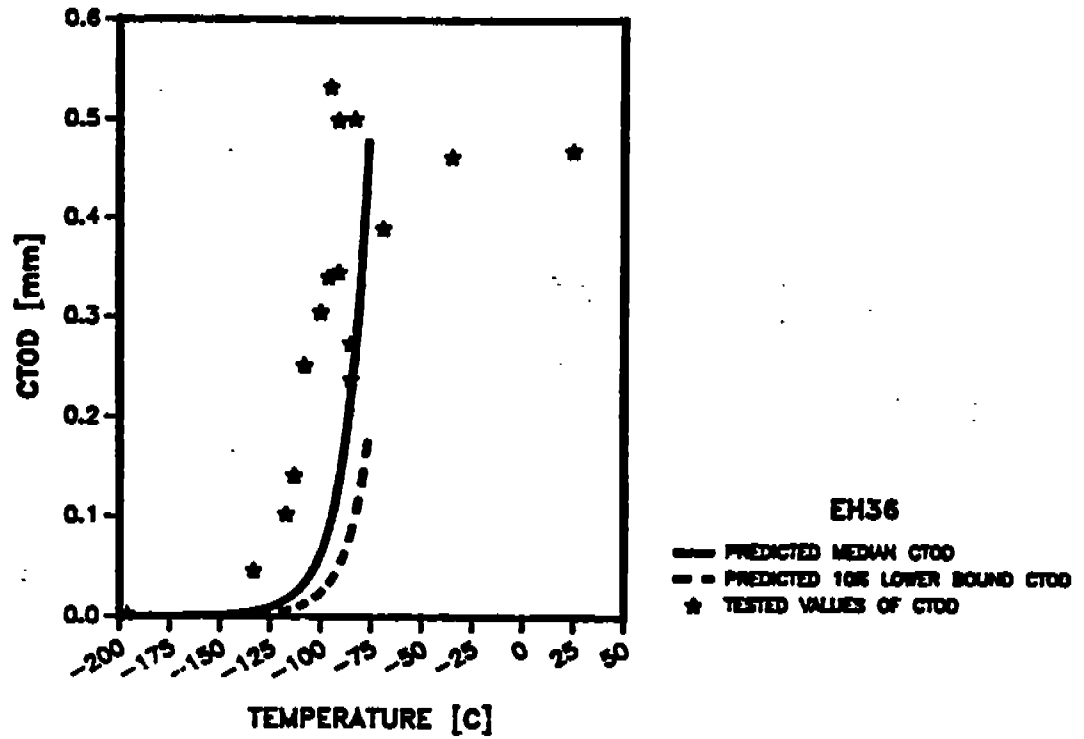


FIG. 3.36 Comparison of experimental CTOD data in the transition region with curves predicted from CVN data (94). The material is a 25 mm thick plate of ABS Grade EH36 steel.

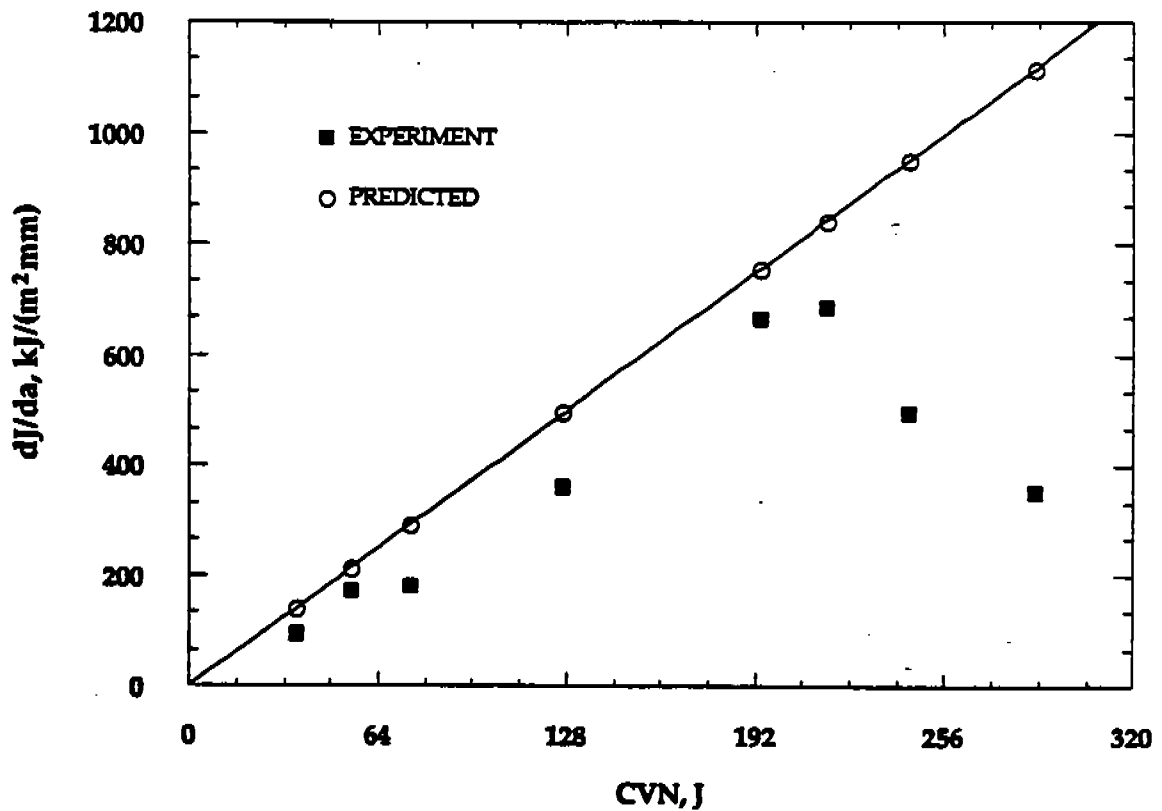


FIG. 3.37 Comparison of predicted and experimental R curve slope for various steels (95).

4. APPLICATION TO STRUCTURES

A crack will grow when the driving force for fracture exceeds the material's resistance to fracture. Chapter 3 addressed the material resistance side of the equation. This chapter focuses on the driving force.

4.1 HISTORICAL BACKGROUND

Fracture mechanics design analyses and driving force equations have evolved considerably over the last 30 years. The first analyses were based on linear elastic theory and applied only to simple configurations such as a center cracked panel. Now there are approaches which take account of most complications which arise in real structures, such as complex shapes, residual stress and large scale plasticity.

4.1.1 Linear Elastic Fracture Mechanics (LEFM)

The LEFM approach to design can be summarized by restating Eq. [2.6]:

$$K_I = Y\sigma \sqrt{\pi a} \quad [4.1]$$

where Y is a geometry correction factor, σ is a characteristic stress, and a is a characteristic crack dimension. The above relationship describes the driving force for fracture. The material fails when $K_I \geq K_{IC}$, the material's resistance to fracture.

Since Irwin (5) and Williams (6) first applied the Westergaard (4) analysis to practical problems in 1957, most of the developments in LEFM have involved the generation of stress intensity solutions (Y) for specific configurations. Most of the early analyses were theoretical or experimental. Today, however, stress intensity solutions are usually determined from finite element analysis.

Several handbooks (8-10) contain compilations of stress intensity factors. The most recent (and most complete) handbook (10) contains K solutions for several hundred configurations. It is now possible to find published K solutions that closely match nearly any practical situation.

A number of variations to the LEFM approach attempt to correct for plasticity, as discussed in Chapter 2. The Irwin plastic zone correction, where crack size is replaced by an effective crack length, extends LEFM to approximately 80% of the yield load (see Fig. 2.9). The Dugdale-Barenblatt strip yield model (12,13) enables an effective K to be computed up to limit load in nonhardening materials.

The development of J integral test methods enables a linear elastic driving force relationship to be applied in situations where it is not possible to measure valid K_{IC} values in laboratory tests. As discussed in Section 2.3.7, the J integral can often characterize the crack tip conditions in a small specimen, even though that specimen contains a large plastic zone. A small specimen and large structure loaded to the same J value experience the same crack tip environment, as illustrated in Fig. 2.18. If the structure is sufficiently large that the global behavior is elastic, the crack tip conditions can be characterized by either J or K. Thus it is possible to estimate the K_{IC} of the large structure from the J_{IC} of the small specimen:

$$K_{IC} = \sqrt{\frac{J_{IC} E}{1-\nu^2}} \quad [4.2]$$

Furthermore, one can use linear elastic driving force relationships (or LEFM with a plastic zone correction) to estimate critical crack size or failure stress in the structure.

4.1.2 The CTOD Design Curve

The CTOD concept was applied to structural steels beginning in the late 1960s. The British Welding Research Institute (now known as The Welding Institute) and other laboratories performed CTOD tests on structural steels and welds. At that time there was no way to apply these results to welded structures because CTOD driving force equations did not exist. Burdekin and Stone (18) developed the CTOD equivalent of the strip yield model in 1966. Although their model provides a basis for a CTOD driving force relationship, they were unable to modify the strip yield model to account for residual stresses and stress concentrations. (These difficulties were later overcome when a strip yield approach became the basis of the R6 design method.)

In 1971, Burdekin and Dawes (97) developed the CTOD design curve, a semi-empirical driving force relationship, that utilized fracture mechanics theory, where available, and relied on empirical correlations and conservative assumptions for circumstances theory did not address. For linear elastic conditions, fracture mechanics theory was reasonably well developed, but the theoretical framework required to estimate the driving force under elastic-plastic and fully plastic conditions did not exist until the late 1970s. Burdekin and Dawes based their elastic-plastic driving force relationship on an empirical correlation between small scale CTOD tests and wide center cracked tension panels made from the same material. The wide plate specimens were loaded to failure, and the failure strain and crack size of a given large scale specimen were correlated with the critical CTOD in the corresponding small scale test.

The correlation that resulted in the CTOD design curve is illustrated schematically in Fig. 4.1. The critical CTOD is nondimensionalized by the half crack length, a , of the wide plate and is shown on the ordinate of the graph. The nondimensional CTOD is plotted against the failure strain in the wide plate, normalized by the elastic yield

strain, ϵ_y . Based on a plot similar to Fig. 4.1, Burdekin and Dawes proposed the following two-part relationship:

$$\Phi = \frac{\delta_{crit}}{2\pi \epsilon_y a} = \left(\frac{\epsilon_f}{\epsilon_y}\right)^2 \quad \text{for } \frac{\epsilon_f}{\epsilon_y} \leq 0.5 \quad [4.3a]$$

and

$$\Phi = \frac{\delta_{crit}}{2\pi \epsilon_y a} = \frac{\epsilon_f}{\epsilon_y} - 0.25 \quad \text{for } \frac{\epsilon_f}{\epsilon_y} > 0.5 \quad [4.3b]$$

where Φ is the nondimensional CTOD. Equation [4.3a], which was derived from LEFM theory, includes a safety factor of 2.0 on crack size. Equation [4.3b] represents an upper envelope of the the experimental data.

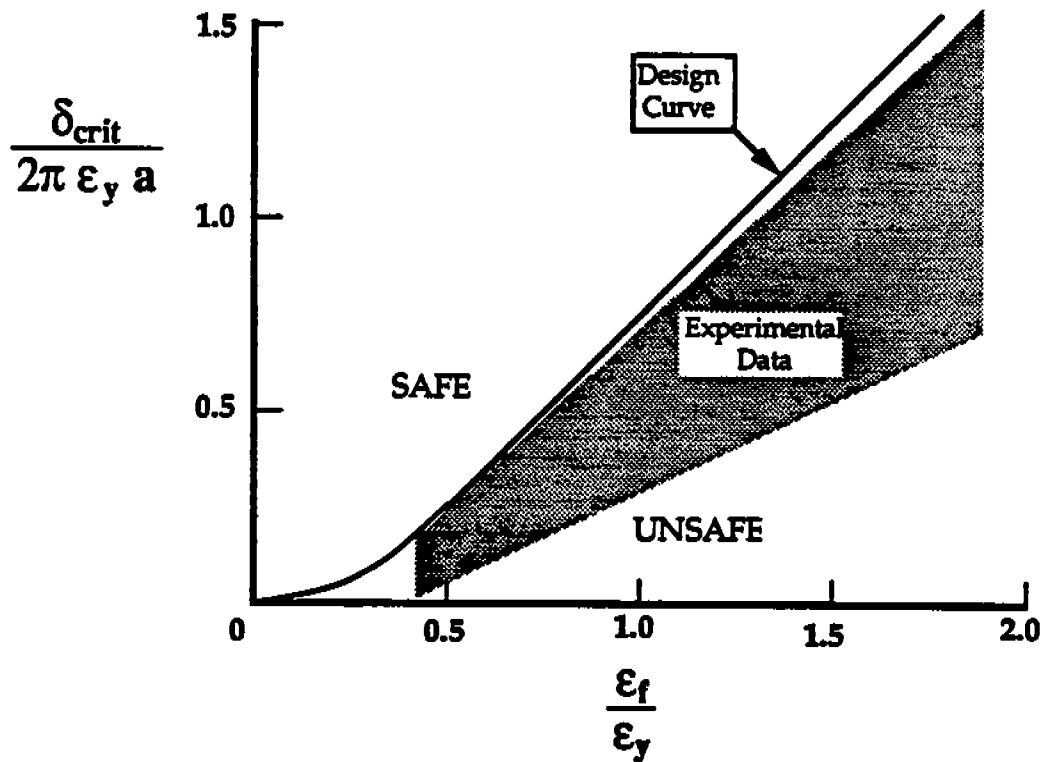


FIG. 4.1 The semi-empirical CTOD design curve.

The applied strain and flaw size in a structure, along with the critical CTOD for the material, can be plotted on Fig. 4.1. If the point lies above the design curve, the structure is considered safe because all observed failures are below the design line. Equations [4.3 a-b] conform to the classical view of a fracture mechanics analysis, in relating stress (or strain in this case) to fracture toughness (δ_{crit}) and flaw size (a). The CTOD design curve is conservative, however, and does not relate *critical* combinations of these variables.

The CTOD design curve approach was modified in the mid 1970s to include stress concentration effects, residual stresses, and flaws other than through thickness. In 1980, this approach was incorporated into the British Standards document PD6493 (98).

The PD6493:1980 approach addresses flaws of various shapes by relating them back to an equivalent through-thickness dimension, \bar{a} . For example, if a structure contains a surface flaw of length l and depth t , the equivalent through-thickness flaw produces the same stress intensity when loaded to the same stress as the structure with the surface flaw. Thus \bar{a} is a generalized measure of a flaw's severity. The CTOD design curve can be applied to any flaw by replacing a with \bar{a} in Eq. [4.3].

The original CTOD design curve was based on correlations with flat plates loaded in tension. Real structures, however, often include complex shapes that result in stress concentrations. In addition the structure may be subject to bending and residual stresses, as well as tensile (membrane) stresses. The PD6493:1980 approach accounts for complex stress distributions simply and conservatively by estimating the maximum total strain in the cross section and assuming that this strain acts through the entire cross section. The maximum strain can be estimated from the following equation:

$$\epsilon_1 = \frac{1}{E} [k_t(P_m + P_b) + Q] \quad [4.4]$$

where k_t is the elastic stress concentration factor, P_m is the primary membrane stress, P_b is the primary bending stress, and Q is the secondary stress, which may include thermal or residual stresses. Since the precise distribution of residual stresses is usually unknown, Q is often assumed to equal the yield strength in an as-welded weldment.

When Burdekin and Dawes developed the CTOD design curve, the CTOD and wide plate data were limited; the curve they constructed lay above all available data. In 1979, Kamath (99) reassessed the design curve approach with additional wide plate and CTOD data generated between 1971 and 1979. His analysis was essentially identical to that eventually adopted in PD6493:1980. In most cases, there were three CTOD tests for a given condition. Kamath used the lowest measured CTOD value to predict failure in the corresponding wide plate specimen. When he plotted the

results in the form of Fig. 4.1, a few data points lay below the design curve, indicating Eq. [4.3] was nonconservative in these instances. The CTOD design curve, however, was conservative in most cases. Kamath estimated the average safety factor on crack size to be 1.9, although individual safety factors ranged from less than 1 to greater than 10. With this much scatter, the concept of a safety factor is of little value. A much more meaningful quantity is the confidence level. Kamath estimated that the CTOD design curve method corresponds to a 97.5% confidence of survival. That is, the method in PD6493:1980 is conservative approximately 97.5% of the time.

4.1.3 The R-6 Failure Assessment Diagram

Structures made from materials with sufficient toughness may not be susceptible to brittle fracture, but they can fail by plastic collapse if they are overloaded. The PD6493:1980 approach does not explicitly address plastic collapse, but implicitly seeks to avoid collapse through an arduous flaw recategorization procedure.

The Central Electricity Generating Board (CEGB) in Great Britain developed a design methodology that takes account of fracture and collapse, as well as the interaction between these two failure mechanisms. The CEGB approach, known as the R-6 method (100), is based on a modified strip yield model due to Heald et al. (101). The R-6 method was first published in 1976, with minor revisions in 1977 and 1980. (A third, more radical revision published recently is discussed in Section 4.2.)

The R-6 method introduced the concept of a failure assessment diagram (FAD) to describe the interaction between fracture and collapse. The modified strip yield model and the failure assessment diagram that form the basis of the early versions of the R-6 procedure are described below.

The effective stress intensity for a through-thickness crack in plane stress, according to the Burdekin and Stone (18) strip yield model, is given by

$$K_{\text{eff}} = \sigma_{YS} \sqrt{\pi a} \left[\frac{8}{\pi^2} \ln \sec \left(\frac{\pi}{2} \frac{\sigma}{\sigma_{YS}} \right) \right]^{1/2} \quad [4.5]$$

which is a restatement of Eq. [2.16]. As shown in Fig. 2.9, the above relationship is asymptotic to the yield strength. This expression can be modified for real structures by replacing σ_{YS} with the collapse stress, σ_c , for the structure. This would ensure that the strip yield model predicts failure as the applied stress approaches the collapse stress. For a structure loaded in tension, collapse occurs when the stress on the net cross section reaches the flow stress of the material. Thus σ_c depends on the tensile properties of the material and the flaw size relative to the total cross section of the structure. The next step in deriving a failure assessment diagram from the strip yield model entails dividing the effective stress intensity by the linear elastic K:

$$\frac{K_{eff}}{K_I} = \frac{\sigma_c}{\sigma} \left[\frac{8}{\pi^2} \ln \sec \left(\frac{\pi \sigma}{2 \sigma_c} \right) \right]^{1/2} \quad [4.6]$$

This modification not only expresses the driving force in a dimensionless form but also eliminates the square root term that contains the the half crack length of the through crack. Thus Eq. [4.6] is more general, in that it applies to all configurations, and not just a through-thickness crack in an infinite plate. This is analogous to the PD6493 approach, where the driving force relationship was generalized by defining an equivalent through thickness flaw, \tilde{a} . As a final step, we can define the stress ratio, S_r , and the K ratio, K_r , as follows:

$$K_r = \frac{K_I}{K_{eff}} \quad [4.7]$$

and

$$S_r = \frac{\sigma}{\sigma_c} \quad [4.8]$$

The failure assessment diagram is then obtained by inserting the above definitions into Eq. [4.5] and taking the reciprocal:

$$K_r = S_r \left[\frac{8}{\pi^2} \ln \sec \left(\frac{\pi}{2} S_r \right) \right]^{-1/2} \quad [4.9]$$

Equation [4.9] is plotted in Fig. 4.2. The curve represents the locus of predicted failure points. Fracture is predicted when $K_{eff} = K_{IC}$. If the toughness is very large, the structure fails by collapse when $S_r = 1.0$. A brittle material will fail when $K_r = 1.0$. In intermediate cases, collapse and fracture interact, and both K_r and S_r are less than 1.0 at failure. All points inside of the FAD are considered safe; points outside of the diagram are unsafe.

In order to assess the significance of a particular flaw in a structure, one must determine the applied values of K_r and S_r and plot the point on Fig. 4.2. The stress intensity ratio for the structure is given by

$$K_r (\text{structure}) = \frac{K_I}{K_{IC}} \quad [4.10]$$

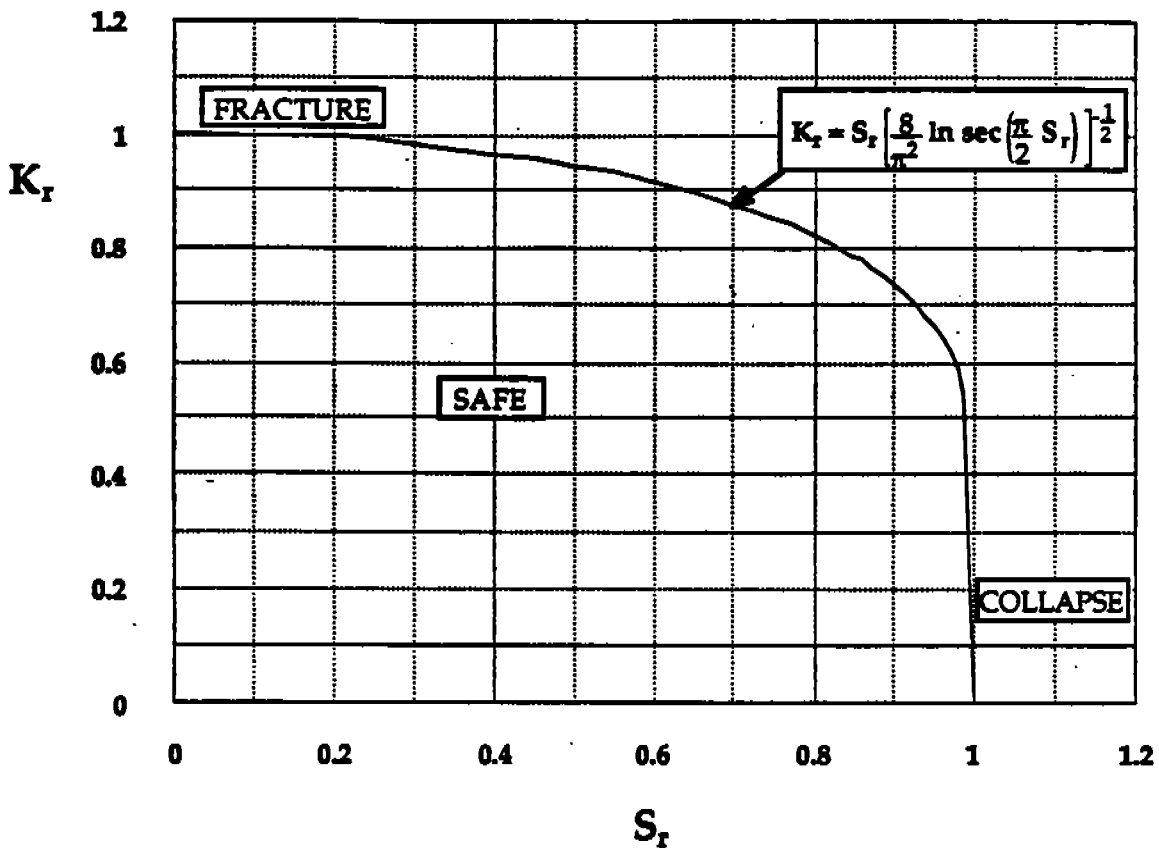


FIG. 4.2 The R-6 failure assessment diagram based on the strip yield model.

The applied stress ratio can be defined as the ratio of the applied stress to the collapse stress. Alternatively, the applied S_r can be defined in terms of axial forces or moments. If the applied conditions in the structure place it inside of the FAD, the structure is safe.

The 1980 R-6 document (100) offers practical advice on how to apply the strip yield FAD to real structures. For example, it recommends that stresses be taken into account through a secondary stress intensity. The total stress intensity is obtained by adding the primary and secondary components:

$$K_I = K_{IP} + K_I^s \quad [4.11]$$

Only the primary stresses are used to compute S_r because secondary stresses, by definition, do not contribute to collapse. Note that K_I is the LEM stress intensity; it does not include a plastic zone correction. Plasticity effects are taken into account through the formulation of the failure assessment diagram (Eq. [4.9]).

The R-6 procedure recommends that the fracture toughness input be obtained through testing the material according to ASTM E399 or the equivalent British

Standard. When it is not possible to obtain a valid K_{IC} value experimentally, one can measure J_{IC} in the material and convert this toughness to an equivalent K_{IC} by means of Eq. [4.2].

4.1.4 The EPRI J Estimation Procedure

The R-6 failure assessment diagram is based on a strip yield model. Since it assumes elastic-perfectly plastic material behavior, it is conservative when applied to strain hardening materials.

In 1976, Shih and Hutchinson (102) proposed a more advanced methodology for computing the fracture driving force which takes account of strain hardening. Their approach, developed further and validated at the General Electric Corporation in Schenectady, New York in the late 1970s and early 1980s, was published as an engineering handbook by the Electric Power Research Institute (EPRI) in 1981 (82).

The EPRI procedure provides a means for computing the applied J integral under elastic-plastic and fully plastic conditions. The elastic and plastic components of J are computed separately and added to obtain the total J:

$$J_{tot} = J_{el} + J_{pl} \quad [4.12]$$

The elastic J is equal to G, the energy release rate. The EPRI handbook states that J_{el} should include a modified first order plastic zone correction, but this correction typically affects the total J by no more than 5% (102). Since this plastic zone correction has no theoretical basis and severely complicates the analysis, many engineers omit the correction on J_{el} .

For the fully plastic J, Shih and Hutchinson assumed a power law stress-plastic strain curve (Eq. [2.22]). The nonlinear elastic assumption on which J integral theory is based implies proportional loading; local stresses must increase in proportion to remotely applied forces and moments. Hence the HRR singularity (Eqs. [2.23] and [2.24]) implies that J_{pl} is proportional to P^{n+1} , where P is a remote load. Shih and Hutchinson invoked proportional loading and dimensional analysis to show that J_{pl} can be expressed in the following form:

$$J_{pl} = \alpha \epsilon_0 \sigma_0 b h_1(a/W, n) \left(\frac{P}{P_0} \right)^{n+1} \quad [4.13]$$

where P_0 is a reference load and h_1 is a dimensionless constant that depends on the configuration and the strain hardening exponent. The terms α , ϵ_0 , and σ_0 are material flow properties, as defined in Eq. [2.22], and b is the uncracked ligament length in the structure or test specimen. Shih and Hutchinson also derived expressions for the plastic crack mouth opening displacement, V_p , and the plastic load line displacement, Δ_p :

$$V_p = \alpha \epsilon_0 a h_2(a/W, n) \left(\frac{P}{P_0} \right)^n \quad [4.14]$$

$$\Delta_p = \alpha \epsilon_0 a h_3(a/W, n) \left(\frac{P}{P_0} \right)^n \quad [4.15]$$

where h_2 and h_3 are dimensionless constants for the corresponding displacement measurements. The EPRI handbook lists h_1 , h_2 and h_3 values for a variety of configurations and strain hardening rates. These constants were determined by finite element analysis.

Figure 4.3 is a plot of applied J in a center cracked panel with $a/W = 0.5$ and $n = 7$. Note that the elastic term dominates at low loads and the plastic term dominates at high loads.

The elastic-plastic driving force estimated from the EPRI procedure can also be expressed in terms of a failure assessment diagram, an idea first proposed by Bloom (103) and Shih et al (104). The J ratio and stress ratio are defined as follows.

$$J_r = \frac{G}{G + J_{pl}} \quad [4.16a]$$

and

$$S_r = \frac{P}{P_0} \quad [4.16b]$$

The equivalent K_r is equal to the square root of J_r .

Figure 4.4 shows the applied J for center cracked panels with $a/W = 0.5$ and 0.75 , plotted in terms of failure assessment diagrams. The R-6 diagram is included for comparison. Note that the shape of the FAD changes when strain hardening is taken into account. The R-6 diagram is conservative in this case because it assumes collapse will occur when the net section stresses equal σ_0 ; a panel made from a strain hardening material could withstand somewhat greater stresses. Figure 4.4 also illustrates that failure assessment diagrams derived from the EPRI procedure are geometry dependent, while the R-6 diagram is geometry independent. This makes fracture analyses with the EPRI approach more complicated, because a different FAD must be generated for each configuration analyzed.

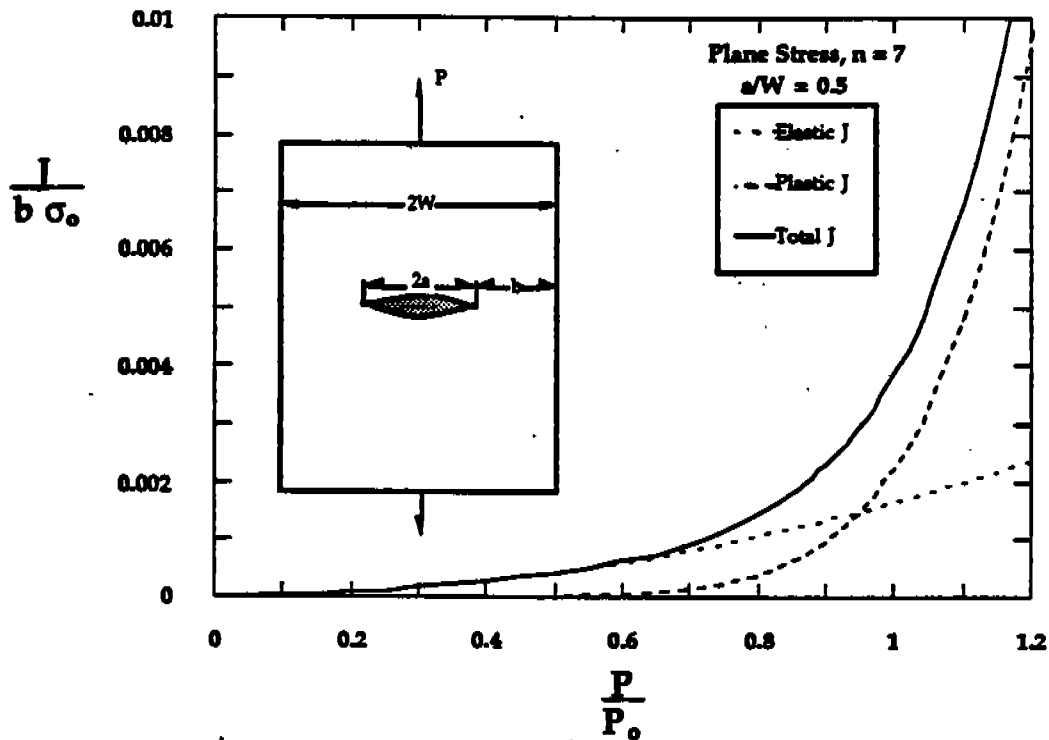


FIG. 4.3 Applied J in a center crack panel, as computed from the EPRI J estimation procedure(82).

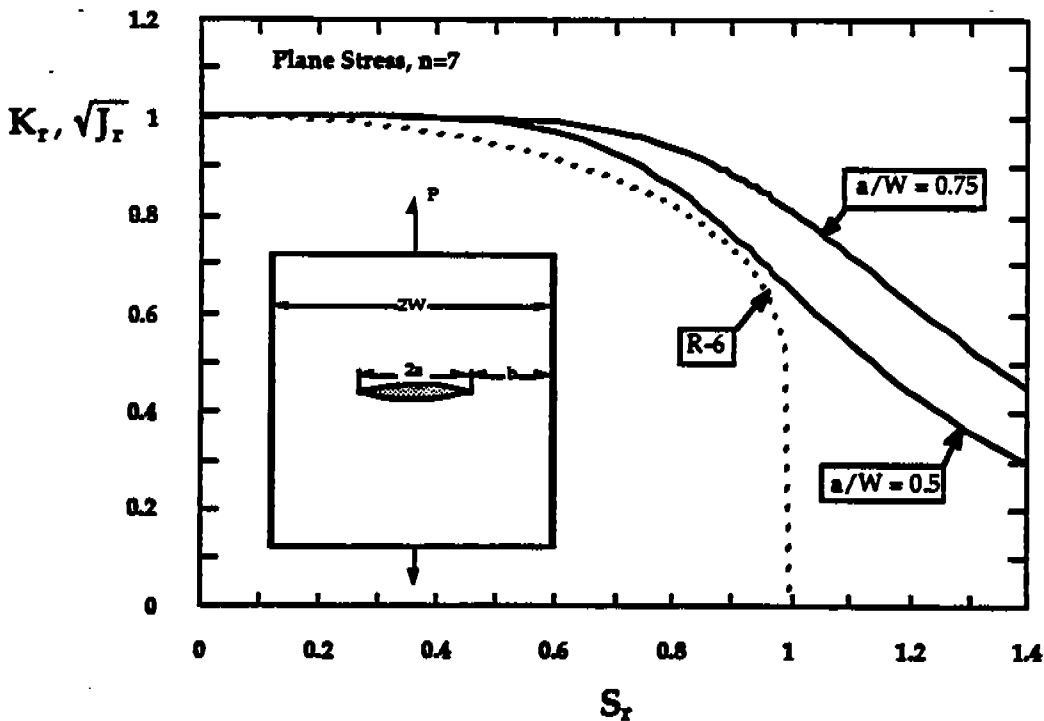


Fig. 4.4 Failure assessment diagrams generated with the EPRI approach(82), compared with the R-6 FAD.

Section 4.1.5 Recent Advances in Elastic-Plastic Analysis

The CTOD design curve was the first elastic-plastic fracture analysis, developed when elastic-plastic fracture mechanics was in its infancy. The theoretical work of Rice and others had not yet filtered down to engineers. Burdekin and Dawes had to rely on empirical correlations and conservative assumptions to develop a comprehensive elastic-plastic fracture design approach. The CEGB R-6 method, which was developed a few years later, was based on an oversimplified theory of crack tip plasticity. The work of Shih and Hutchinson in 1976 was the first sound theoretical framework for analyzing nonlinear fracture in structures. Their work became the basis of the EPRI approach, published in 1981.

One problem with the EPRI procedure has been that it can only be applied to relatively simple configurations. In addition, this method gives no guidance on the treatment of secondary stresses. Recent advances have improved the EPRI approach somewhat; additional configurations have been analyzed (105-107) since the original EPRI report was published, and Bloom (108) has proposed a failure assessment diagram approach that utilizes EPRI J solutions and a secondary stress analysis similar to that of the R6 procedure.

Both the R-6 method and PD6493 have been revised recently to incorporate some of the theoretical work upon which the EPRI handbook is based. These new documents combine the flexibility and wide applicability of previous versions with more sound elastic-plastic driving force analyses.

Recent work by Ainsworth (109) allowed the two British procedures to be updated while retaining their flexibility. Ainsworth's main contribution was to simplify the EPRI approach without sacrificing accuracy. The basis of Ainsworth's reference stress model is described below.

4.2 THE REFERENCE STRESS APPROACH

The EPRI equation for fully plastic J, Eq. [4.13], assumes that the material's stress-plastic strain curve follows a simple power law. Many materials, however, have flow behavior that deviates considerably from a power law. For example, most low carbon steels exhibit a plateau in the flow curve immediately after yielding. Applying Eq. [4.13] to such a material, results in significant errors. Ainsworth (109) modified Eq. [4.13] to reflect more closely the flow behavior of real materials. He defined a reference stress as follows:

$$\sigma_{\text{ref}} = (P/P_0) \sigma_0 \quad [4.17]$$

He further defined the reference strain as the total axial strain when the material is loaded to a uniaxial stress of σ_{ref} . Substituting these definitions into Eq. [4.13] gives

$$J_{pl} = \sigma_{ref} b h_1 \left(\epsilon_{ref} - \frac{\sigma_{ref} \epsilon_0}{\sigma_0} \right) \quad [4.18]$$

For materials that obey a power law, Eq. [4.18] agrees precisely with Eq. [4.13], but Eq. [4.18] is more general, in that it is applicable to all types of stress-strain behavior.

Equation [4.18] still contains h_1 , the geometry factor which depends on the power law hardening exponent n . Ainsworth proposed redefining P_0 for a given configuration to produce another constant, h_1' , that is insensitive to n . He noticed, however, that even without the modification of P_0 , h_1 was relatively insensitive to n except at high n values (low hardening materials). Ainsworth was primarily interested in developing a driving force procedure for high hardening materials such as austenitic stainless steels. The strip yield failure assessment diagram was considered suitable for low hardening materials. He proposed the following approximation.

$$h_1(n) \equiv h_1(1) \quad [4.19]$$

where $h_1(n)$ is the geometry constant for a material with a strain hardening exponent of n and $h_1(1)$ is the corresponding constant for a linear material. By substituting $h_1(1)$ into Eq. [4.18] (or [4.19]), Ainsworth was able to relate the plastic J to the linear elastic stress intensity factor:

$$J_{pl} = \frac{\mu K_I^2}{E} \left(\frac{E \epsilon_{ref}}{\sigma_{ref}} - 1 \right) \quad [4.20]$$

where $\mu = 0.75$ for plane strain and $\mu = 1.0$ for plane stress.

Ainsworth's work has important ramifications. When applying the EPRI approach, one must obtain a stress intensity solution to compute the elastic J , and a separate solution for h_1 in order to compute the plastic term. The h_1 constant is a plastic geometry correction factor. However, Eq. [4.20] makes it possible to estimate J_{pl} from an elastic geometry correction factor. The original EPRI handbook (82) and subsequent additions (105-107) contain h_1 solutions for a relatively small number of configurations; but there are several hundred stress intensity solutions in handbooks and the literature. Thus Eq. [4.20] is not only simpler than Eq. [4.13], but also more widely applicable. The relative accuracy of Ainsworth's simplified equation is examined in Section 4.4.

Ainsworth made additional simplifications and modifications to the reference stress model in order to express it in terms of a failure assessment diagram. This FAD has been incorporated into a revision of the R-6 procedure. The new document also contains more accurate procedures for analyzing secondary stresses. The revised R-6 approach still permits application of the strip yield FAD to low hardening materials.

The reference stress FAD has also been included in the revised PD6493 procedure, to be published in late 1989 or early 1990. This approach, described below, is broadly similar to the revised R-6 method.

4.3 THE THREE-TIER APPROACH (REVISED PD6493)

The CTOD design curve, which is the basis of PD6493:1980, suffers from a number of shortcomings. For example, the driving force equation is mostly empirical and has a variable level of conservatism. In addition, this approach does not explicitly consider failure by plastic collapse. Improved driving force equations became available with the R-6 and EPRI procedures, but the CTOD design curve had already been widely accepted by the welding fabrication industry in the United Kingdom and elsewhere. Many engineers are reluctant to discard PD6493:1980. Structures designed according to the original PD6493 method might have to be re-analyzed with the new procedure if the CTOD design curve were rendered obsolete. An additional problem with improving the procedure the tendency for the more accurate elastic-plastic fracture analyses to be more complex and require more training.

The conflicting goals of improving PD6493 and maintaining continuity with the past have been largely satisfied by a three-tier approach. This idea was originally suggested by Anderson et al. (110). The three tier philosophy assesses fracture problems at a level of complexity and accuracy appropriate for the situation. All three levels of PD 6493 are expressed as failure assessment diagrams. Level 1 is consistent with the CTOD design curve approach; Level 2 utilizes a strip yield model and is similar to the 1980 version of the R-6 method; Level 3 is based on the reference stress model and is nearly identical to the revised R-6 procedure. Unlike the R-6 approach, however, the revised PD 6493 permits assessments based on CTOD as well as J and K.

Although the new PD6493 procedure has not been published, a number of recent articles (111, 112) describe its salient features. Information in the following subsections is based on these articles.

4.3.1 Level 1

Level 1 is consistent with the CTOD design curve in the 1980 version of PD6493. The main differences are that the equations are expressed in terms of a failure assessment diagram, and an explicit collapse analysis is included. Level 1, which is conservative, is intended as a screening tool.

If K_{IC} data are used (or equivalent K values from J data), the K ratio is defined by Eq. [4.10]. For CTOD data, K_r is replaced by $\sqrt{\delta_r}$, defined as

$$\sqrt{\delta_r} = \sqrt{\frac{\delta_I}{\delta_{crit}}} \quad [4.21]$$

where δ_I is the applied CTOD obtained from a modified form of the CTOD design curve:

$$\delta_I = \frac{K_I^2}{\sigma_{YS} E} \quad \text{for } \sigma_1/\sigma_{YS} \leq 0.5 \quad [4.22a]$$

where $\sigma_1/E = \epsilon_1$, the maximum membrane strain defined in Eq. [4.3]. Recall that ϵ_1 (and thus σ_1) takes residual stresses, bending stresses, and stress concentrations into account by assuming that the maximum value of the total stress acts uniformly through the cross section. Unlike Eq. [4.2a], the above expression does not include a safety factor of two on crack size. In the revised approach, this safety factor is included in the formulation of the FAD, which is a horizontal line at $\sqrt{\delta_r} = 1/\sqrt{2}$ for $\sigma_1/\sigma_{YS} \leq 0.5$. The Level 1 failure assessment diagram is illustrated in Fig. 4.5 (111, 112). For higher stress levels, the assessment line is defined from the empirical portion of the CTOD design curve:

$$\delta_I = \frac{K_I^2}{\sigma_{YS} E} \left(\frac{\sigma_{YS}}{\sigma_1} \right)^2 \left(\frac{\sigma_1}{\sigma_{YS}} - 0.25 \right) \quad \text{for } \sigma_1/\sigma_{YS} > 0.5 \quad [4.22b]$$

The influence of Equation [4.22b] on the FAD is illustrated in Fig. 4.5. The revised CTOD design curve contains a conservative collapse check in the form of a maximum stress ratio, S_r . For Level 1, S_r is defined as

$$S_r = \frac{\sigma_n}{\sigma_{flow}} \quad [4.23]$$

where σ_n is the effective primary net section stress and σ_{flow} is the flow stress, defined as $(\sigma_{YS} + \sigma_{TS})/2$ or $1.2 \sigma_{YS}$, whichever is less. As Fig. 4.5 indicates, the Level 1 approach is restricted to $0.8 S_r$ because Eq. [4.22] can be nonconservative near limit load (110).

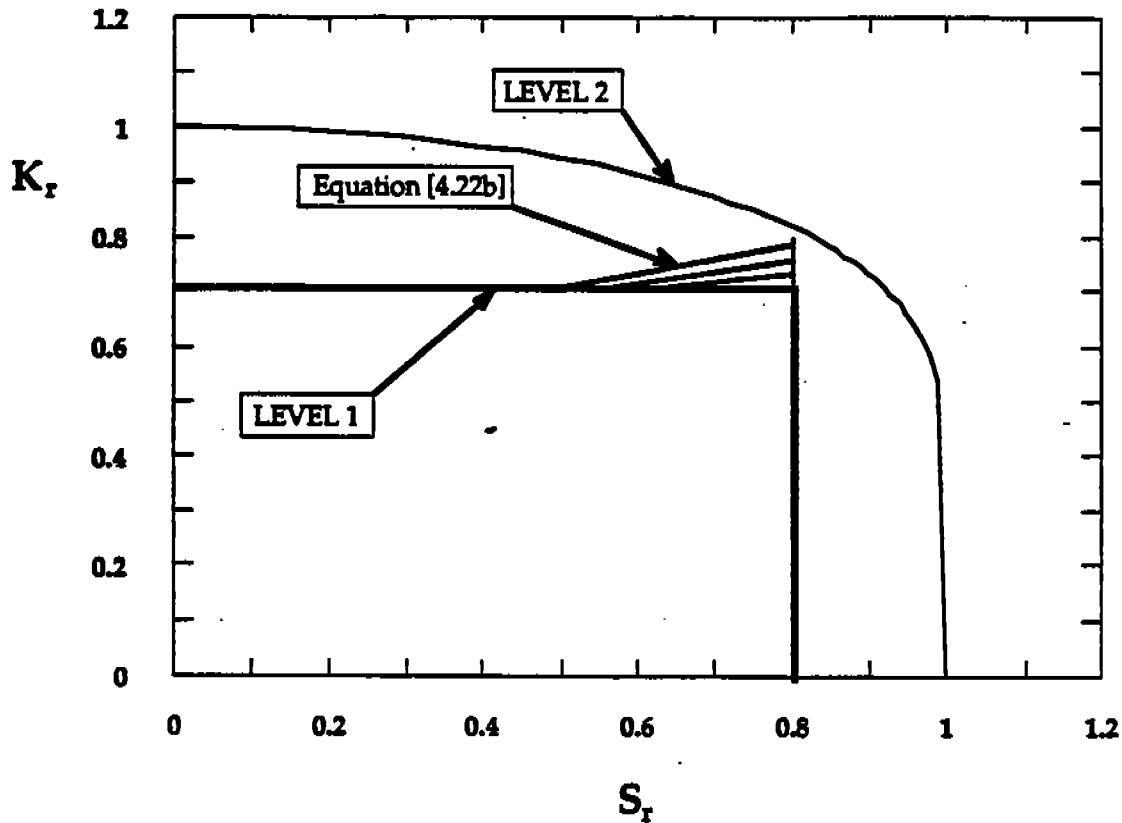


FIG. 4.5 The failure assessment diagrams for Levels 1 and 2 of PD6493(111,112).

4.3.2 Level 2

Level utilizes a strip yield failure assessment diagram. The assessment equation is identical to the original R-6 relationship (Eq. [4.8]), except that it allows CTOD based analyses:

$$K_r, \sqrt{\delta_r} = S_r \left[\frac{8}{\pi^2} \ln \sec \left(\frac{\pi}{2} S_r \right) \right]^{-\frac{1}{2}} \quad [4.24]$$

Figure 4.5 compares the Level 1 and Level 2 failure assessment diagrams. Note that the Level 1 FAD is always conservative compared to the Level 2 method.

The treatment of stress concentration effects and secondary stresses is more complex in the upper two levels. The procedure recommends that accurate stress intensity solutions be obtained for the actual primary and secondary stress distributions. If this is not feasible, an approximate solution can be obtained by linearizing the stress distribution and separating the stresses into bending and membrane components. For example, consider a surface crack of depth a . If the primary and secondary stresses are resolved into bending and membrane components, the approximate stress intensity factors are computed from the following expressions:

$$K_I^P = \frac{\sqrt{\pi a}}{\phi} (M_m P_m + M_b P_b) \quad [4.25a]$$

$$K_I^S = \frac{\sqrt{\pi a}}{\phi} (M_m Q_m + M_b Q_b) \quad [4.25b]$$

where ϕ is the flaw shape parameter, P_m and P_b are the primary membrane and bending stresses, Q_m and Q_b are the secondary stresses, and M_m and M_b are constants obtained from the Newman and Raju stress intensity solutions (113). If, as in many cases, the actual distribution of secondary stresses is unknown, one should assume that Q acts uniformly across the section. The document recommends that Q be assumed to equal the material's yield strength in the case of as-welded components. For thoroughly stress relieved weldments, the estimate of Q can be reduced to 30% of yield parallel to the weld and 15% of yield transverse to the weld.

The total K_I is the sum of the primary and secondary contributions. For assessments based on CTOD, δ_I is estimated from K_I by assuming plane stress conditions:

$$\delta_I = \frac{K_I^2}{\sigma_{YS} E} \quad [4.26]$$

There is a plastic interaction between primary and secondary interaction that must be taken into account in Level 2. This is achieved with the correction factor, ρ , based on the work of Ainsworth (114). The applied toughness ratios for the structure are given by

$$K_r = \frac{K_I}{K_{crit}} + \rho \quad [4.27]$$

and

$$\sqrt{\delta_r} = \sqrt{\frac{\delta_I}{\delta_{crit}}} + \rho \quad [4.28]$$

The value of the ρ factor decreases as the limit load is approached because secondary stresses are relieved by plastic strain. When a structure is proof tested, a portion of the residual stresses are relieved. The revised PD6493 approach lets the user incorporate the benefits of proof testing into the analysis.

The stress ratio, S_r , is defined as the ratio of the effective net section stress to the flow stress, as in Level 1. When the point defined by Eqs [4.23], [4.27] and [4.28] falls inside of the Level 2 assessment line (Eq. [4.24]), the structure is considered safe.

4.3.3 Level 3

The Level 3 failure assessment diagram is based on Ainsworth's reference stress approach (109). The FAD is related to the material's stress-strain behavior:

$$K_r, \sqrt{\delta_r} = \left(\frac{E \ln(1 + \epsilon_{ref})}{\sigma_{ref}(1 + \epsilon_{ref})} + \frac{\sigma_{ref}^3 (1 + \epsilon_{ref})^3}{2 \sigma_{YS}^2 E \ln(1 + \epsilon_{ref})} \right)^{-1/2} \quad [4.29]$$

The above quantity is plotted against the load ratio, L_r , defined as

$$L_r = \frac{\sigma_{ref}}{\sigma_{YS}} = \frac{\sigma_n}{\sigma_{YS}} \quad [4.30]$$

Note that the reference stress and the effective net section stress are equivalent. Since the load ratio is defined in terms of the yield strength rather than the flow stress, L_r can be greater than 1. The load ratio cannot exceed $\sigma_{flow}/\sigma_{YS}$, where σ_{flow} is defined as the average between yield and tensile strengths. For Level 3, the alternate definition of flow stress ($\sigma_{flow} = 1.2 \sigma_{YS}$) does not apply. For $L_r > \sigma_{flow}/\sigma_{YS}$, $K_r = 0$.

If the stress-strain curve for the material is not available, such as would be the case when analyzing a flaw in the heat affected zone, the following FAD equation can be applied at Level 3:

$$K_r, \sqrt{\delta_r} = (1 - 0.14 L_r^2) \left[0.3 + 0.7 \exp(-0.65 L_r^6) \right] \quad [4.31]$$

This expression also has a cut-off at $L_r = \sigma_{flow}/\sigma_{YS}$. Equation [4.31] was adopted from the latest version of the R-6 procedure (115). This alternate FAD requires a knowledge of only the yield and tensile strengths of the material, but this relationship can be excessively conservative (112). For many materials, Eq. [4.31] is more conservative than the Level 2 FAD. Figure 4.6 is a plot of Eq. [4.31]. Note that the upper cut-off on L_r depends on the hardening characteristics of the material. If the material has a yield plateau, the revised PD6493 recommends that Eq. [4.31] be restricted to $L_r \leq 1$.

The Level 3 analysis of K_r (or $\sqrt{\delta_r}$) for the structure is identical to the Level 2 procedures (Eqs. [4.26] - [4.28]), but Level 3 includes guidelines for ductile instability and tearing analysis. This type of analysis is described in Section 4.5.

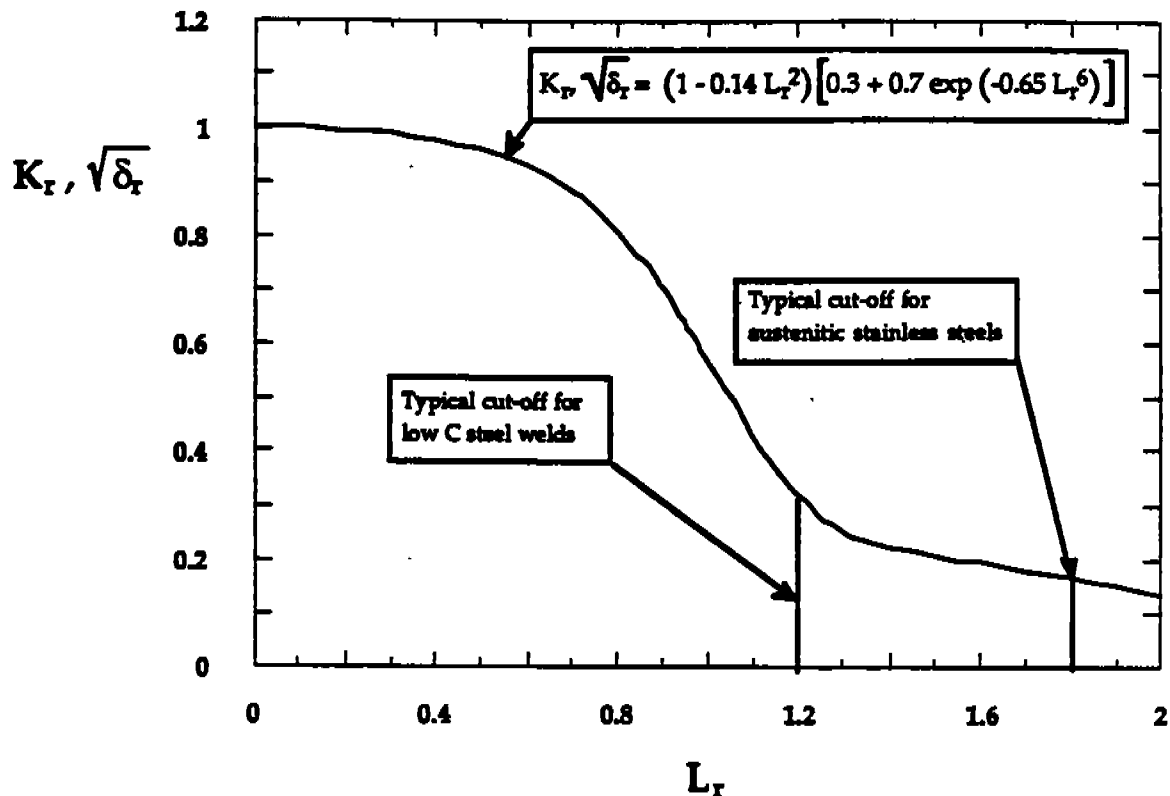


FIG 4.6 Alternate Level 3 failure assessment diagram for PD6493 (106).

4.4 COMPARISON OF DRIVING FORCE EQUATIONS: A PARAMETRIC STUDY

The primary advantage of Ainsworth's reference stress approach is in accounting for the geometry of a cracked structure through a linear elastic stress intensity solution. The h_1 factor is replaced by an LEFM geometry factor. The other contribution of Ainsworth's analysis, the generalization to stress-strain laws other than power-law, is of secondary importance.

In most cases, the EPRI procedure and Ainsworth's simplified approach produce nearly identical estimates of critical flaw size and failure stress. This section presents the results of a parametric study of the accuracy of Ainsworth's approach relative to that of the EPRI procedure. The relative accuracy of the strip yield model was also evaluated. A power law hardening material was assumed for all analyses, since the main purpose of this exercise was to evaluate the errors associated with the LEFM geometry correction factor in the elastic-plastic regime.

For a power-law material, the Ainsworth model gives the following expression for the total J :

$$J = \frac{K_I^2}{E} \left[(1-\nu^2) + \alpha \mu \left(\frac{P}{P_0} \right)^{n-1} \right] \quad [4.32]$$

Since stress intensity is proportional to load, this relationship has the form

$$J = C_1 P^2 + C_2 P^{n+1}$$

The first term dominates under linear elastic conditions; the second term dominates under fully plastic conditions. The EPRI approach (Eqs. [4.12] and [4.14]) has the same form. The only difference between the EPRI equation and Eq. [4.32] is the value of the constant C_2 ; the equations agree precisely in the linear elastic range. Thus any discrepancies between the two approaches are observed only when the plastic term is significant.

When the plastic term dominates, J is very sensitive to the applied load. A small error in the estimate of P results in a large error in the estimate of J , but this sensitivity be an advantage when predicting failure. Since J is very sensitive to load, P is very *insensitive* to J , implying that the failure load in the plastic range is insensitive to the fracture toughness; i.e. the critical J . In the fully plastic range, failure is essentially collapse controlled rather than fracture controlled, as seen clearly in the failure assessment diagram in Fig. 4.2. As the stress ratio approaches unity, the diagram becomes nearly vertical, indicating that the failure stress is independent of the toughness ratio. At these high stress ratios, the failure stress is governed by the material's flow properties rather than its fracture toughness.

The predicted failure stress in the fully plastic range is also insensitive to the differences between the EPRI approach and the Ainsworth model. The latter approach assumes that the geometry factor, $h_1(n)$, is equal to the linear elastic value, $h_1(1)$. Errors in J that result from applying Eq. [4.32] are proportional to the ratio $h_1(n)/h_1(1)$, plotted against n in Fig. 4.7 for a center cracked panel in plane strain with $a/W = 0.75$. Note that the h_1 ratio in this configuration is sensitive to the hardening exponent. Thus Eq. [4.32] leads to significant errors in J , particularly at high n values. However, when the h_1 ratio is raised to the power $1/(n+1)$, it is insensitive to n . This latter ratio is indicative of the differences in the predicted failure stress between the Ainsworth and EPRI approaches.

A design engineer often wishes to use a fracture mechanics analysis to estimate the critical flaw size at a given applied stress. To determine the sensitivity of critical flaw size estimates to the driving force equation, a series of calculations were performed with the EPRI, Ainsworth, and strip yield models on center cracked panels and edge cracked bend specimens. Hardening exponents of 5, 10 and 20 were assumed. Only plane strain conditions were considered.

The material was assumed to follow perfectly the power law expression (Eq. [2.22]) for stress versus plastic strain. The constants α and ϵ_0 were fixed 1.0 and 0.002, respectively, for all n values; thus σ_0 corresponds exactly to the 0.2% offset yield strength.

Two separate strip yield analyses were performed for each case: one assumed that the collapse stress was equal to the yield strength; the other based collapse on the flow stress, defined as the average of yield and tensile strengths. For a material whose true stress-true strain curve follows a power law, the flow stress can be estimated from the following expression:

$$\sigma_{\text{flow}} = \frac{\sigma_{\text{YS}}}{2} \left[1 + \frac{\left(\frac{N}{0.002} \right)^N}{\exp(N)} \right] \quad [4.33]$$

where $N = 1/n$.

The results of the analysis of the center cracked tension panel are plotted in Figs. 4.8 to 4.13. Critical crack size, normalized by W , is plotted against critical J , normalized by width and yield strength. Figures 4.8 to 4.10 compare the EPRI, Ainsworth, and strip yield equations for a constant nominal stress equal to $2/3$ yield. At low toughness levels, all predictions agree because linear elastic conditions prevail. At high toughness levels, the curves are relatively flat, indicating that critical crack size is insensitive to toughness. In this region, failure is controlled primarily by plastic collapse of the remaining cross section. The EPRI and Ainsworth equations agree well at all hardening rates.

The strip yield model is nonconservative for the high hardening material (Fig. 4.8) when it is based on the flow stress. For this material, the flow stress, as estimated from Eq. [4.33], was $1.53 \sigma_{\text{YS}}$, but PD6493 restricts the flow stress to 1.2 times yield in Level 2 assessments. Thus the nonconservatism observed in Fig. 4.8 would not occur with the restrictions in PD6493. For $n = 10$ and $n = 20$, the estimated flow stress was 1.17 and 1.06 times yield, respectively. In both cases (Figs. 4.9 and 4.10), the strip yield model, when based on flow stress, produces good estimates of critical crack size. When the strip yield model utilizes the yield strength, it is always conservative.

Figures 4.11 to 4.13 compare the EPRI and Ainsworth approaches at various stress levels. In all cases, the agreement between the two approaches is very good. The Ainsworth model tends to be slightly conservative for the center cracked configuration.

The bend specimen results are presented in Figs. 4.14 to 4.19. In Figs. 4.14 to 4.16, the load is fixed at 50% of P_u , the limit load of an unnotched plate in plane strain. The load is varied in Figs 4.17 to 4.19. The bend results are similar to the center cracked panel. The strip yield model works best for low and moderate hardening materials.

In addition, the EPRI and Ainsworth analyses agree well in most cases, but the Ainsworth model appears to be slightly nonconservative for the high hardening material (Figs. 4.14 and 4.17), especially at high stresses.

These analyses indicate that the Ainsworth model can predict either critical crack size or failure stress in the elastic, elastic-plastic, and fully plastic regimes. The strip yield model gives reasonable results, provided the flow stress is restricted to 1.2 times yield.

Predictions of applied J in the fully plastic regime can vary widely for the three approaches analyzed. Initially one might conclude that the EPRI model always gives the best predictions of J because it is based on the most sound theory. This is not necessarily the case, however. Because the plastic component of J is very sensitive to load, a slight variation in flow properties leads to major variations in J_p at a fixed load. The yield strength is proportional to P_0 , which is raised to a power of $n+1$ in both the EPRI and Ainsworth equations. Thus errors in J resulting from the Ainsworth approximation may lie within the scatter band of errors resulting from variations in material flow properties. The more complex EPRI formulation may lead to no more accurate predictions than the simpler approaches.

Figure 4.20 illustrates the effect of varying flow properties on predictions with the EPRI approach. A 10% overestimate or underestimate of σ_0 for the material leads to approximately a 10% error in the prediction of a_{crit} in the plastic regime. Such an uncertainty in flow properties corresponds to a 260% uncertainty in the applied J when $n=10$. Since flow properties typically vary by several percent within a given plate and as much as 20% between heats, accurate predictions of the applied J in a structure in the plastic regime appear to be impossible.

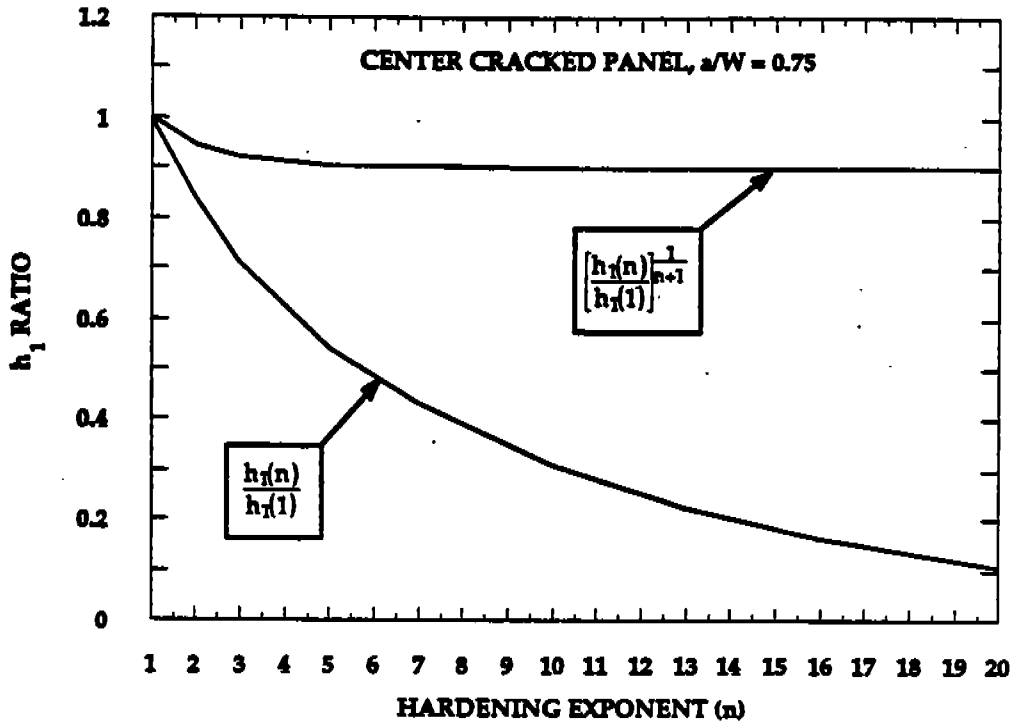


FIG 4.7 The effect of strain hardening exponent on the h_1 factor in a center cracked panel in plane strain with $a/W = 0.75$.

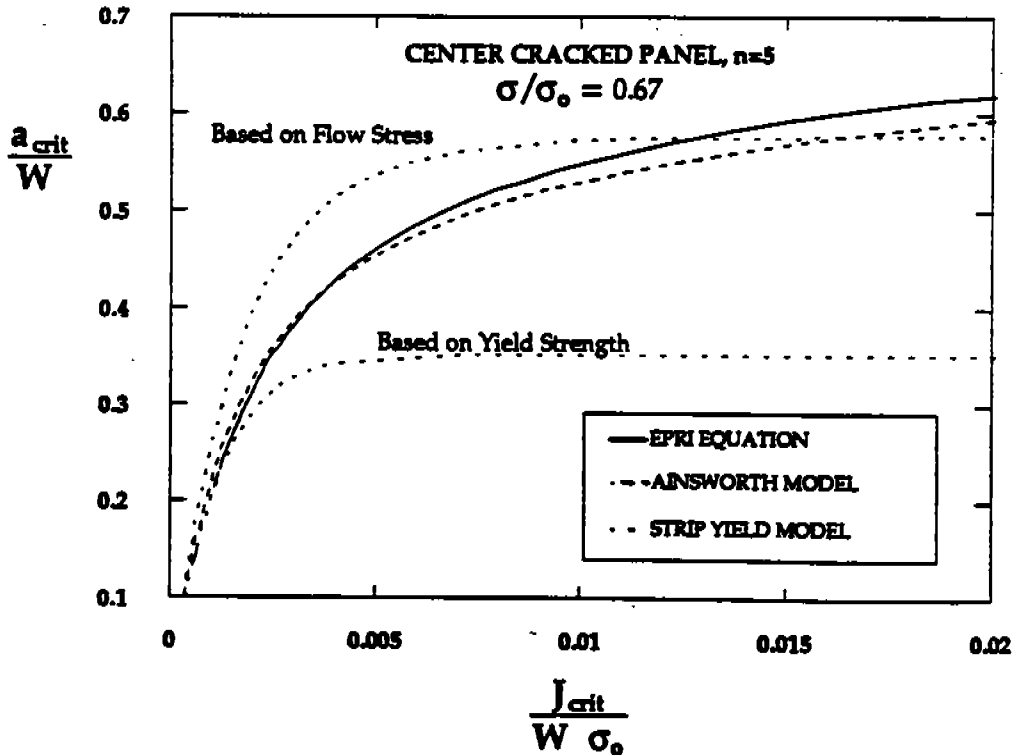


FIG. 4.8 The effect of fracture toughness on critical crack size in a center cracked panel with $n=5$ and nominal stress equal to 0.67 times yield.

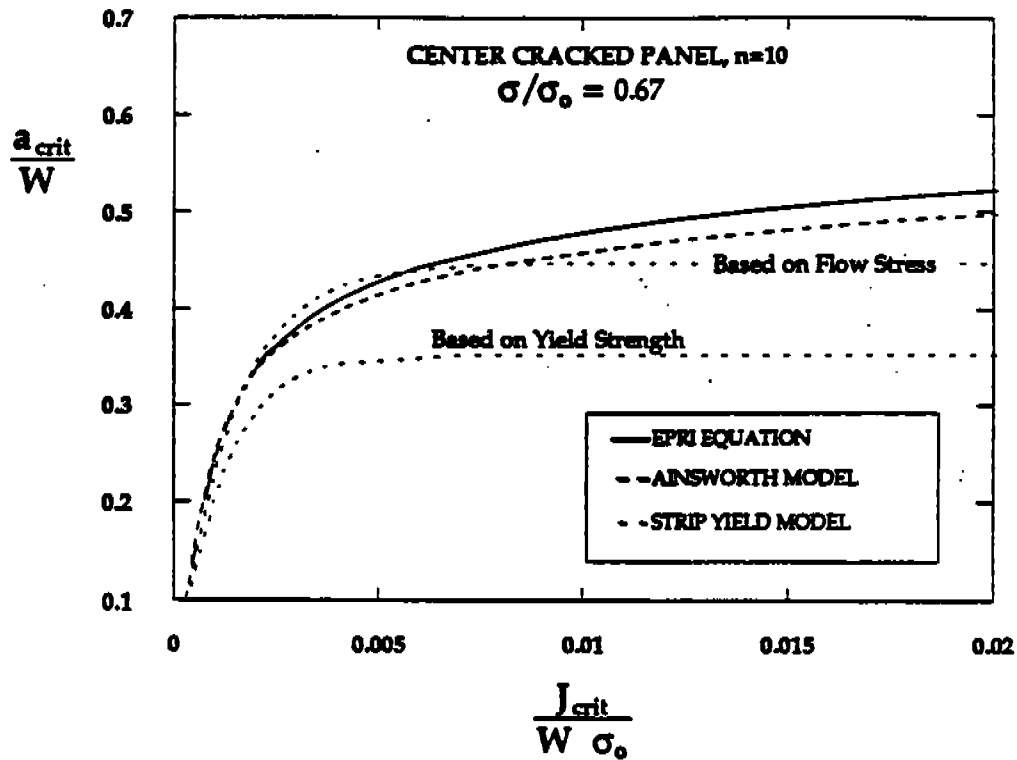


FIG. 4.9 The effect of fracture toughness on critical crack size in a center cracked panel with $n = 10$ and nominal stress equal to 0.67 times yield.

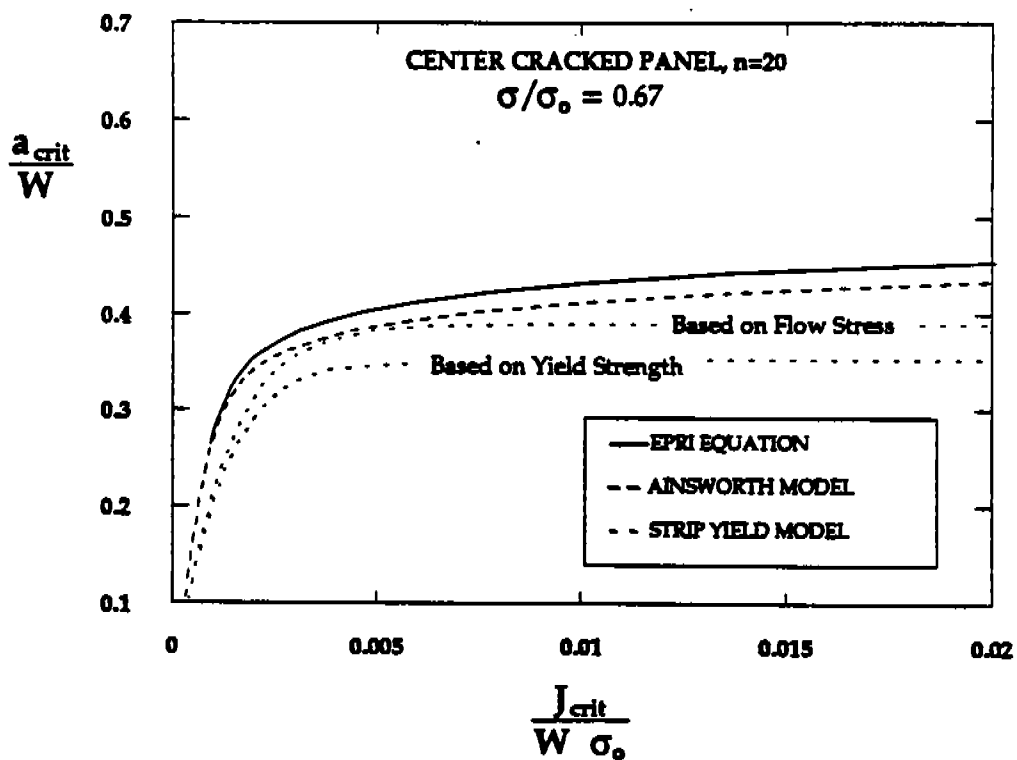


FIG. 4.10 The effect of fracture toughness on critical crack size in a center cracked panel with $n = 20$ and nominal stress equal to 0.67 times yield.

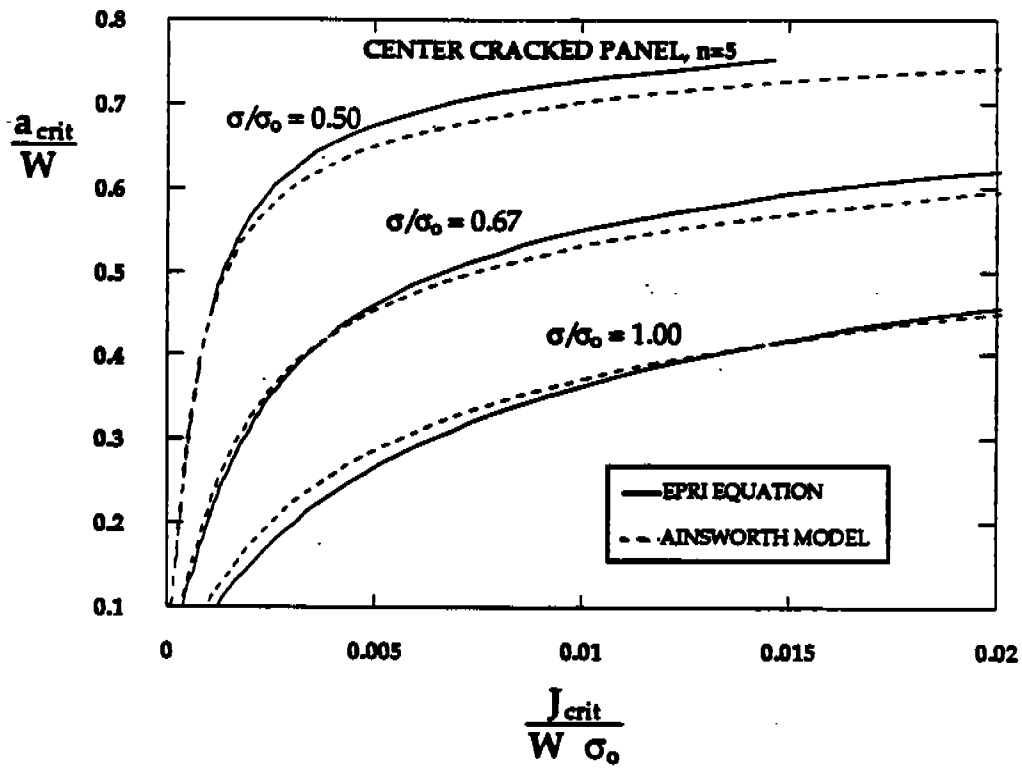


FIG. 4.11 The effect of fracture toughness on critical crack size in a center cracked panel with $n=5$ at various stress levels.

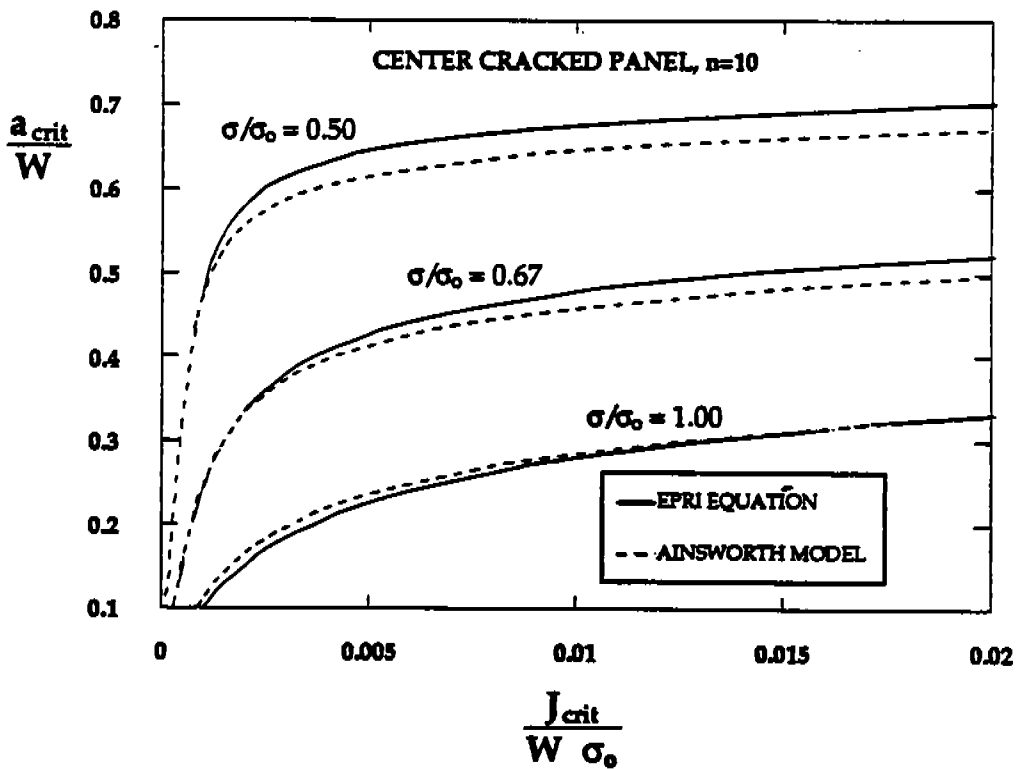


FIG. 4.12 The effect of fracture toughness on critical crack size in a center cracked panel with $n=10$ at various stress levels.

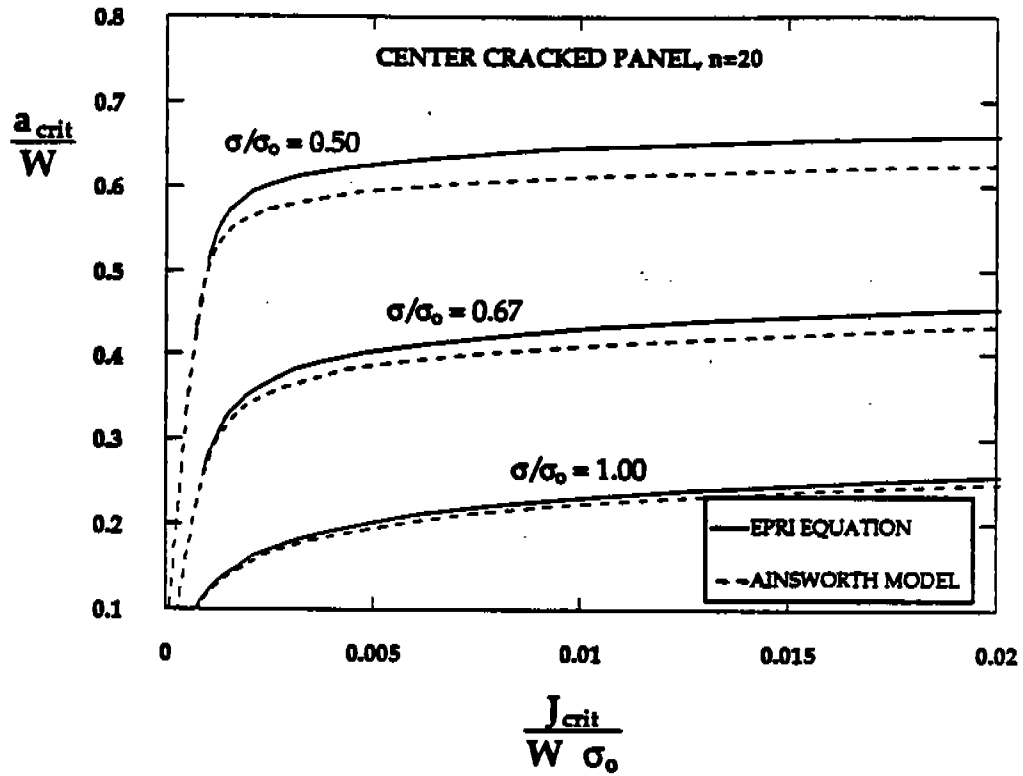


FIG. 4.13 The effect of fracture toughness on critical crack size in a center cracked panel with $n = 20$ at various stress levels.

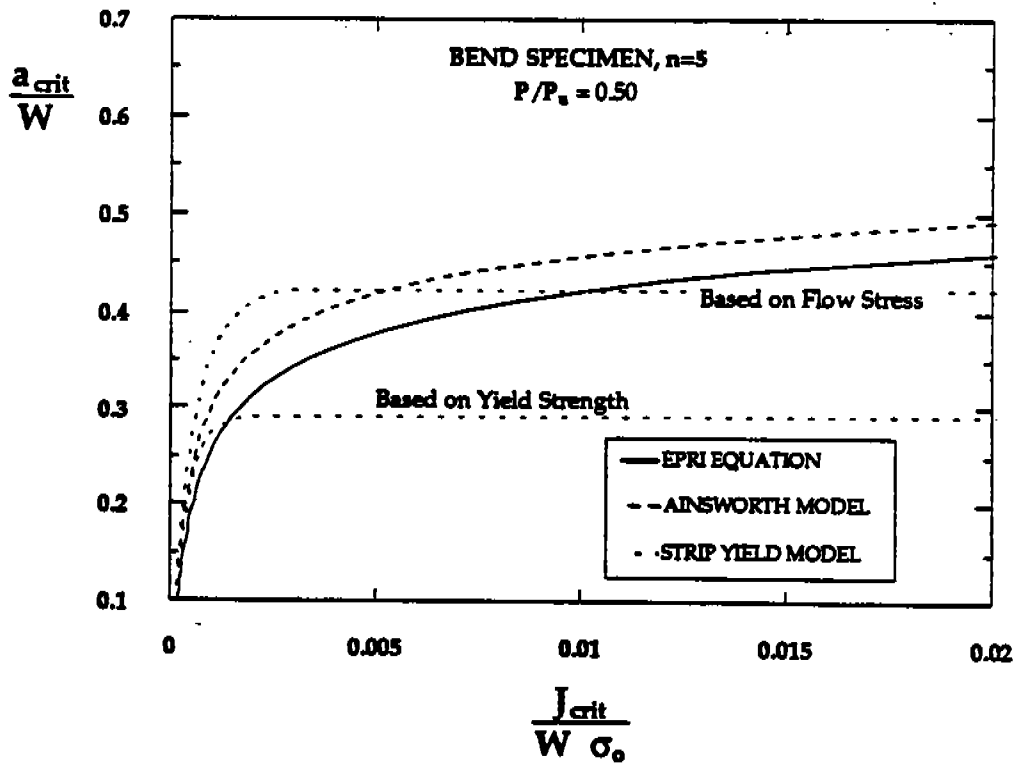


FIG. 4.14 The effect of fracture toughness on critical crack size in a bend specimen with $n = 5$ and the load equal to half the unnotched limit load.

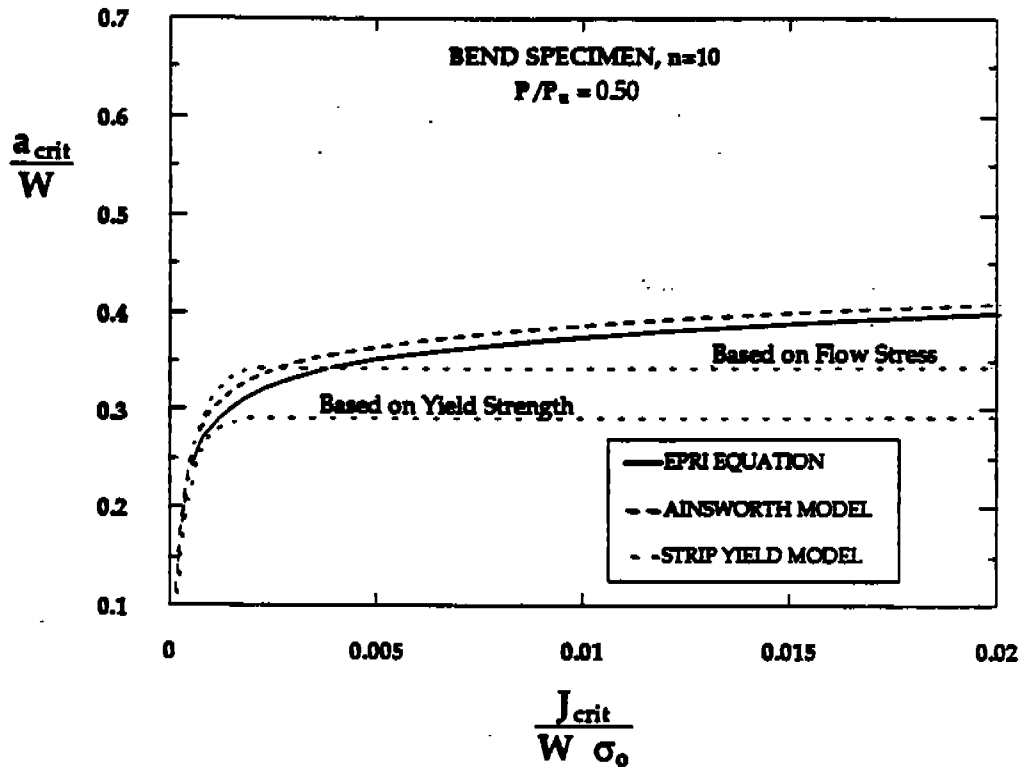


FIG. 4.15 The effect of fracture toughness on critical crack size in a bend specimen with $n = 10$ and the load equal to half the unnotched limit load.

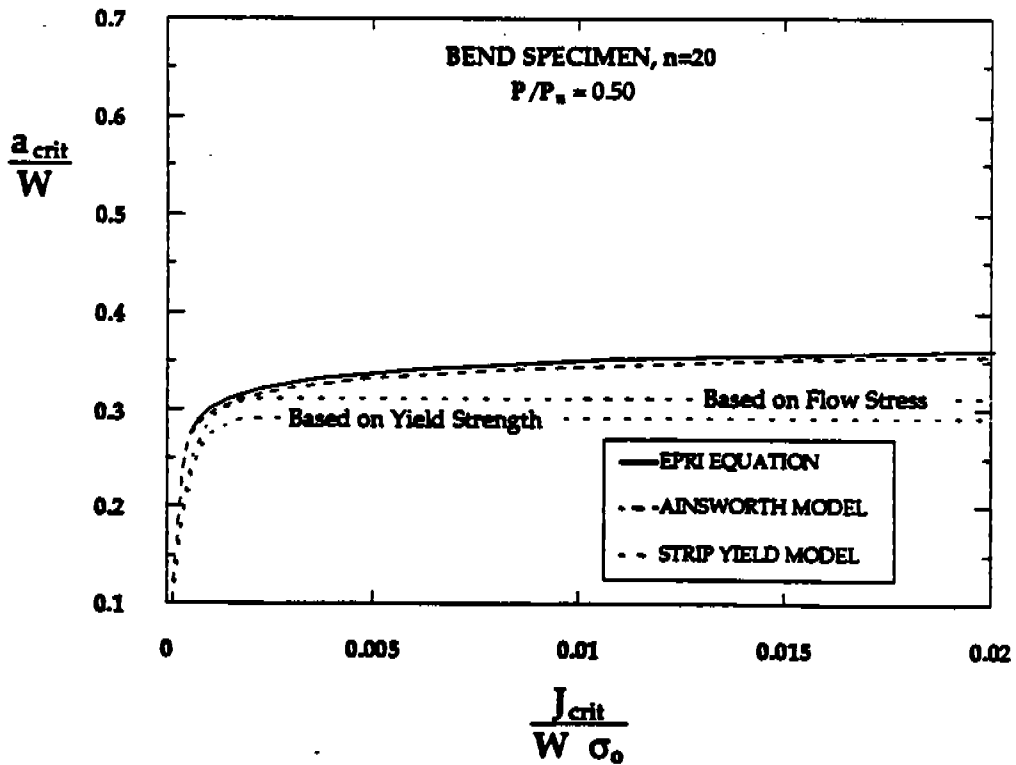


FIG. 4.16 The effect of fracture toughness on critical crack size in a bend specimen with $n = 20$ and the load equal to half the unnotched limit load.

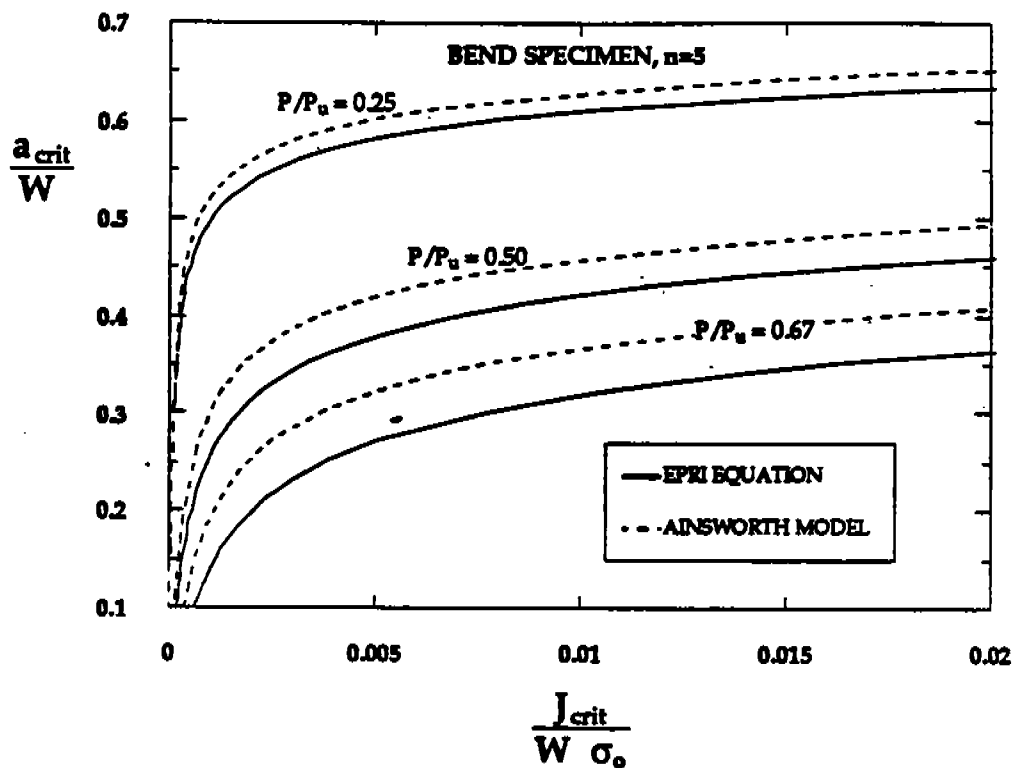


FIG. 4.17 The effect of fracture toughness on critical crack size in a bend specimen with $n = 5$ at various load levels.

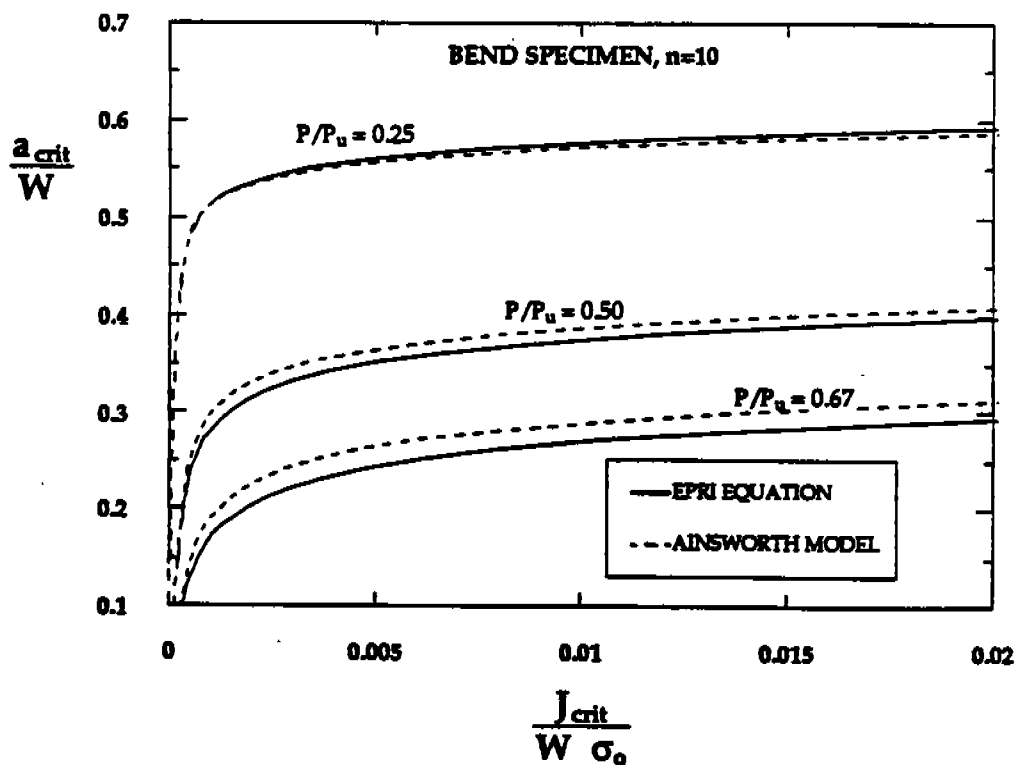


FIG. 4.18 The effect of fracture toughness on critical crack size in a bend specimen with $n = 10$ at various load levels.

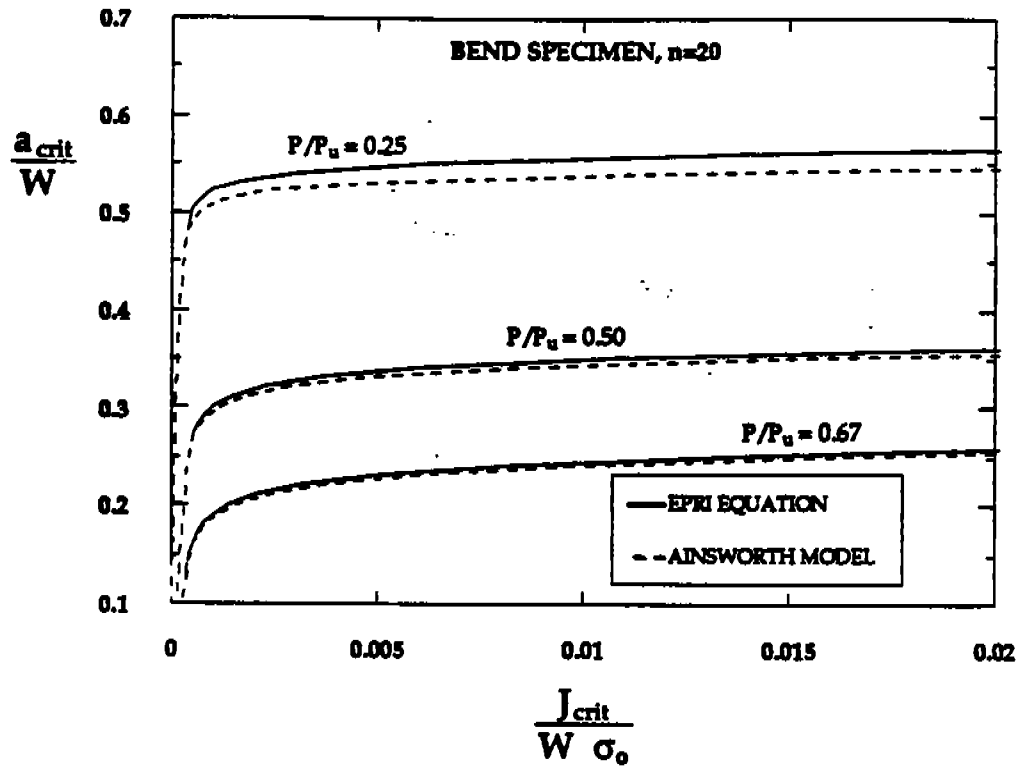


FIG. 4.19 The effect of fracture toughness on critical crack size in a bend specimen with $n = 20$ at various load levels.

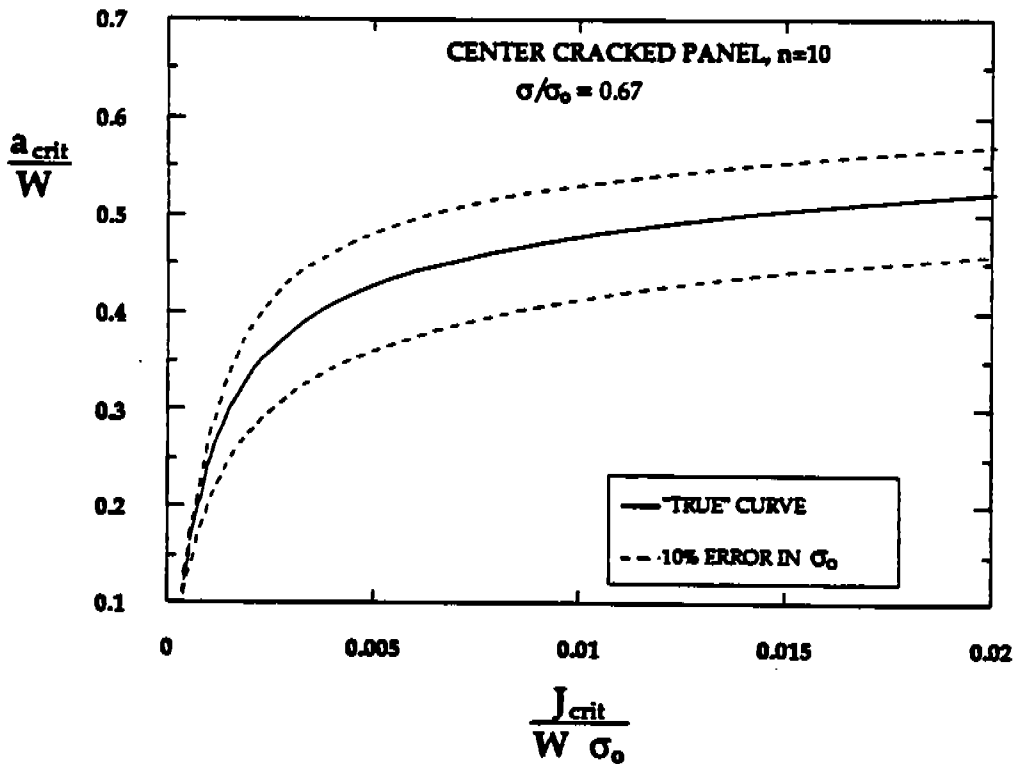


FIG. 4.20 The effect of a 10% error in flow properties on critical crack size estimates from the EPRI approach.

4.5 PROBABILISTIC FRACTURE MECHANICS

Most fracture mechanics analyses are deterministic; i.e., a single value of fracture toughness is used to estimate failure stress or critical crack size. Much of what happens in the real world, however, is not predictable. Since fracture toughness data in the ductile-brittle transition region are widely scattered, it is not appropriate to view fracture toughness as a single-valued material constant. Other factors also introduce uncertainty into fracture analyses. A structure may contain a number of flaws of various sizes, orientations and locations. Extraordinary events such as hurricanes, tidal waves and accidents can result in stresses significantly above the intended design level. Because of these complexities, fracture should be viewed probabilistically rather than deterministically.

Figure 4.21 is a schematic probabilistic fracture analysis. The curve on the left represents the distribution of flaws in the structure; the curve on the right is the critical flaw distribution. This distribution depends on the applied stress and the distribution of fracture toughness. The critical flaw size corresponding to a particular stress and toughness can be computed from one of the driving force equations described in previous sections. When the distributions of critical and actual flaws overlap, there is a finite probability of failure, indicated by the shaded area. Time-dependent crack growth, such as fatigue and stress corrosion cracking, can be taken into account by applying the appropriate growth law to the flaw distribution. This distribution moves to the right with time, increasing the failure probability.

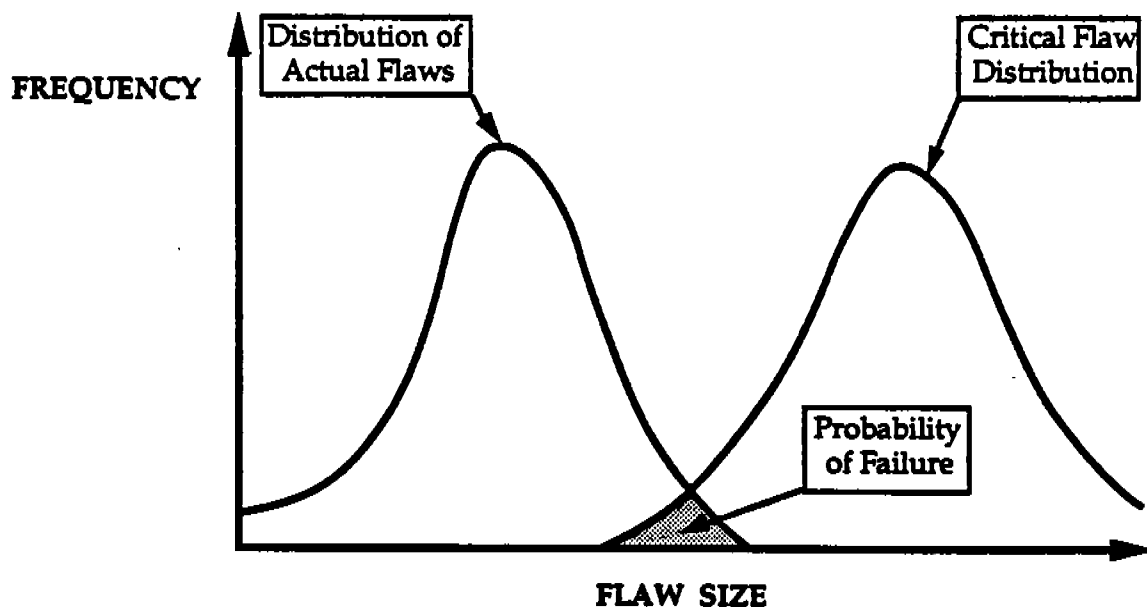


FIG. 4.21 Schematic of a probabilistic fracture analysis.

The mathematics of probabilistic analysis is well established (116). Reliability engineering is currently applied in a variety of circumstances, ranging from quality control in manufacturing to structural integrity. Probabilistic fracture analyses are rare, however, because the input data are usually not available.

Scatter in fracture toughness data is the main culprit for uncertainty in critical flaw size. A probabilistic analysis traditionally requires performing a large number of fracture toughness tests to define the toughness distribution, but recent research results may greatly reduce the amount of testing required.

Section 3.5 describes a statistical model for fracture in the transition region that indicates that cleavage fracture toughness data follow a characteristic distribution. With knowledge of the shape of the toughness distribution, one needs only to establish its absolute position. This requires far fewer tests than needed if nothing is known about the distribution. An added benefit is a means for analyzing the probabilistic effect of microstructural variations and local brittle zones. This model has recently been applied to probabilistic fracture analysis of nuclear reactor pressure vessels.

4.6 TEARING INSTABILITY ANALYSIS

So far, this chapter has focused on initiation of fracture at a critical value of J , K , or $CTOD$. However, a ductile material with a rising R curve does not usually fail when J_{IC} is reached. A tearing instability analysis is required to predict ultimate failure of structures made from materials with rising R curves.

Chapter 2 introduced the concept of stable and unstable crack growth. As Fig. 2.2 illustrates, unstable crack propagation occurs when the rate of change in driving force is greater than the rate of change in material resistance. Cleavage fracture is usually unstable because the material resistance decreases with crack extension (Fig. 3.32). However, crack growth in structural steels on the upper shelf is usually stable because the R curves are relatively steep. On the other hand, high strength aluminum alloys can fracture in an unstable manner because the R curves are fairly flat.

Figure 4.22 illustrates a tearing instability analysis based on J . The relative stability of the structure depends on how it is loaded. The solid driving force lines represent load control; the dashed lines indicate displacement control. When load is fixed, the driving force increases with crack extension, but the driving force decreases with crack extension when the displacement is fixed. The load controlled structure eventually becomes unstable as load increases, but the same structure in displacement control may remain stable.

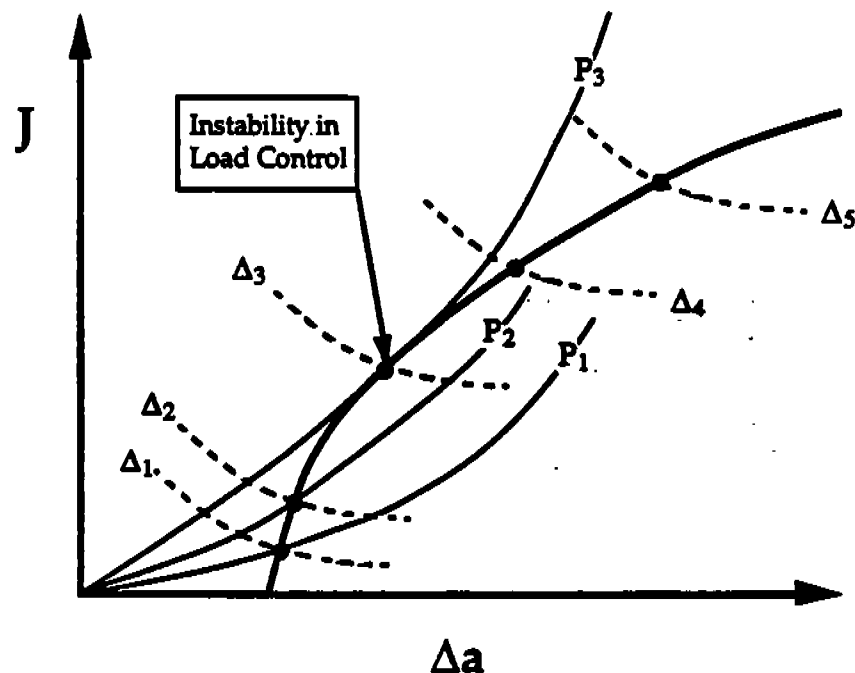


FIG. 4.22 Comparison of crack growth resistance (heavy line) with driving force in load control (solid curves) and displacement control (dashed curves).

Most structures exist somewhere between pure load control and pure displacement control. The general case can be represented schematically as a spring in series with the structure, as in Fig. 4.23. In displacement control, the system compliance, C_M , is zero; i.e., the system is infinitely stiff. Load control corresponds to an infinitely compliant system. Elastic energy stored by the "spring" helps to drive the crack. Thus the more compliant the system, the more available potential energy, and the less stable the system tends to be.

The load-displacement behavior of a hypothetical structure is illustrated in Fig. 4.24. If the structure is load controlled, it becomes unstable at the maximum load plateau. In pure displacement control, the structure remains stable, even after significant amounts of crack growth. At the intermediate condition, instability occurs after maximum load.

Paris and Hutchinson (117) have developed a detailed instability analysis for ductile materials that takes account of system compliance. Their approach has been incorporated into the EPRI elastic-plastic fracture handbook.

Paris and Hutchinson introduced the concept of the stability assessment diagram. Their approach requires that slopes of the driving force and resistance curves be nondimensionalized by means of the tearing modulus. The tearing modulus for the material is defined as

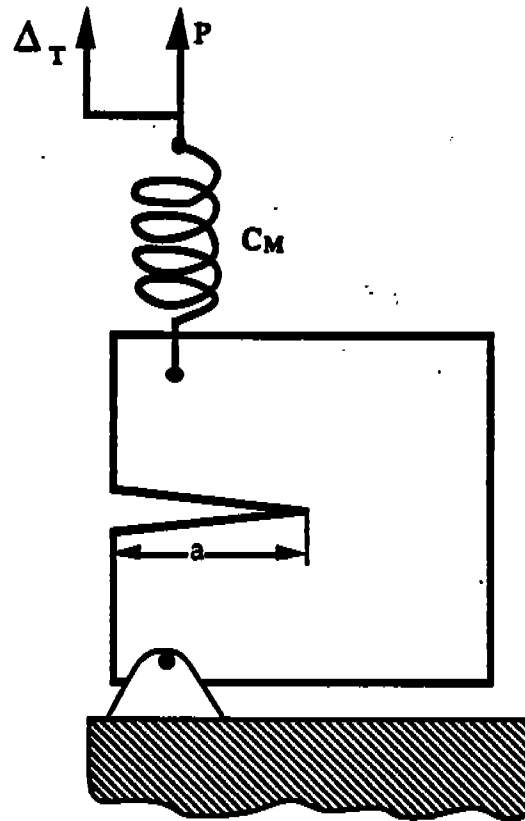


FIG. 4.23 Schematic structure loaded to a fixed remote displacement. C_M is the system compliance.

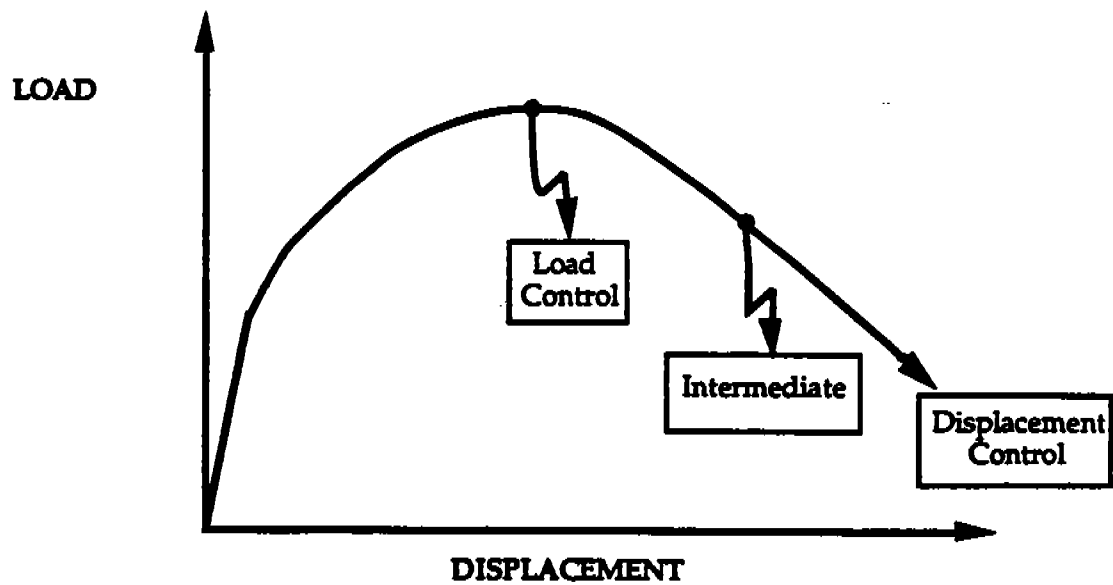


FIG. 4.24 Schematic load-displacement curve. The relative stability of the structure depends on C_M .

$$T_{JR} = \frac{E}{\sigma_0^2} \frac{dJ_R}{da} \quad [4.34]$$

where J_R is the value of J on the R curve. The applied T depends on the partial derivative of J at a fixed remote displacement:

$$T_J = \frac{E}{\sigma_0^2} \left(\frac{\partial J}{\partial a} \right)_{\Delta_T} \quad [4.35]$$

The conditions for stable and unstable crack extension are as follows.

$$T_J < T_{JR} \quad (\text{stable}) \quad [4.36a]$$

$$T_J \geq T_{JR} \quad (\text{unstable}) \quad [4.36b]$$

The above conditions for stability are analogous to those presented in Chapter 2 for linear elastic conditions (Eq. [2.2]). The partial derivative in Eq. [4.35] is obtained from a rather complex expression:

$$\left(\frac{\partial J}{\partial a} \right)_{\Delta_T} = \left(\frac{\partial J}{\partial a} \right)_P - \left(\frac{\partial J}{\partial P} \right)_a \left(\frac{\partial \Delta}{\partial a} \right)_P \left[C_M + \left(\frac{\partial \Delta}{\partial P} \right)_a \right]^{-1} \quad [4.37]$$

Each of the terms in the above expression is obtained separately from the relationships for P , Δ , and J in the EPRI handbook. The computation is laborious if done manually; but for most practical situations, one can make the conservative assumption that the structure is load controlled and $C_M = \infty$, simplifying Eq. [4.37] considerably:

$$\left(\frac{\partial J}{\partial a} \right)_{\Delta_T} = \left(\frac{\partial J}{\partial a} \right)_P \quad [4.38]$$

The situations in which one would perform a complete analysis with Eqs. [4.34] to [4.37] are rare. As illustrated in Fig. 4.4, instability occurs after maximum load if the system compliance is finite, but no competent designer would let a structure to go beyond limit load under normal service conditions. The only time a detailed tearing analysis is appropriate is for prediction of the behavior of the structure under extraordinary loading. The above approach was originally developed to analyze hypothetical accidents in nuclear reactors. Actual service stresses in a reactor pressure vessel are low enough to ensure that the structure is loaded well below the J_{IC} of the material.

4.7 SIMPLIFIED ELASTIC-PLASTIC ANALYSES

Complete tearing instability analyses can be extremely complex and there is no guarantee of accuracy, since computed J values are highly sensitive to the input data (Section 4.4). Even the three-tier approach can be complicated.

There are many instances when simple screening criteria would be useful. The analyses in Section 4.4 illustrate that if fracture toughness is above a certain level, structural failure is controlled primarily by the material's flow properties. In such cases, the designer can avoid failure merely by ensuring that the structure is stressed well below its limit load. Thus one purpose of a fracture toughness screening criterion is to define the boundary between collapse controlled failure and fracture controlled failure.

Two simple fracture toughness screening criteria have been published recently (71,118). One approach pertains to fracture initiation, either by cleavage or ductile tearing, and the other relates to tearing instability.

4.7.1 The Yield-Before-Break Criterion

The yield-before-break criterion (71) is analogous to the leak-before-break approach, a toughness criterion designed to ensure that a crack in pressure vessel or pipe grows through the wall before it becomes unstable. As its name suggests, the yield-before-break criterion quantifies the required level of toughness to ensure that fracture initiation occurs after net section yield.

Consider a structure that contains a surface flaw of depth a . If the flaw is small compared to the total cross section of the structure, the CTOD at net section yield can be estimated conservatively from the following equation.

$$\delta_{NSY} = \frac{M_m^2 a}{\phi^2} (1.25 \epsilon_Y + 0.002) \quad [4.39]$$

where M_m and ϕ are as defined in Eq. [4.25]. This equation was derived from the reference stress approach. This simple result was obtained by assuming nominal stress, reference stress, and yield strength are equal.

The yield-before-break concept can be illustrated with a simple example. If a 25 mm (1.0 in) thick plate contains a semicircular surface flaw 12 mm deep, $\delta_{NSY} = 0.09$ mm, assuming $\epsilon_Y = 0.002$. Thus if the material is at least this tough, the structure will not fail, as long as the applied stresses are below yield.

Equation [4.39] can be modified to take account of residual stresses and stress concentration effects. If yield magnitude residual stresses are present and there is a local stress concentration, k_t , the yield-before-break CTOD is given by

$$\delta_{NSY} = \frac{k_t^2 M_m^2 a}{\phi^2} (2.25 \epsilon_Y + 0.002) \quad [4.40]$$

This modified equation is based on a number of conservative assumptions. Therefore it will tend to overestimate δ_{NSY} .

A word of caution is necessary when applying this approach in the transition region. Since cleavage fracture toughness data in the transition region are invariably scattered, it is not sufficient for the *average* toughness to be above the yield-before-break threshold. In order to ensure a high probability of yield-before-break conditions, the designer should compare a *lower bound* toughness (from Table 3.1) to δ_{NSY} .

4.7.2 Critical Tearing Modulus

Not only does the reference stress model simplify fracture analyses in the transition region, it can also simplify tearing instability analysis. Anderson et al. (118) showed that it is possible to obtain closed-form solutions for ductile fracture in a number of simple configuration. These solutions can define the boundary between fracture controlled failure and collapse controlled failure on the upper shelf.

Consider a center cracked panel in plane strain. The following closed form expression was derived for the critical tearing modulus at maximum load:

$$T_c = \frac{2}{\sqrt{3}} \alpha \pi (n+1) \sec\left(\frac{\pi a}{2W}\right) \frac{a}{W} \left(1 - \frac{a}{W}\right) \left(\frac{\sigma_n}{\sigma_{YS}}\right)^{n+1} \quad [4.41]$$

By fixing the ratio σ_n/σ_{YS} , it is possible to calculate the necessary tearing modulus to reach σ_n . Figure 4.25 is a plot of sample calculations with Eq. [4.41]. The net section stress was fixed at yield and 10% above yield. The flow property constants n and α were fixed at 10 and 2.0, respectively. According to this plot, the structure will reach net section yield before tearing instability, as long as the crack is small relative to the width and the material's tearing modulus is greater than approximately 10. Since typical structural steels have tearing moduli greater than 50, nearly all steel structures on the upper shelf must completely yield before tearing instability is a possibility.

A similar expression to Eq. [4.41] has been derived for surface flaws (71). The computed T_c values are similar to the center cracked results.

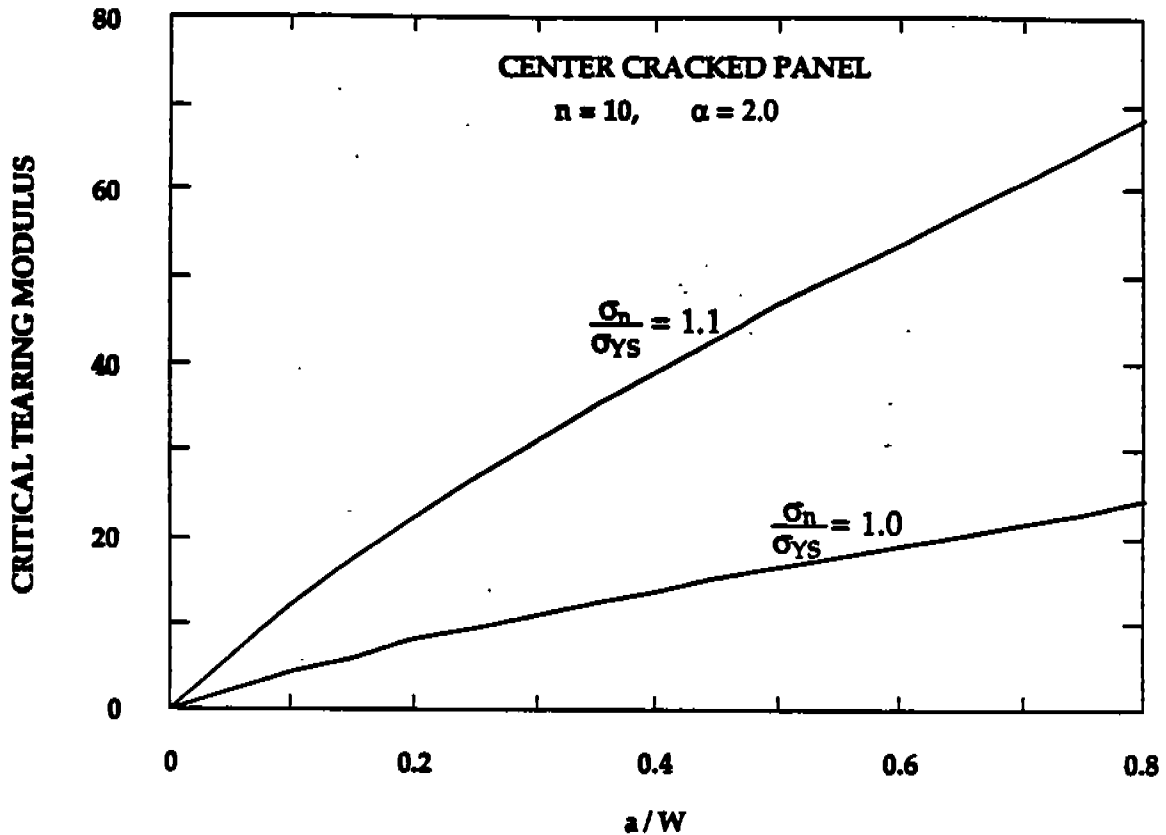


FIG. 4.25 Critical tearing modulus for a center cracked panel in plane strain(112).

With a philosophy similar to that of the yield-before-break approach, if the material is on the upper shelf and its tearing modulus is greater than the critical value, the structure will not fail as long as the net section stresses are kept below the yield strength or flow stress.

4.8 UNRESOLVED ISSUES IN ELASTIC-PLASTIC FRACTURE ANALYSIS

Although some of the fracture design analyses discussed in this chapter are complex, they still do not take into account all aspects of the problem. These analyses are two-dimensional and assume that the material is homogeneous. In addition, all fracture design analyses contain an inherent assumption that the computed driving force parameter (K , J , or $CTOD$) uniquely characterizes crack tip conditions.

The items discussed in this section do not constitute an exhaustive list of unresolved issues, but are key areas which need to be understood better before fracture analysis methods can be improved.

It should be noted that current methods of fracture analyses are generally safe. The effects discussed below tend to make current predictions conservative. A better understanding of these complexities would merely make analyses of critical conditions more accurate.

4.8.1 Driving Force in Weldments

A steel weld invariably has different flow properties than the parent metal. In most cases, the yield strength of the weld metal overmatches that of the parent metal, although undermatching sometimes occurs. Analyses such as the EPRI approach are unable to handle structures whose flow properties are heterogeneous. If a crack occurs in or near a weld, it is impossible to determine the driving force accurately without performing an elastic-plastic finite element analysis of the component.

This problem can be illustrated by citing an example from Ref. (112). Three welded aluminum center cracked panels were fabricated, with the weld metal undermatching the strength of the parent metal. The crack in each panel was in the weld, which ran perpendicular to the loading direction. Narrow strips were extracted from each weld for tensile testing. Each tensile specimen was loaded perpendicular to the welding axis, so as to be representative of loading in the wide plates. The gage section contained parent metal on either side of the weld. A strain gage was mounted on the weld to measure the effective flow properties of the weldment. These flow properties, along with crack growth resistance curves from small scale specimens, were used in conjunction with the reference stress model to perform a tearing analysis of each wide plate specimen. These analyses underestimated the failure stress by as much as 32%, despite extra care in measuring the true flow properties of these panels. The apparent explanation for the discrepancy is that the weld metal in the narrow tensile specimens was less constrained than in the wide plates. Hence the effective yield strength was higher in the wide panels.

4.8.2 Residual Stresses

The assumptions for secondary stresses have a significant effect on predictions with either the R-6 method or PD6493, but accurate information on the distribution of residual stresses is rarely available for the weld in question.

Conventional methods for measuring the through-thickness distribution of residual stress are destructive. Material from one side of the welded plate is typically removed by a milling machine while strain gage readings on the other side of the plate are recorded. Such an approach is obviously impractical for a structure in service. The center hole drilling technique does minimal damage to the structure, but it only provides information on the surface stresses. The only available method for through-thickness residual stress measurement is neutron diffraction, a technique is not portable.

A reliable, portable, nondestructive method for measuring residual stresses is desperately needed. Accurate finite element models that predict the residual stress distribution from the joint geometry and welding procedure are also desirable.

4.8.3 Three-Dimensional Effects

Existing elastic-plastic analyses do not account for the variation of the driving force along the crack front. Parks (113) has conducted numerical studies and Reuter et al. (114) have performed experiments that demonstrate that both J and CTOD vary considerably along the tips of surface flaws. Thus the crack tip conditions cannot be uniquely characterized with a single value of J or CTOD.

These three-dimensional effects influence both cleavage and ductile tearing. Since cleavage is statistical, good predictions will come only from summing the incremental failure probabilities along the crack front. Such a calculation must take account of the variation in the crack driving force with position. Since ductile crack growth occurs fastest where the driving force is highest, accurate tearing predictions are possible only with a three-dimensional analysis.

4.8.4 Crack Tip Constraint

Constraint is related to the three-dimensional issue. Plane strain fracture analyses assume that J or CTOD uniquely characterizes crack tip stresses and strains. If the entire crack front is not in plane strain, however, there are regions where a single parameter does not characterize crack tip conditions. Similarly, the single parameter assumption breaks down under large scale plasticity, which decrease the crack tip constraint. This constraint loss can occur at very low J (or CTOD) values in structures loaded predominantly in tension (see Section 3.5.2). In such cases, the structure has a higher apparent toughness than the small scale fracture toughness tests, which were loaded predominantly in bending.

The experiments and analyses of surface cracks by Reuter et al. (120) and Parks (121) demonstrate the complexities of constraint. The apparent driving force, quantified by either J or CTOD, was highest at the maximum crack depth; i.e., along an axis perpendicular to the plate surface. The J and CTOD values decreased smoothly along the crack front, reaching a minimum at the free surface, but the maximum crack growth occurred along an axis approximately 45° from the free surface. Parks' finite element analyses indicated that this was also the location of the highest normal stresses, even though J and CTOD were highest at the maximum crack depth. The crack tip constraint had apparently relaxed at the point of maximum depth, which was close to the back surface of the plate. Because of constraint effects, the highest *true* driving force and the maximum *apparent* driving force were at two different locations.

4.8.5 Gross-Section Yielding

The presence of a crack reduces the cross section in the structure; the net section is defined as the portion of the cross section not occupied by the crack. Net-section yielding refers to the point when the plastic zone spreads throughout the net cross section. Gross-section yielding occurs when plasticity encompasses the entire cross section.

Net-section yielding tends to occur with deep cracks, while gross section yielding is more common with shallow flaws. Since deep cracks are usually avoided in structures, gross-section yielding is much more common. Unfortunately, most elastic-plastic fracture analyses are not equipped to handle this type of deformation.

Elastic-plastic fracture analyses such as the EPRI and R-6 methods assume net-section yielding in the structure, and are conservative when gross-section yielding occurs. According to the EPRI approach, J in the fully plastic range should scale with P^{n+1} . However, experimental results of Read (121) indicate that gross-section yielding causes the applied J to increase much more gradually than expected. Thus an elastic-plastic fracture analysis can greatly overestimate the applied J in the case of gross-section yielding. Read's results indicate that gross-section yielding is most likely when the crack comprises less than 5% of the cross section.

5. DISCUSSION

This chapter is intended to provide a perspective on the state of the art in elastic-plastic fracture mechanics. Many of the issues raised in Chapters 3 and 4 are discussed below. Where appropriate, recommendations for future directions are made.

The field of fracture mechanics is relatively mature. The current state of technology is sufficiently advanced to make a major contribution to industry. Not all of the important questions have been answered. But enough is known to apply fracture mechanics to practical situations.

One sign of the field's maturity is that all of the simple problems have been solved; those that remain are very complex. Future researchers must be very creative to make significant contributions.

5.1 FRACTURE TOUGHNESS TESTING

Chapter 3 demonstrates that the K_{IC} test is of limited value for testing low- and medium-strength steels. If a steel can satisfy the size requirements of ASTM E399-83 (25), it is probably too brittle for structural applications. Thus fracture toughness in such materials must be quantified by elastic-plastic tests.

Fracture toughness testing procedures for materials on the upper shelf are well established. The J_{IC} and J-R curve standards (26, 50) provide guidelines for measuring the material's resistance to ductile fracture initiation and crack growth. One problem receiving some attention is the crack growth limits in ASTM E1152-87. Ernst (122) proposed a modified J integral, which has been moderately successful in producing geometry independent R curves beyond the normal crack growth limits. This research is driven primarily by the nuclear industry, where accurate tearing instability analyses are important, but this problem is only marginally important to the rest of the welding fabrication community.

Just as materials that satisfy the K_{IC} size criterion are usually too brittle, materials on the upper shelf are sufficiently tough so that fracture is not often a significant problem. The fracture research area most important to the welding fabrication industry is the ductile-brittle transition region.

Until recently, the transition region has received little attention from the fracture mechanics community in the United States. The CTOD standard (51), the first standardized method which can be applied to the transition region, was published in

1989 by ASTM, whereas the British Standards Institute published a CTOD standard in 1979, and CTOD data were applied to welded structures 15 years earlier.

Because J integral test methods were originally developed for the upper shelf, there is no standardized J-based test that applies to the transition region. Such a standard should be developed so that J-based driving force approaches can be applied to structures in the transition region.

One problem with both J and CTOD testing in the transition region is the lack of size criteria to guarantee a single parameter characterization of fracture. The J_{IC} size requirements are probably not restrictive enough for cleavage, and the K_{IC} requirements are too severe for elastic-plastic fracture parameters. The appropriate size requirements can be established through a combination of finite element analysis and micromechanics models, such as that described in Section 3.5.

When a single parameter description of fracture toughness is not possible, as in shallow notched specimens and tensile panels, the issue of crack tip constraint becomes important. This is a very difficult problem. Unless a simple analysis is developed that characterizes constraint loss, these effects will be impossible to quantify without performing three-dimensional, elastic-plastic finite element analyses on every configuration of interest. The two-parameter approach described in Section 3.5.2 shows some promise but requires further study.

Another important issue is fracture toughness testing of weldments. Existing standards do not address the special considerations required for weldment testing. The Welding Institute and other organizations have developed informal procedures over the years, but they need to be standardized.

Fracture toughness data in the transition region are invariably scattered, whether the tests are performed on welds or base materials, although the problem is worse in the heat-affected zone of welds. The nature of scatter in the lower transition region is reasonably well understood; procedures have been developed which allow for estimating lower-bound toughness with as few as three fracture toughness values. The problem of scatter in the upper transition region is more complicated; constraint loss and ductile crack growth combine to increase the level of scatter. Further work is necessary to quantify these effects.

An accurate correlation between Charpy energy and fracture toughness would be extremely useful. The empirical correlations developed to date are unreliable. Some progress has been made in developing theoretical correlations, but these models do not take into account all factors. If an accurate relationship can be developed, material toughness criteria based on Charpy energy can be established rationally.

5.2 APPLICATION TO STRUCTURES

Although linear elastic fracture mechanics is of limited use in fracture toughness testing of structural steels, LEFM driving force relationships are suitable for many situations. A structure of interest, if it is sufficiently large or the stresses are low, may be subjected to nearly pure linear elastic conditions. Fracture toughness can be characterized on a small specimen by a critical J value, which can then be converted to an equivalent K_{IC} and compared to the applied K_I in the structure.

Pure LEFM analysis does carry risks, however. If the stresses are above approximately half the yield strength, plasticity effects can be significant. If the LEFM analysis does not contain some type of plasticity correction, it gives no warning when the linear elastic assumptions become suspect. Sufficient skill is necessary to determine whether or not an LEFM analysis is valid in a given situation.

It is perhaps better to apply an elastic-plastic driving force relationship to all problems; then, the appropriate plasticity corrections are available when needed. When a linear elastic analysis is acceptable, the elastic-plastic approach will reduce to the LEFM solution. Thus the analysis decides whether or not a plasticity correction is needed.

Several types of elastic-plastic fracture analyses are available. The CTOD design curve, based primarily on an empirical correlation between wide plate tests and CTOD data, is largely obsolete. Analyses based on the strip yield model are still useful for low hardening materials. The EPRI procedure is the probably the most advanced analysis, but it is currently applicable to a limited range of configurations. The reference stress model, which is a modified version of the EPRI approach, is widely applicable. Any of these approaches can be expressed in terms of a failure assessment diagram. This is done merely for convenience, and has no significant effect on the outcome of the analysis.

The parametric study in Section 4.4 produced some interesting results. As expected, the strip yield, Ainsworth, and EPRI analyses all agreed in the linear elastic range. In the elastic-plastic and fully plastic ranges, where the three analyses might be expected to differ, predictions of failure stress and critical crack size were quite close in most cases; the only exception was when the strip yield model was applied to the high hardening ($n=5$) material. All the analyses predicted similar failure stresses and critical crack sizes because failure in the fully plastic range is governed by the flow properties of the material. Above a certain level of toughness, critical values of stress and crack size are insensitive to fracture toughness.

The analyses do differ in the prediction of the applied J , but for a designer, critical crack size and failure stress are much more important quantities. Accurate predictions of the applied J may be impossible, even with an analysis that is theoretically perfect. The applied driving force in the plastic range is highly sensitive

to the P/P_0 ratio. A slight overestimate or underestimate of P_0 significantly effects the results. If the flow properties vary even by a few percent, the resulting error in P_0 leads to a large error in the J calculation.

In summary, the driving force expression probably does not matter in most cases. The only requirements are that the expression reduce to the LEFM solution for small scale yielding and predict the correct collapse limit under large scale yielding conditions. An additional proviso is that the strip yield approach or other nonhardening models should not be applied to high hardening materials.

Since the Ainsworth model works as nearly well as the EPRI approach, there is little justification for the EPRI approach in non-nuclear applications. The EPRI procedure is more cumbersome because it requires a fully plastic geometry correction factor. The Ainsworth model produces similar results to the EPRI analysis and has the advantage of a geometry factor based on stress intensity solutions. Currently, there are many more published K solutions than h_1 solutions.

There are other not to worry about applying accurate plastic geometry factors. Real structures, especially welded structures, pose many complex problems that existing analyses cannot address. As Section 4.8 indicates, the elastic-plastic driving force in a weldment cannot be represented accurately by a solution for a homogeneous structure. Additional factors such as residual stresses, three-dimensional effects, and crack tip constraint, and gross-section yielding combine to increase the uncertainty and potential errors in fracture analyses. These errors are much more significant than those that might arise from choosing the strip yield or Ainsworth analysis over the EPRI approach. Until the complexities discussed in Section 4.8 can be addressed, one may as well adopt a simple elastic-plastic analysis.

As a first step in a fracture analysis, a simple screening criterion may be appropriate. Two such approaches are introduced in Section 4.7. The yield-before-break criterion estimates of the level of toughness required for the structure to reach net section yielding before fracture initiation. If the toughness is adequate to ensure yield-before-break conditions, fracture can be avoided simply by ensuring that the structure is loaded well below its limit load. An analogous quantity, the critical tearing modulus, is designed to ensure that the tearing resistance is adequate to avoid a tearing instability below the limit load.

6. CONCLUSIONS AND RECOMMENDATIONS

6.1 FRACTURE TOUGHNESS TESTING

- K_{IC} testing is of little value for structural steels. Fracture toughness should be quantified by elastic-plastic parameters such as J and CTOD.
- The ductile-brittle transition region is the critical area of concern in welded steel structures. If a material is on the lower shelf of toughness, it is too brittle for structural application. If the material is on the upper shelf, fracture is not a significant problem.
- A standard for J testing in the transition region should be developed.
- Size requirements for both J and CTOD measurements in the transition region should be established. Constraint loss should be quantified for cases where these size requirements are violated.
- Sufficient service experience exists to develop a standard for weldment testing, which is desperately needed.
- The nature of scatter in the lower transition region is understood reasonably well. Further work is necessary to characterize the upper transition region, where crack growth and constraint loss increase the level of scatter.
- Accurate and reliable correlations between Charpy energy and fracture toughness are not available.

6.2 APPLICATION TO STRUCTURES

- Many structures behave in a linear elastic manner but it is safer to apply a more general analysis that corrects for plasticity when necessary.
- Predictions of critical crack size and failure stress are insensitive to the driving force equation.
- Of the available elastic-plastic driving force relationships, the strip yield model and the Ainsworth reference stress approach are the most suitable for welded steel structures, but the strip yield model should not be applied to high hardening materials.

- If the toughness of the material is above a certain level, failure of the structure is controlled by the flow properties of the material rather than the fracture properties. Simple approaches to estimate the required toughness for collapse controlled failure are available.
- Future research should focus on a number of areas, including driving force in welded structures, residual stress measurements, three-dimensional effects, crack tip constraint, and gross-section yielding.

7. REFERENCES

1. Harrison, J.D., Garwood, S.J., and Dawes, M.G. "Case Studies and Failure Prevention in the Petrochemical and Offshore Industry." Presented at *Fracture 84*, 2nd National Conference on Fracture, Johannesburg, South Africa, November 26-28, 1984.
2. Griffith, A.A. "The Phenomena of Rupture and Flow in Solids." *Philosophical Transactions, Series A*, Vol. 221, 1920, pp. 163-198.
3. Irwin, G.R., "Onset of Fast Crack Propagation in High Strength Steel and Aluminum Alloys." *Sagamore Research Conference Proceedings*, Vol. 2, 1956, pp. 289-305.
4. Westergaard, H.M., "Bearing Pressures and Cracks." *Journal of Applied Mechanics*, Vol. 6, 1939, pp. 49-53.
5. Irwin, G.R., "Analysis of Stresses and Strains near the End of a Crack Traversing a Plate." *Journal of Applied Mechanics*, Vol. 24, 1957, pp. 361-364.
6. Williams, M.L., "On the Stress Distribution at the Base of a Stationary Crack." *Journal of Applied Mechanics*, Vol. 24, 1957, pp. 109-114.
7. Brown W.F. Jr. and Srawley, J.E., "Plane Strain Crack Toughness Testing of High Strength Metallic Materials." ASTM STP 410, 1966.
8. Rooke, D.P. and Cartwright, D.J., *Compendium of Stress Intensity Factors*. Her Majesty's Stationary Office, London, 1976.
9. Tada, H., Paris, P.C., and Irwin, G.R. *The Stress Analysis of Cracks Handbook*. Del Research Corporation, Hellertown, Pa, 1973.
10. Murakami, Y. *Stress Intensity Factors Handbook*. Pergamon Press, New York, 1987.
11. Irwin, G.R., "Plastic Zone Near a Crack and Fracture Toughness." *Sagamore Research Conference Proceedings*, Vol. 4, 1961.
12. Dugdale, D.S., "Yielding in Steel Sheets Containing Slits." *Journal of the Mechanics and Physics of Solids*, Vol 8, pp. 100-104.

13. Barenblatt, G.I., "The Mathematical Theory of Equilibrium Cracks in Brittle Fracture." *Advances in Applied Mechanics*, Vol VII, Academic Press, 1962, pp. 55-129.
14. Wells, A.A., "Unstable Crack Propagation in Metals: Cleavage and Fast Fracture." *Proceedings of the Crack Propagation Symposium*, Vol 1, Paper 84, Cranfield, UK, 1961.
15. Rice, J.R. " A Path Independent Integral and the Approximate Analysis of Strain Concentration by Notches and Cracks." *Journal of Applied Mechanics*, Vol. 35, 1968, pp. 379-386.
16. Hertzberg, R.W., *Deformation and Fracture of Engineering Materials*. Third Edition, John Wiley & Sons, New York, 1989.
17. Tuba, I.S., "A Method of Elastic-Plastic Plane Stress and Strain Analysis." *Journal of Strain Analysis* Vol. 1, pp. 115-122, 1966, as referenced by Broek, David, *Elementary Engineering Fracture Mechanics* (4th ed.), Kluwer Academic Publishers, Norwell, MA, 1988.
18. Burdekin, F.M. and Stone, D.E.W., "The Crack Opening Displacement Approach to Fracture Mechanics in Yielding Materials." *Journal of Strain Analysis*, Vol. 1, 1966, pp. 144-153.
19. Eshelby, J.D., "The Continuum Theory of Lattice Defects." *Solid State Physics*, Vol. 3, 1956.
20. Hutchinson, J.W., "Singular Behavior at the End of a Tensile Crack Tip in a Hardening Material." *Journal of the Mechanics and Physics of Solids*, Vol. 16, 1968, pp. 13-31.
21. Rice, J.R. and Rosengren, G.F., "Plane Strain Deformation near a Crack Tip in a Power-Law Hardening Material." *Journal of the Mechanics and Physics of Solids*, Vol. 16, 1968, pp. 1-12.
22. Shih, C.F. "Relationship between the J-Integral and the Crack Opening Displacement for Stationary and Extending Cracks." *Journal of the Mechanics and Physics of Solids*, Vol 29, 1981, pp. 305-326.
23. Anderson, T.L. "The Effect of Crack-Tip Region Constraint on Fracture in the Ductile-to-Brittle Transition Region." Ph.D. Dissertation, Colorado School of Mines, Golden, CO, October, 1983.

24. McMeeking, R.M. and Parks, D.M., "On Criteria for J-Dominance of Crack-Tip Fields in Large-Scale Yielding." ASTM STP 668, American Society of Testing and Materials, Philadelphia, PA, 1979, pp. 175-194.
25. E399-83, "Standard Test Method for Fracture Toughness of Metallic Materials." American Society for Testing and Materials, Philadelphia, PA, 1983.
26. E813-87, "Standard Test Method for J_{IC} , a Measure of Fracture Toughness." American Society for Testing and Materials, Philadelphia, PA, 1987.
27. Wellman, G.W., Sorem, W.A., Dodds, Jr., R.H., and Rolfe, S.T., "Specimen Thickness Effects for Elastic-Plastic CTOD Toughness of A36 Steel." ASTM STP 945, American Society of Testing and Materials, Philadelphia, PA, 1988 pp. 535-554.
28. Knott, J.F., "Micromechanisms of Fracture and the Fracture Toughness of Engineering Alloys, *Fracture 1977*, Vol 1, ICF4, Waterloo Canada, June 1977, p. 61.
29. *Fractography and Atlas of Fractographs*, Metals Handbook, Eight Edition, Vol. 9, American Society for Metals, Metals Park, Ohio, 1974.
30. McMahan, C.J. Jr and Cohen, M., "Initiation of Cleavage in Polycrystalline Iron." *Acta Metallurgica*, Vol 13, 1965, p. 591.
31. Smith, E., "The Nucleation and Growth of Cleavage Microcracks in Mild Steel." *Proceedings of the Conference on the Physical Basis of Fracture*, Institute of Physics and Physics Society, 1966, p. 36.
32. Cottrell, A.H., "Theory of Brittle Fracture in Steel and Similar Metals." *Transactions of the ASME*, Vol 212, 1958, p. 192.
33. Dolby, R.E. and Knott, J.F., *Journal of the Iron and Steel Institute*, Vol 210, 1972, p. 857.
34. Gerberich, W.W. "Metallurgical Aspects of Crack Tip Failure Processes." ASTM STP 945, American Society of Testing and Materials, Philadelphia, PA, 1988 pp. 5-18.
35. Lin, T., Evans, A.G. and Ritchie, R.O., "Statistical Model of Brittle Fracture by Transgranular Cleavage." *Journal of the Mechanics and Physics of Solids*, Vol 34, 1986, pp. 477-496.
36. Irwin, G.R., Presentation at the meetings of ASTM Committee E24 on Fracture Testing, Reno, NV, April 1988.

37. Ritchie, R.O., Knott, J.F., and Rice, J.R. "On the Relationship between Critical Tensile Stress and Fracture Toughness in Mild Steel." *Journal of the Mechanics and Physics of Solids*, Vol. 21, 1973, p. 395.
38. Curry D.A. and Knott, J.F., "Effect of Microstructure on Cleavage Fracture Toughness in Mild Steel." *Metal Science*, Vol. 13, 1979, p. 341.
39. Curry, D.A., "Comparison between Two Models of Cleavage Fracture." *Metal Science*, Vol 14, 1980, p.78.
40. Wallin, K., Saario, T., and Törrönen, K., "Statistical Model for Carbide Induced Brittle Fracture in Steel." *Metal Science*, Vol. 18, 1984, p. 13.
41. Beremin, F.M., "A Local Criterion for Cleavage Fracture of a Nuclear Pressure Vessel Steel." *Metallurgical Transactions*, Vol. 14A, 1983, p. 2277.
42. Evans, A.G.. "Statistical Aspects of Cleavage Fracture in Steel.", *Metallurgical Transactions*, Vol. 14A, 1983, p. 1349.
43. Anderson, T.L., "A Combined Statistical/Constraint Model for the Ductile-Brittle Transition Region." ASTM STP 995, American Society of Testing and Materials, Philadelphia, PA, 1989, pp. II-563 - II-583.
44. Anderson, T.L. and Stienstra, D., "A Model to Predict the Sources and Magnitude of Scatter in Toughness Data in the Transition Region." *Journal of Testing and Evaluation*, Vol. 17, 1989, pp. 46-53.
45. Rice, J.R. and Tracey, D.M., "On the Ductile Enlargement of Voids in Triaxial Stress Fields." *Journal of the Mechanics and Physics of Solids*, Vol. 17, 1969, pp. 201-217.
46. d'Escata, Y. and Devaux, J.C., "Numerical Study of Initiation, Stable Crack Growth, and Maximum Load with a Ductile Fracture Criterion Based on the Growth of Holes." ASTM STP 668, American Society of Testing and Materials, Philadelphia, PA, 1979, pp. 229-248.
47. Devaux; J.C., Rousselier, G., Mudry, and Pineau, "An Experimental Program for the Validation of Local Ductile Fracture Criteria Using Axisymmetrically Cracked Bars and Compact Tension Specimens." *Engineering Fracture Mechanics*, Vol. 21, 1985, pp. 273-283.
48. Heerens, J. and Read, D.T., "Fracture Behavior of a Pressure Vessel Steel in the Ductile-to-Brittle Transition Region." NISTIR 88-3099, National Institute for Standards and Technology, Boulder, CO, December, 1988.

49. Watanabe, J., Iwadate, T., Tanaka, Y., Yokoboro, T. and Ando, K., "Fracture Toughness in the Transition Region." *Engineering Fracture Mechanics*, November 1987.
50. E1152-87 "Standard Test Method for Determining J-R Curves." American Society for Testing and Materials, Philadelphia, PA, 1987.
51. E1290-89 "Standard Test Method for Crack Tip Opening Displacement Testing." American Society for Testing and Materials, Philadelphia, PA, 1989.
52. BS5762: 1979, "Methods for Crack Opening Displacement (COD) Testing." British Standards Institution, 1979.
53. Dawes, M.G. "Elastic-Plastic Fracture Toughness Based on the COD and J-Contour Integral Concepts." ASTM STP 668, American Society of Testing and Materials, Philadelphia, PA, 1979, pp. 306-333.
54. Anderson, T.L., McHenry, H.I. and Dawes, M.G., "Elastic-Plastic Fracture Toughness Testing with Single Edge Notched Bend Specimens." ASTM STP 856, American Society of Testing and Materials, Philadelphia, PA, 1985. pp. 210-229.
55. Dawes, M.G., Pisarski, H.G. and Squirrell, H.G., "Fracture Mechanics Tests on Welded Joints" ASTM STP 995, American Society of Testing and Materials, Philadelphia, PA, 1989, pp. II-191 - II-213.
56. Satok K. and Toyoda, M., "Guidelines for Fracture Mechanics Testing of WM/HAZ." Working Group on Fracture Mechanics Testing of Weld Metal/HAZ, International Institute of Welding, Commission X, IIW Document X-1113-86.
57. RP 2Z, "Recommended Practice for Preproduction Qualification of Steel Plates for Offshore Structures." American Petroleum Institute, 1987.
58. Towers O.L. and Dawes, M.G., "Welding Institute Research on the Fatigue Pre-cracking of Fracture Toughness Specimens." ASTM STP 856, American Society of Testing and Materials, Philadelphia, PA, 1985. pp. 23-46.
59. Steffen, A.A., Packman, P.F. and Dawes, M.G., "The Effect of Pre-cracking Variables R and K_{FMAX} on Fracture Toughness." *Proceedings of the Seventh International Conference on Fracture (ICF7)*, 1989, pp. 1445-1452.
60. Fairchild, D.P., "Local Brittle Zones in Structural Weldments." in *Welding Metallurgy of Structural Steels*, The Metallurgical Society of AIME, Warrendale, PA, 1987.

61. Anderson, T.L., "Crack Tip Parameters for Large Scale Yielding and Low Constraint Configurations." Accepted for publication in *International Journal of Fracture*, to appear 1989.
62. Wallin, K., "The Scatter in K_{IC} Results." *Engineering Fracture Mechanics*, Vol. 19, 1984, p. 1085.
63. Slatcher, S., and Evandt, O., "Practical Application of the Weakest-link Model to Fracture Toughness Problems." *Engineering Fracture Mechanics*, Vol. 24, 1986, p. 508.
64. Stienstra, D., Anderson T.L., and Ringer, L.J., "Statistical Inferences on Cleavage Fracture Toughness Data", to be published in *Journal of Engineering Materials and Technology*.
65. Jones M.H. and Brown, W.F. Jr., "The Influence of Crack Length and Thickness in Plane Strain Fracture Toughness Tests." ASTM STP 463, American Society of Testing and Materials, Philadelphia, PA, 1970, p. 63.
66. Landes J.D. and Shaffer, D.H., "Statistical Characterization of Fracture in the Transition Region." ASTM STP 700, American Society of Testing and Materials, Philadelphia, PA, 1980, p. 368.
67. Anderson, T.L. and Williams, S., "Assessing the Dominant Mechanism for Size Effects in the Ductile-to-Brittle Transition Region.", ASTM STP 905, American Society of Testing and Materials, Philadelphia, PA, 1986, pp. 715-740.
68. Royer, C.P., "A User's Perspective on Heat-Affected Zone Toughness." *Welding Metallurgy of Structural Steels*, The Metallurgical Society of AIME, Warrendale, PA, 1987.
69. Pisarski, H.G. and Pargeter, R.J., "Fracture Toughness of HAZs in Steels for Offshore Structures." *Metal Construction*, Vol. 16, 1984, pp. 412-417.
70. Shih, C.F. and German, M.D., "Requirements for a One Parameter Characterization of Crack Tip Fields by the HRR Singularity." *International Journal of Fracture*, Vol. 17, 1981, pp. 27-43.
71. Anderson, T.L., "Ductile and Brittle Fracture Analysis of Surface Flaws Using CTOD." *Experimental Mechanics*, June 1988, pp. 188-193.
72. Towers, O.L., Williams, S., and Harrison, J.D., ECSC Collaborative Elastic-Plastic Fracture Toughness Testing and Assessment Methods." The Welding Institute Report 3571/10M/84, June 1984.

73. Wallin, K., "The Effect of Ductile Tearing on Cleavage Fracture Probability in Fracture Toughness Testing." *Engineering Fracture Mechanics*, in press.
74. Wallin, K., *Engineering Fracture Mechanics*, in press.
75. Kanninen, M.F. and Popelar, C.H., *Advanced Fracture Mechanics*. Oxford Science Publications, New York, 1985.
76. Naus, D.J., Nanstad, R.K., Bass, B.R., Merkle, J.G., Pugh, C.E., Corwin, W.R., and Robinson G.C., "Crack-Arrest Behavior in SEN Wide Plates of Quenched and Tempered A 533 Grade B Steel Tested under Nonisothermal Conditions." NUREG/CR-4930, U.S. Nuclear Regulatory Commission and Oak Ridge National Laboratory, August 1987.
77. Nakamura, T., Shih, C.F. and Freund, L.B., "Analysis of a Dynamically Loaded Three-Point-Bend Ductile Fracture Specimen." *Engineering Fracture Mechanics*, Vol. 25, 1986, pp. 323-339.
78. Joyce J.A. and Hacket, E.M., "Dynamic J-R Curve Testing of a High Strength Steel Using the Multispecimen and Key Curve Techniques." ASTM STP 905, American Society of Testing and Materials, Philadelphia, PA, 1984, pp. 741-774.
79. Joyce J.A. and Hacket, E.M., "An Advanced Procedure for J-R Curve Testing Using a Drop Tower." ASTM STP 995, American Society of Testing and Materials, Philadelphia, PA, 1989.
80. Barsom, J.M., "Development of the AASHTO Fracture Toughness Requirements for Bridge Steels." *Engineering Fracture Mechanics*, Vol. 7, 1975, pp. 605-618.
81. E1221-88, "Standard Method for Determining Plane-Strain Crack-Arrest Toughness, K_{Ia} , of Ferritic Steels." American Society of Testing and Materials, Philadelphia, PA, 1988.
82. Kumar, V., German, M.D., and Shih, C.F., "An Engineering Approach for Elastic-Plastic Fracture Analysis." EPRI Report NP-1931, Electric Power Research Institute, Palo Alto, CA, 1981.
83. Anon, "Brittle-Ductile Transition of Bridge Steels." Request for Proposal No. DTFH-61-86-R-00028, Federal Highway Administration, Washington, D.C., November 1985.
84. Pisarski, H.G., "A Review of Correlations Relating Charpy Energy to K_{Ic} ." *The Welding Institute Research Bulletin*, December, 1978, pp. 362-367.

85. Marandet, B. and Sanz, G., "Evaluation of the Toughness of Thick Medium Strength Steels by LEFM and Correlations Between K_{IC} and CVN." ASTM STP 631, American Society of Testing and Materials, Philadelphia, PA, 1977, pp. 72-95.
86. Rolfe, S.T. and Novak, S.T., "Slow Bend K_{IC} Testing of Medium Strength High Toughness Steels." ASTM STP 463, American Society of Testing and Materials, Philadelphia, PA, 1970, pp. 124-159.
87. Barsom, J.M. and Rolfe, S.T., "Correlation Between K_{IC} and Charpy V Notch Test Results in the Transition Temperature Range." ASTM STP 466, American Society of Testing and Materials, Philadelphia, PA, 1970, pp. 281-301.
88. Sailors, R.H. and Corten, H.T., "Relationship between Material Fracture Toughness Using Fracture Mechanics and Transition Temperature Tests." ASTM STP 514, American Society of Testing and Materials, Philadelphia, PA, 1973, pp. 164-191.
89. Begley, J.A. and Logsdon, W.A., "Correlation of Fracture Toughness and Charpy Properties for Rotor Steels." Westinghouse Report, Scientific Paper 71-1E7, MSLRF-P1-1971.
90. Ito, T., Tanaka, K. and Sato, M. "Study of Brittle Fracture Initiation from Surface Notch in Welded Fusion Line." IIW Document X-704-73, September 1973.
91. Wellman, G.W. and Rolfe, S.T., "Engineering Aspects of Crack-Tip Opening Displacement Fracture Toughness Testing." ASTM STP 856, American Society of Testing and Materials, Philadelphia, PA, 1985, p. 230.
92. Dolby, R.E., "Some Correlations between Charpy V and COD Test Data for Ferritic Weld Metals." The Welding Institute Report 109/1980, April 1980.
93. Norris, D.M., Reaugh, J.E., and Server, W.L., "A Fracture-Toughness Correlation Based on Charpy Initiation Energy." ASTM STP 743, American Society of Testing and Materials, Philadelphia, PA, 1981, p.207.
94. Anderson, T.L. and Zapata, J.E. "A Theoretical Charpy-Fracture Toughness Correlation for the Transition Region." to be published.
95. Anderson, T.L., unpublished work.
96. Garwood, S.J., A Crack-Tip Opening Displacement Method for the Analysis of Ductile Materials, ASTM STP 945, American Society of Testing and Materials, Philadelphia, PA, 1988, pp. 957-985.

97. Burdekin, F.M. and Dawes, M.G., "Practical Use of Linear Elastic and Yielding Fracture Mechanics with Particular Reference to Pressure Vessels." Proceedings of the Institute of Mechanical Engineers Conference, London, May 1971, p.28.
98. PD6493:1980, "Guidance on Some Methods for the Derivation of Acceptance Levels for Defects in Fusion Welded Joints." British Standards Institution, March 1980.
99. Kamath, M.S., "The COD Design Curve: An Assessment of Validity Using Wide Plate Tests." The Welding Institute Report 71/1978/E, September 1978.
100. Harrison, R.P., Loosemore, K., Milne, I, and Dowling, A.R., "Assessment of the Integrity of Structures Containing Defects." Central Electricity Generating Board Report R/H/R6-Rev 2, April 1980.
101. Heald, P.T., Spink, G.M., and Worthington, P.J., Post Yield Fracture Mechanics." *Materials Science and Engineering*, Vol. 10, 1972, Vol. 10, pp. 129-137.
102. Shih, C.F. and Hutchinson, J.W., "Fully Plastic Solutions and Large-Scale Yielding Estimates for Plane Stress Crack Problems." *Journal of Engineering Materials and Technology*, Vol. 98, 1976, pp. 289-295.
103. Bloom, J.M., "Prediction of Ductile Tearing Using a Proposed Strain Hardening Failure Assessment Diagram." *International Journal of Fracture*, Vol. 6., 1980, pp. R73-R77.
104. Shih, C.F., Kumar, and German, M.D., "Studies on the Failure Assessment Diagram Using the Estimation Scheme and J-Controlled Crack Growth Approach." ASTM STP 803, American Society of Testing and Materials, Philadelphia, PA, 1988, pp. II-239 - II-261.
105. Kumar, V., German, M.D., Wilkening, W.W., Andrews, W.R., deLorenze, H.G., and Mowbray, D.F., "Advances in Elastic-Plastic Fracture Analysis." EPRI Report NP-3607, Electric Power Research Institute, Palo Alto, CA, 1984.
106. Kumar, V. and German, M.D., "Elastic-Plastic Fracture Analysis of Through-Wall and Surface Flaws in Cylinders." EPRI Report NP-5596, Electric Power Research Institute, Palo Alto, CA, 1988.
107. Zahoor, A. "Ductile Fracture Handbook, Volume 1: Circumferential Throughwall Cracks." EPRI Report NP-6301-D, Electric Power Research Institute, Palo Alto, CA, 1989.

108. Bloom, J.M., Simplified Procedures for Handling Self-Equilibrating Secondary Stresses in the Deformation Plasticity Failure Assessment Diagram Approach." ASTM STP 995, American Society for Testing and Materials, Philadelphia, PA, 1989, pp. II-280 - II-305.
109. Ainsworth, R.A., "The Assessment of Defects in Structures of Strain Hardening Materials." *Engineering Fracture Mechanics*, Vol. 19, 1984, p. 633.
110. Anderson, T.L., Leggatt, R.H., and Garwood, S.J., "The Use of CTOD Methods in Fitness for Purpose Analysis." *The Crack Tip Opening Displacement in Elastic-Plastic Fracture Mechanics*, Springer-Verlag, Berlin, 1986, pp. 281-313.
111. Garwood, S.J., Willoughby, A.A., Leggatt, R.H., and Jutla, T., "Crack Tip Opening Displacement (CTOD) Methods for Fracture Mechanics Assessments: Proposals for Revisions to PD 6493." Presented at ASFM 6, Ispra, Italy, October 1987.
112. Burdekin, F.M., Garwood, S.J., and Milne, I., "The Basis for the Technical Revisions to the Fracture Clauses of PD 6493." Presented at the International Conference on Weld Failures, London, November 1988.
113. Newman, J.C and Raju, I.S., "Stress Intensity Factor Equations for Cracks in Three Dimensional Finite Bodies." ASTM STP 791, American Society of Testing and Materials, Philadelphia, PA, 1983, pp. 238-265.
114. Ainsworth, R.A., "The Treatment of Thermal and Residual Stresses in Fracture Assessments." Central Electricity Generating Board Report TPRD/0479/N84, 1984.
115. Milne, I, Ainsworth, R.A., Dowling, A.R., and Stewart, A.T., "Assessment of the Integrity of Structures Containing Defects." Central Electricity Generating Board Report R/H/R6-Rev 3, May 1986.
116. Bain, L.J., *Statistical Analysis of Reliability and Life-Testing Models*, Marcel Dekker, Inc. New York, 1978.
117. Hutchinson, J.W. and Paris, P.C., "Stability Analysis of J-Controlled Crack Growth." in *Elastic-Plastic Fracture Mechanics*, ASTM STP 668, American Society for Testing and Materials, Philadelphia, PA, 1979, pp. 37-64.
118. Anderson, T.L., Gordon, J.R. and Garwood, S.J., "On the Application of R-Curves and Maximum Load Toughness to Structures." ASTM STP 969, American Society for Testing and Materials, Philadelphia, PA, 1988, pp. 291-317.

119. Parks, D., "A Surface Crack Review: Elastic and Plastic Behavior." Proc. Symposium on Surface-Crack Growth: Models, Experiments, and Structures. Reno, NV, April 1988.
120. Reuter, W.G. and Lloyd, W.R., "Measurements of CTOD and CTOA Around Surface-Crack Perimeters and Relationships Between Elastic and Plastic CTOD Values." Proc. Symposium on Surface-Crack Growth: Models, Experiments, and Structures. Reno, NV, April, 1988.
121. Read, D.T., "Applied J-Integral in HY130 Tensile Panels and Implications for Fitness for Service Assessment." Report NBSIR 82-1670, National Bureau of Standards, Boulder, CO, 1982.
122. Ernst, H.A., "Material Resistance and Instability Beyond J-Controlled Crack Growth." ASTM STP 803, American Society for Testing and Materials, Philadelphia, PA, 1983, pp. I-191 - I-213.

COMMITTEE ON MARINE STRUCTURES

Commission on Engineering and Technical Systems

National Academy of Sciences - National Research Council

The COMMITTEE ON MARINE STRUCTURES has technical cognizance over the interagency Ship Structure Committee's research program.

Stanley G. Stiansen (Chairman), Riverhead, NY
Mark Y. Berman, Amoco Production Company, Tulsa, OK
Peter A. Gale, Webb Institute of Naval Architecture, Glen Cove, NY
Rolf D. Glasfeld, General Dynamics Corporation, Groton, CT
William H. Hartt, Florida Atlantic University, Boca Raton, FL
Paul H. Wirsching, University of Arizona, Tucson, AZ
Alexander B. Stavovy, National Research Council, Washington, DC
Michael K. Parmelee, Secretary, Ship Structure Committee,
Washington, DC

LOADS WORK GROUP

Paul H. Wirsching (Chairman), University of Arizona, Tucson, AZ
Subrata K. Chakrabarti, Chicago Bridge and Iron Company, Plainfield, IL
Keith D. Hjelmstad, University of Illinois, Urbana, IL
Hsien Yun Jan, Martech Incorporated, Neshanic Station, NJ
Jack Y. K. Lou, Texas A & M University, College Station, TX
Naresh Maniar, M. Rosenblatt & Son, Incorporated, New York, NY
Solomon C. S. Yim, Oregon State University, Corvallis, OR

MATERIALS WORK GROUP

William H. Hartt (Chairman), Florida Atlantic University, Boca Raton, FL
Fereshteh Ebrahimi, University of Florida, Gainesville, FL
Santiago Ibarra, Jr., Amoco Corporation, Naperville, IL
Paul A. Lagace, Massachusetts Institute of Technology, Cambridge, MA
John Landes, University of Tennessee, Knoxville, TN
Mamdouh M. Salama, Conoco Incorporated, Ponca City, OK
James M. Sawhill, Jr., Newport News Shipbuilding, Newport News, VA

SHIP STRUCTURE COMMITTEE PUBLICATIONS

- SSC-332 Guide for Ship Structural Inspections by Nedret S. Basar & Victor W. Jovino 1985
- SSC-333 Advance Methods for Ship Motion and Wave Load Prediction by William J. Walsh, Brian N. Leis, and J. Y. Yung 1989
- SSC-334 Influence of Weld Porosity on the Integrity of Marine Structures by William J. Walsh , Brian N. Leis, and J. Y. Yung 1989
- SSC-335 Performance of Underwater Weldments by R. J. Dexter, E. B. Norris, W. R. Schick, and P. D. Watson 1986
- SSC-336 Liquid Slosh Loading in Slack Ship Tanks; Forces on Internal Structures & Pressures by N. A. Hamlin 1986
- SSC-337 Part 1 - Ship Fracture Mechanisms Investigation by Karl A. Stambaugh and William A. Wood 1987
- SSC-337 Part 2 - Ship Fracture Mechanisms - A Non-Expert's Guide for Inspecting and Determining the Causes of Significant Ship Fractures by Karl A. Stambaugh and William A. Wood 1987
- SSC-338 Fatigue Prediction Analysis Validation from SL-7 Hatch Corner Strain Data by Jen-Wen Chiou and Yung-Kuang Chen 1985
- SSC-339 Ice Loads and Ship Response to Ice - A Second Season by C. Daley, J. W. St. John, R. Brown, J. Meyer, and I. Glen 1990
- SSC-340 Ice Forces and Ship Response to Ice - Consolidation Report by C. Daley, J. W. St. John, R. Brown, and I. Glen 1990
- SSC-341 Global Ice Forces and Ship Response to Ice by P. Minnick, J. W. St. John, B. Cowper, and M. Edgecomb 1990
- SSC-342 Global Ice Forces and Ship Response to Ice - Analysis of Ice Ramming Forces by Yung-Kuang Chen, Alfred L. Tunik, and Albert P-Y Chen 1990
- SSC-343 Global Ice Forces and Ship Response to Ice - A Second Season by P. Minnick and J. W. St. John 1990
- SSC-344 Development of an Onboard Strain Recorder by Eric Greene and William A. Wood 1987
- None Ship Structure Committee Publications - A Special Bibliography 1983